UNIVERSITY OF CALIFORNIA

Los Angeles

Dark Matter Signals

A dissertation submitted in partial satisfaction of the

requirements for the degree Doctor of Philosophy

in Physics

by

Samuel Joseph Witte

2017

ABSTRACT OF THE DISSERTATION

Dark Matter Signals

by

Samuel Joseph Witte

Doctor of Philosophy in Physics

University of California, Los Angeles, 2017

Professor Graciela B. Gelmini, Chair

A vast number of independent astrophysical and cosmological observations suggest that the dominant form of matter in the Universe, known as dark matter, is neither luminous nor baryonic. Despite nearly half a decade of research, the non-gravitational nature of dark matter, if any, remains a mystery. Motivated primarily by preferred theoretical extensions of the Standard Model and a relatively simple production mechanism, the weakly interacting massive particle (WIMP) has long been considered to be among the most appealing dark matter particle candidates. This dissertation is comprised of largely independent works that focus on understanding and constraining various signals that could arise from WIMP dark matter. Specifically, Chapters 2 and 3 address the impact that non-standard astrophysics and particle physics could have on the observed scattering rate in direct dark matter detection experiments; Chapter 4 presents a halo-dependent and an halo-independent update on the viability of a dark matter interpretation of the CDMS-II-Si data; Chapter 5 generalizes the halo-independent analysis formalism such that the compatibility of multiple experiments

can be assessed, and the preferred halo-independent parameter space can be identified, for global likelihoods comprised of at least one extended likelihood; Chapter 6 discusses the prospects for detecting gamma-rays from dark matter annihilating in local dark matter subahlos; Chapter 7 presents updated constraints on simplified dark matter models that are consistent with the Galactic Center excess; and Chapter 8 discusses the extent to which future direct detection experiments may be able to elucidate the high-energy dark matter theory from observations of low-energy nuclear recoils.

The dissertation of Samuel Joseph Witte is approved.

Alexander Kusenko

David Saltzberg

Terrance Tao

Graciela B. Gelmini, Committee Chair

University of California, Los Angeles

2017

Acknowledgements

I would like to acknowledge all those who made this work possible. First and foremost I would like to thank my advisor, Graciela Gelmini, for her support, commitment, and patience. Graciela consistently went above and beyond as an advisor, ensuring that I have been both engaged and challenged, and providing fantastic opportunities for me to develop as a physicist. Please know that I am incredibly grateful for everything you have done.

I owe a large debt of gratitude to Dan Hooper for hosting my stay at Fermilab, and for serving as an advisor during my time at the facility. Your engagement, inclusivity, and guidance, has undoubtedly made me a better physicist.

It goes without saying that this dissertation would not have been possible without the support of my collaborators. I am incredibly grateful for the contributions from the following individuals:

- my advisor, Graciela Gelmini (Chapters 2–5)
- Eugenio Del Nobile (Chapters 2 & 3)
- Ji-Haeng Huh (Chapter 5)
- Dan Hooper (Chapters 6 & 7)
- Miguel Escudero (Chapter 7)
- Vera Gluscevic and Samuel McDermott (Chapter 8).

Finally I would like to thank my friends and family for their emotional and financial support, I certainly would not be here without all of you.

BIOGRAPHICAL SKETCH

Samuel J. Witte

EDUCATION

Master of Science, Physics — **December, 2014**
University of California, Los Angeles — Los Angeles, CA

Bachelor of Arts — **May, 2013**
Washington University in St. Louis — St. Louis, MO
Major: Physics; Minor: Mathematics
Summa Cum Laude

PUBLICATIONS

S. J. Witte and G. B. Gelmini, *Updated Constraints on the Dark Matter Interpretation of CDMS-II-Si Data*, JCAP 1705 (2017) 026, [1703.06892].

S. J. Witte, V. Gluscevic and S. D. McDermott, *Prospects for Distinguishing Dark Matter Models Using Annual Modulation*, JCAP 1702 (2017) 044, [1612.07808].

M. Escudero, D. Hooper and S. J. Witte, *Updated Collider and Direct Detection Constraints on Dark Matter Models for the Galactic Center Gamma-Ray Excess*, JCAP 1702 (2017) 038, [1612.06462].

D. Hooper and S. J. Witte, Gamma Rays From Dark Matter Subhalos Revisited: Refining the Predictions and Constraints, JCAP 1704 (2017) 018, [1610.07587].

G. B. Gelmini, J.-H. Huh and S. J. Witte, *Assessing Compatibility of Direct Detection Data: Halo-Independent Global Likelihood Analyses*, JCAP 1610 (2016) 029, [1607.02445].

D. Ding, A. Rios, H. Dussan, W. H. Dickhoff, S. J. Witte, A. Polls et al., *Pairing in high-density neutron matter including short- and long-range correlations*, Phys. Rev. C94 (2016) 025802, [1601.01600].

E. Del Nobile, G. B. Gelmini and S. J. Witte, *Prospects for detection of target-dependent annual modulation in direct dark matter searches*, JCAP 1602 (2016) 009, [1512.03961].

E. Del Nobile, G. B. Gelmini and S. J. Witte, *Gravitational Focusing and Substructure Effects*

on the Rate Modulation in Direct Dark Matter Searches,JCAP 1508 (2015) 041, [1505.07538].

E. Del Nobile, G. B. Gelmini and S. J. Witte, *Target dependence of the annual modulation in direct dark matter searches*, Phys. Rev. D91 (2015) 121302, [1504.06772].

D. Ding, A. Rios, W. H. Dickhoff, H. Dussan, A. Polls and S. J. Witte, *Pairing in high-density neutron matter including short- and long-range correlations*, 1502.05673.

D. Ding, S. J. Witte, W. H. Dickhoff, H. Dussan, A. Rios and A. Polls, *Pairing in bulk nuclear matter beyond BCS*, AIP Conf. Proc. 1619 (2014) 7380, [1406.7789].

AWARDS

URA Visiting Scholars Award	**June, 2016**
UCLA Dissertation Year Fellowship	**September, 2016**
UCLA Distinguished Teaching Assistant	**December, 2016**

Contents

1 Introduction to Dark Matter **1**

2 Gravitational Focusing and Substructure Effects on the Rate Modulation in Direct Dark Matter Searches **8**

2.1 Introduction 8

2.2 DM signal and its modulation 11

2.3 Modulation analysis for various halo models 15

2.3.1 SHM 15

2.3.2 Sagittarius Stream 17

2.3.3 Dark Disk 23

2.4 Estimate of required number of events 29

2.5 Summary 34

3 Target dependence of the annual modulation in direct dark matter searches **37**

3.1 Introduction to Target-Dependent Modulation 37

3.2 DM signal and its modulation 40

3.2.1 Direct detection rate 40

3.2.2 Time dependence of the rate 43

3.3 Annual modulation for magnetic dipole DM 50

3.3.1 Elastic scattering 50

3.3.2 Inelastic scattering 63

3.3.3 Identification of non-factorizable cross sections 69

3.4 Summary 70

4 Updated Halo-Independent Constraints on CDMS-II-Si 72

4.1 Introduction 72

4.2 Halo-Independent Analysis 74

4.2.1 Halo-Independent Bounds 74

4.2.2 Halo-Independent Confidence Band 79

4.3 Data Analysis 81

4.3.1 CDMS-II-Si 83

4.3.2 XENON100 83

4.3.3 CDMSlite 2016 84

4.3.4 LUX 2016 85

4.3.5 PandaX-II 85

4.3.6 PICO-60 85

4.3.7 XENON1T 87

4.3.8 SuperCDMS SNOLAB Ge(HV) 87

4.3.9 LZ 88

4.3.10 DARWIN 88

4.3.11 DarkSide-20k 89

4.3.12 PICO-250 89

4.4 Results 89

4.5 Conclusions 96

5 Assessing Compatibility of Direct Detection Data: Halo-Independent Global Likelihood Analyses **98**

5.1 Introduction . . . 98

5.2 Review of the Extended Maximum-Likelihood Halo-independent (EHI) Analysis Method . . . 102

5.2.1 Generalized halo-independent analysis . . . 102

5.2.2 Extended maximum likelihood analysis . . . 106

5.2.3 Construction of the best fit halo function and confidence band from an extended likelihood . . . 109

5.3 Extension of EHI analysis to a global maximum likelihood . . . 112

5.4 Global Likelihood Analysis of CDMS-II-Si and SuperCDMS data . . . 118

5.5 Constrained Goodness-of-Fit Analysis . . . 122

5.6 Summary . . . 130

6 Gamma Rays From Dark Matter Subhalos Revisited: Refining the Predictions and Constraints **134**

6.1 Introduction . . . 134

6.2 Subhalo Populations in Cosmological Simulations . . . 137

6.2.1 The Via Lactea II and ELVIS Simulations . . . 139

6.2.2 The Dark Matter Profiles of Simulated Subhalos . . . 140

6.3 Detecting Dark Matter Subhalos With Gamma-Ray Telescopes . . . 152

6.3.1 Gamma-Rays from Dark Matter Subhalos . . . 152

6.3.2 Placing Constraints on the Dark Matter Annihilation Cross Section . 154
6.3.3 Prospects for Detecting Spatial Extension 156
6.3.4 Uncertainties 162
6.4 Summary and Conclusion 167

7 Updated Collider and Direct Detection Constraints on Dark Matter Models for the Galactic Center Gamma-Ray Excess 169

7.1 The Galactic Center Excess 169
7.2 Constraints 172
7.2.1 LHC 173
7.2.2 LEP-II 174
7.2.3 BaBar 175
7.2.4 Direct Detection 175
7.3 Pseudoscalar Mediated Dark Matter 176
7.4 Vector Mediated Dark Matter 185
7.5 Dark Matter Annihilating Through t-Channel Mediators 188
7.6 Summary 189

8 Prospects for Distinguishing Dark Matter Models Using Annual Modulation 193

8.1 Model Selection From Direct Detection Experiments 193
8.2 Scattering in Direct Detection Experiments 196
8.2.1 Momentum and Velocity Dependence 198

8.2.2 Time Dependence . . . 199
8.3 Distinguishing Scattering Models . . . 202
8.3.1 Summary of Models . . . 203
8.4 Simulations . . . 206
8.4.1 Analysis method . . . 208
8.5 Results . . . 210
8.6 Summary . . . 218

9 Conclusion **220**

A Dissertation Appendix **224**

A.1 The zeros of the $q(v_{\min})$ function

[Pertains to Chapter 5] . . . 224

A.1.1 The zeros are isolated above a certain $v_{\min}$ value . . . 224

A.1.2 Maximum number of isolated zeros of the function $q(v_{\min})$ for a global likelihood . . . 227

A.2 The uniqueness of the best-fit halo function

[Pertains to Chapter 5] . . . 232

A.2.1 Statement of the proof . . . 232

A.2.2 Proof that the locations of the steps cannot change . . . 235

A.2.3 Evaluation of the second directional derivatives of L . . . 236

A.3 Model Selection Prospects in Xenon (SI Interaction)

[Pertains to Chapter 8] . . . 238

1 Introduction to Dark Matter

Understanding the exact nature of dark matter has been at the forefront of astrophysics and particle physics research for more than 30 years. Despite accounting for roughly 26% of the energy density of the Universe, only the indirect gravitational influence of this mysterious matter has been observed. What follows in this Chapter is a brief review of the history of dark matter than began over a century ago. This introduction is intended to provide the reader with sufficient perspective to both frame and justify the work presented in Chapters 2-8, which focus on identifiable signals from, analysis techniques for, and constraints on one particular dark matter particle candidate, the weakly interacting massive particle (WIMP).

The earliest known reference to the term 'dark matter' has been traced to a 1906 manuscript by Henri Poincaré, however the notion of dark matter at this time hardly resembles the ideas of today [1]. Poincaré's manuscript had been referencing work by Lord Kelvin presented in 1904, that had attempted to quantify the amount non-luminous mass that could reside is the galaxy without disrupting the observed velocity dispersions [2]. Unlike today, these early works were not speculating about the existence of exotic new forms of matter, but were rather acknowledging that the limits of their technology may prevent observations of dim astrophysical objects. Despite the difference in intent, these contributions (as well as later works by the likes of Ernst Öpik, Jacobus Kapteyn, James Jeans, and Jan Oort [3–5]) developed tools and reasoning that would later be applied when evidence for non-luminous matter first arose.

In the early 1930s, Edwin Hubble and Milton Humason observed an abnormally large

scatter in the apparent velocity of eight galaxies in the Coma Cluster [6]. Two years later Fritz Zwicky applied the virial theorem to estimate the total mass of this system, and found a predicted velocity dispersion that was over an order of magnitude discrepant from the observations of Hubble and Humason [7]. Three years later, an estimation of the mass of the Virgo Cluster by Sinclair Smith yielded results that were multiple orders of magnitude discrepant with the mass projections of Hubble [8]. Skepticism and intrigue surrounded the observed discrepancies of galaxy clusters in the following decades, but additional information was required before this problem became fully accepted by the community (see e.g. [9–12] for subsequent work on observed discrepancies in galaxy clusters).

The apparent need for a non-visible component of galaxies first arose in 1970, when spectroscopic observations of the Andromeda Galaxy made by Vera Rubin and Kent Ford [13], and 21cm observations of M33 and NGC300 made by Ken Freeman [14], indicated that the rotation of visible matter within these galaxies could only be consistent with Newtonian gravity if a substantial fraction of the mass of these galaxies was 'dark', and extended far beyond the visible component. Subsequent observations confirmed these discrepant rotation curves where a generic feature of galaxies (see e.g. [15–22]), and by the end of the decade, the 'missing mass' problem was understood in the astronomy and astrophysics communities to be an increasingly serious issue [23].

At the time, the initial and most obvious solution was that the missing mass was in dark compact astrophysical objects (e.g. planets, brown dwarfs, white dwarfs, black holes, etc.), which later became known as MACHOs – short for massive compact halo objects. Two major developments in the following two decades proved fatal for this hypothesis, such that

the consensus today is that MACHOs do not comprise a significant fraction of the dark matter (with perhaps the one exception being primordial black holes, which for particular mass distributions may still account for all of the dark matter). The first of these developments was gravitational microlensing searches; these experiments attempted to measure variations in the brightness of stars that should result from the lensing of light around intermediate compact objects, should they exist in sufficient numbers [24–26]. The second, and highly complementary constraint on MACHOs, came from detailed measurements of the Universe's baryon budget (i.e. the contribution of baryons to the energy density of the Universe). These constraints arose from the requirement that precision measurements of the abundances of light elements [27–30] and the cosmic microwave background (CMB) [31, 32] remain consistent with the theory of Big Bang nucleosynthesis (BBN) (i.e. the theory which explains the production of light elements during the early Universe)[1]; to date, these measurements constrain baryons to comprise less than 20% of the total matter in the Universe [32].

In 1982, Mordehai Milgrom wrote a series of papers in which he proposed a modification to Newton's second law that allowed for galactic rotation curves to be explained without the presence of unseen matter [34–36] (this proposal was known as Modified Newtonian Dynamics, or MOND). While the theory in its original form had countless issues (e.g. it did not conserve momentum, angular momentum, or energy, and it was not obvious that it could be made consistent with relativity), contributions over the next two decades (see e.g. [37, 38]) culminated in a realistic solution (appearing in 2002), known as Tensor-Scalar-

[1] It was also pointed out in 1982, that under certain cosmological assumptions (that were only later validated), the observed fluctuations in the CMB were incompatible with a Universe comprised entirely of baryonic matter; this problem could be remedied by introducing a new massive particle with weak interactions, thereby allowing density fluctuations to grow prior to recombination [33].

Vector gravity [39]. Problems arose for theories of MOND in 2006, when weak lensing and X-ray maps of a pair of merging clusters, known as the Bullet Cluster, showed with high significance that the mass of the clusters did not trace the baryons [40]. While this has not dismayed the MOND-enthusiast community, the inability of these theories to address any major cosmological questions beyond the rotation curves of galaxies has left this community in the minority (see e.g. [41] for a modern review of the subject).

The leading theory in the community today is that dark matter likely consists of a new particle (or particles). The arguments for particle dark matter are rather simple. In order to explain galactic rotation curves, the dark matter particles must reside in a diffuse, approximately spherical, halo. Baryonic matter collapses into a disk because it dissipates energy efficiently, a consequence of coupling directly to a massless gauge boson (i.e. the photon). The statement that dark matter particles are 'dark', is a direct reflection of the fact that these particles cannot have large couplings to the photon, and thus do not dissipate energy efficiently[2]. Being non-baryonic, dark matter particles naturally allow for a consistency of the measurements of the CMB and the abundances of light elements with BBN [27–32]. As previously mentioned, Ref. [33] pointed out that CMB anisotropy measurements could be made consistent with the observed structure of the Universe if there exist a large number of massive and weakly interacting particles to seed density perturbations prior to photon decoupling – dark matter particle candidates naturally satisfy these conditions as well.

With all of this in mind, it is natural to ask what properties a viable dark matter particle

[2]There do exist theories, for example double disk dark matter [42], that introduce dissipative dynamics into the dark sector via the inclusion of a new $U(1)$ gauge symmetry that carries with it a massless boson. For such theories to remain compatible with observations of rotation curves, only a small subdominant component of the dark matter can be charged under this new $U(1)$ (or alternatively the time scale for dissipation must be long enough such that the collapse of these halos has not yet occurred.).

candidate must have? Since the abundance of dark matter observed today is consistent with the abundance observed in the early Universe (e.g. as measured by the CMB), one should expect the dark matter candidate to be either stable, or have a lifetime greater than the age of the Universe. Specifically, in order to solve the aforementioned cosmological and astrophysical discrepancies, dark matter must have an energy density of $\Omega_{\rm DM}h^2 \simeq 0.1186$ [32,43]. In order to remain 'dark' and undetected, dark matter particles must have heavily suppressed couplings to the photon and gluons. Beginning in the 1980s, numerical simulations have consistently shown that the observed structure of the Universe is inconsistent with 'hot' dark matter (i.e. dark matter that was relativistic in the early Universe); alternatively, these simulations have shown preference for cold collision-less dark matter (i.e. nonrelativistic in the early Universe)[3]. If one assumes that dark matter was in thermal equilibrium in the early Universe[4], constraints from structure formation exclude dark matter masses below $\mathcal{O}$(keV) [44] – in fact, this was among the reasons Standard Model (SM) neutrinos were rejected from the list of viable dark matter candidates (note that neutrinos are the only known particles satisfying the conditions that dark matter be weakly interacting and stable). Despite nearly 50 years of extensive research, this list roughly encompasses the generic model-independent statements that can be made about particle dark matter.

Given how little is actually known about the underlying nature of particle dark matter, the favored dark matter particle candidates became those with strong theoretical motivation. Among these favored candidates is the WIMP, characterized by a weak-scale self-annihilation

[3]Consistency can also be achieved for some models of warm dark matter, or more complex dark sectors with mixed components.

[4]This need not be the case, many enticing dark matter models have non-thermal histories (e.g. the axion).

cross section and a mass approximately in the range $\mathcal{O}(\text{GeV}) - \mathcal{O}(100\ \text{TeV})$ range. There are two primary reasons why the WIMP has been one of most extensively studied dark matter candidates: *(i)* assuming dark matter is in thermal equilibrium in the early Universe (like all SM particles), the conventional freeze-out scenario[5] conveniently and rather generically predicts the observed modern day relic abundance; *(ii)* well-motivated extensions of the SM (e.g. R-parity conserving Minimal Supersymmetric Standard Model), intended to solve other pressing problems in particle physics (e.g. the hierarchy problem, gauge coupling unification, etc.), predict new stable particles at exactly this scale. This work focuses exclusively on this type of dark matter candidate.

There exist three generic search strategies that have been developed to search for WIMP dark matter. The first, known as indirect dark matter detection, searches for the byproducts of dark matter annihilation (e.g. in the form of gamma-rays, x-rays, neutrinos, anti-matter, etc.) [45, 46], or the subsequent impact of these byproducts on the surrounding medium. The thermal origin of WIMP dark matter provides a specific prediction for the size of this annihilation signal, and thus these search strategies have proven to be a powerful probe of this candidate (see e.g. [47,48]). The second strategy, known as direct dark matter detection, attempts to observe the recoil energy imparted to nuclei after scattering with dark matter particles bound to the Galactic halo [49]. Finally, it may be possible to produce dark matter particles with colliders; if produced, the dark matter particle may carry away a significant amount of energy, leaving a distinctive signature of 'missing transverse energy'[6]. These

[5]The term freeze-out refers the decoupling of a given particle species from the plasma; this event occurs when the annihilation rate falls below the expansion rate of the Universe.

[6]It is also possible to search for new particles which may mediate dark matter interactions with the SM, producing alternative signatures in the process (e.g. deviations in particular search channel from the predicted SM rates).

methods are highly complementary, and in recent years have begun significantly probing the parameter space associated with WIMP dark matter.

What follows in Chapters 2-8 are a collection of independent papers that I have published during my time here at UCLA, all of which are related to understanding experimental signatures that may be produced by WIMP dark matter. Specifically, Chapters 2 and 3 analyze distinct signatures that may appear in the observed scattering rate of direct dark matter detection experiments arising from non-standard particle physics and astrophysics; Chapter 4 presents an update on the viability of the dark matter interpretation of CDMS-II-Si data, using both halo-dependent and halo-independent analyses; Chapter 5 extends the halo-independent analysis formalism, proving that unique best-fit halo functions and two-sided pointwise confidence bands can be constructed from global likelihoods comprised of at least one extended likelihood function; Chapter 6 attempts to analyze the signatures that would arise from dark matter annihilation in local subhalos; Chapter 7 analyzes direct detection and collider constraints on viable dark matter interpretations of the Galactic Center excess using a simplified model framework; and Chapter 8 discusses the prospects for distinguishing dark matter scattering models in the event that future direct detection experiments observe a putative signal. All papers have been maintained in their original published form. This implies there may exist a certain amount of repetition between Chapters, however it allows for each Chapter to be read as an independent entity.

2 Gravitational Focusing and Substructure Effects on the Rate Modulation in Direct Dark Matter Searches

2.1 Introduction

Astrophysical and cosmological observations indicate that dark matter (DM) is the dominant form of matter in the Universe. One of the most well-motivated candidates for DM is the weakly interacting massive particle (WIMP) [50]. WIMPs are particles with weak-scale interaction cross sections, and with masses roughly between a few GeV and hundreds of TeV. They could be detected through their scattering with atomic nuclei using sensitive, low threshold detectors. Many such direct detection experiments are currently in operation, employing a variety of target nuclei and detection techniques, attempting to gain further insight into the exact nature of DM.

Due to Earth's rotation around the Sun, we expect the DM flux seen at Earth, and therefore the scattering rate direct detection experiments (even with non-directional detectors), to be annually modulated. While the signal of WIMP scattering off of target nuclei can be faked, for example by scattering of neutrons emitted by radioactive processes in the vicinity of the detector, an annual modulation in the rate with the expected features is a much more difficult signature to be reproduced by spurious sources. Moreover, while the energy spectrum of DM events depends on the WIMP mass and interactions, a modulation in the rate will be present regardless of these details and it is therefore sometimes claimed to be a model-independent signature of DM.

In order to determine the modulation amplitude and its spectrum in energy measured by

a particular experiment, a model for the DM halo must be assumed. The standard choice for the main virialized component is the Standard Halo Model (SHM), an isothermal sphere at rest with respect to the galaxy with an isotropic Maxwellian velocity distribution [51]. Despite its simple form, the SHM is believed to capture the relevant characteristics of the dark halo and thus has been widely used in the literature. However, we expect the actual halo to deviate from this simple model. The local density and velocity distribution could actually be very different if Earth is within a DM clump (although this is unlikely [52]), stream, dark disk (DD), and/or tidal debris [53–67].

Both a stream and a DD are well motivated candidates for DM velocity substructure, capable of significantly altering the expected modulation [53–55,57–59,61–65]. Observations of the Sagittarius (Sgr) dwarf galaxy show that tidally stripped stars are currently passing through the galactic plane not far from the Sun. Simulations of this merger suggest that the DM component of the Sgr stream may be passing through the Solar System and could contribute as much as 5% to the local DM density [66,68]. A DD is a subcomponent of the halo that has a spatial distribution roughly coincident with the visible disk, co-rotating with it, but with a lagging angular velocity [61–65]. Numerical simulations have shown that DDs can form in Milky Way-type galaxies from mergers of satellite galaxies [62–64] (although recent measurements suggest this may be unlikely [69,70]). Alternatively, if a subdominant portion of DM is dissipative in nature it has the potential to collapse and form a DD, a process comparable to the formation of the baryonic disk [65].

Ref. [71] recently performed a Fourier analysis of the expected modulation and considered how the annual and higher harmonics are influenced by the eccentricity of Earth's orbit

and the possible existence of DM velocity substructure. Since the eccentricity is small, $e \approx 0.016722$, it is not expected to impact the leading harmonic. DM substructure, however, was shown in Refs. [57, 71] to profoundly impact all harmonics, including the unmodulated rate. Furthermore, Ref. [71] pointed out that if the DM velocity distribution is smooth and isotropic in the galactic frame, there exist ratios of the amplitudes of the harmonics that are independent of the scattering energy, and thus they concluded that these ratios could be used to probe the level and nature of anisotropy in the DM halo.

The annual modulation of a DM signal can also be affected by the gravitational focusing (GF) of DM by the Sun [72–74]. The extent to which the annual (first) and biannual (second) harmonics in the SHM are influenced by GF was studied in Refs. [73, 74]. They found that GF has a nearly negligible effect on the amplitude of the first harmonic, but can significantly enhance the amplitude of the second harmonic and generate energy-dependent phases in both the first and second harmonics, especially at low energy.

While the Fourier analysis of the rate has been studied for the SHM by taking into account both GF and the eccentricity of Earth's orbit [73, 74], the modification of the leading harmonics in the presence of DM substructure has only been studied for an eccentric orbit without GF [71]. The aim of this paper is to study the effect of GF on a DM halo hosting substructure. We begin by considering the relative importance of GF and the eccentricity of Earth's orbit for the first two harmonics within the SHM, and analyze the extent to which the conclusions of Ref. [71] hold when GF is considered. We then study the effect of the Sgr stream and a DD on the annual and biannual harmonics.

In Section 2.2 we review the Fourier expansion of the rate and the procedure by which

the effect of GF is incorporated. Section 2.3 presents the amplitudes and phases of the first and second harmonics for the SHM with and without DM substructure. We specifically discuss how GF affects the ability of these harmonics to probe the nature of DM velocity substructure and the extent to which it is present in the galaxy. In Section 2.4 we provide rough estimates of the minimum number of events that would be needed to confirm the existence of an annual modulation for the different halo models we consider, as well as the number of events needed to differentiate between these models. A summary and our conclusions are provided in Section 2.5.

2.2 DM signal and its modulation

Since WIMPs in the galactic halo are nonrelativistic, $v/c \sim 10^{-3}$, the amplitude for DM scattering with a nucleus initially at rest is usually expanded in powers of the small WIMP speed v and momentum transfer $q = \sqrt{2m_T E_{\rm R}}$, with m_T the mass of the target nucleus and $E_{\rm R}$ its recoil energy. The zeroth order term of the scattering amplitude in this expansion is v-independent and is usually the only term retained (unless it vanishes). This makes the angular differential WIMP-target nuclide (T) cross section $\mathrm{d}\sigma_T/\mathrm{d}\cos\theta$ independent of the WIMP speed. However, a more useful quantity entering the analysis of experimental data is the differential cross section in recoil energy $\mathrm{d}\sigma_T/\mathrm{d}E_{\rm R}$. For elastic scattering, $E_{\rm R} = v^2(1-\cos\theta)\mu_T^2/m_T$, with μ_T the WIMP-nucleus reduced mass, and one finds $\mathrm{d}\sigma_T/\mathrm{d}E_{\rm R} \propto 1/v^2$. This proportionality also holds in the leading order term for inelastic scattering.

When the scattering amplitude is independent of v, we have $\mathrm{d}\sigma_T/\mathrm{d}E_{\rm R} = \sigma_T(E_{\rm R})m_T/(2\mu_T^2 v^2)$, where $\sigma_T(E_{\rm R})$ is a factor with units of a cross section. Considering the additional factor of

v coming from the DM flux, the scattering rate reads

$$\frac{\mathrm{d}R_T}{\mathrm{d}E_\mathrm{R}} = C_T \frac{\sigma_T(E_\mathrm{R})}{2m\mu_T^2} \rho\, \eta(v_\mathrm{min}(E_\mathrm{R}), t) \ , \tag{2.1}$$

where C_T is the target mass fraction in the detector, ρ is the local DM mass density, $v_\mathrm{min}(E_\mathrm{R}) = \sqrt{m_T E_\mathrm{R}/2\mu_T^2}$ is the minimum WIMP speed necessary to induce an elastic scattering event with nuclear recoil energy E_R, and

$$\eta(v_\mathrm{min}, t) \equiv \int_{v \geqslant v_\mathrm{min}} \frac{f(\boldsymbol{v}, t)}{v}\, \mathrm{d}^3 v \tag{2.2}$$

with $f(\boldsymbol{v}, t)$ the local DM velocity distribution in Earth's rest frame.

To interpret the outcome of direct DM detection experiments within models of particle DM, one typically needs to assume a specific form of the DM velocity distribution. Once this is specified in some reference frame R, e.g. the galactic rest frame, the velocity distribution in Earth's rest frame can be obtained by the Galilean transformation $f(\boldsymbol{v}, t) = f_\mathrm{R}(\boldsymbol{v} + \boldsymbol{v}_\mathrm{ES}(t) + \boldsymbol{v}_\mathrm{SR})$, where f_R is the velocity distribution in R, $\boldsymbol{v}_\mathrm{ES}(t)$ is Earth's velocity with respect to the Sun, and $\boldsymbol{v}_\mathrm{SR}$ is the Sun's velocity in R. The time dependence of $\boldsymbol{v}_\mathrm{ES}(t)$ is due to the annual rotation of Earth about the Sun. For our analysis we take $\boldsymbol{v}_\mathrm{ES}(t)$ from Ref. [71].

In the Sun's reference frame, DM particles that are on average at rest with respect to the galaxy are seen to have a preferred direction of motion that opposes $\boldsymbol{v}_\mathrm{SR}$. For this reason, the Sun experiences a constant "wind" of DM particles. The gravitational potential of the Sun bends the trajectories of these DM particles, acting as a gravitational lens that focuses the DM particles on the leeward side. As a consequence, the DM density and velocity

distribution acquire a dependence on Earth's relative location to the Sun (see e.g. Fig. 1 of [73] for a diagrammatic representation).

The effect of GF is taken into account by replacing $f_{\rm R}(\boldsymbol{v}+\boldsymbol{v}_{\rm ES}(t)+\boldsymbol{v}_{\rm SR})$ with $f_{\rm R}(\boldsymbol{v}_{\rm SR}+\boldsymbol{v}_\infty[\boldsymbol{v}_{\rm ES}(t)+\boldsymbol{v}])$, where $\boldsymbol{v}_\infty[\boldsymbol{v}]$ is the velocity a WIMP had very far away from the Sun, where the Sun's gravity is negligible, such that its velocity when it reaches Earth is $\boldsymbol{v}$ [72, 73]. Ref. [72] has shown that $\boldsymbol{v}_\infty[\boldsymbol{v}]$ is given by

$$\boldsymbol{v}_\infty[\boldsymbol{v}] = \frac{v_\infty^2\boldsymbol{v} + \frac{1}{2}v_\infty u_{\rm esc}^2\hat{\boldsymbol{r}} - v_\infty\boldsymbol{v}(\boldsymbol{v}\cdot\hat{\boldsymbol{r}})}{v_\infty^2 + \frac{1}{2}u_{\rm esc}^2 - v_\infty(\boldsymbol{v}\cdot\hat{\boldsymbol{r}})} \ , \tag{2.3}$$

where $u_{\rm esc} = \sqrt{2GM_\odot/r} \approx 40$ km/s is the escape velocity of the Solar System at Earth's position, r is the Sun-Earth distance, and $\hat{\boldsymbol{r}}$ is the unit vector pointing from the Sun to Earth. Energy conservation ensures that $v_\infty^2 = v^2 - u_{\rm esc}^2$.

The velocity integral in Eq. (2.2) can be written as a Fourier series,

$$\eta(v_{\rm min}, t) = a_0(v_{\rm min}) + \sum_{n=1}^{\infty}\left(a_n(v_{\rm min})\cos[n\omega(t-t_0)] + b_n(v_{\rm min})\sin[n\omega(t-t_0)]\right) \ , \tag{2.4}$$

with $\omega = 2\pi/\text{year}$ and t_0 an arbitrary phase parameter. If Earth's orbit is assumed to be perfectly circular and the DM velocity distribution is isotropic, choosing t_0 to be the time at which the speed of Earth with respect to the galaxy is maximum simplifies Eq. (2.4) by setting all $b_n = 0$. Accounting for astrophysical uncertainties in the velocity of the Local Standard of Rest, the time at which the speed of Earth with respect to the galaxy is

maximum occurs somewhere between May 30$^{\text{th}}$ and June 2$^{\text{nd}}$ [7] [75].

While the coefficients of Eq. (2.4) are more easily computed, we find that it is more intuitive and accessible to characterize each harmonic by a single amplitude and a single $v_{\min}$-dependent phase:

$$\eta(v_{\min}, t) = A_0(v_{\min}) + \sum_{n=1}^{\infty} A_n(v_{\min}) \cos[n\omega(t - t_n(v_{\min}))] \ , \tag{2.5}$$

with all $A_n \geqslant 0$. Comparing Eq. (2.5) with Eq. (2.4) we find

$$A_n = \sqrt{a_n^2 + b_n^2} \ , \qquad t_n = -\frac{1}{n\omega} \arctan\left[\frac{a_n \sin(n\omega t_0) - b_n \cos(n\omega t_0)}{a_n \cos(n\omega t_0) + b_n \sin(n\omega t_0)}\right] . \tag{2.6}$$

In the next section we compare the amplitudes and phases of the first few Fourier modes of $\eta(v_{\min}, t)$ for a variety of DM velocity distributions, both with and without GF. These can be computed analytically if one excludes the contribution of GF, otherwise the calculation needs to be done numerically [73].

When considering more than one halo component (e.g. SHM plus a stream or a DD), we assume that the DM consists of a single type of particle, unless otherwise noted. In this case the amplitude of each mode in the expansion Eq. (2.4) for the various halo components can be combined linearly, weighted by their density contribution, i.e. $a_n^{\text{tot}}(v_{\min}) = \sum_i (\rho_i/\rho_{\text{tot}}) a_{n,i}(v_{\min})$ (and analogous equation for $b_n(v_{\min})$), where i labels the various DM

[7] This quoted uncertainty does not account for the fact that the exact date at which Earth's speed is maximum with respect to the Galaxy shifts on an annual basis. This arises from the fact that the Gregorian calendar is not perfectly aligned with Earth's rotation about the sun (this mismatch is of course corrected for by adding an additional day to the calendar once every four years, referred to as a leap year). In principle, this effect can easily be corrected for as the exact nature of this shift is understood.

subcomponents and $\rho_{\rm tot} \equiv \sum_i \rho_i$. Notice that the amplitude A_n of the expansion in Eq. (2.5) is not in general obtained by linearly combining the Fourier amplitudes of different DM subcomponents, since the phases will in general be different. If the DM is assumed to be composed of multiple types of particles with different masses and/or interactions, the combination is not so straightforward and one must take into account the whole factor multiplying $\eta(v_{\rm min}, t)$ in Eq. (2.1). This will be relevant for the case of DM with a dissipative component [65] in Section 2.3.3.

2.3 Modulation analysis for various halo models

2.3.1 SHM

In the SHM the DM velocity distribution in the galactic rest frame is described by an isotropic Maxwellian truncated at the galactic escape speed $v_{\rm esc}$:

$$f_{\rm R}(\boldsymbol{v}) = \frac{e^{-\boldsymbol{v}^2/v_0^2}}{(\pi v_0^2)^{3/2}\, N_{\rm esc}}\, \Theta(v_{\rm esc} - |\boldsymbol{v}|)\ , \tag{2.7}$$

where v_0 is the most probable speed in the galactic rest frame and the normalization is chosen so that $\int \mathrm{d}^3 v\, f_{\rm R}(\boldsymbol{v}) = 1$,

$$N_{\rm esc} = \mathrm{Erf}(v_{\rm esc}/v_0) - \frac{2 v_{\rm esc}}{\sqrt{\pi} v_0} e^{-v_{\rm esc}^2/v_0^2}\ . \tag{2.8}$$

We assume v_0 to be equal to the speed of the Local Standard of Rest, $v_0 = 220$ km/s [76], we take the Sun's velocity with respect to the galaxy from Ref. [71], $\boldsymbol{v}_{\rm SR} = (11, 232, 7)$ km/s,

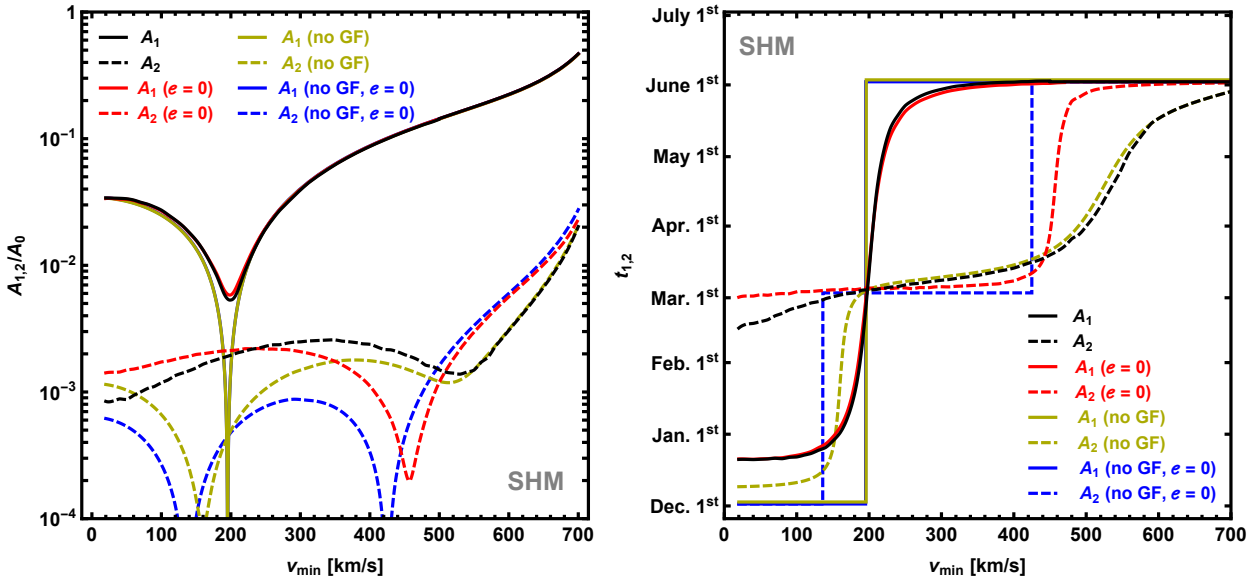

Figure 2.1: Amplitudes (left) and phases (right) for the first (solid) and second (dashed) harmonics, for the SHM including the effect of GF and the eccentricity of Earth's orbit (black), including GF but neglecting the eccentricity (red), including the eccentricity but neglecting GF (yellow), and neglecting both GF and the eccentricity (blue). The eccentricity has a negligible impact on the first harmonic, therefore the solid black line extensively overlaps the red, and the solid dark yellow line completely overlaps the blue, for both the amplitude and the phase.

and $v_{\rm esc} = 533$ km/s [77].

Fig. 2.1 shows the amplitudes and phases of the first (solid lines) and second (dashed lines) harmonic including both GF and the eccentricity of Earth's orbit in the calculations (black), including the eccentricity but neglecting GF (yellow), including GF but neglecting the eccentricity (red), and neglecting both the eccentricity and GF (blue). Notice that, due to the negligible impact of the eccentricity on the first harmonic, the solid black line extensively overlaps the red, and the solid dark yellow line completely overlaps the blue, for both the amplitude and the phase. In agreement with Refs. [73, 74], Fig. 2.1 shows that the inclusion of GF causes an approximate 20 day shift in the phase of the annual harmonic for $v_{\rm min} \lesssim 100$ km/s and eliminates the sudden phase flips, i.e. the occurrence of a jump in the

phase of a given harmonic by half the period. The phase flip can also be identified by the vanishing of the amplitude of a given harmonic. When GF is included, the amplitudes no longer vanish and the phases develop a softer $v_{\rm min}$ dependence. Actually, the presence of any anisotropy eliminates the phase flip and leads to continuous transitions in the phase. For the remainder of this paper we will loosely use the term phase flip to refer to both the previously defined jump in the phase, and the rapid, but continuous, phase transitions that may appear when anisotropy is present.

The conclusion of Ref. [71] that the ratios of the amplitudes of various harmonics can be used to probe the anisotropy of the DM halo was based on the assumption that the DM velocity distribution is isotropic in the galactic frame. The existence of GF is not consistent with this assumption. Thus the ratios in Ref. [71] only hold for large $v_{\rm min}$, where the effect of GF is not significant because DM particles spend little time in Sun's gravitational potential. Fig. 2.2 shows the ratio of coefficients b_1 and a_1, defined in Eq. (2.4), with GF (solid blue line) and without GF (dashed purple line). One can see that without GF this ratio would be independent of the scattering energy and remains at a constant value of $\simeq 1/59$, as found in Ref. [71]. GF significantly alters this result for $v_{\rm min} \lesssim 300$ km/s.

2.3.2 Sagittarius Stream

Since the parameters governing the velocity and dispersion of the Sgr stream are not well known, we will follow the assumptions of [55]. In the galactic coordinate system, we take the mean velocity of the Sgr stream in the galactic frame to be $\boldsymbol{v}_{\rm Sgr} = (-65, 135, -249)$ km/s, and model this component with an isotropic Maxwellian with dispersion $v_0 = 30\sqrt{2/3}$ km/s ≈ 25

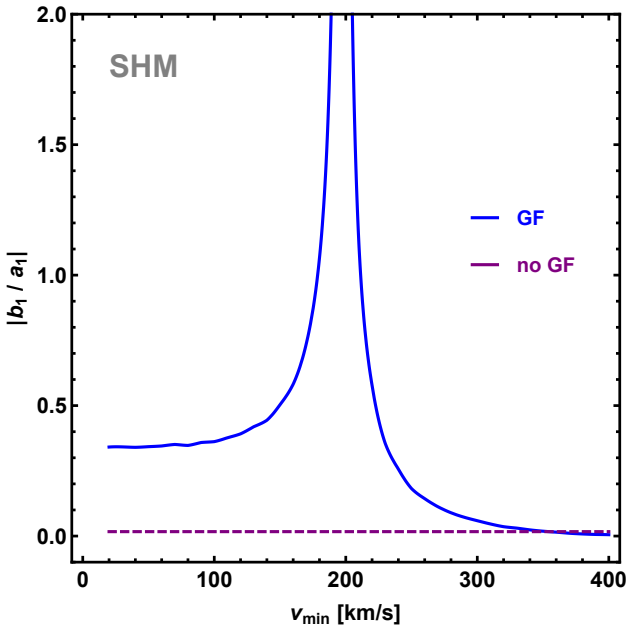

Figure 2.2: Ratio $|b_1/a_1|$ (see Eq. (2.4)) for the SHM, with GF (solid blue line) and without GF (dashed purple line). Without GF this ratio is approximately 1/59.

km/s. We model the smooth virialized component of the halo with the SHM.

Ref. [66] recently studied the effect of the Sgr stream with a self-consistent N-body simulation and found that the addition of the stream can noticeably alter $\eta(v_{\rm min}, t)$. Specifically, they found four major changes. First, incorporating the Sgr stream in a realistic halo model with a baryonic disk produced a 10–20% increase in the direct search event rate for values of $v_{\rm min}$ larger than the typical relative stream speed. Additionally, Ref. [66] found a 20–30% decrease in the fractional modulation amplitude defined as

$$\Delta \equiv \frac{\eta_{\rm max} - \eta_{\rm min}}{\eta_{\rm max} + \eta_{\rm min}} \ , \tag{2.9}$$

where $\eta_{\rm max}(v_{\rm min})$ and $\eta_{\rm min}(v_{\rm min})$ are the maximum and minimum of $\eta(v_{\rm min}, t)$ in time. If the modulation is perfectly sinusoidal with a period of one year, Δ coincides with the amplitude

of the sinusoid normalized by the unmodulated component of $\eta(v_{\rm min}, t)$, i.e. A_1/A_0. Furthermore, the phase flip of the dominant harmonic was found to occur about 10–15 km/s lower in $v_{\rm min}$, and deviations of up to about 20 days were found in the phase of the modulation at values of $v_{\rm min}$ near the typical speed of a WIMP belonging to the stream as seen in the Sun's reference frame. We begin by investigating if and how these conclusions change when GF is taken into account.

The left panel of Fig. 2.3 contains the relative increase in the unmodulated component of $\eta(v_{\rm min}, t)$ when the Sgr stream is added to the SHM (Sgr+SHM), for stream densities ranging from 1% to 5% of the DM halo density. While Fig. 2.3 does show an increase in the unmodulated component, GF appears to have no additional effect. The reason for this is explained in further detail in the following paragraphs.

The right panels of Fig. 2.3 show the fractional amplitude as defined in Eq. (2.9) for the Sgr+SHM, for $\rho_{\rm Sgr}/\rho_{\rm SHM} = 0.01$ (dashed) and 0.05 (solid), with (top) and without (bottom) GF. Here and in the following, the shaded regions between the dashed and solid lines highlight where lines corresponding to intermediate densities lie. As with the unmodulated component of the rate, the fractional modulation amplitude for Sgr+SHM seems to not be affected by GF. Small deviations from the SHM do occur at $v_{\rm min} \lesssim 200$ km/s, and at values of $v_{\rm min}$ near the speed of the stream in Earth's frame, regardless of GF. However, Fig. 4 of Ref. [66] shows that the uncertainty in the velocity distribution of the virialized component of the dark halo, specifically deviations from the assumed Maxwellian distribution, have a larger influence on $\Delta(v_{\rm min})$ than the addition of the Sgr stream to the SHM.

The effect of GF is known to increase as the relative WIMP velocity in the solar frame de-

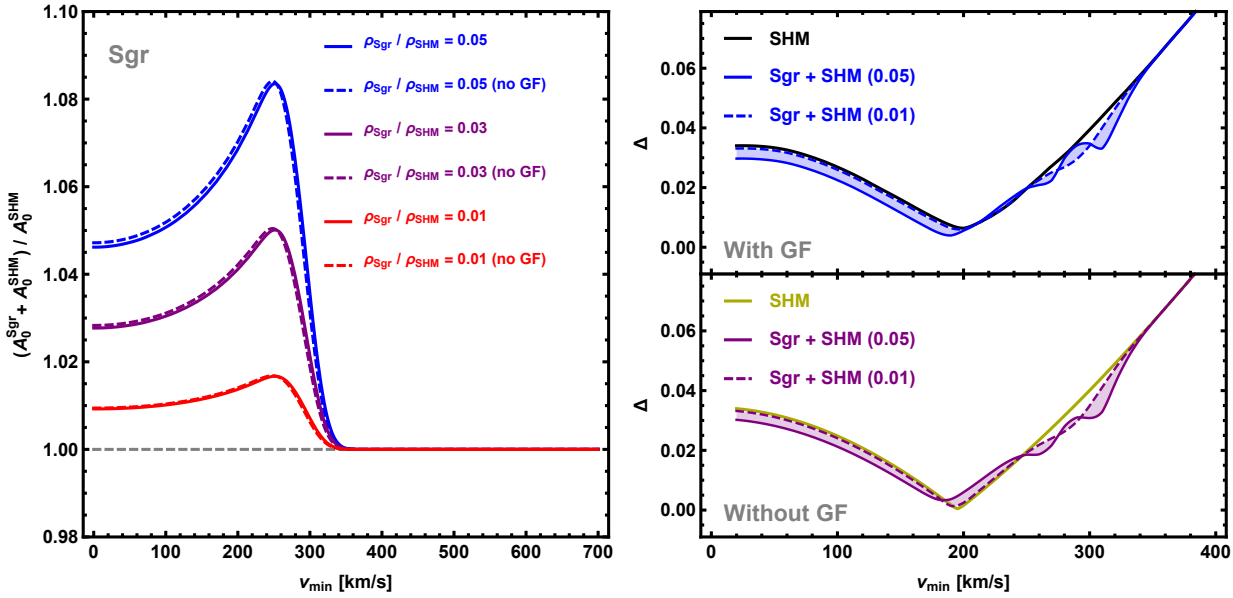

Figure 2.3: Left: Unmodulated component of $\eta(v_{\min}, t)$, A_0, for Sgr+SHM, normalized by the unmodulated component for the SHM alone, for $\rho_{\rm Sgr}/\rho_{\rm SHM} = 0.01$ (red), $\rho_{\rm Sgr}/\rho_{\rm SHM} = 0.03$ (purple), and $\rho_{\rm Sgr}/\rho_{\rm SHM} = 0.05$ (blue), with GF (solid) and without GF (dashed). Right: Fractional modulation amplitude, as defined in Eq. (2.9), for Sgr+SHM with GF (top panel) and without GF (bottom panel), and for stream densities ranging from $\rho_{\rm Sgr}/\rho_{\rm SHM} = 0.01$ (dashed) to $\rho_{\rm Sgr}/\rho_{\rm SHM} = 0.05$ (solid). Results are compared with the SHM alone, with GF (black) and without GF (yellow).

creases. This is because slower WIMPs spend more time in the Sun's gravitational potential. The parameters of the Sgr stream chosen in this paper imply the majority of the WIMPs coming from the Sgr stream move at roughly $v_{\rm Sgr}^{\rm S} \equiv 300$ km/s in the Sun's frame, with very few traveling below 250 km/s. Thus we do not find it surprising that GF has little impact on the unmodulated component of $\eta(v_{\rm min}, t)$ and the fractional modulation amplitude when the Sgr stream is added to the SHM. Notice that the SHM component of the Sgr+SHM has a lower average WIMP speed and a much larger dispersion with respect to the Sgr component, implying WIMPs from the background component of the dark halo will be more affected by GF than those in the stream. Figs. 2.4 and 2.5 show how this influences the amplitudes and phases of the first and second harmonics.

Fig. 2.4 shows the amplitude A_1 (left) and the phase t_1 (right) of the first harmonic. Without GF, A_1 would experience almost no deviation from the SHM, except around the $v_{\rm min}$ values where the SHM has a dip due to the phase flip, and in a small region near $v_{\rm Sgr}^{\rm S}$ where it decreases by at most a factor of 2. Including GF does not noticeably affect these results. When GF is accounted for, the flip of t_1 in the Sgr+SHM is delayed relative to the SHM alone, but it occurs more rapidly, causing a deviation in the phase by up to two months. As found in Ref. [66], when the Sgr stream is added to the smooth component of the halo there appears to be a significant deviation of up to two months in the phase of the annual modulation near $v_{\rm min} \simeq v_{\rm Sgr}^{\rm S}$. This effect occurs regardless of GF, and the inclusion of GF even appears to enhance this deviation for low density streams, resulting in an approximately 20 day phase shift for $\rho_{\rm Sgr}/\rho_{\rm SHM} = 0.01$.

Fig. 2.5 shows the amplitude A_2 (left) and the phase t_2 (right) of the second harmonic.

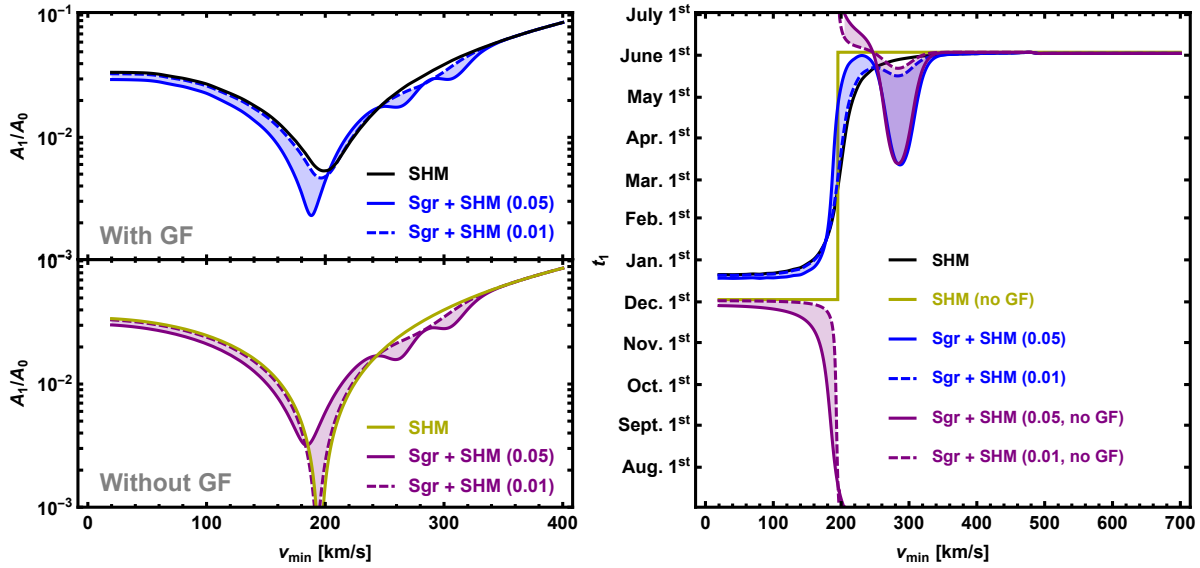

Figure 2.4: Amplitudes (left) and phases (right) of the first harmonic for the Sgr+SHM. Dashed lines are for a low density stream, $\rho_{\rm Sgr}/\rho_{\rm SHM} = 0.01$, while solid lines are for a high density stream, $\rho_{\rm Sgr}/\rho_{\rm SHM} = 0.05$. Blue lines and regions include GF, while purple lines and regions neglect GF. Results are compared with the SHM alone, with GF (black) and without GF (yellow).

The results for the phase of the second harmonic are very similar to those of the first. Without GF, A_2 would deviate significantly from the SHM only at $v_{\rm min} \simeq v_{\rm Sgr}^{\rm S}$ and around the point where the SHM amplitude has a dip due to a phase flip. When GF is included the dip vanishes but the enhancement of the amplitude at $v_{\rm min} \simeq v_{\rm Sgr}^{\rm S}$ remains. This enhancement is roughly a factor of 4 for $\rho_{\rm Sgr}/\rho_{\rm SHM} = 0.05$. Without GF, the phase would exhibit a flip at smaller $v_{\rm min}$ values and would experience strong deviations from the SHM of up to ~ 50 days for 250 km/s $< v_{\rm min} <$ 350 km/s. The inclusion of GF again washes out the low $v_{\rm min}$ deviations, but leaves those above $v_{\rm min} \approx 200$ km/s intact. Thus one would expect a 1% density stream to have a second harmonic phase similar to the SHM's, except in the region $v_{\rm min} \approx v_{\rm Sgr}^{\rm S}$, where the stream could cause deviations of as much as 45 days.

To summarize, including GF in Sgr+SHM calculations does not affect the unmodulated

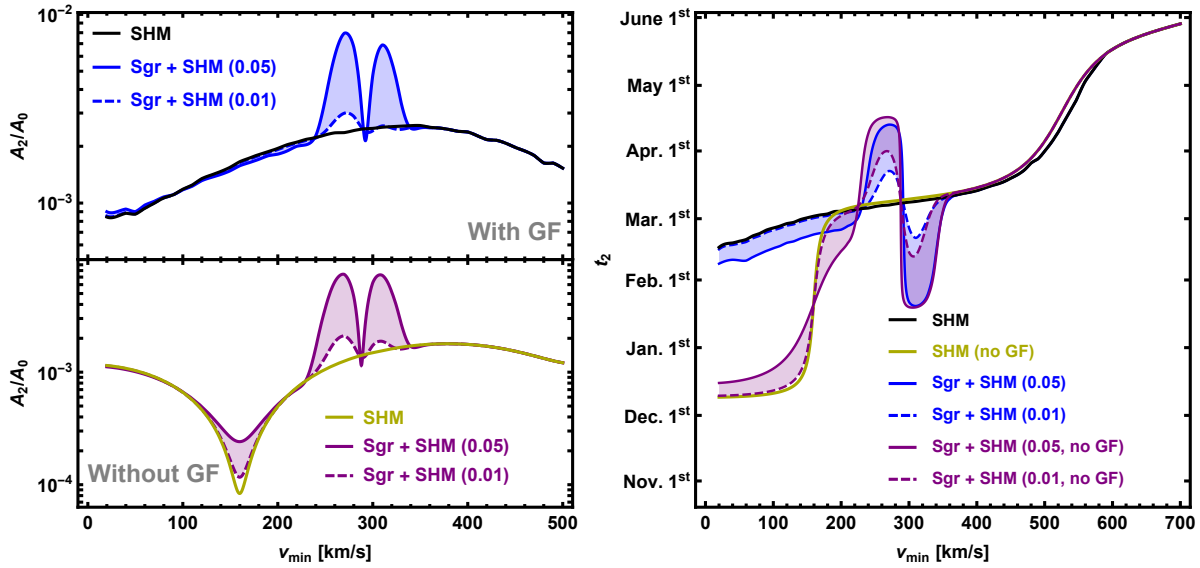

Figure 2.5: Same as Fig. 2.4, but for the second harmonic.

rate or the fractional amplitude. Furthermore, it appears to wash out characteristics that may allude to the potential existence of DM substructure in the phases of the first and second harmonics for values of $v_{\rm min} \lesssim 200$ km/s. The features arising from the substructure near $v_{\rm min} \approx v_{\rm Sgr}^{\rm S}$, however, are left intact. Since the effect of GF is negligible at $v_{\rm min} \gtrsim 300$ km/s, should the Sgr stream contribute non-negligibly to the local DM density, anisotropies arising from the Sgr stream could be probed using the ratios of harmonics as proposed in Ref. [71].

2.3.3 Dark Disk

We consider here two distinct types of DDs. The first could form from accretions of massive satellites onto the galactic disk [61–64]. In this scenario, the DM in the halo of the satellite galaxies and the DM comprising our own galaxy's halo is expected to be of the same type, i.e. non-dissipative in nature. While the DM in the halo must be non-dissipative in order to maintain its known spatial distribution, Ref. [65] has shown that a subdominant portion of

at most 5% could be dissipative. If such a component exists, it would form a DD in much the same way the baryonic matter dissipates energy and forms the visible disk. We refer to this second scenario as dissipative dark disk (DDD). Densities of DDs are expected to range from $\rho_{\rm disk}/\rho_{\rm halo} = 0.2$ to 1, with this ratio being strictly less than 3 and likely less than 2 [63].

We model both the non-dissipative DD and the DDD using a truncated Maxwellian. Consistent with the values found in numerical simulations, we model the DD with a rotation velocity 50 km/s slower than the Local Standard of Rest ($v_{\rm lag} = 50$ km/s) and with velocity dispersion $v_0 = 70$ km/s [62]. While we present our results for a non-dissipative DD together with a SHM halo (DD+SHM), results for the DDD are obtained without a background halo component, as a specific particle model for all (dissipative and non-dissipative) DM components would be required before the velocity integrals of SHM and DDD could be combined.

The left panel of Fig. 2.6 shows the enhancement of the unmodulated component of $\eta(v_{\rm min}, t)$, A_0, for a DD combined with the SHM (DD+SHM) relative to that of the SHM alone, for $\rho_{\rm DD}/\rho_{\rm SHM} = 0.2$ (green), 0.5 (red), 1 (purple), and 2 (blue), with (solid) and without (dashed) GF. When GF is neglected, adding a DD to the halo can increase the unmodulated rate by as little as 150% for $\rho_{\rm DD}/\rho_{\rm SHM} = 0.2$, or as much as 775% for $\rho_{\rm DD}/\rho_{\rm SHM} = 2$, but only for $v_{\rm min} \leqslant 200$ km/s. GF does not appreciably change this result for the low density DD, but can increase the unmodulated component of the high density DD by an additional 60%.

The right panel of Fig. 2.6 shows the fractional modulation amplitude $\Delta(v_{\rm min})$ for the DD+SHM, defined in Eq. (2.9). For values of $v_{\rm min}$ below 300 km/s, where one expects GF

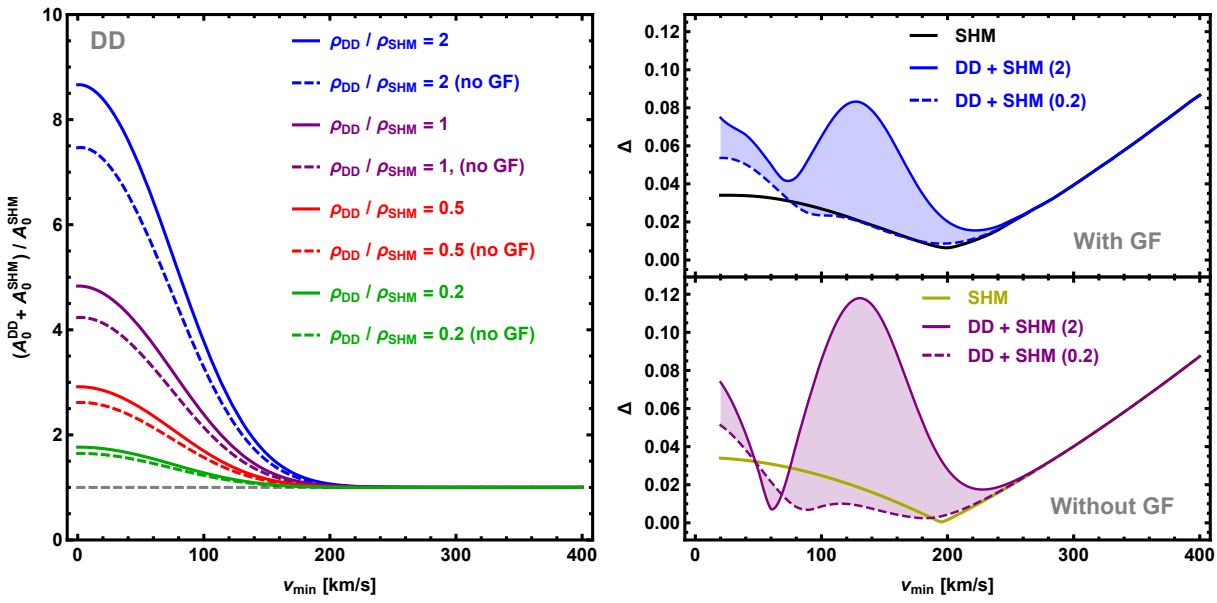

Figure 2.6: Left: Unmodulated component of $\eta(v_{\min}, t)$, A_0, for the DD+SHM normalized by the unmodulated component for the SHM alone, for $\rho_{\rm DD}/\rho_{\rm SHM} = 0.2$ (green), $\rho_{\rm DD}/\rho_{\rm SHM} = 0.5$ (red), $\rho_{\rm DD}/\rho_{\rm SHM} = 1$ (purple), and $\rho_{\rm DD}/\rho_{\rm SHM} = 2$ (blue), with GF (solid) and without GF (dashed). Right: Fractional modulation amplitude, as defined in Eq. (2.9), for the DD+SHM with (top) and without (bottom) GF, and densities ranging from $\rho_{\rm DD}/\rho_{\rm SHM} = 0.2$ (dashed) to $\rho_{\rm DD}/\rho_{\rm SHM} = 2$ (solid). Results are compared with the SHM alone, with GF (black) and without GF (yellow).

and a DD with small $v_{\rm lag}$ to be most influential, the SHM predicts a fractional modulation amplitude of at most $\sim 4\%$. Without GF, the addition of the DD to the SHM would increase Δ to as much as 12%. The presence of GF reduces the influence of the DD, resulting in at most an 8% fractional modulation amplitude. For $v_{\rm min} > 250$ km/s, the influence of the DD and GF vanish and the DD+SHM results are identical to those of the SHM.

The left panel of Fig. 2.7 shows the amplitude of the first harmonic. Without GF (purple), the addition of the DD would either increase or decrease the relative amplitude of the first harmonic, depending on the values of $\rho_{\rm DD}/\rho_{\rm SHM}$ and $v_{\rm min}$. Due to GF the addition of the DD primarily enhances the amplitude of the first harmonic. This enhancement can be as large as a factor of 5 for $\rho_{\rm DD}/\rho_{\rm SHM} = 2$.

The right panel of Fig. 2.7 shows how the DD impacts the expected phase of the first harmonic, with (blue) and without (purple) GF. Regardless of whether or not GF is included, the phase of the first harmonic of the DD+SHM looks identical to that of the SHM for $v_{\rm min} > 250$ km/s. Without GF, the phase of the first harmonic would deviate from the SHM by nearly 6 months for $v_{\rm min}$ between 70 km/s and 200 km/s. When GF is accounted for, this phase difference between the DD+SHM and SHM is at most 4 months, and the range of $v_{\rm min}$ at which this deviation occurs is reduced to 100 km/s $\leqslant v_{\rm min} \leqslant$ 180 km/s.

Fig. 2.8 shows the effect of a DD on the second harmonic. As for the first harmonic, the DD affects neither the relative amplitude nor the phase for $v_{\rm min} > 250$ km/s. Below this value, the relative amplitude of the second harmonic of the DD+SHM is primarily enhanced when GF is neglected, except in very narrow regions around $v_{\rm min} \simeq 50$ and $v_{\rm min} \simeq 140$ km/s, depending on $\rho_{\rm DD}$. When GF is included, the amplitude for the DD+SHM is enhanced by

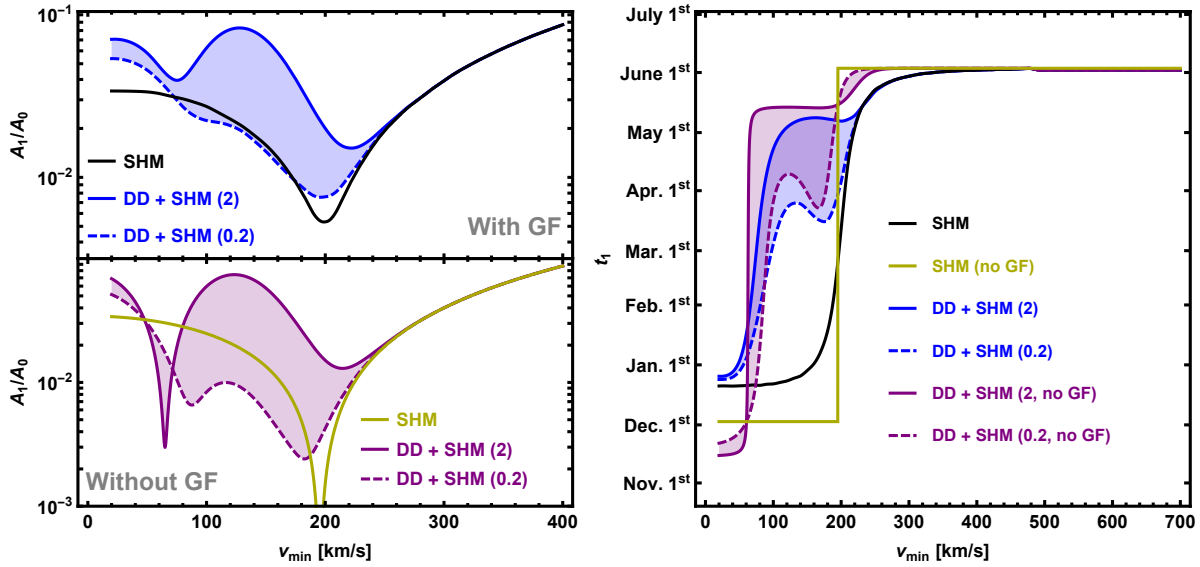

Figure 2.7: Amplitudes (left) and phases (right) of the first harmonic for the DD+SHM. Dashed lines are for a low density DD, $\rho_{\rm DD}/\rho_{\rm SHM} = 0.2$, while solid lines are for a high density DD, $\rho_{\rm DD}/\rho_{\rm SHM} = 2$. Blue lines and regions include GF, while purple lines and regions neglect GF. Results are compared with the SHM alone, with GF (black) and without GF (yellow).

up to a factor of 10 for $\rho_{\rm DD}/\rho_{\rm SHM} = 2$ and a factor of 3 for $\rho_{\rm DD}/\rho_{\rm SHM} = 0.2$, but only at values of $v_{\rm min}$ below 180 km/s. A slight reduction in the amplitude occurs for all DD densities plotted between $v_{\rm min}$ values of 180 km/s and 250 km/s. The phase of the second harmonic without GF would consistently differ from the SHM by up to 75 days for values of $v_{\rm min}$ below 250 km/s. GF slightly reduces the difference in t_2 between DD+SHM and SHM alone for $v_{\rm min} < 250$ km/s. The maximum phase difference between DD+SHM and the SHM is roughly 50 days, but may be as little as 15 days for $\rho_{\rm DD}/\rho_{\rm SHM} = 0.2$.

In summary, we find that the existence of a DD with a lag speed of 50 km/s and dispersion of 70 km/s can significantly alter the unmodulated rate, the fractional modulation amplitude, and the phases of the dominant harmonics, but only for $v_{\rm min} \lesssim 250$ km/s. A larger (smaller) $v_{\rm lag}$ would increase (decrease) the $v_{\rm min}$ values at which the features associated with the DD

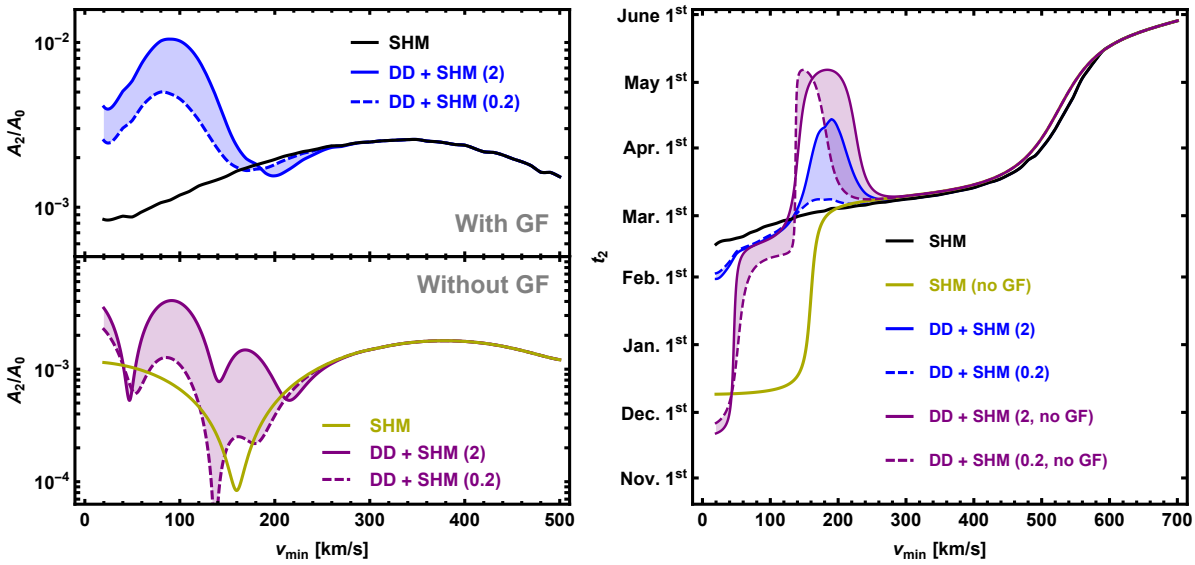

Figure 2.8: Same as Fig. 2.7 but for the second harmonic.

appear. GF is shown to further enhance the unmodulated rate and fractional amplitude, but it diminishes the influence of the DD on the phases of the dominant harmonics. However, one should keep in mind that the relative importance of GF seen in this paper is dependent upon the chosen rotation velocity of the DD.

We notice that the method of Ref. [71] for probing the nature of anisotropies in the dark halo with ratios of harmonics may not be useful for a DD, as the region in which deviations occur directly overlaps with the region made anisotropic by GF (at least in the example provided here). The effect of GF would be noticeably reduced should the DD rotate at a velocity significantly different from the rotation velocity of the Sun. This is because, in the Sun's reference frame, WIMPs from the DD will be moving faster and spend less time in the Sun's gravitational potential.

We also show in Fig. 2.9 the amplitudes (left panel) and phases (right panel) of the first (solid lines) and second (dashed lines) harmonics for the DDD alone, with (light blue) and

without (purple) GF. The amplitudes for the DDD look very similar to those of the SHM, but they appear at much lower $v_{\rm min}$ values for the DDD lag speed we assume (50 km/s). This should be expected, as the DDD contains WIMPs coming from approximately the same direction as the dark halo but with a lower relative speed and a smaller dispersion. The most notable differences occur in the phases. For all values of $v_{\rm min}$, the phases of the first and second harmonic for the DDD are shifted approximately half a month earlier when compared to the phases of the SHM (see Fig. 2.1 for comparison).

2.4 Estimate of required number of events

We begin by providing a rough estimate of the number of events that would be necessary to observe the annual modulation in the Sgr+SHM, the DD+SHM, and the SHM, using a very simple two-bin analysis. Let us split an annual cycle into two six-month periods, one of which is centered about the time of maximum of the rate and the other is centered 6 months later. For a fixed energy range, we denote the number of events in the two time bins N_+ and N_-. To estimate the number of events needed to establish the existence of an annual modulation with a significance level corresponding to α standard deviations, we require that

$$\Delta N \equiv N_+ - N_- \geqslant \alpha\sqrt{N_{\rm tot}}\ , \tag{2.10}$$

with $N_{\rm tot} \equiv N_+ + N_-$ the total number of observed events. We assume that the uncertainty of N_+ and N_- is $\sqrt{N_{\rm tot}/2}$. Assuming the phase $\bar{t}$ is constant in the energy range considered, we can approximate the integrated rate as $R(t) \simeq R_0 + R_1 \cos\left(2\pi(t-\bar{t})/\text{year}\right)$, where R_0 is

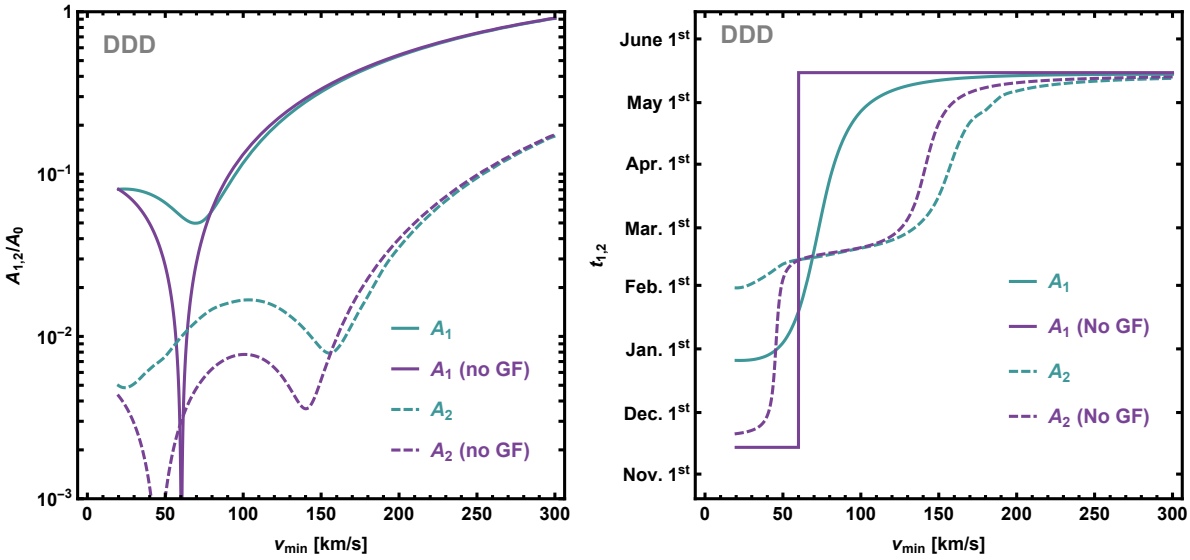

Figure 2.9: Amplitudes (left panel) and phases (right panel) of the first (solid) and second (dashed) harmonics for the DDD, with GF (light blue) and without GF (purple).

the unmodulated component of the rate and R_1 is the modulation amplitude. For a fixed exposure MT, $N_\pm \simeq MT(R_0/2 \pm R_1/\pi)$, where the factor of $1/\pi$ arises from integrating the cosine term over the temporal region defining each bin.

Solving Eq. (2.10) for $N_{\rm tot}$ in terms of R_0 and R_1 then yields

$$N_{\rm tot} \geqslant \frac{\alpha^2\pi^2}{4}\left(\frac{R_0}{R_1}\right)^2 . \tag{2.11}$$

R_0 and R_1 can be replaced by the integral of A_0 and A_1 over the energy range considered, since all additional constants relating R_0 to A_0 and R_1 to A_1 cancel in the ratio. A_0 and A_1 are functions of $v_{\rm min}$ and we use the relation between $v_{\rm min}$ and $E_{\rm R}$ for elastic scattering given below Eq. (2.1).

Since we would ultimately like to know how distinguishable the Sgr+SHM and DD+SHM

are from the SHM, we choose to evaluate Eq. (2.11) in an energy range where the amplitude and phase of the Sgr+SHM and DD+SHM deviate most strongly from the SHM. For the Sgr+SHM, this region corresponds to $v_{\rm min}$ values between 280 km/s and 300 km/s (see Fig. 2.4). This region is roughly consistent with a 1 keV bin centered at about 6.6 keV, for a 25 GeV DM particle scattering off xenon. Evaluating Eq. (2.11) in this region we find the modulation amplitude in the Sgr+SHM, for $\rho_{\rm Sgr}/\rho_{\rm SHM} = 0.05$, requires roughly $2900\alpha^2$ events to be detected with significance α sigma, while the amplitude in the SHM requires $2000\alpha^2$ events. The Sgr+SHM requires more events to be observed than the SHM because the modulation arising from the Sgr stream and the SHM are out of phase, leading to a reduction in the modulation amplitude as shown in Fig. 2.4. For the DD+SHM, we consider $v_{\rm min}$ values between 130 km/s and 150 km/s (see Fig. 2.7). This region approximately coincides with a 1 keV bin centered at about 4.5 keV, for a 50 GeV DM particle scattering off xenon. The DD+SHM, for $\rho_{\rm DD}/\rho_{\rm SHM} = 2$, would require $170\alpha^2$ events to be detected at significance α sigma while the SHM would require roughly $7500\alpha^2$ events. The addition of the DD to the SHM significantly reduces the number of necessary events because the DD+SHM has a significantly larger modulation amplitude, as seen in Fig. 2.7.

An important question to ask is, if an experiment were to view the annual modulation with a significance of α standard deviations, would additional events be necessary in order to distinguish these models? It is clear from Fig. 2.4 that the modulation features of the Sgr+SHM deviate most from those in the SHM in the phase of the first harmonic. Thus the question to ask for the Sgr+SHM is, how many events must be observed between $v_{\rm min} = 280$ km/s and $v_{\rm min} = 300$ km/s in order to distinguish a phase occurring in mid March from a

phase occurring in late May. The first harmonic in the DD+SHM differs strongly from that of the SHM in both the phase and the amplitude, and thus it is important to check which feature will be more easily distinguishable from the SHM.

We will begin with a rough analysis of the number of events necessary to discern the difference between the amplitude of the modulation for the DD+SHM, assuming $\rho_{\rm DD}/\rho_{\rm SHM} = 2$, from the SHM amplitude. Consider once again the same bin analysis previously used to determine the detectability of the modulation amplitude. The condition for distinguishing the modulation amplitude of the DD+SHM from the modulation amplitude of the SHM is simply that the difference between $\Delta N_{\rm DD+SHM}$ and $\Delta N_{\rm SHM}$ must be larger than the uncertainty, $\sqrt{N_{\rm tot}}$, in the measurement of ΔN. This implies

$$\Delta N_{\rm DD+SHM} - \Delta N_{\rm SHM} \geqslant \alpha\sqrt{N_{\rm tot}}\ . \tag{2.12}$$

With similar manipulations as above, one can arrive at the following condition on $N_{\rm tot}$:

$$N_{\rm tot} \geqslant \frac{\pi^2\alpha^2}{4}\left[\left(\frac{R_1}{R_0}\right)_{\rm DD+SHM} - \left(\frac{R_1}{R_0}\right)_{\rm SHM}\right]^{-2}\ . \tag{2.13}$$

Evaluating Eq. (2.13) in the energy range previously defined for the DD+SHM, we find that approximately $225\alpha^2$ events are necessary to distinguish the amplitude of the DD+SHM from the SHM at a significance of α sigma. This implies that approximately $55\alpha^2$ more events must be detected after the annual modulation is observed in order to discriminate the DD+SHM from the SHM using only the amplitude of the modulation.

We now consider how the phase of the modulation could be used to estimate the number

of events that must be observed in order to distinguish the various models. Assume for a moment that an annual modulation has been detected and the number of events can be plotted against time to form a sinusoidal-like figure. Let us assume that one of the data points lies at $(t_*, \bar{N})$, where $\bar{N}$ is the average number of events observed. Two cosine functions, one passing through the data point itself with phase t_a, and the other passing through the upper end of its error bar with phase t_b, can then be used to characterize the uncertainty with which the phase is known. The upper bound of the data point is proportional to the square root of the number of events in the temporal bin $\sqrt{N_{\rm bin}}$. We will assume events are evenly distributed across temporal bins, implying $\sqrt{N_{\rm bin}} \simeq \sqrt{N_{\rm tot}}/4$. Assuming ΔN is known, the conditions that by definition must be satisfied are

$$\frac{\Delta N}{2}\cos(\omega(t_* - t_a)) = 0 \ , \tag{2.14}$$

$$\frac{\Delta N}{2}\cos(\omega(t_* - t_b)) \simeq \frac{\alpha}{4}\sqrt{N_{\rm tot}} \ . \tag{2.15}$$

We solve Eq. (2.14) for t_* and restrict our attention to the solution that is closer in phase with the data. Substituting this result into Eq. (2.15) yields

$$\sin(\omega\Delta t) \simeq \frac{\alpha\sqrt{N_{\rm tot}}}{2\Delta N} \ , \tag{2.16}$$

where $\Delta t \equiv t_a - t_b$. To be conservative, we choose to restrict the uncertainty in the phase

to be at most one month, for which $\sin(\omega\Delta t) = \sin(\pi/6) = 1/2$, which then implies

$$N_{\rm tot} \geqslant \frac{\alpha^2\pi^2}{4}\left(\frac{R_0}{R_1}\right)^2 , \tag{2.17}$$

which coincidentally is the as same as Eq. (2.11). We note that the above analysis is only one sided in that it fails to account for the lower part of the $(t_*, \bar{N})$ error bar. The true uncertainty in the phase thus has a full width of two months, extending to one month to either side of the best-fit value.

Since Eq. (2.11) and Eq. (2.17) coincide, the number of events required to distinguish the phases (with a two month error) of the Sgr+SHM or DD+SHM modulations from the phase of the SHM modulation are approximately the same as those required to confirm the existence of the modulation itself. We thus expect any experiment measuring the modulation in an energy range where the phases of the models significantly differ, to measure the phase with high enough accuracy to differentiate the SHM from the Sgr+SHM and DD+SHM.

2.5 Summary

We have considered how gravitational focusing of DM due to the Sun's gravitational potential would alter the time modulation of a DM signal. Previous studies have separately considered extracting information using a harmonic analysis [71] and investigating how anisotropies in the DM halo might influence direct DM detection experiments [72–74]. The purpose of this paper is to unify these analyses and investigate how GF would alter the results of a harmonic analysis in the presence of DM velocity substructure.

We performed our analysis on a dark halo described by the standard halo model (SHM), a SHM with an added DM stream as expected from the tidal disruption of the Sgr dwarf galaxy by the Milky Way, a SHM plus a dark disk (DD) with lag speed $v_{\rm lag} = 50$ km/s, and a dissipative dark disk alone (DDD) with the same lag speed. Our results for the SHM alone are in agreement with Ref. [74]. Additionally, the conclusion of Ref. [71] that there should exist ratios of the amplitudes of harmonics independent of $v_{\rm min}$ was shown to be inconsistent with the presence of GF at $v_{\rm min} \lesssim 300$ km/s. This does not come as a surprise as the result of [71] assumes that the local DM halo in the galactic frame is isotropic, and GF inherently makes the halo anisotropic.

For the Sgr stream, modeled with a velocity $\boldsymbol{v}_{\rm Sgr} = (-65, 135, -249)$ km/s in galactic coordinates, we found that GF is unlikely to significantly affect any DM particles coming from the stream, but can affect the smooth halo component, and thus can alter the relative contributions of the Sgr stream and the smooth halo to the velocity integral $\eta(v_{\rm min}, t)$. We showed that by increasing the relative importance of the background halo, GF tends to reduce characteristic features that would otherwise be expected to appear in the phases of the annual and biannual harmonics from the inclusion of the Sgr stream component. In spite of this, GF does not eliminate the more prominent features which have the potential to alter the expected phase of the annual modulation by more than two months for values of $v_{\rm min} \approx v^{\rm S}_{\rm Sgr}$ with respect to the SHM alone, where $v^{\rm S}_{\rm Sgr}$ is the speed of the Sgr stream in the Sun's reference frame.

For our DD+SHM analysis we considered a dark disk co-rotating with the baryonic disk but with a smaller rotational velocity. Since the relative velocity of DM in the DD is much

smaller than in the SHM or Sgr stream, one would expect GF to have a much larger influence in this model. Indeed we showed that the inclusion of a DD has a large influence on the unmodulated rate, the fractional amplitude, the amplitudes of the annual and biannual harmonics, and the phases of the annual and biannual harmonics. However, these effects appear only at $v_{\rm min} \lesssim 250$ km/s.

We also provided rough estimates of how many events should be observed in order to differentiate between the Sgr+SHM, DD+SHM, and SHM. We have determined that should an experiment measure the annual modulation in an energy range where the phase of the Sgr+SHM and DD+SHM differ noticeably from that of the SHM, the uncertainty in the measured phase will be small enough to allow for a discrimination between these models.

Our conclusions support the idea that analyzing the harmonic series of the DM differential scattering rate could potentially shed light on the distribution of DM in our galaxy. We have found that when DM velocity substructure is present, GF washes out some of the more distinctive features that would appear in the amplitudes and phases of the dominant harmonics were GF neglected. This is so because GF enhances the density of the low velocity WIMPs in the smooth halo component. However, deviations with respect to the SHM, most notably in the phases of the harmonics, can still persist and could provide insight into the astrophysical nature of DM.

3 Target dependence of the annual modulation in direct dark matter searches

3.1 Introduction to Target-Dependent Modulation

Despite being the dominant form of matter in the Universe, the exact nature of the dark matter (DM) is still unknown. One of the most well-motivated candidates for DM is a particle with few GeV to hundreds of TeV mass and weak-scale interactions, referred to as a weakly interacting massive particle (WIMP). Efforts to shed light on the non-gravitational interactions of WIMP DM primarily focus on either detecting the byproducts of DM annihilation or decay (indirect detection), producing DM in the laboratory through collisions of standard model particles, or detecting interactions between DM in the galactic halo and terrestrial nuclei (direct detection).

Direct DM detection experiments attempt to gain insight into both the particle physics properties of DM and the local DM velocity distribution by observing the energy deposited by DM particles interacting with nuclei as they pass through detectors. A key feature of any convincing direct detection signal would be the annual modulation of the scattering rate caused by Earth's rotation around the Sun [78]. For DM velocity distributions that are locally smooth and isotropic in the galactic frame, it is usually expected that the differential rate for dark matter scattering off a target nuclide T is nearly sinusoidal and can be well represented by

$$\frac{\mathrm{d}R_T}{\mathrm{d}E_\mathrm{R}}(E_\mathrm{R}, t) \simeq S_0(E_\mathrm{R}) + S_\mathrm{m}(E_\mathrm{R}) \cos\left(\frac{2\pi}{1\ \mathrm{year}}(t - t_0)\right), \tag{3.1}$$

where $E_{\rm R}$ is the nuclear recoil energy. Allowing the modulation amplitude $S_{\rm m}(E_{\rm R})$ to assume both positive and negative values, the phase t_0 is independent of $E_{\rm R}$. Taking instead $S_{\rm m}(E_{\rm R})$ to be non-negative, as we do in this paper, t_0 changes from early June at large $E_{\rm R}$ to early December at small $E_{\rm R}$, with the transition occurring sharply at a single $E_{\rm R}$ value. Accounting for the presence of anisotropy in the DM halo modifies this picture, most notably by modifying the $E_{\rm R}$ dependence of the modulation phase. The extent to which various forms of anisotropy, including DM substructure, the gravitational focusing (GF) of DM particles by the Sun, and triaxial halo models, modify Eq. (3.1) has been investigated e.g. in [79–90].

At fixed recoil energies, experiments employing different target elements are not necessarily expected to measure the same modulation of the rate. However, for most interactions, some observables associated with the annual modulation like the modulation fraction or the time of maximum and minimum signal, $t_{\rm max}$ and $t_{\rm min}$, do not depend on the target nuclide when expressed as functions of $v_{\rm min}$. This is the minimum speed a DM particle must have in Earth's frame to impart a recoil energy $E_{\rm R}$ on a target nucleus. This definition naturally treats $v_{\rm min}$ as an $E_{\rm R}$-dependent function. Alternatively, it is possible to think of $E_{\rm R}$ as a $v_{\rm min}$-dependent function. In this context, $E_{\rm R}$ is interpreted as the extremum energy (corresponding to a maximum energy if the scattering is elastic, and either a maximum or minimum energy if the scattering is inelastic) that can be imparted to a nucleus by an incoming DM particle traveling with speed $v = v_{\rm min}$ in Earth's frame. For each nuclide there exists a bijective relation between $E_{\rm R}$ and $v_{\rm min}$ dictated by the scattering kinematics, and the choice of one or the other as the independent variable may lead to different insights. As commented above, for most interactions (e.g. the standard spin-independent (SI) and spin-

dependent (SD) interactions) observables like $t_{\rm max}$ and $t_{\rm min}$ are nuclide-independent functions of $v_{\rm min}$ (this is no longer true when expressed as functions of $E_{\rm R}$, since the $E_{\rm R}$-$v_{\rm min}$ relation is target dependent). Therefore for studying the signal modulation for single-element targets it is convenient to adopt $v_{\rm min}$ as the independent variable (averaging over different isotopes). For targets consisting of multiple elements, one must choose whether to treat $E_{\rm R}$ or $v_{\rm min}$ as the independent variable (see e.g. [91–93]). When we consider multiple targets in Sec. 3.3.1 we choose to return to using $E_{\rm R}$ as the independent variable.

We pointed out in [94] that when the DM-nucleus differential cross section has a non-factorizable velocity dependence, as for DM interacting through a magnetic dipole or an anapole moment, $t_{\rm max}$ and $t_{\rm min}$ are no longer target-independent functions of $v_{\rm min}$. Here, we reconsider the analysis performed in [94] and examine more extensively how target-dependent modulation arises, how various experiments can actually observe such a signal, and the extent to which putative signals could identify DM with a non-factorizable velocity dependence in its differential scattering cross section. Specifically, we consider how *(i)* integrating the scattering rate over a finite energy range, *(ii)* the presence of multiple target elements with non-negligible contributions to the rate, and *(iii)* different DM-nucleus scattering kinematics affect the potential observability of target-dependent modulation.

This Chapter is organized as follows. In Section 3.2 we introduce the formalism and discuss what conditions must be present for target-dependent modulation. In Section 3.3 we take the particular example of DM interacting with nucleons through an anomalous magnetic dipole moment and discuss how observables associated with the annual modulation of the rate depend on $v_{\rm min}$ for specific targets employed in currents experiments. Additionally, we

examine how experiments would view a signal arising from magnetic dipole DM a function of the observed energy E' and the extent to which the expected signal would be distinguishable from a signal arising from a standard SI or SD contact interaction, for both elastic and inelastic scattering. We conclude in Section 3.4.

3.2 DM signal and its modulation

3.2.1 Direct detection rate

Direct DM detection experiments try to measure the recoil energy $E_{\rm R}$ a nucleus initially at rest in the detector acquires after scattering with a DM particle with initial velocity $\boldsymbol{v}$ in the detector's rest frame. The differential scattering rate on a nuclide T per unit detector mass is

$$\frac{\mathrm{d}R_T}{\mathrm{d}E_{\rm R}}(E_{\rm R},t) = \frac{C_T}{m_T}\frac{\rho}{m}\int_{v\geqslant v_{\rm min}(E_{\rm R})} v\, f(\boldsymbol{v},t)\,\frac{\mathrm{d}\sigma_T}{\mathrm{d}E_{\rm R}}\,\mathrm{d}^3v\ , \tag{3.2}$$

where $\rho = 0.3$ GeV/cm^3 is the local DM density, m is the DM particle mass, C_T is the nuclide mass fraction in the detector, m_T is the target nuclide mass, and $f(\boldsymbol{v},t)$ is the DM velocity distribution in Earth's frame. The energy dependence of $v_{\rm min}(E_{\rm R})$, is dictated by the scattering kinematics, for instance for elastic scattering

$$v_{\rm min}(E_{\rm R}) = \sqrt{\frac{m_T E_{\rm R}}{2\mu_T^2}}\ . \tag{3.3}$$

Experiments do not measure directly the recoil energy, but a proxy for it denoted here with E'. This detected energy can e.g. be measured in keVee (keV electron-equivalent energy)

or photoelectrons. For experiments that bin their data, the energy-integrated scattering rate between detected energies E'_1 and E'_2 is

$$R_{[E'_1,E'_2]}(t) = \sum_T \int_{E'_1}^{E'_2} \mathrm{d}E' \, \epsilon(E') \int_0^\infty \mathrm{d}E_\mathrm{R} \, G_T(E_\mathrm{R}, E') \frac{\mathrm{d}R_T}{\mathrm{d}E_\mathrm{R}}(E_\mathrm{R}, t) \ , \tag{3.4}$$

where $\epsilon(E')$ is the counting efficiency and $G_T(E_\mathrm{R}, E')$ describes the probability that an event detected with energy E' resulted from a nuclear recoil having energy E_R. $G_T(E_\mathrm{R}, E')$ is frequently taken to be a Gaussian with mean value $\langle E' \rangle = Q_T E_\mathrm{R}$, where $Q_T(E_\mathrm{R})$ is an element-dependent quenching factor.

Typically one assumes the DM is on average at rest with respect to the galaxy, and the velocity distribution in the galactic frame $f_\mathrm{G}(\boldsymbol{v})$ is smooth and isotropic. The DM velocity distribution in Earth's frame is then obtained via the Galilean transformation $f(\boldsymbol{v}, t) = f_\mathrm{G}(\boldsymbol{v} + \boldsymbol{v}_\oplus(t) + \boldsymbol{v}_\odot)$, where $\boldsymbol{v}_\oplus(t)$ is the velocity of Earth with respect to the Sun and $\boldsymbol{v}_\odot$ the velocity of the Sun with respect to the galaxy. In this paper we choose to model the velocity of Earth with respect to the Sun following the procedure of Ref. [95], and take the velocity of the Sun with respect to the Galaxy to be $\boldsymbol{v}_\odot = (11, 232, 7)$ km/s in galactic coordinates. Furthermore, for concrete applications we assume the Standard Halo Model (SHM), in which the velocity distribution of the dark halo is a truncated Maxwellian,

$$f_\mathrm{G}(\boldsymbol{v}) = \frac{e^{-\boldsymbol{v}^2/v_0^2}}{(\pi v_0^2)^{3/2} N_\mathrm{esc}} \theta(v_\mathrm{esc} - |\boldsymbol{v}|) \ , \tag{3.5}$$

with galactic escape velocity $v_\mathrm{esc} = 533$ km/s [96] and velocity dispersion $v_0 = 220$ km/s [97].

The normalization,

$$N_{\rm esc} = {\rm Erf}(v_{\rm esc}/v_0) - \frac{2v_{\rm esc}}{\sqrt{\pi}v_0} e^{-v_{\rm esc}^2/v_0^2} \ , \tag{3.6}$$

is chosen such that $\int {\rm d}^3 v \, f_{\rm G}(\boldsymbol{v}) = 1$.

DM that is on average at rest with respect to the Galaxy has a preferred direction of motion in the Sun's reference frame. For this reason, DM particles viewed in the Sun's reference frame appear as a constant "wind", with velocities preferentially opposed to $\boldsymbol{v}_\odot$. The gravitational potential of the Sun bends the trajectories of DM particles as they pass by, resulting in a focusing effect that is maximized at Earth's location when Earth is on the leeward side with respect to the Sun, occurring on March 1$^{\rm st}$. This effect, referred to as GF, implies the DM density and velocity distribution at Earth's location depend on Earth's position relative to the Sun. The influence of GF is larger on slower moving particles as they spend more time in the Sun's gravitational potential, and is negligible on WIMPs traveling faster than a few hundred km/s in the Solar reference frame. The effect of GF is taken into account by replacing $f_{\rm G}(\boldsymbol{v} + \boldsymbol{v}_\oplus(t) + \boldsymbol{v}_\odot)$ with $f_{\rm G}(\boldsymbol{v}_\infty[\boldsymbol{v} + \boldsymbol{v}_\oplus(t)] + \boldsymbol{v}_\odot)$, where

$$\boldsymbol{v}_\infty[\boldsymbol{v}] = \frac{v_\infty^2 \boldsymbol{v} + \frac{1}{2} v_\infty u_{\rm esc}^2 \hat{\boldsymbol{r}} - v_\infty \boldsymbol{v}(\boldsymbol{v}\cdot\hat{\boldsymbol{r}})}{v_\infty^2 + \frac{1}{2}u_{\rm esc}^2 - v_\infty(\boldsymbol{v}\cdot\hat{\boldsymbol{r}})} \tag{3.7}$$

is the velocity a DM particle had asymptotically far away from the Sun's gravitational potential, such that its velocity when arriving at Earth is $\boldsymbol{v}$ [98]. Here $u_{\rm esc} = \sqrt{2GM_\odot/r} \approx 40$ km/s is the escape velocity of the Solar System at Earth's location, r is the Sun-Earth distance, $\hat{\boldsymbol{r}}$ is the unit vector pointing from the Sun to Earth, and $v_\infty^2 = v^2 - u_{\rm esc}^2$.

3.2.2 Time dependence of the rate

For the commonly considered SI and SD contact interactions, the differential scattering cross section for DM-nucleus elastic scattering has the form

$$\frac{\mathrm{d}\sigma_T}{\mathrm{d}E_\mathrm{R}}(E_\mathrm{R}, v) = \frac{m_T \sigma_T F_T(E_\mathrm{R})^2}{2\mu_T^2} \frac{1}{v^2} \ , \tag{3.8}$$

where μ_T is the DM-nucleus reduced mass, σ_T is the total cross section for a point-like nucleus, and $F_T(E_\mathrm{R})$ is the appropriate nuclear form factor normalized as $F_T(0) = 1$. This general form arises every time the scattering amplitude for a point-like nucleus is (at least approximately) independent of the scattering angle, i.e. of the recoil energy. In this case,

$$\sigma_T \equiv \int_0^{E_\mathrm{R}^\mathrm{max}} \frac{\mathrm{d}\sigma_T}{\mathrm{d}E_\mathrm{R}} \, \mathrm{d}E_\mathrm{R} = E_\mathrm{R}^\mathrm{max} \frac{\mathrm{d}\sigma_T}{\mathrm{d}E_\mathrm{R}} \tag{3.9}$$

where $E_\mathrm{R}^\mathrm{max} = 2\mu_T^2 v^2 / m_T$ is the maximum recoil energy a nucleus can get from scattering elastically with a DM particle with speed v. The effect of the finite size of the nucleus is then taken into account with the appropriate form factor. The differential rate for cross sections of the form in Eq. (3.8) then reads

$$\frac{\mathrm{d}R_T}{\mathrm{d}E_\mathrm{R}}(E_\mathrm{R}, t) = C_T \frac{\rho}{m} \frac{\sigma_T F_T(E_\mathrm{R})^2}{2\mu_T^2} \eta_0(v_\mathrm{min}(E_\mathrm{R}), t) \ , \tag{3.10}$$

with

$$\eta_0(v_\mathrm{min}, t) \equiv \int_{v \geqslant v_\mathrm{min}} \frac{f(\boldsymbol{v}, t)}{v} \, \mathrm{d}^3 v \ . \tag{3.11}$$

The modulation of the differential rate is determined solely by the time dependence in the velocity integral $\eta_0(v_{\rm min}, t)$, which is a target-independent function of $v_{\rm min}$, and therefore common to all experiments. Even though what enters the rate is the function $\eta_0(v_{\rm min}(E_{\rm R}), t)$, which depends on the target through $v_{\rm min}(E_{\rm R})$, one can express $E_{\rm R}$ as a function of $v_{\rm min}$ and study $\mathrm{d}R_T/\mathrm{d}E_{\rm R}(E_{\rm R}(v_{\rm min}), t)$, which is proportional to the target-independent quantity $\eta_0(v_{\rm min}, t)$ (see e.g. [92, 93]).

The target-independent nature of the time dependence of the differential rate for the standard SI and SD contact interactions is a consequence of the fact that velocity and target dependence can be factored in the differential cross section shown in Eq. (3.8). One may then ask, in general, under what circumstances observables associated with the modulation of the rate, such as $t_{\rm max}$ and $t_{\rm min}$, are target-dependent functions of $v_{\rm min}$. Following our preliminary study [94], we find that this can only happen when the following conditions are met:

1. the velocity and target dependence in the differential cross section cannot be factored, and

2. the scattering events that can be recorded by an experiment probe portions of the DM velocity distribution that are locally anisotropic in the galactic frame.

As shown in Ref [94], it is possible to meet both requirements and thus have a target-dependent modulation. Regarding point 2, anisotropy in the local DM velocity distribution can arise from an anisotropy in the smooth component of the halo, DM substructure, and gravitational interactions of DM with nearby massive objects such as the Sun. In this paper

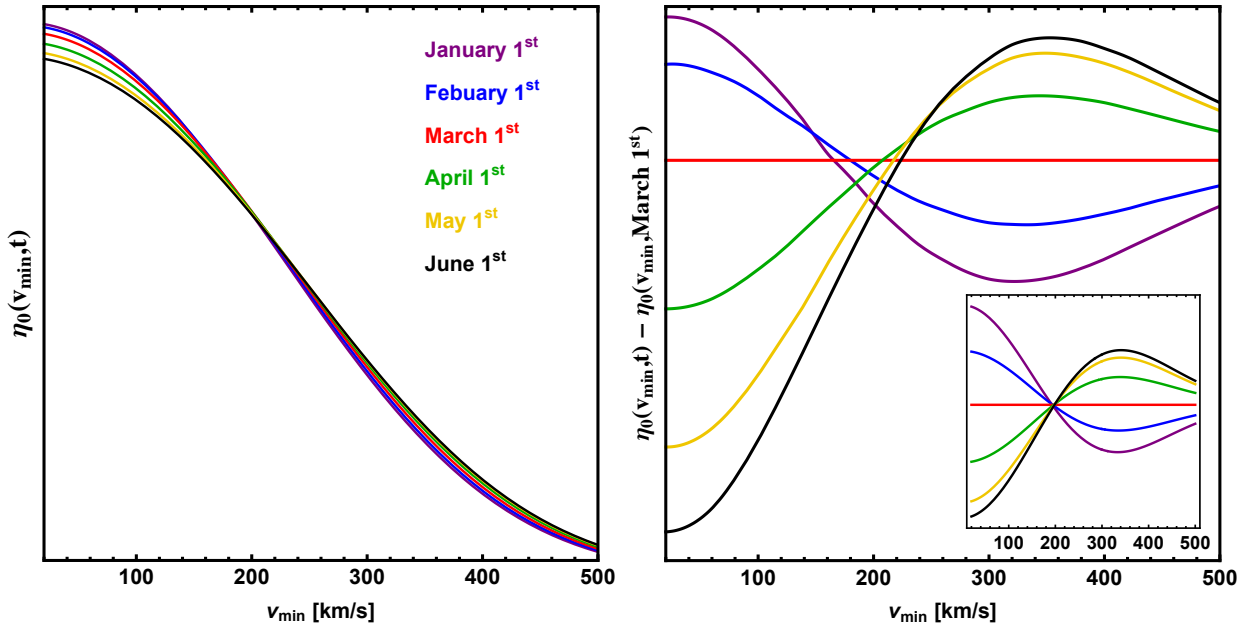

Figure 3.1: Left: η_0 plotted as a function of $v_{\rm min}$ at fixed times. Right: The difference between $\eta_0(v_{\rm min}, t)$ and $\eta_0(v_{\rm min}, t = \text{March } 1^{\rm st})$ evaluated at various times. The inset depicts the same figure should GF be neglected.

we choose to introduce anisotropy by only including the effect of GF of DM particles by the Sun because this anisotropy necessarily exists and is well understood [79, 80, 98].

Regarding point 1, the factorizable velocity and target dependence of the differential cross section, despite being very common, is not a completely general feature. The differential scattering cross section for DM interacting through a magnetic dipole [93, 99–123] or an anapole moment [99, 120–127] actually contains two terms with unique velocity dependences and energy-dependent coefficients. These types of differential cross sections also appear with the interactions described by some of the effective operators studied e.g. in [128–133] (see [118, 134–137] for explicit formulas of scattering amplitudes). In all these examples, velocity dependences other than the $\mathrm{d}\sigma_T/\mathrm{d}E_{\rm R} \propto 1/v^2$ in Eq. (3.8) are present. This happens e.g. when higher order terms in the nonrelativistic (small v) expansion of the scattering

amplitude become important. To be concrete, we can take for example the scattering rate to be

$$\frac{\mathrm{d}R_T}{\mathrm{d}E_\mathrm{R}}(E_\mathrm{R},t) = r_0(E_\mathrm{R},t) + r_1(E_\mathrm{R},t) \tag{3.12}$$

with

$$r_n(E_\mathrm{R},t) \propto \eta_n(v_\mathrm{min}(E_\mathrm{R}),t), \qquad\qquad n = 0,1, \tag{3.13}$$

where we generalized the definition of the velocity integral in Eq. (3.11) to

$$\eta_n(v_\mathrm{min},t) \equiv \int_{v\geqslant v_\mathrm{min}} v^{2n}\,\frac{f(\boldsymbol{v},t)}{v}\,\mathrm{d}^3v\ . \tag{3.14}$$

The interesting case for us is when r_0 and r_1 have similar magnitudes. The proportionality factor between r_i and η_i in Eq. (3.13) is in general E_R dependent, and this dependence must balance the suppression provided by the extra powers of v in η_1 with respect to η_0 in order for r_0 and r_1 to be comparable. We will see below that the scattering rate of a DM particle interacting through an anomalous magnetic moment has exactly this form. As is clear from Eq. (3.12), the time dependence of the rate does not coincide in general with that of a single velocity integral, as it happened instead in the simple case of Eq. (3.10). It is therefore useful to denote with τ_max (τ_min) the time of maximum (minimum) of each velocity integral, to distinguish it from the time of maximum (minimum) of the rate denoted t_max (t_min).

To understand the time-dependent behavior of η_n we begin by considering the behavior of η_0. The left panel of Fig. 3.1 shows η_0 evaluated at the first day of the month for the

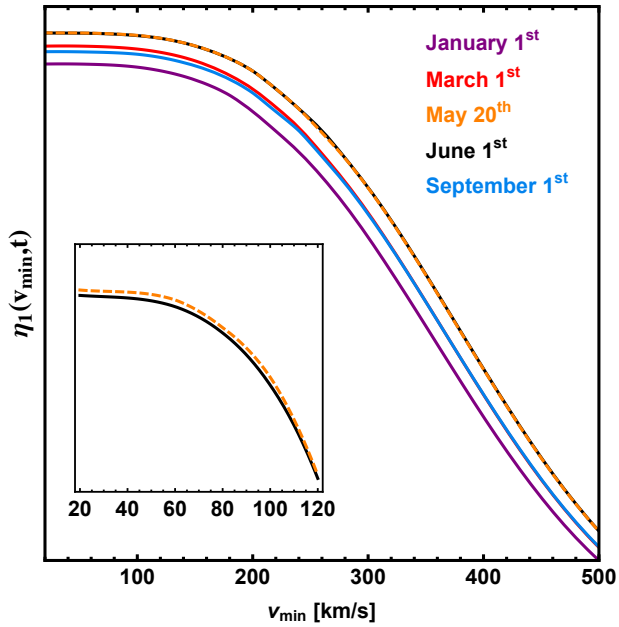

Figure 3.2: η_1 plotted as a function of $v_{\rm min}$ at fixed times. The inset zooms in on the region where the time of maximum $\tau_{\rm max}$ transitions from late May, occurring at small values of $v_{\rm min}$, to early June, occurring for $v_{\rm min} \gtrsim 300$ km/s.

first six months of the year as a function of $v_{\rm min}$. Since the behavior of the curves is difficult to discern, we plot in the right panel of Fig. 3.1 the difference between each of the curves in the left panel and η_0 evaluated at March 1$^{\rm st}$. Here, $\tau_{\rm max}$, the time of maximum of the velocity integral, can be seen to transition from early January to early June as $v_{\rm min}$ increases from ≈ 140 km/s to ≈ 260 km/s (actually, $\tau_{\rm max}$ occurs before January 1$^{\rm st}$, during the month of December at low values of $v_{\rm min}$). The inset in the right panel of Fig. 3.1 shows how η_0 changes with time should GF be neglected. Without GF, $\tau_{\rm max}$ still transitions from January 1$^{\rm st}$ to June 1$^{\rm st}$, but this transition occurs very rapidly over a very narrow range of $v_{\rm min}$ values.

Fig. 3.2 shows η_1 as a function of $v_{\rm min}$ for various fixed times. Unlike η_0, there appears to be a fixed separation between the various fixed time curves across nearly all values of $v_{\rm min}$. This occurs because the additional factor of v^2 entering the velocity integral of η_1 weights the

high velocity part of the spectrum, where the fixed time curves of η_0 are visibly separated. The inset of Fig. 3.2 zooms in on the low $v_{\rm min}$ region to emphasize that $\tau_{\rm max}$ of η_1 does have a small $v_{\rm min}$ dependence, transitioning from late May at small values of $v_{\rm min}$, to early June for $v_{\rm min} \gtrsim 300$.

For $n > 1$, one would expect the high end of the velocity distribution to become increasingly weighted, which within the SHM should result in a time dependence similar to that of η_1, but even more independent of $v_{\rm min}$. This is shown in Fig. 3.3, where $\tau_{\rm max}$ and $\tau_{\rm min}$ are plotted for η_0, η_1, and η_2. Instead of plotting $\tau_{\rm min}$, we plot $\tau_{\rm min} - \hat{\tau}_{\rm min}$, where $\hat{\tau}_{\rm min} \equiv \tau_{\rm max} + 6$ months. Fig. 3.3 shows the effect of including (solid) and neglecting (dashed) GF.[8] For η_2, $\tau_{\rm max}$ is hardly affected by GF and thus only a single solid line is plotted. The results for $\tau_{\rm min} - \hat{\tau}_{\rm min}$ without GF are not shown as in this case $\tau_{\rm min}$ is nearly indistinguishable from $\hat{\tau}_{\rm min}$.

Fig. 3.3 shows that, within the SHM, η_0 is the only η_n whose time-dependent behavior differs markedly from $\eta_{n\geqslant 1}$. Thus, for the target-dependent features of the modulation to appear, assuming no other forms of anisotropy are present within the dark halo, the differential cross section must not only contain a non-factorizable velocity dependence, but one of the terms in the differential cross section must be proportional to η_0. Should $\tau_{\rm max}$ and $\tau_{\rm min}$ of η_0 become $v_{\rm min}$ dependent above 300 km/s, e.g. due to the presence of DM substructure [81], the approximate degeneracy of $\eta_{n\geqslant 1}$ (and near exact degeneracy of $\eta_{n\geqslant 2}$) would break and the previous requirement would no longer be necessary.

We would like to note that any η_n can actually be rewritten in terms of, and thus

[8] Unless otherwise stated, GF and the eccentricity of Earth's orbit are included in all calculations.

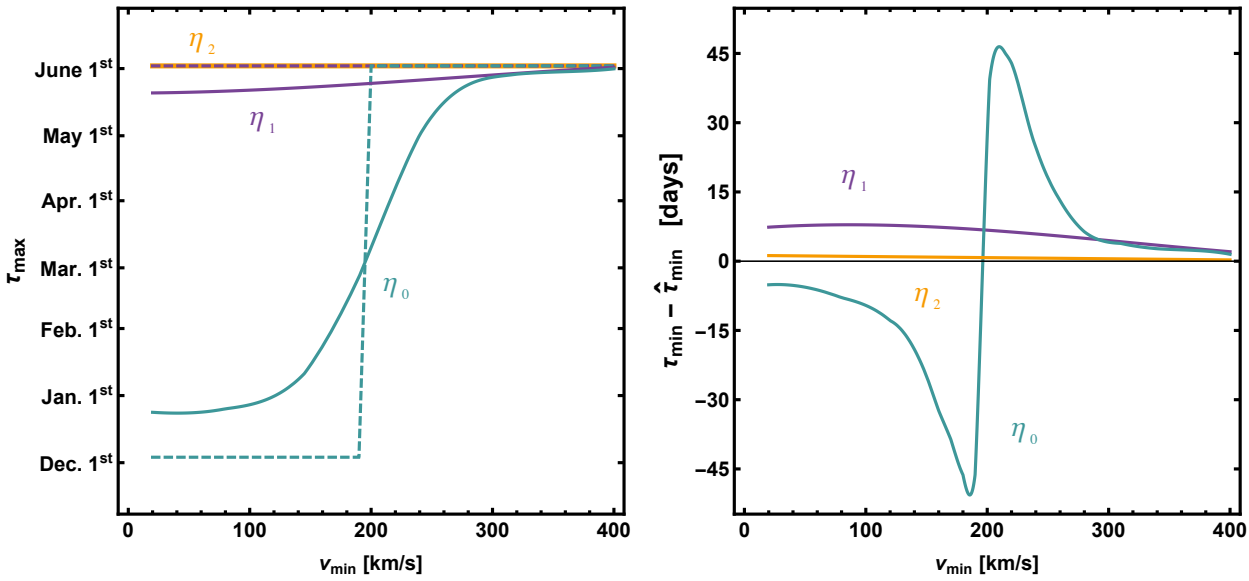

Figure 3.3: Time of maximum $\tau_{\rm max}$ (left) and minimum $\tau_{\rm min}$ (right) of η_0, η_1, and η_2 assuming the SHM, with (solid) and without (dashed) GF. In the right panel we plot $\tau_{\rm min} - \hat{\tau}_{\rm min}$, where $\hat{\tau}_{\rm min}$ is $\tau_{\rm max} + 6$ months. Neglecting GF, $\tau_{\rm min}$ is nearly indistinguishable from $\hat{\tau}_{\rm min}$, and thus is not shown.

computed from, η_0. Defining $F(v,t) \equiv v^2 \int \mathrm{d}\Omega\, f(\boldsymbol{v},t)$ with $\mathrm{d}^3 v = v^2\, \mathrm{d}v\, \mathrm{d}\Omega$, one can write

$$\eta_n = \int_{v \geqslant v_{\rm min}} v^{2n}\, \frac{f(\boldsymbol{v},t)}{v}\, \mathrm{d}^3 v = \int_{v_{\rm min}}^{\infty} v^{2n} \frac{F(v,t)}{v}\, \mathrm{d}v \ , \tag{3.15}$$

which implies

$$\eta_n = -\int_{v_{\rm min}}^{\infty} v^{2n} \frac{\mathrm{d}\eta_0(v,t)}{\mathrm{d}v}\, \mathrm{d}v \ , \tag{3.16}$$

as can be seen by differentiating Eq. (3.11). Finally, integrating Eq. (3.16) by parts yields

$$\eta_n(v_{\rm min},t) = v_{\rm min}^{2n} \eta_0(v_{\rm min},t) + 2n \int_{v_{\rm min}}^{\infty} v^{2n-1} \eta_0(v,t)\, \mathrm{d}v \ , \tag{3.17}$$

where we used the fact that $\eta_0(\infty,t) = 0$. With a similar set of manipulations, any arbitrary η_n can be written in terms of any other arbitrary $\eta_{n'}$. Therefore, in principle, one

may choose to express the rate in terms of any of the η_n (or even in terms of $f(\boldsymbol{v},t)$ itself, as shown in Eq. (18) of [93]). Some of the η_n may have good properties for specific calculations, for example the normalization condition $\int f(\boldsymbol{v},t)\,\mathrm{d}^3v = 1$ can be written either as $\int_0^\infty \eta_0(v_\mathrm{min},t)\,\mathrm{d}v_\mathrm{min} = 1$ (see e.g. [138, 139]) or $\eta_{\frac{1}{2}}(0) = 1$. Moreover, whenever the velocity integrals need to be computed numerically (e.g. for complicated halo models, or when computing the effect of GF), Eq. (3.17) can be used to straightforwardly determine $\eta_{n\neq 0}$ once η_0 is known.

The different time dependence of the the various η_n can be understood by looking at Eq. (3.17). Were it only for the first term on the right-hand side, $\eta_{n\neq 0}$ and η_0 would obviously have the same time dependence at fixed v_min. Because of the second term, however, $\eta_n(v_\mathrm{min},t)$ is a function of time that depends in a nontrivial way on $\eta_0(v,t)$ for all $v \geqslant v_\mathrm{min}$.

3.3 Annual modulation for magnetic dipole DM

3.3.1 Elastic scattering

We study here in detail the case of a Dirac fermion DM candidate χ elastically scattering with nuclei through an anomalous magnetic dipole moment λ_χ, with interaction Lagrangian $\mathscr{L} = (\lambda_\chi/2)\,\bar{\chi}\sigma_{\mu\nu}\chi F^{\mu\nu}$. The differential cross section for elastic scattering off a target nuclide T with Z_T protons and spin S_T is

$$\frac{\mathrm{d}\sigma_T}{\mathrm{d}E_\mathrm{R}}(v_\mathrm{min},v) = \alpha\lambda_\chi^2\left\{Z_T^2\frac{m_T}{2\mu_T^2}\left[\frac{1}{v_\mathrm{min}^2}-\frac{1}{v^2}\left(1-\frac{\mu_T^2}{m^2}\right)\right]F_{\mathrm{SI},T}^2(E_\mathrm{R}(v_\mathrm{min}))+ \right.$$
$$\left. \frac{\hat{\lambda}_T^2}{v^2}\frac{m_T}{m_p^2}\left(\frac{S_T+1}{3S_T}\right)F_{\mathrm{M},T}^2(E_\mathrm{R}(v_\mathrm{min}))\right\}, \quad (3.18)$$

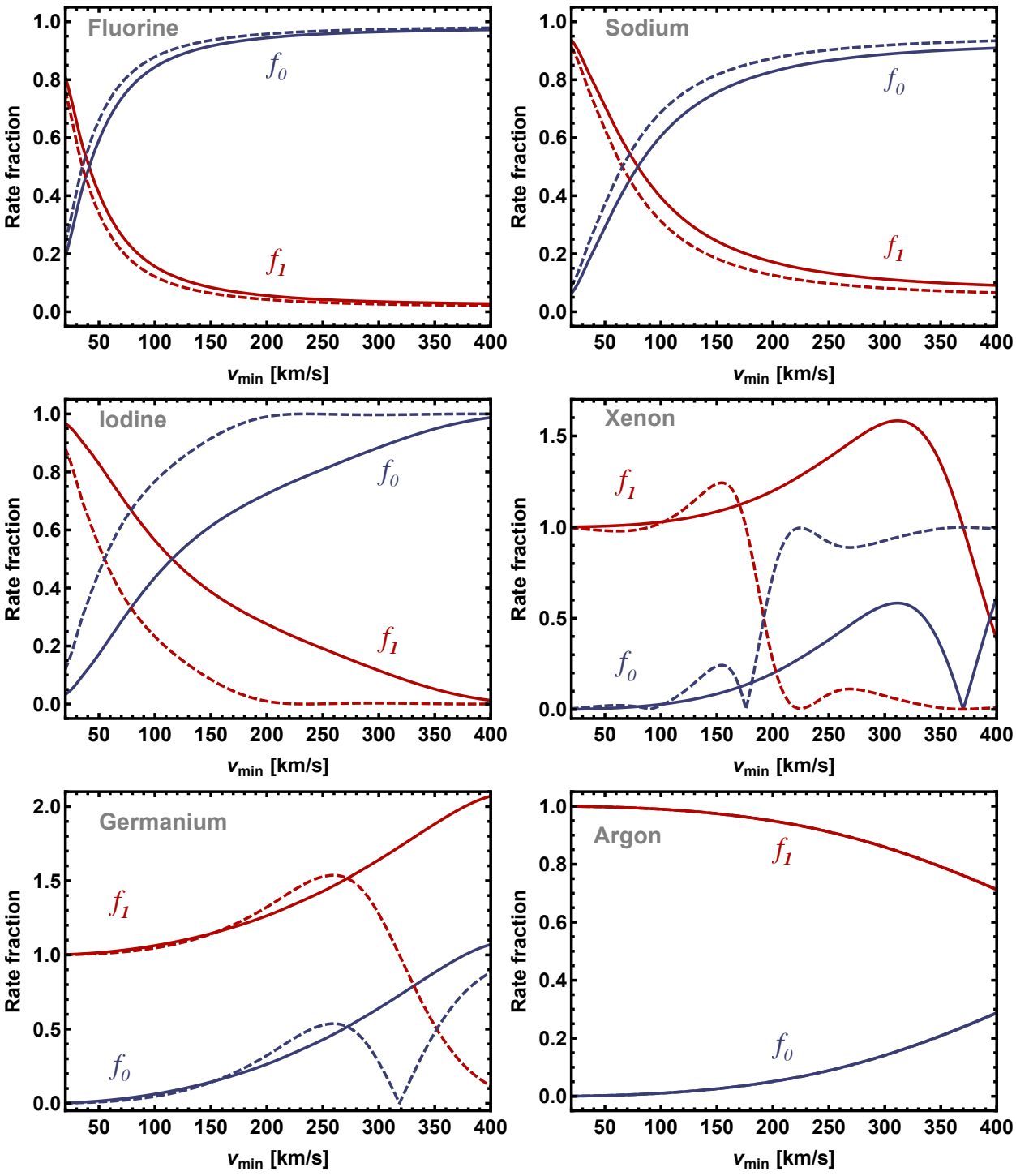

Figure 3.4: Rate fractions f_0 and f_1, as defined in Eq. (3.19), for fluorine (top left), sodium (top right), iodine (middle left), xenon (middle right), germanium (bottom left), and argon (bottom right). Solid (dashed) lines correspond to $m = 100$ GeV (1 TeV).

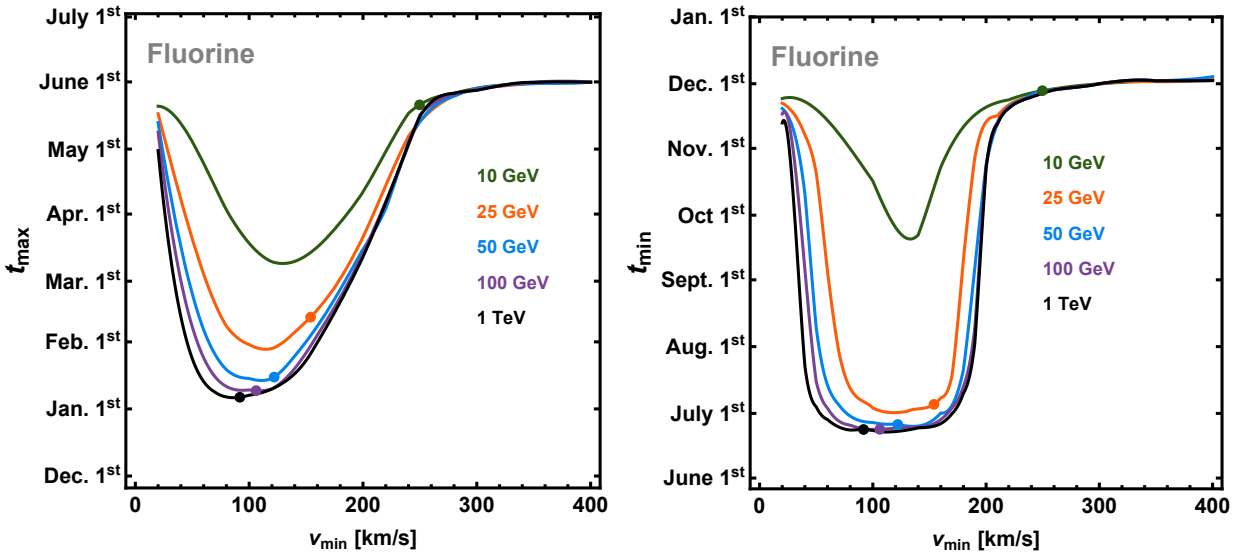

Figure 3.5: Time of maximum $t_{\rm max}$ (left) and minimum $t_{\rm min}$ (right) of the differential rate for magnetic DM scattering off fluorine, plotted for various DM masses as a function of $v_{\rm min}$. The current low energy threshold for PICO has been mapped onto $v_{\rm min}$ for each DM mass and is shown as a small solid dot.

with $\alpha = e^2/4\pi$ the electromagnetic fine structure constant, m_p the proton mass, $\hat{\lambda}_T$ the nuclear magnetic moment in units of the nuclear magneton $e/(2m_p) = 0.16$ GeV^{-1}, and $E_{\rm R}(v_{\rm min}) = 2\mu_T^2 v_{\rm min}^2/m_T$ [93]. The differential cross section contains two terms, one arising from the charge-dipole interaction and the other arising from the dipole-dipole interaction. The former thus depends on the nuclear charge and contains a spin-independent form factor while the latter depends on the nuclear spin and contains a magnetic form factor. Both form factors are normalized to 1 at zero recoil energy. We compute the cross section with the formalism and form factors provided in [134, 135].

Since the magnetic DM differential cross section contains terms proportional to $\eta_0(v_{\rm min}, t)$ and $\eta_1(v_{\rm min}, t)$, the modulation of the differential rate is a direct consequence of the interplay of these two functions and their respective coefficients. The relative importance of each of these functions is determined by the target and DM mass-dependent coefficients. We define

$r_0(E_\mathrm{R}, t)$ and $r_1(E_\mathrm{R}, t)$ as the terms of the differential rate containing η_0 and η_1 respectively, as in Eqs. (3.12) and (3.13), and $\bar{r}_0(E_\mathrm{R})$ and $\bar{r}_1(E_\mathrm{R})$ to be their time average. The time-averaged differential rate reads then $\mathrm{d}\bar{R}_T(E_\mathrm{R})/\mathrm{d}E_\mathrm{R} = \bar{r}_0 + \bar{r}_1$. Fig. 3.4 depicts the absolute value of the time-averaged rate fractions,

$$f_0 \equiv \frac{|\bar{r}_0|}{\bar{r}_0 + \bar{r}_1} \,, \qquad\qquad f_1 \equiv \frac{|\bar{r}_1|}{\bar{r}_0 + \bar{r}_1} \,, \tag{3.19}$$

as functions of v_min, for six elements (fluorine, iodine, sodium, xenon, germanium, and argon) employed by current DM direct detection experiments. When more than one isotope is present, i.e. for germanium and xenon, r_0 and r_1 are understood to be summed over isotopes. Solid (dashed) lines correspond to a 100 GeV (1 TeV) DM particle.

The target dependence of t_max and t_min can be understood by combining the information on the time dependence of η_0 and η_1 in Fig. 3.3 with the information on the rate fraction of the corresponding element shown in Fig. 3.4. t_max and t_min as functions of v_min are shown in Figs. 3.5–3.8 for magnetic DM scattering off fluorine, sodium, iodine, and xenon. We have chosen not to plot t_max and t_min for germanium and argon because the results for all DM masses below 10 TeV are identical due to their small (germanium) or zero (argon) nuclear magnetic moment (see Ref. [94] for details). For each element, t_max (left panels) and t_min (right panels) are plotted for various DM masses ranging from 10 GeV to 10 TeV. Also shown, depicted as dots on the t_max and t_min curves, are the E_R thresholds for LUX [140] (3.1 keV [139], employing Xe), DAMA [141] (6.7 keV for Na with $Q_\mathrm{Na} = 0.3$ and 22.2 keV for I with $Q_\mathrm{I} = 0.09$), and PICO [142] (3.2 keV, employing F), translated into v_min for elastic

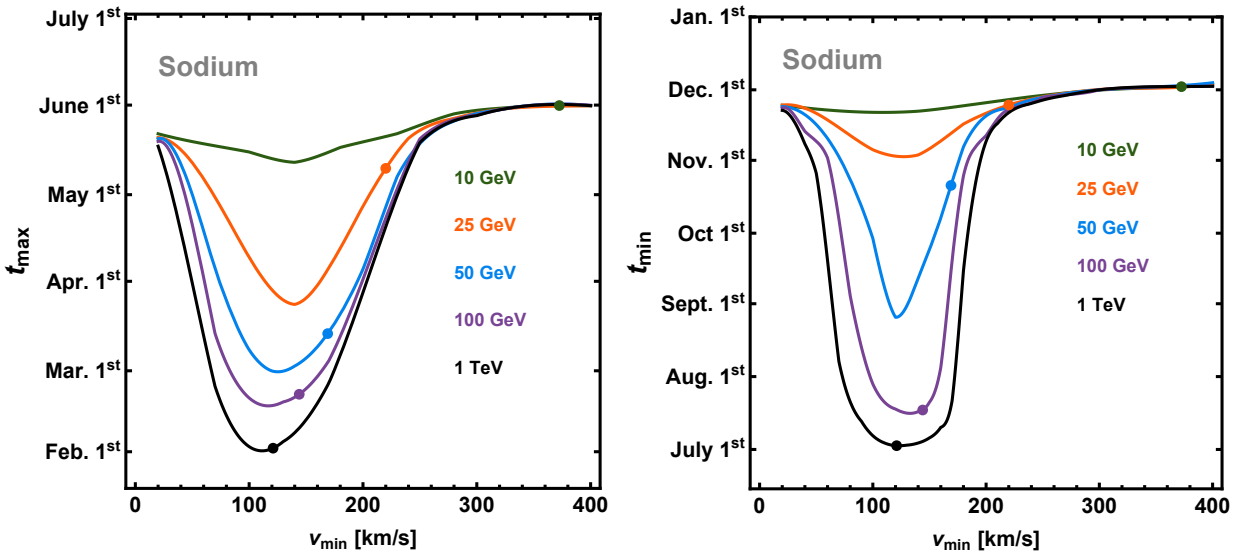

Figure 3.6: Time of maximum $t_{\rm max}$ (left) and minimum $t_{\rm min}$ (right) of the differential rate for magnetic DM scattering off sodium, plotted for various DM masses as functions of $v_{\rm min}$. The current low energy threshold for DAMA has been mapped onto $v_{\rm min}$, assuming a quenching factor $Q_{\rm Na} = 0.3$, for each DM mass and is shown as a small solid dot.

scattering with each DM mass. When multiple isotopes are present, the value of m_T in Eq. (3.3) is replaced with $\sum_T \xi_T m_T$, where ξ_T is the numerical abundance of element T.

Figs. 3.5–3.8 show that $t_{\rm max}$ and $t_{\rm min}$ become target and DM mass independent for $v_{\rm min} \gtrsim 300$ km/s. This is due to the fact that the difference in the time-dependent behavior between η_0 and η_1, which are central to the target-dependent features, vanish above $v_{\rm min} \approx 300$ km/s (see Fig. 3.3), if the only source of anisotropy in the local halo is GF.

Fig. 3.4 confirms that at sufficiently small values of $v_{\rm min}$ the contribution to the differential rate from the term proportional to η_0 can be neglected. This is because the r_1 term contains the factor $1/v_{\rm min}^2$, which dominates the $v_{\rm min}$ dependence of the rate at small $v_{\rm min}$ values. Thus, in the small $v_{\rm min}$ limit, $t_{\rm max}$ occurs in late May and $t_{\rm min}$ occurs in late November, regardless of the target element and DM mass. This behavior is a feature of elastic magnetic DM and other DM models could behave in a qualitatively different way.

For target elements that have a nonzero average nuclear magnetic moment (i.e., all elements considered here except argon), at large enough values of $v_{\rm min}$ the dipole-dipole interaction inevitably becomes dominant, and thus $r_0 > r_1$. This is because the spin-independent form factor in Eq. (3.18) decreases significantly faster than the magnetic form factor. Fig. 3.4 confirms that for all elements considered except argon, there exists a value of $v_{\rm min}$ below which r_1 is the dominant contribution to the rate, and above which r_0 is the dominant contribution to the rate. The location in $v_{\rm min}$ of this transition and how fast or gradual it is determine the unique element-dependent features of $t_{\rm max}$ and $t_{\rm min}$ in Figs. 3.5–3.8.

The mass of the DM particle can have a large influence on the appearance of target-dependent features. Consider for instance the difference between a 100 GeV and 1 TeV DM particle scattering off xenon. For a 100 GeV DM particle, Fig. 3.4 shows that the $v_{\rm min}$ point at which r_0 becomes dominant is around $v_{\rm min} \approx 400$ km/s. Since this value of $v_{\rm min}$ lies in the target-independent region, $t_{\rm max}$ is effectively determined solely by the time dependence of η_1. As the DM mass increases, the point at which r_0 becomes dominant with respect to r_1 shifts to lower values of $v_{\rm min}$. This is partly due to the fact that the $v_{\rm min}$ value corresponding to a given $E_{\rm R}$ decreases, but also because the terms $1/\mu_T^2$ and μ_T^2/m^2 multiplying the SI component of Eq. (3.18) decrease. Consequently, for a 1 TeV DM particle scattering off xenon, the $v_{\rm min}$ value at which r_0 becomes dominant appears in a $v_{\rm min}$ region where the time dependence of η_1 and η_0 differ, leading to the appearance of a unique target-dependent feature in the $t_{\rm max}$ and $t_{\rm min}$ curves.

Up to this point we have only discussed how target-dependent modulation arises and how, under the assumption of magnetic DM, observables associated with the modulation of

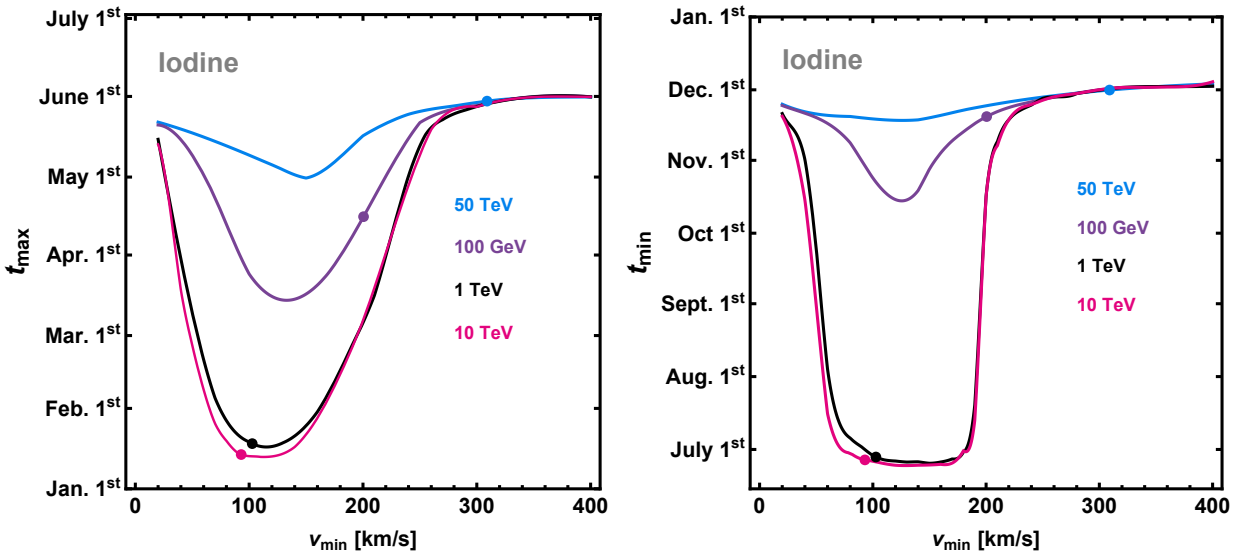

Figure 3.7: Time of maximum $t_{\rm max}$ (left) and minimum $t_{\rm min}$ (right) of the differential rate for magnetic DM scattering off iodine, plotted for various DM masses as functions of $v_{\rm min}$. The current low energy threshold for DAMA has been mapped onto $v_{\rm min}$, assuming a quenching factor $Q_{\rm I} = 0.09$, for each DM mass and is shown as a small solid dot.

the rate in $v_{\rm min}$ can potentially change. We have not yet discussed how these effects would manifest in present day experiments. To determine if experiments are capable of observing these target-dependent features, one must take into account the experimental threshold, the efficiency, the energy resolution, and the binning method.

The obvious requirement for these target-dependent effects to be observable, is that the experimental threshold in $v_{\rm min}$ must be below 300 km/s. The threshold in $v_{\rm min}$ depends on the threshold in E', the DM particle mass, and the scattering kinematics. Figs. 3.5 and 3.8 show that present thresholds are already low enough to give rise to a four month difference in $t_{\rm max}$ for a 50 GeV DM particle scattering elastically off fluorine and xenon (while the 50 GeV curve is not shown for xenon, it directly overlaps with the 100 GeV curve), should the differential scattering rate be measured with perfect energy resolution, which is not possible for actual experiments.

Since we would like to see how observable this target dependence could be, we choose to consider experiments employing elements with large nuclear magnetic moments. For this reason we begin by considering the fluorine-based experiment PICO. PICO measures the energy-integrated rate as a function of threshold energy $E_{\rm th}$, and has an energy-dependent efficiency function that reduces the contribution of the scattering events near threshold. Figs. 3.5 and 3.9 can be used to understand how much the modulation features in the differential rate are erased in the energy-integrated rate. Fig. 3.9 depicts the time-averaged differential rate (summed over isotopic composition) for a 100 GeV DM particle scattering off fluorine, sodium, iodine, argon, germanium, and xenon, for magnetic DM as a function of $E_{\rm R}$. Fig. 3.9 includes both log-linear (left) and log-log (right) plots to show the different features of the spectra. If the differential rate were very steep, the integrated rate would be dominated by the differential rate at threshold, and thus have a similar annual modulation. As the differential rate flattens, an increasingly unweighted averaging occurs for all energies above threshold. The flattening of fluorine's differential rate occurs below PICO's 3.2 keV threshold, and thus the pronounced features appearing in $t_{\rm max}$ of the differential rate should be strongly suppressed in the integrated rate.

Fig. 3.10 depicts how PICO would realistically observe the time of maximum of the energy-integrated rate as a function of the threshold energy for a 100 GeV DM particle interacting through a magnetic dipole (solid blue line) or with the standard SI/SD contact interaction (dashed red line). As PICO does not provide an analytic form of their efficiency,

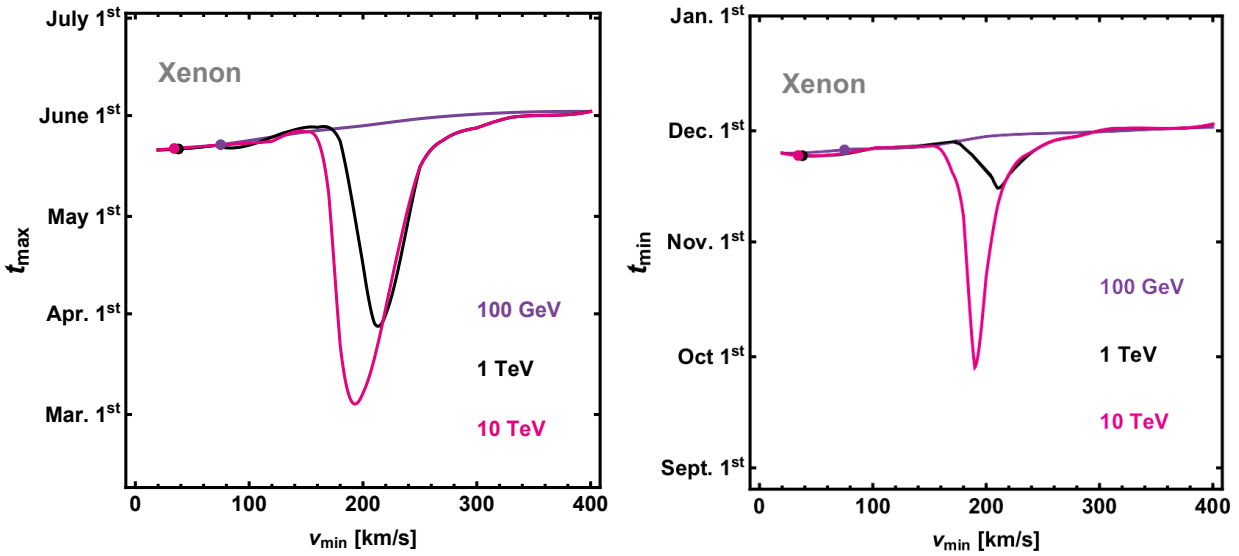

Figure 3.8: Time of maximum $t_{\rm max}$ (left) and minimum $t_{\rm min}$ (right) of the differential rate for magnetic DM scattering off xenon, plotted for various DM masses as functions of $v_{\rm min}$. The current low energy threshold for LUX has been mapped onto $v_{\rm min}$ for each DM mass and is shown as a small solid dot.

we take the parametrization used by PICASSO,

$$\epsilon(E') = 1 - e^{\alpha(1-E'/E_{\rm th})} \ , \tag{3.20}$$

with $\alpha = 5$ for fluorine [143]. We also assume a perfect energy resolution, $G_T(E_{\rm R}, E') = \delta(E_{\rm R} - E')$. We have checked that the contribution from carbon is negligible for all energies so we consider only fluorine. Fig. 3.10 shows that the time of maximum of the rate as would be measured by PICO is nearly identical for the magnetic dipole interaction (dashed red line) and the standard SI/SD contact interactions (solid blue line), for all threshold energies we examined (larger than 0.1 keV). To determine if the two interactions could be differentiated by binning the data, we also consider a fluorine-based experiment capable of measuring the rate in 1 keV bins. For this hypothetical experiment we take the same

efficiency function we used for PICO, and plot the result as horizontal bars in Fig. 3.10 for the magnetic dipole interaction (blue) and standard SI/SD contact interaction (red). The difference in the time of maximum of the energy-integrated rate for the two interactions in this hypothetical experiment ranges from 7 days to 20 days for threshold energies between 1 and 10 keV.

There are a number of reasons for the unique target-dependent features shown in Fig. 3.5 to be strongly suppressed when calculating the energy-integrated rate. First, the features in $t_{\rm max}$ for the magnetic dipole interaction differ the most from the standard SI/SD contact interactions in the $v_{\rm min}$ region where the r_0 and r_1 terms in Eq. (3.12) cross over. For fluorine, this occurs at very small $v_{\rm min}$ values, $v_{\rm min} \lesssim 70$ km/s. The top axis of Fig. 3.10 shows that this region of $v_{\rm min}$ corresponds to very low energies, far below PICO's current threshold. Additionally, for elastic scattering $E_{\rm R} \propto v_{\rm min}^2$, and since the integration of the differential rate is over $E_{\rm R}$, the Jacobian's dependence on $v_{\rm min}$ must be included in the integrand when performing the integral in $v_{\rm min}$ instead. This additional factor increases the weight of the large $v_{\rm min}$ region in the integration where the modulation is target independent. Finally, as previously mentioned, the differential rate decreases rather slowly as a function of $E_{\rm R}$, smearing the target-dependent features.

Let us see if other experiments could better preserve the target-dependent features. Let us consider DAMA/LIBRA, henceforth referred to as DAMA (or any of the upcoming DAMA-like experiment as KIMS-NaI, ANAIS, DM-Ice17, and SABRE, see e.g. [144, 145] and references therein). DAMA is an interesting experiment to consider as both sodium and iodine have reasonably large nuclear magnetic moments and bin their data in small, 0.5 keVee, in-

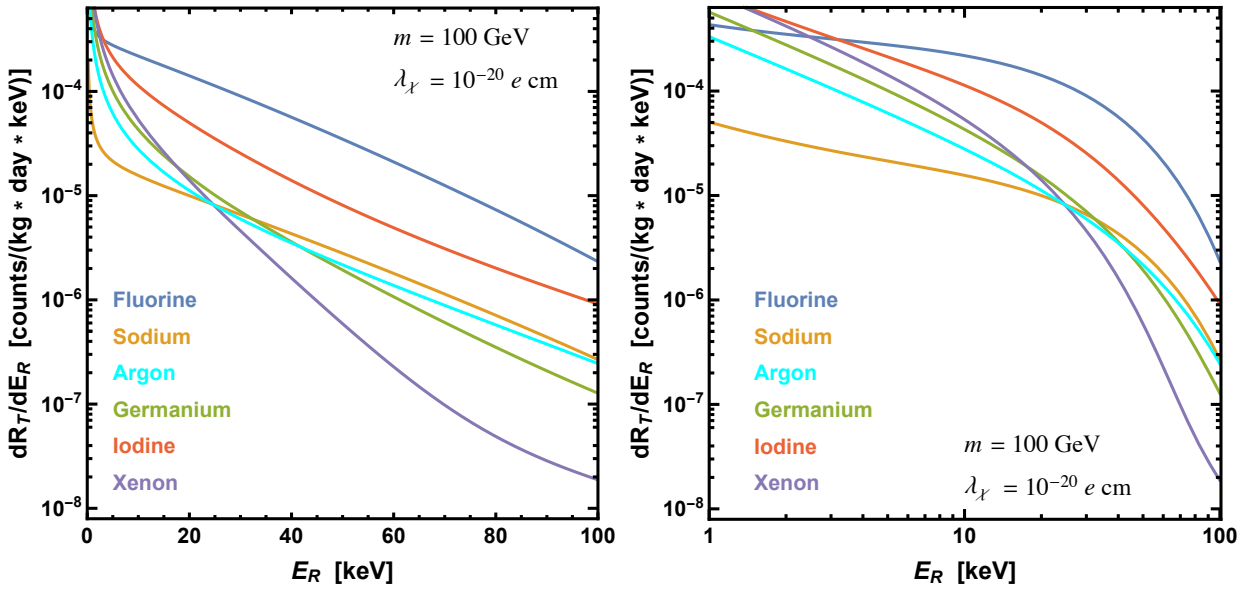

Figure 3.9: The time-averaged differential rate (summed over isotopes) in units of counts/(kg day keV) for a 100 GeV magnetic DM particle scattering off various elements as a function of recoil energy, shown on a semi-log (left) and log-log (right) plot. λ_χ has been set to $10^{-20}\,e$ cm.

tervals. In the left panel of Fig. 3.11 we plot the time of maximum of the DAMA binned rate as a function of E' for both the magnetic dipole interaction (blue) and the standard SI/SD contact interaction (red), assuming elastic scattering with a 100 GeV DM particle. Also depicted with a vertical dashed line is DAMA's current low energy threshold of 2 keVee for the analysis of the modulated signal. The results for DAMA are calculated using quenching factors $Q_{\rm Na} = 0.3$ and $Q_{\rm I} = 0.09$, and a gaussian energy resolution function with standard deviation $0.448\sqrt{E'} + 0.0091E'$ [146]. The results for the two interactions are nearly indistinguishable above 4 keVee, and only differ by about a month in the lowest observable energy bin. It is worth mentioning that DAMA will soon extend their low-energy threshold down to 1 keVee which should result in a further observable difference between modulation arising from the standard SI/SD contact interactions and magnetic DM.

Like PICO, DAMA also sees a strong suppression in the target element dependent features of the modulation. The reason for the suppression in DAMA, however, is not primarily due to integrating over the differential rate, but rather due to the fact that DAMA has two non-negligible target elements. The independent contribution to the time-averaged differential rate from sodium (yellow) and iodine (green) as a function of detected energy is shown in the right panel of Fig. 3.11. Since each element has a different $v_{\min}$ to E' (average) mapping, and neither element dominates the differential rate in the 2–6 keVee range, the target-dependent region of $t_{\max}$ for sodium is partially averaged with the target-independent region of iodine, leading to a large suppression of the target-dependent features. Furthermore, the small quenching factor of iodine pushes the most pronounced differences of the $t_{\max}$ curve below threshold. The horizontal dashed lines in the left panel of Fig. 3.11 show how the $v_{\min}$ values for sodium (yellow) and iodine (green) independently map to E', in average.

Since experiments do not know the DM particle mass or the scattering kinematics a priori, it is nontrivial to obtain $t_{\max}$ as a function of $v_{\min}$ from the data. For this reason, and because $t_{\max}$ as a function of E_{R} is necessarily known to be target element dependent, it is logical to ask how $t_{\max}$ for magnetic DM differs from $t_{\max}$ for the standard SI/SD contact interactions as functions of E_{R}. This comparison is made in Fig. 3.12, where the left panel shows $t_{\max}$ for SI/SD interactions while the right panel shows $t_{\max}$ for magnetic DM, both as functions of E_{R}. In both cases we assume a 100 GeV DM particle scattering elastically with various target elements (note that the curves for argon, germanium, and xenon in the right panel overlap almost entirely).

For the standard contact interaction with only r_0 in the rate (see Eqs. (3.12) and (3.13)),

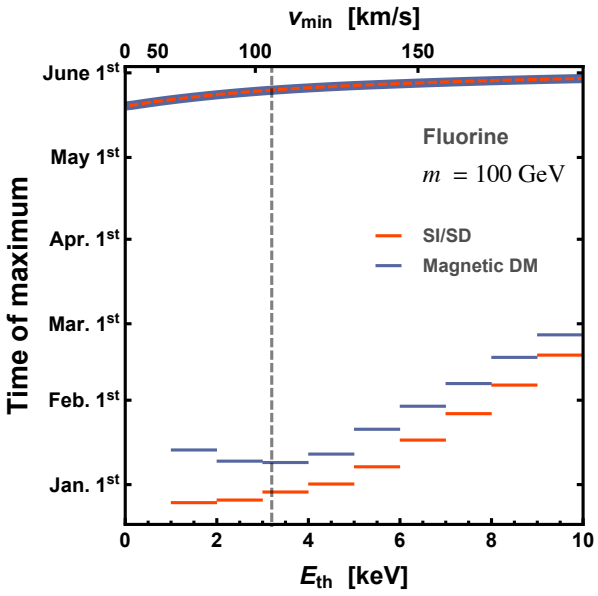

Figure 3.10: Time at which the energy-integrated rate is maximum as a function of threshold energy $E_{\rm th}$ (the corresponding $v_{\rm min}$ value has been plotted on the upper horizontal axis), as observed by a fluorine detector for a 100 GeV DM particle scattering elastically through a magnetic dipole (blue) and the standard SI/SD contact interaction (red). The solid and dashed lines depict the result of integrating the rate from a fixed threshold energy $E_{\rm th}$, while horizontal bars show the result of binning data into 1 keV bins. The efficiency function in Eq. (3.20) has been incorporated into all calculations. The vertical dashed line corresponds to PICO's 3.1 keV lowest energy threshold.

as the SI/SD interaction, the differences in the curves is determined solely by the mass of the target nuclide. The largest difference in $t_{\rm max}$ therefore occurs between fluorine and xenon and is around three months for recoil energies between 15 and 20 keV. While this is a rather large discrepancy, the shape of the $t_{\rm max}$ curves for the standard SI/SD interactions are all stretched and compressed images of each other. In fact, all curves are obtained from the curve for η_0 in Fig. 3.3 with the $E_{\rm R}$-$v_{\rm min}$ relation for elastic scattering in Eq. (3.3), which of course only differ in each case for the choice of m_T. In this sense, $t_{\rm max}$ and other observables associated with the modulation are not truly target dependent for interactions with only r_0 in the rate. The same cannot be said for magnetic DM. The right panel of

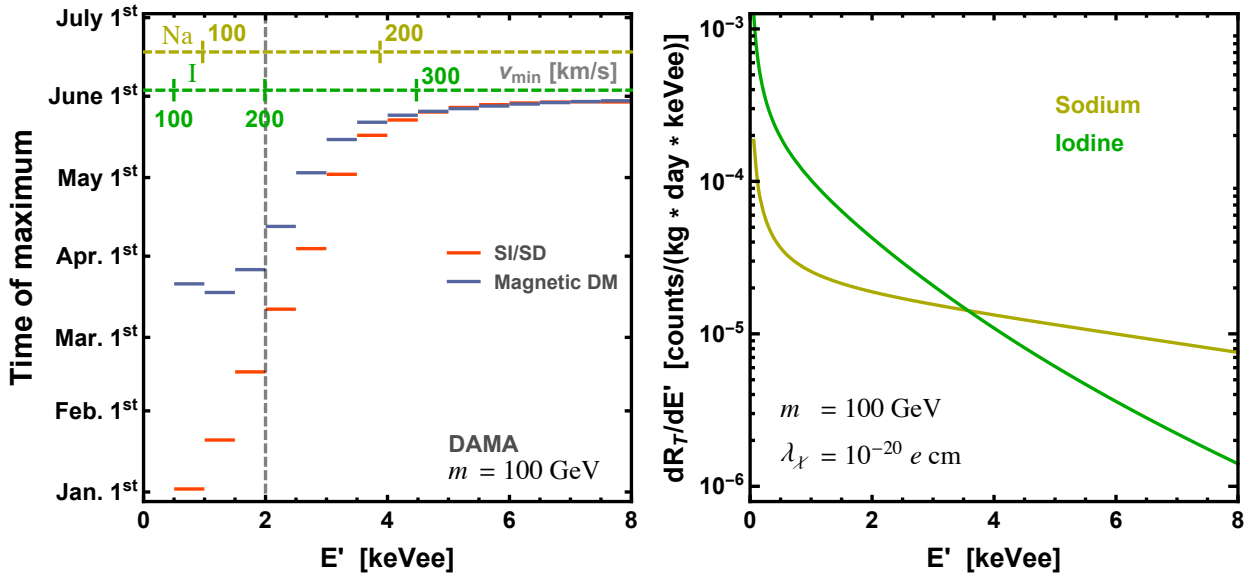

Figure 3.11: Left: $t_{\rm max}$ seen by DAMA for a 100 GeV WIMP interacting through a magnetic dipole (blue) and the standard SI/SD contact interaction (red). Plotted with a vertical dashed line is the current DAMA low energy threshold. The horizontal dashed lines show the mapping of $v_{\rm min}$ onto E' for sodium (yellow) and iodine (green) assuming quenching factors of $Q_{\rm Na} = 0.3$ and $Q_{\rm I} = 0.09$. Right: The time-averaged differential event rate for a 100 GeV magnetic DM particle scattering off sodium (yellow) and iodine (green) as a function of detected energy.

Fig. 3.12 shows that the difference between various $t_{\rm max}$ curves is more pronounced than when the standard interactions are considered, and furthermore, the curves have a more individualized shapes. The only exception are the curves for germanium, argon, and xenon, which completely overlap for a 100 GeV DM particle, a consequence of having a small or zero (for argon) average nuclear magnetic moment.

3.3.2 Inelastic scattering

Prior to this point we have only considered DM-nuclei elastic scattering. It has been shown that inelastic scattering, which can occur when there exist at least two DM particles with nearly degenerate masses m and $m + \delta$ with $\delta \ll m$, has the potential to significantly alter

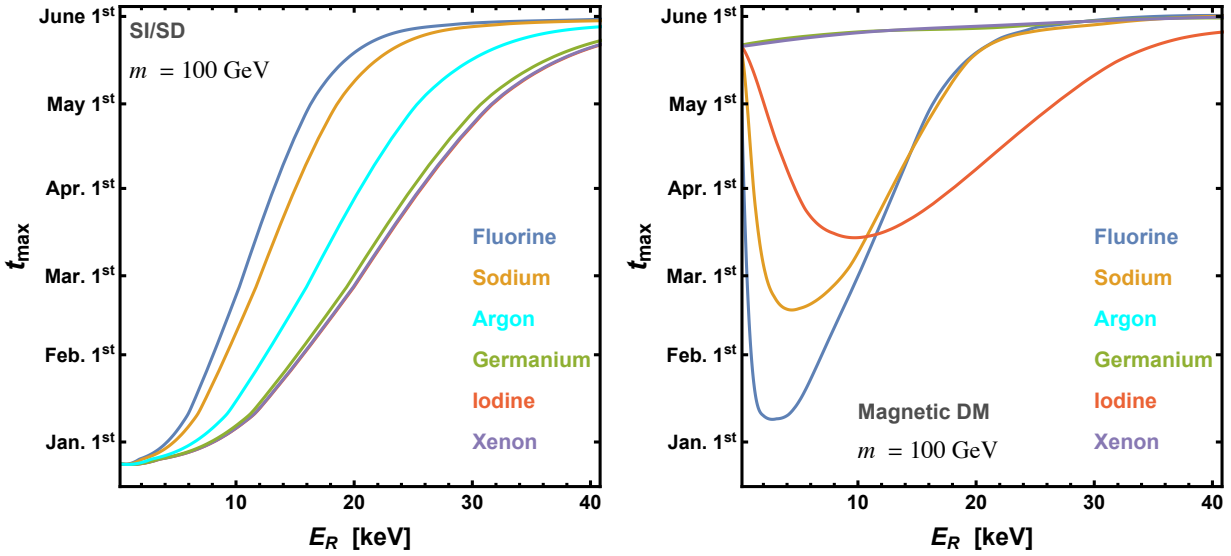

Figure 3.12: $t_{\max}$ for a 100 GeV WIMP interacting with various elements through the standard SI/SD contact interaction (left) and a magnetic dipole (right) as a function of recoil energy. Note that the curves in the right panel for argon, germanium, and xenon all overlap and are nearly indistinguishable.

the scattering kinematics and the observed annual modulation [147, 148].

Inelastic endothermic scattering occurs when the light DM state scatters into the heavy DM state, $\delta > 0$. Since this process requires additional energy, only DM particles traveling at speeds greater than or equal to $v_\delta^T \equiv \sqrt{2\delta/\mu_T}$ can scatter off a particular target T. If GF is the sole source of anisotropy, target-dependent modulation can only occur when speeds of about 200 km/s are probed. This implies that for a fixed DM mass, there exists a maximum mass splitting $\delta_{\max}$ for which target-dependent modulation can occur. For a 100 GeV DM particle scattering off fluorine, sodium, and iodine, this corresponds to values of $\delta_{\max} \approx 3.3$ keV, 4 keV, and 12 keV, respectively. These values of δ are quite small with respect to the typical momentum transfer in the interaction, and thus we expect the scattering kinematics to be almost elastic. Without an additional form of anisotropy, endothermic scattering is therefore ineffective in probing values of $v_{\min}$ which can lead to target-dependent modulation.

Inelastic exothermic scattering, occurring when the heavier DM particle down-scatters into the lighter DM state ($\delta < 0$), can be potentially more interesting for target-dependent modulation. To illustrate how exothermic scattering can alter the observed modulation, we plot in the left panel of Fig. 3.13 $t_{\max}$ for DM interacting with various elements through the standard SI/SD contact interaction, assuming $m = 100$ GeV and $\delta = -10$ keV, as a function or $E_{\rm R}$. This result is obtained by mapping the $\tau_{\max}(v_{\min})$ line corresponding to η_0 shown in Fig. 3.3 onto $E_{\rm R}$ by using the $E_{\rm R}$-$v_{\min}$ relation for inelastic scattering,

$$v_{\min}(E_{\rm R}) = \frac{1}{\sqrt{2m_T E_{\rm R}}} \left| \frac{m_T E_{\rm R}}{\mu_T} + \delta \right| \tag{3.21}$$

(remember that for the SI/SD interaction $t_{\max}$ coincides with $\tau_{\max}$).

We have chosen not to plot $t_{\max}$ for magnetic exothermic dark matter because, for all elements considered, the results mirror what would be expected should the differential cross section either be independent of velocity, or proportional to v^{-2}. That is to say for a given element, only the term proportional to η_0 or the term proportional to η_1 is relevant, never both. To understand why this is the case, it is necessary to first consider the differential cross section [102]:

$$\begin{aligned} \frac{\mathrm{d}\sigma_T}{\mathrm{d}E_{\rm R}}(E_{\rm R}, v) = \alpha \lambda_\chi^2 \Bigg\{ \frac{Z_T^2}{E_{\rm R}} \Bigg[1 - \frac{E_{\rm R}}{v^2} \left(\frac{1}{2m_T} - \frac{1}{m^2} \right) \\ - \frac{\delta}{v^2} \left(\frac{1}{\mu_T} + \frac{\delta}{2m_T E_{\rm R}} \right) \Bigg] F_{{\rm SI},T}^2(E_{\rm R}) + \frac{\hat{\lambda}_T^2}{v^2} \frac{m_T}{m_p^2} \left(\frac{S_T + 1}{3S_T} \right) F_{{\rm M},T}^2(E_{\rm R}) \Bigg\} . \end{aligned} \tag{3.22}$$

There are two additional terms with respect to the elastic case in Eq. (3.18), both contribut-

ing to the charge-dipole term for inelastic magnetic dark matter, one of which is proportional to $E_{\rm R}^{-1}$ and the other to $E_{\rm R}^{-2}$. Both of these terms are contained within f_0 (see Sec. 3.3.1), and since the target dependence relies on the interplay between f_0 and f_1, it is important to understand how these two new terms contribute to the relative rate fractions.

In Sec. 3.3.1, we showed that for elastic scattering f_1 is always the dominant contribution to the rate at low $v_{\rm min}$. This is a consequence of having a term proportional to $v_{\rm min}^{-2} \propto E_{\rm R}^{-1}$. For inelastic magnetic DM, f_0 now has a term proportional to $E_{\rm R}^{-2}$, thus at very low energies r_0 is always the dominant contribution to the rate. This might be avoided, however, because there may exist a lower limit on $E_{\rm R}$ which depends on $v_{\rm esc}$, and this may be above the region where $E_{\rm R}^{-2}$ is the dominant factor (see Fig. 1 of [149]). At large energies, both of the new terms will be suppressed, and as for elastic scattering, the rate should be controlled by the term containing the magnetic form factor, r_0 (assuming the target element has a non-negligible nuclear magnetic moment). Whether r_0 or r_1 dominates the rate at intermediate energies depends strongly on the target element, the DM mass, and δ.

To illustrate how these variables affect the potential appearance of target-dependent modulation, we plot in the right panel of Fig. 3.13 the rate fraction for magnetic exothermic DM scattering off fluorine, assuming $m = 100$ GeV and $\delta = -10$ keV. The blue and red lines show the terms proportional to f_0 and f_1, respectively. The green region highlights values of $E_{\rm R}$ where target-dependent modulation could potentially be observed (i.e. $v_{\rm min} \lesssim 200$ km/s, assuming GF is the sole source of anisotropy), and the dot-dashed orange line depicts the energy corresponding to $v_{\rm min} = 0$ km/s. To compute the rate we again use the form factors provided in [134,135]. While these only apply to elastic scattering, [118] showed that

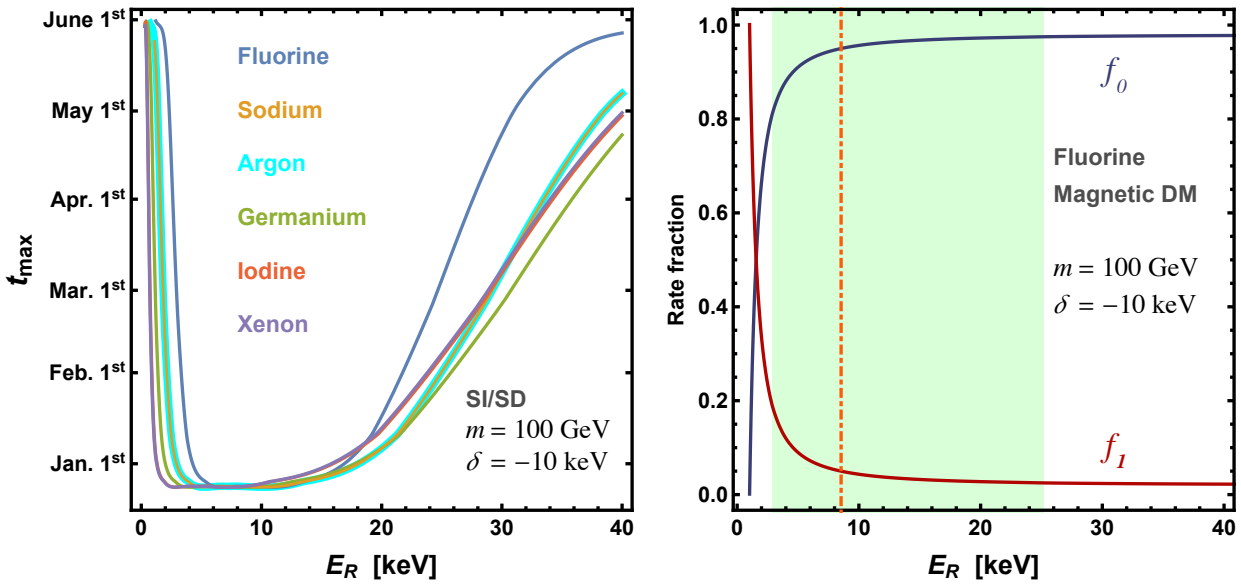

Figure 3.13: Left: $t_{\rm max}$ for the exothermic scattering with various elements assuming the standard SI/SD contact interactions, a DM mass of 100 GeV, and a mass splitting $\delta = -10$ keV, as a function of $E_{\rm R}$. Right: Rate fractions f_0 (blue) and f_1 (red) for magnetic DM (as defined in Sec. 3.3.1) for 100 GeV DM scattering off fluorine, assuming $\delta = -10$ keV. The shaded green region highlights recoil energies corresponding to values of $v_{\rm min} < 200$ km/s, and the dot-dashed orange line depicts the $E_{\rm R}$ value corresponding to $v_{\rm min} = 0$ km/s.

they can be adapted to inelastic scattering by properly taking into account the modification to $\boldsymbol{v}^\perp = \boldsymbol{v} + \boldsymbol{q}/2\mu_N$, the component of $\boldsymbol{v}$ orthogonal to the momentum transfer $\boldsymbol{q}$, due to inelastic kinematics (μ_N being here the DM-nucleon reduced mass). Therefore one simply needs to replace the variable $\boldsymbol{v}^\perp$ in the form factors of [134, 135] with the true orthogonal component of the DM velocity for inelastic scattering, $\boldsymbol{v}^\perp_{\rm inel} = \boldsymbol{v}^\perp + \delta\boldsymbol{q}/|\boldsymbol{q}|^2$.

Two comments are in order. We previously stated that f_0 should be the dominant term at low values of $E_{\rm R}$ due to the $E_{\rm R}^{-2}$ term in the differential cross section. While this may not appear to be the case in Fig. 3.13, this is simply because we have not plotted the low $E_{\rm R}$ regime, as it is not relevant for target-dependent modulation (low $E_{\rm R}$ corresponds to large WIMP velocities where GF is unimportant). Next, for the current choice of parameters, f_0

is the only relevant term in the $E_{\rm R}$ range where the effect GF is important, and thus the $t_{\rm max}$ curve is identical to the fluorine curve shown in the left panel of Fig. 3.13. We stress that the unique target-dependent features seen in the $t_{\rm max}$ and $t_{\rm min}$ curves of Figs. 3.5–3.8 only arise if both f_0 and f_1 contribute in a non-negligible way within the region capable of probing low DM speeds.

It is interesting to see how changing m, δ, and the target element alter the results of Fig. 3.13. Changing the DM particle mass results in two distinct effects. Contrary to elastic scattering, lower values of m increase the importance of f_0 relative to f_1 at fixed $E_{\rm R}$, and thus the point at which f_0 becomes dominant relative to f_1 shifts to lower values of $E_{\rm R}$. The second and more import effect arises from changing the value of m in Eq. (3.21), which causes the $E_{\rm R}$ range where the effect of GF is relevant in the right panel of Fig. 3.13 to shift. Using Eq. (3.21), one can see that decreasing the DM mass shifts the influence of GF to lower values of $E_{\rm R}$. We have checked that for $\delta \geqslant 10$ keV, lowering the DM particle mass to 10 GeV does not bring the point at which f_0 and f_1 cross into the region where target dependent modulation could occur.

Increasing the magnitude of δ (i.e. making δ more negative) also has two effects. First, it shifts the point at which f_0 and f_1 cross to higher values of $E_{\rm R}$. This effect is completely negligible, however, when compared with how this change in δ shifts the $E_{\rm R}$ range where the effect of GF is relevant (see Eq. (3.21)).

The negligible nuclear magnetic moments of germanium, xenon, and argon lead to a complete dominance of f_1 over f_0 for essentially all values of $E_{\rm R}$, regardless of the DM mass and δ. This implies that inelastic magnetic DM scattering with these elements will

always lead to an observation of $t_{\rm max}$ between late May and early June, and the annual modulation will be consistent with inelastic scattering through differential cross sections that are independent of velocity. For iodine and sodium we have checked that the crossover from f_1 to f_0 as the dominant contribution to the rate, either always occurs far below threshold, or does not occur in the region where target-dependent modulation would arise. Identifying this type of scattering would then necessitate at least one experiment employing germanium, xenon, or argon, and another experiment employing fluorine, sodium, or iodine, to observe the annual modulation.

3.3.3 Identification of non-factorizable cross sections

The target-dependent effects described thus far have relied on two assumptions: experiments probe anisotropy in the DM halo and velocity and target dependence cannot be factored in the DM-nucleus differential scattering cross section. The question remains how a differential cross section of this form could be identified. A single experiment can never uniquely determine the underlying particle physics and astrophysics; it is only possible for a single experiment to say that their findings are consistent with some set of assumptions on the distribution of DM, the DM mass, a particular DM-nucleus interaction, etc. The most model-independent information is likely to come from a comparison of the outcomes of different experiments. We believe the most effective way to confirm the existence of a DM-nucleus cross section with a non-factorizable target and velocity dependence is to show that there exists no $E_{\rm R}$-$v_{\rm min}$ relation capable of mapping observables associated with the modulation of the rate from experiments employing different target elements onto a unique function of $v_{\rm min}$.

We emphasize however that finding unique functions of $v_{\rm min}$ capable of reconciling the results of multiple experiments does not preclude the existence of non-factorizable differential cross sections. In the case of inelastic magnetic DM, elements with small average nuclear magnetic moments, e.g. germanium, xenon, argon, and carbon, will all yield similar results because the differential cross section is dominated by a single term, at least for the $v_{\rm min}$ region where the local DM distribution is made anisotropic by GF.

3.4 Summary

It is typically assumed that observables associated with the annual modulation of the rate in direct detection experiments, when expressed as functions of $v_{\rm min}$ (the minimum DM speed necessary to impart a given recoil energy to a target nucleus), are unique target-independent functions. We have shown that this is not necessarily the case, and in fact the existence of a DM-nucleus differential cross section with a non-factorizable target and velocity dependence naturally leads to target-dependent modulation. The identification of this type of differential cross section is not straightforward and must be done through a process of elimination. In the event that multiple experiments with putative signals cannot find an $E_{\rm R}$-$v_{\rm min}$ relation that can reconcile the differences between the observed modulations, one may then infer the potential existence of a non-factorizable differential cross section. We emphasize, however, that the reverse is not true. That is to say, finding an $E_{\rm R}$-$v_{\rm min}$ relation that maps observables associated with the modulation from multiple experiments onto unique $v_{\rm min}$-dependent functions does not necessarily ensure that the modulation is target independent.

As a specific example, we have shown how $t_{\rm max}$ ($t_{\rm min}$), the time of maximum (minimum) of the differential rate, depends on the target nuclide for magnetic dipole DM elastically scattering with fluorine, germanium, iodine, sodium, argon, and xenon. We have also discussed how the annual modulation would appear should DM scatter inelastically with these elements. In our calculations we assume the SHM and included the effect of GF. We have shown that in an idealized experiment, the observed difference in $t_{\rm max}$ for DM scattering off fluorine and xenon at a fixed value of $v_{\rm min}$ could differ by as much as four months for DM masses above 50 GeV, however, accounting for the limitations of a realistic detector and integrating the differential rate can significantly suppress these differences. The plausible presence of DM substructure or forms of anisotropy other than GF could nevertheless enhance the target dependence of the modulation.

4 Updated Halo-Independent Constraints on CDMS-II-Si

4.1 Introduction

Despite an overwhelming amount of evidence for the existence of dark matter, very little is known about it beyond what is inferred from its gravitational influence. Motivated largely by theoretical expectations, weakly interacting massive particles (WIMPs) with mass at the GeV to $\simeq 100\,\text{TeV}$-scale remain among the most studied candidates.

Direct dark matter experiments search for the energy deposited into nuclei in underground detectors by collisions with WIMPs gravitationally bound to the galactic halo. While no definitive detections have been made, a number of collaborations have observed potential dark matter signals [150–156]; however, such observations are typically viewed to be in conflict with the null results of many other experiments [142, 143, 157–170].

The difficulty in making definitive statements regarding the nature of potentially viable signals arises from the fact that there exists a vast amount of uncertainty in the analysis of direct dark matter detection data. This is because both the particle physics and the astrophysics entering the computation of the expected scattering rates are, at best, poorly understood. In standard analyses of direct detection data, assumptions must be made on the local dark matter density, the dark matter velocity distribution, the dark matter-nuclei interaction, and the scattering kinematics. Bounds are then placed as a function of the dark matter mass and overall scale of the cross section. The obvious problem is that adjusting assumptions, e.g. on the velocity distribution, unevenly alters the predicted rates in different

experiments. This happens to be particularly true for the region of parameter space where potential dark matter signals have arisen, as this region sits near the low-energy threshold of many experiments.

In recent years, 'halo-independent' data comparison methods that avoid making any assumptions about the local dark matter halo characteristics have been developed, thereby reducing the uncertainty in experimental comparisons (see e.g. [91,93,122,126,138,149,171–193]). The original halo-independent analyses were rather limited in that putative signals often required averaging the signal over some energy range, potentially removing valuable information and making the comparison with upper limits ambiguous (see e.g. [91,93,171,173]). Recently, methods were developed which, for putative signals, allow for the construction of halo-independent confidence bands, resulting in a better comparison between upper limits and potential signals [92, 179, 192]. These methods, however, rely on the ability to use an extended likelihood [194] for at least one of the experiments observing a putative signal. At the moment, CDMS-II-Si is the only experiment that has claimed a potential dark matter signal for which such a method can be applied.

Halo-dependent analyses strongly constrain the excess observed by CDMS-II-Si (see e.g. [177, 182, 195]). A halo-independent analysis performed on the CDMS-II-Si data in 2014 showed that the only WIMP candidates still consistent with the upper limits of null searches were those with spin-independent isospin-violating interactions, and either elastic or exothermic scattering [92]. Here, we revisit the viability of the CDMS-II-Si excess, using both halo-dependent, assuming the standard halo model (SHM), and halo-independent analyses, incorporating the latest bounds produced by LUX (using their complete expo-

sure) [168], PandaX-II [169], and PICO-60 [170]. We also assess the projected sensitivity of XENON1T [196,197], LZ [198,199], DARWIN [200], DarkSide-20k [201,202], PICO-250 [203], and the high-voltage germanium detectors of SuperCDMS to be installed at SNOLAB [204]. We show that models with highly exothermic kinematics and a neutron-to-proton coupling ratio f_n/f_p set to minimize the scattering rate in xenon-target experiments are not currently excluded, nor can they be rejected by XENON1T.

In Sec. 4.2 we review the halo-independent analysis and the procedure for constructing the two-sided pointwise halo-independent confidence band. The analysis for each experiment is explained in Sec. 4.3. In Sec. 4.4, we present our results, specifically focusing on isospin conserving and isospin-violating [205,206] (with $f_n/f_p = -0.8$ and $f_n/f_p = -0.7$) interactions with elastic and exothermic scattering [148, 207, 208]. We conclude in Sec. 4.5.

4.2 Halo-Independent Analysis

4.2.1 Halo-Independent Bounds

Here, we briefly review the generalized halo-independent analysis implemented in Sec. 4.4, concentrating on the extended halo independent (EHI) analysis [92] in the following subsection (the reader is encouraged to consult [91, 93, 175, 182, 209] for additional details).

In direct detection experiments, the differential rate per unit detector mass of a target T, induced by collisions with a WIMP of mass m, as a function of nuclear recoil energy $E_{\rm R}$ is given by

$$\frac{\mathrm{d}R_T}{\mathrm{d}E_{\rm R}} = \frac{\rho}{m}\frac{C_T}{m_T}\int_{v\geqslant v_{\rm min}(E_{\rm R})} \mathrm{d}^3\, v\, f(\boldsymbol{v},t)\, v\, \frac{\mathrm{d}\sigma_T}{\mathrm{d}E_{\rm R}}(E_{\rm R},\boldsymbol{v})\,, \tag{4.1}$$

where m_T is the mass of the target element, ρ is the local dark matter density, C_T is the mass fraction of a nuclide T in the detector, $\mathrm{d}\sigma_T/\mathrm{d}E_\mathrm{R}$ is the dark matter-nuclide differential cross section in the lab frame, and $f(\boldsymbol{v}, t)$ is the dark matter velocity distribution in the lab frame. The temporal dependence of $f(\boldsymbol{v}, t)$ arises from Earth's rotation about the Sun. For the halo-dependent analyses in Sec. 4.4, we assume the SHM, i.e. $f(\boldsymbol{v}, t)$ is an isotropic Maxwellian velocity distribution in the Galactic frame, with the astrophysical parameters adopted in [180].

The integration in Eq. (5.2) runs over all dark matter particle speeds larger than or equal to $v_\mathrm{min}(E_\mathrm{R})$, the minimum speed necessary to impart an energy E_R to the nucleus. Should multiple target nuclides be present in the detector, the total differential scattering rate is given by

$$\frac{\mathrm{d}R}{\mathrm{d}E_\mathrm{R}} = \sum_T \frac{\mathrm{d}R_T}{\mathrm{d}E_\mathrm{R}} \,. \tag{4.2}$$

For elastic scattering, the value of v_min is given by

$$v_\mathrm{min} = \sqrt{\frac{m_T E_\mathrm{R}}{2\mu_T^2}} \,, \tag{4.3}$$

where μ_T is the WIMP-nuclide reduced mass. It may be possible that the dominant WIMP-nuclei interaction proceeds instead through an inelastic collision, whereby the dark matter particle χ scatters into a new state χ' with mass $m' = m + \delta$ (with $|\delta| \ll m$) [148, 207, 208]. In the limit that $\mu_T|\delta|/m^2 \ll 1$, $v_\mathrm{min}(E_\mathrm{R})$ is instead given by

$$v_\mathrm{min}(E_\mathrm{R}) = \frac{1}{\sqrt{2m_T E_\mathrm{R}}} \left| \frac{m_T E_\mathrm{R}}{\mu_T} + \delta \right| \,, \tag{4.4}$$

where $\delta < 0$ ($\delta > 0$) corresponds to an exothermic (endothermic) scattering process. Eq. (4.4) can be inverted to find the possible range of recoil energies which can be imparted by a dark matter particle with speed v in the lab frame $E_{\rm R}^{T,-} \leq E_{\rm R} \leq E_{\rm R}^{T,+}$, where

$$E_{\rm R}^{T,\pm}(v) = \frac{\mu_T^2 v^2}{2m_T}\left(1 \pm \sqrt{1 - \frac{2\delta}{\mu_T v^2}}\right)^2 . \tag{4.5}$$

It should be clear from Eq. (4.5) that for endothermic scattering, for which $\delta > 0$, there exists a non-trivial kinematic endpoint for the WIMP speed given by $v_\delta^T = \sqrt{2\delta/\mu_T} > 0$, such that dark matter particles traveling at speeds $v < v_\delta^T$ cannot induce nuclear recoils. In this paper we will be focusing exclusively on elastic ($\delta = 0$) and exothermic ($\delta < 0$) scattering, for which $v_\delta^T = 0$. Interpreting the CDMS-II-Si data using models with endothermic spin-independent interactions are clearly experimentally rejected. Notice that Eq. (4.5) implies only a finite range of recoil energies around the energy $E_{\rm R}(v_\delta^T) = \mu_T|\delta|/m_T$ can be probed for inelastic scattering.

Experiments do not directly measure the recoil energy of the nucleus, but rather a proxy for it that we denote E'. The differential rate in this new observable energy E' is given by

$$\frac{{\rm d}R}{{\rm d}E'} = \sum_T \int_0^\infty {\rm d}E_{\rm R}\, \epsilon(E_{\rm R}, E')\, G_T(E_{\rm R}, E')\, \frac{{\rm d}R_T}{{\rm d}E_{\rm R}}\,, \tag{4.6}$$

where $\epsilon(E_{\rm R}, E')$ is the detection efficiency and $G_T(E_{\rm R}, E')$ is the energy resolution; jointly, these two functions give the probability that a detected recoil energy E' resulted from a true nuclear recoil energy $E_{\rm R}$.

Changing the order of integration in Eq. (4.6) allows the differential rate to be expressed

as

$$\frac{\mathrm{d}R}{\mathrm{d}E'} = \frac{\sigma_{\mathrm{ref}}\rho}{m} \int_{v \geqslant v_\delta^T} \mathrm{d}^3 v \, \frac{f(\boldsymbol{v},t)}{v} \, \frac{\mathrm{d}\mathcal{H}}{\mathrm{d}E'}(E', \boldsymbol{v}) \,, \tag{4.7}$$

where we have defined

$$\frac{\mathrm{d}\mathcal{H}}{\mathrm{d}E'}(E', \boldsymbol{v}) \equiv \sum_T \begin{cases} \dfrac{C_T}{m_T} \displaystyle\int_{E_{\mathrm{R}}^{T,-}}^{E_{\mathrm{R}}^{T,+}} \mathrm{d}E_{\mathrm{R}} \epsilon(E_{\mathrm{R}}, E') \, G_T(E_{\mathrm{R}}, E') \, \frac{v^2}{\sigma_{\mathrm{ref}}} \, \frac{\mathrm{d}\sigma_T}{\mathrm{d}E_{\mathrm{R}}}(E_{\mathrm{R}}, \boldsymbol{v}) & \text{if } v \geqslant v_\delta^T \,, \\ 0 & \text{if } v < v_\delta^T \ . \end{cases} \tag{4.8}$$

Here, we have explicitly factored out an overall normalization σ_{ref} from the differential cross section. For spin-independent interactions, the differential WIMP-nucleus cross section is given by

$$\frac{\mathrm{d}\sigma_T^{SI}}{\mathrm{d}E_{\mathrm{R}}}(E_{\mathrm{R}}, v) = \sigma_p \frac{\mu_T^2}{\mu_p^2} [Z_T + (A_T - Z_T)(f_n/f_p)]^2 \, \frac{F_T^2(E_{\mathrm{R}})}{2\mu_T^2 v^2 / m_T} \,, \tag{4.9}$$

where $F_T(E_{\mathrm{R}})$ is the nuclear form factor that accounts for the decoherence of the dark matter-nuclide interaction at large momentum transfer. Here, we take this to be the Helm form factor [**?**]. Thus we take $\sigma_{\mathrm{ref}} = \sigma_p$, the WIMP-proton cross section. Interactions with spin- or nuclear magnetic moment-dependencies produce smaller rates in silicon relative to other target elements employed by experiments which have not observed an excess.

Let us define the halo function

$$\tilde{\eta}(v_{\mathrm{min}}, t) \equiv \frac{\rho \sigma_{\mathrm{ref}}}{m} \int_{v_{\mathrm{min}}}^{\infty} \mathrm{d}v \, \frac{F(v,t)}{v} \,, \tag{4.10}$$

where the function $F(v,t)$ is the local dark halo speed distribution, given by $F(v,t) =$

$v^2 \int \mathrm{d}\Omega_v f(\boldsymbol{v}, t)$. Using Eq. (4.10), the differential rate in E' can be written as

$$\frac{\mathrm{d}R}{\mathrm{d}E'} = -\int_{v_\delta}^{\infty} \mathrm{d}v \, \frac{\partial \tilde{\eta}(v,t)}{\partial v} \, \frac{\mathrm{d}\mathcal{H}}{\mathrm{d}E'}(E', v) \,. \tag{4.11}$$

Applying integration by parts on Eq. (4.11), and noting that $\tilde{\eta}(\infty, t) = 0$ and $\mathrm{d}\mathcal{H}/\mathrm{d}E'(E', v_\delta) = 0$, the differential rate can be expressed as

$$\frac{\mathrm{d}R}{\mathrm{d}E'} = \int_{v_\delta}^{\infty} \mathrm{d}v_{\mathrm{min}} \tilde{\eta}(v_{\mathrm{min}}, t) \, \frac{\mathrm{d}\mathcal{R}}{\mathrm{d}E'}(E', v_{\mathrm{min}}) \,, \tag{4.12}$$

where we have defined a WIMP model and experiment dependent "differential response function" $\mathrm{d}\mathcal{R}/\mathrm{d}E'$ as

$$\frac{\mathrm{d}\mathcal{R}}{\mathrm{d}E'}(E', v_{\mathrm{min}}) \equiv \frac{\partial}{\partial v_{\mathrm{min}}} \left[\frac{\mathrm{d}\mathcal{H}}{\mathrm{d}E'}(E', v_{\mathrm{min}}) \right] . \tag{4.13}$$

Approximating the time dependence of the halo function as

$$\tilde{\eta}(v_{\mathrm{min}}, t) \simeq \tilde{\eta}^0(v_{\mathrm{min}}) + \tilde{\eta}^1(v_{\mathrm{min}}) \cos(2\pi(t - t_0)/\mathrm{year}) \,, \tag{4.14}$$

and integrating Eq. (4.12) over E', the unmodulated R^0 and annual modulation amplitude R^1 of the rate, integrated over an observable energy bin $[E'_1, E'_2]$, is given by

$$R^\alpha_{[E'_1, E'_2]} \equiv \int_{v_\delta}^{\infty} \mathrm{d}v_{\mathrm{min}} \, \tilde{\eta}^\alpha(v_{\mathrm{min}}) \int_{E'_1}^{E'_2} \mathrm{d}E' \, \frac{\mathrm{d}\mathcal{R}}{\mathrm{d}E'} \tag{4.15}$$

$$= \int_{v_\delta}^{\infty} \mathrm{d}v_{\mathrm{min}} \, \tilde{\eta}^\alpha(v_{\mathrm{min}}) \, \mathcal{R}_{[E'_1, E'_2]}(v_{\mathrm{min}}) \,, \tag{4.16}$$

where $\alpha = 0, 1$ and the second line has defined the energy integrated "response function" $\mathcal{R}$.

In order to place an upper limit on the function $\tilde{\eta}^0(v_{\rm min})$ (hereby denoted $\tilde{\eta}(v_{\rm min})$), we note that at a particular point in the $v_{\rm min} - \tilde{\eta}$ plane, the halo function producing the smallest number of events in a particular experiment is a downward step-function with the step located at the particular $(v_{\rm min}, \tilde{\eta})$ point. This is a consequence of the fact that, by definition, $\tilde{\eta}(v_{\rm min})$ is a monotonically decreasing function of $v_{\rm min}$. As first shown in [171], 90% CL limits on $\tilde{\eta}$, $\tilde{\eta}^{\rm lim}$, are placed by determining the 90% CL limit on the rate, $R^{\rm lim}_{[E'_1,E'_2]}$, and inverting Eq. (4.16), i.e.

$$\tilde{\eta}^{\rm lim}(v_{\rm min}) = \frac{R^{\rm lim}_{[E'_1,E'_2]}}{\int_{v_\delta}^{v_{\rm min}} {\rm d}v\, \mathcal{R}_{[E'_1,E'_2]}(v)}\,. \tag{4.17}$$

4.2.2 Halo-Independent Confidence Band

It was shown in [92, 179] that an extended likelihood is maximized by a piece-wise constant halo function $\tilde{\eta}_{BF}(v_{\rm min})$ with a number of steps less than or equal to the number of events observed, and furthermore that a two-sided pointwise halo-independent confidence band can be constructed around this best-fit halo function, $\tilde{\eta}_{BF}$. A stream of velocity $\vec{v}_s$ with respect to the Galaxy, such that $|\vec{v}_s + \vec{v}_\oplus| = v_{\rm min}$ (where $\vec{v}_\oplus$ is Earth's velocity with respect to the Galaxy) would produce an $\tilde{\eta}$ function proportional to $\Theta(|\vec{v}_s + \vec{v}_\oplus| - v_{\rm min})$. Thus a piecewise $\tilde{\eta}(v_{\rm min})$ function could be interpreted as corresponding to a series of streams, one for each of its downward steps. More recently, it was shown that this formalism can be extended to more generalized likelihood functions that include at least one extended likelihood [192]. Here, we briefly summarize the process outlined in [92] for producing a two-sided pointwise halo-independent confidence band using an extended likelihood function (which we apply in

Sec. 4.4 to the CDMS-II-Si data) of the form

$$\mathcal{L} = e^{-N_E[\tilde{\eta}]} \prod_{a=1}^{N_{\rm obs}} MT \frac{{\rm d}R_{\rm tot}}{{\rm d}E'}\bigg|_{E'=E_a} , \tag{4.18}$$

where $N_E[\tilde{\eta}]$ is the total number of expected events, $N_{\rm obs}$ is the number of observed events, ${\rm d}R_{\rm tot}/{\rm d}E'$ is the total differential rate, and E'_a is the detected energy of event a.

The confidence band is defined as the region in the $v_{\rm min} - \tilde{\eta}$ plane satisfying

$$\Delta L[\tilde{\eta}] \equiv L[\tilde{\eta}] - L_{\rm min} \leq \Delta L^* , \tag{4.19}$$

where $L[\tilde{\eta}]$ is two times the minus log likelihood, $L_{\rm min}$ is the value of $L[\tilde{\eta}]$ evaluated with the best-fit halo function $\tilde{\eta}_{BF}(v_{\rm min})$, and ΔL^* corresponds to the desired confidence level. That is to say, we seek the collection of all halo functions that produce changes in the log likelihood function less than or equal to the desired value ΔL^*.

While this is a viable definition, in practice finding this complete set of halo functions is not possible. Instead, we consider the subset of $\tilde{\eta}$ functions which minimize $L[\tilde{\eta}]$ subject to the constraint

$$\tilde{\eta}(v^*) = \tilde{\eta}^* . \tag{4.20}$$

We define $L^c_{\rm min}(v^*, \tilde{\eta}^*)$ to be the minimum of $L[\tilde{\eta}]$ subject to the constraint in Eq. (4.20), and we define the function $\Delta L^c_{\rm min}(v^*, \tilde{\eta}^*)$ as

$$\Delta L^c_{\rm min}(v^*, \tilde{\eta}^*) \equiv L^c_{\rm min}(v^*, \tilde{\eta}^*) - L_{\rm min} . \tag{4.21}$$

Should the point $(v^*, \tilde{\eta}^*)$ lie within the confidence band, then at least one halo function passing through this point should satisfy $\Delta L[\tilde{\eta}] \leq \Delta L^*$. It follows that $\Delta L^c_{\rm min}(v^*, \tilde{\eta}^*) \leq \Delta L^*$. On the other hand, should $\Delta L^c_{\rm min}(v^*, \tilde{\eta}^*) > \Delta L^*$, there should not exist any halo functions contained within the confidence band passing through $(v^*, \tilde{\eta}^*)$. Thus, a two-sided pointwise confidence band can be constructed by finding at each value of $v_{\rm min}$, the values of $\tilde{\eta}^*$ around $\tilde{\eta}_{BF}$ which satisfy $\Delta L^c_{\rm min}(v_{\rm min}, \tilde{\eta}^*) \leq \Delta L^*$. For the results presented in Sec. 4.4, we plot the contours of $\Delta L^* = 1.0$ and 2.7, which for a chi-squared distribution[9] with one degree of freedom correspond to 68% and 90% CL confidence bands, respectively [92]. Compatibility of these confidence bands with upper limits can then be assessed at a given CL by determining whether there exists a non-increasing halo function $\tilde{\eta}(v_{\rm min})$ which is entirely contained within a particular band and does not exceed any of the upper limits. A confidence band is said to be excluded if no such halo function can be constructed.

4.3 Data Analysis

Here, we present current halo-dependent and halo-independent constraints on the CDMS-II-Si 68% and 90% regions for a variety of elastic and exothermic spin-independent interaction models. We focus explicitly on isospin conserving ($f_n/f_p = 1$), 'Ge-phobic' (defined by the choice of neutron and proton couplings which minimizes scattering in germanium, i.e. $f_n/f_p = -0.8$), and 'Xe-phobic' models (defined by the choice of neutron and proton couplings which minimizes scattering in xenon, i.e. $f_n/f_p = -0.7$). Halo-independent constraints are presented for three representative choices of m and δ, which had been selected in [92] as

[9] In the limit that $N_{\rm obs}$ is large, Wilk's theorem states that the log-likelihood ratio follows a chi-squared distribution which may not exactly apply with only 3 events.

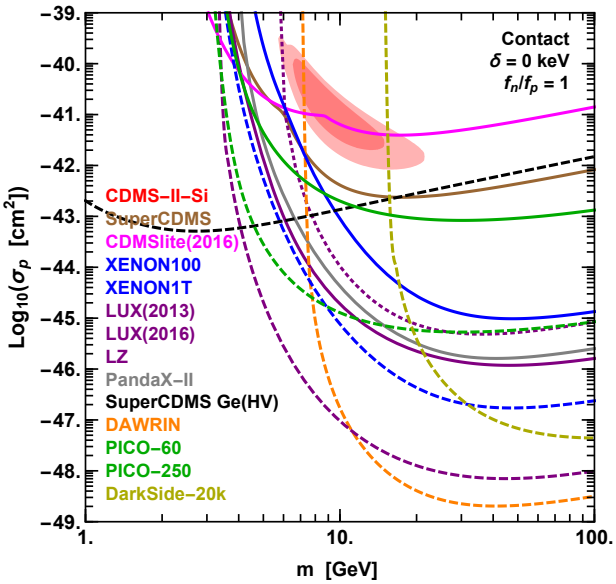

Figure 4.1: Halo-dependent comparison of CDMS-II-Si 68% (dark red) and 90% (light red) regions with current 90% CL upper limits from SuperCDMS (brown), CDMSlite2016 (magenta), XENON100 (blue, solid), LUX2013 (purple, dotted), LUX2016 (purple, solid), PandaX-II (grey), and PICO-60 (green, solid), for an elastic isospin conserving spin-independent interaction. Also shown are projected discovery limits (dashed) for XENON1T (blue), SuperCDMS SNOLAB Ge HV (black), LZ (purple), DARWIN (orange), DarkSide-20k (yellow), and PICO-250 (green).

parameters in the halo-dependent analyses which appeared to provide good compatibility of the CDMS-II-Si signal and the upper bounds from null searches.

Upper limits in this section are presented for the following experiments: SuperCDMS [166], CDMSlite (2016 result) [165], XENON100 [167], LUX (2013 result)[10] [140], LUX (2016 result) [168], PandaX-II [169], and PICO-60 [170]. Also shown are projected bounds for XENON1T [197], SuperCDMS SNOLAB Ge High-Voltage (which we call SuperCDMS Ge(HV)) [204], LZ [198, 199], DARWIN [200], DarkSide-20k [201, 202], and PICO-250 [203]. The procedure for constructing the LUX2013 bound was previously outlined in [122, 175, 177]. We describe here the process used below to produce the remaining experimental bounds.

[10]The LUX2013 bound is presented assuming zero observed events. This bound has been shown to be well representative of the true bound [177].

4.3.1 CDMS-II-Si

The procedure for analyzing the CDMS-II-Si data follows the procedure outlined in [122, 175, 177]. Specifically, we consider the three event signal with energies 8.2, 9.5, and 12.3 keV. CDMS-II-Si had an exposure of 140.2 kg-days and an energy window of 7 keV to 100 keV. Using a profile likelihood ratio test, a preference was found for the WIMP+background hypothesis over the background-only hypothesis with a $p-$value of 0.19% [156]. We use an $E_{\rm R}$-dependent efficiency identical to that shown in Fig. 1 of [156] (solid blue line). Since the energy resolution for silicon in CDMS-II has not been measured, we use a Gaussian resolution function with the energy resolution used for CDMS-II's germanium detectors, taken from in Eq. 1 of [210], $\sigma(E') = \sqrt{0.293^2 + 0.056^2 \times E'/\text{keV}}$ keV. To estimate the differential background rate for each observed event, we take the differential background rates from [211] and normalize each component such that 0.41, 0.13, and 0.08 events are expected from surface events, neutrons, and ^{208}Pb respectively [156]. This procedure reproduces the preferred regions shown in Fig. 4 of [156].

4.3.2 XENON100

The XENON100 bound is produced in the manner outlined in [175], but using the updated 477 day exposure [167]. This procedure accurately reproduces the bound shown in Fig. 11 of [167].

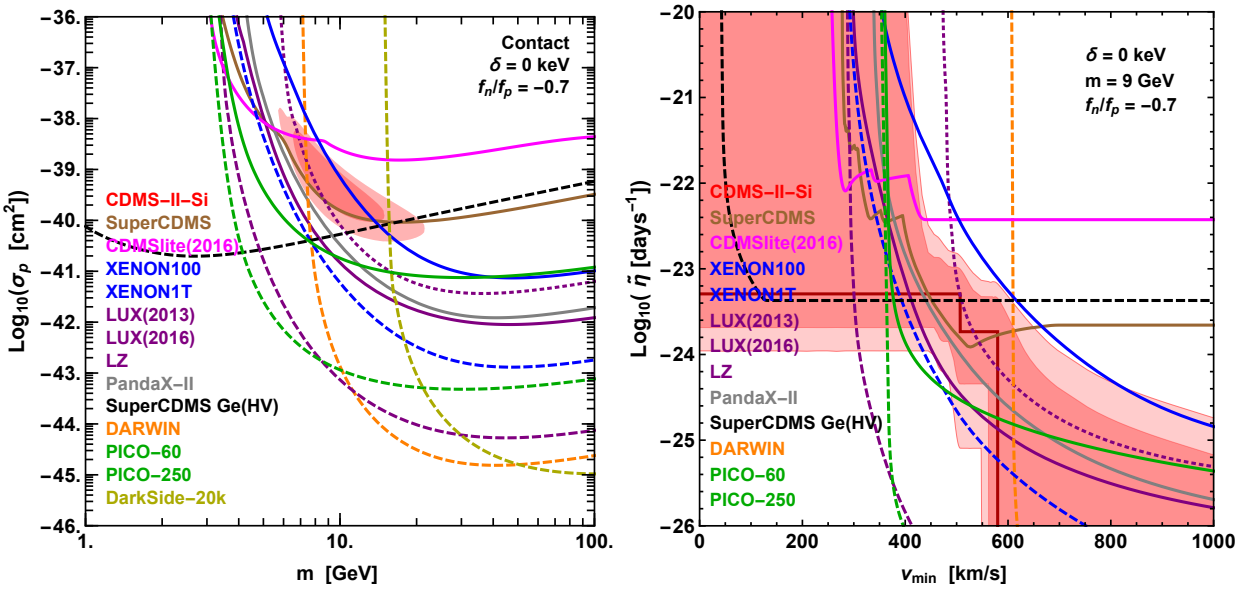

Figure 4.2: (Left) Halo-dependent analysis and (Right) halo-independent analysis for $m = 9$ GeV, assessing the compatibility of the CDMS-II-Si 68% and 90% CL regions (shown in darker and lighter red) with the 90% CL upper limits and projected sensitivities of other experiments, for an elastic spin-independent contact interaction with $f_n/f_p = -0.7$. We include SuperCDMS (brown), CDMSlite (magenta), XENON100 (blue, solid), LUX2013 (purple, dotted), LUX2016 (purple, solid), PandaX-II (grey), and PICO-60 (green, solid) upper limits, and the projected sensitivities (dashed lines) of XENON1T (blue), SuperCDMS Ge(HV) (black), LZ (purple), DARWIN (orange), DarkSide-20k (yellow), and PICO-250 (green). Also shown is the best-fit halo function $\tilde{\eta}_{BF}$ to the CDMS-II-Si data (dark red step function) and the $v_{\rm min}$ value corresponding to the event with the largest observed recoil energy, assuming $E_{\rm R} = E' = 12.3$ keV (vertical dot dashed dark red line).

4.3.3 CDMSlite 2016

The CDMSlite bound (hereby CDMSlite2016) is constructed using results from the recently reported 70.1 kg-day exposure. The detector efficiency and quenching factor are taken from Fig. 1 and Eq. 3 of [165], respectively. The energy of detected events is read off the inset in Fig. 3 in [165], but only between detected energies of 0.36 and 1.04 keVee, and the maximum gap method is then applied. This procedure reproduces the published bound.

4.3.4 LUX 2016

The LUX bound is computed by using the complete LUX exposure (approximately 4.47×10^4 kg-days). The efficiency and fractional resolution as functions of $E_{\rm R}$ are extracted from Fig. 2 (black solid line) and Fig. 5 of [168], respectively. The bound is obtained by determining the cross section required to produce a total of 3.2 events. As mentioned in [168] this procedure reproduces the 90% CL combined LUX exclusion limit.

4.3.5 PandaX-II

The constraint for PandaX-II is based on the 3.3×10^4 kg-day run data published in 2016. To reproduce the published bound, the nuclear recoil efficiency function is taken from Fig. 2 of [169] (black line), and the recoil energies of the three observed events are read off Figs. 4 and 14 of [169]). Applying the maximum gap method [212] yields a bound that reproduces well the published bound for $m \lesssim 30$ GeV, and is slightly stronger at larger masses by a factor of $\lesssim 1.5$.

4.3.6 PICO-60

The constraint for PICO-60 is based on the recent 1167 kg-day run of C_3F_8 [170]. Here, we restrict our attention to scattering off fluorine, as this element accounts for $\simeq 80\%$ of the target mass and has a lower threshold than carbon (after considering the bubble nucleation efficiency in Fig. 4 of [142]). PICO-60 is run at a thermodynamic threshold of 3.3 keV, however this threshold does not correspond to the threshold recoil energy in fluorine required to nucleate a bubble. We take this threshold to be 6 keV using the efficiency function shown

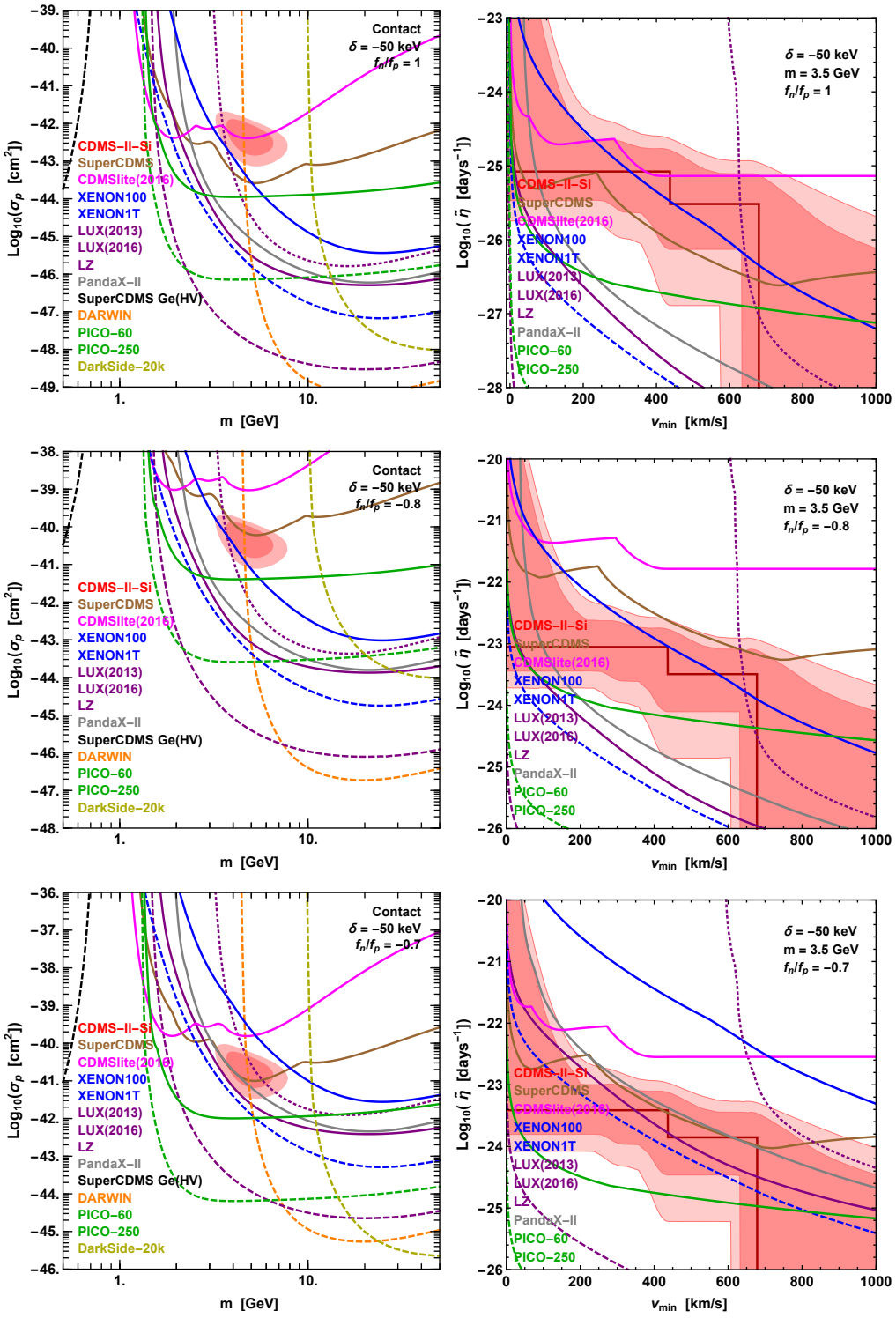

Figure 4.3: (Left) Halo-dependent analysis and (Right) halo-independent analysis for $m = 3.5$ GeV, assessing the compatibility of the CDMS-II-Si 68% and 90% CL regions (shown in darker and lighter red) with the 90% CL upper limits and projected sensitivities of other experiments, for an exothermic spin-independent contact interaction with $\delta = -50$ keV. Results are shown for isospin conserving couplings (top), 'Ge-phobic' couplings (middle), and 'Xe-phobic' couplings (bottom). Experiments included are identical to those shown in Fig. 4.2.

in Fig. 4 of [142] for a 3.2 keV thermodynamic threshold (although this is only determined for a 5 GeV WIMP with a spin-independent interaction). Using Poisson statistics with zero observed events and zero expected background, we find this threshold perfectly reproduces the published bound [170].

4.3.7 XENON1T

The projected bound for XENON1T [197] is computed assuming a 2 ton-year exposure, a flat efficiency of 0.4, and an effective light yield, a low-energy threshold, and an energy resolution equal to those used in the XENON100 analysis of [175]. This procedure produces a sensitivity limit consistent with the $\pm 1\sigma$ confidence intervals of the 2 ton-year sensitivity limit shown in Fig. 8 of [197].

4.3.8 SuperCDMS SNOLAB Ge(HV)

SuperCDMS plans to operate the next generation of their experiment at SNOLAB beginning in 2020; the discovery limits produced here are based on the recent projected sensitivity for their high-voltage germanium, Ge(HV), detectors. Specifically, we assume 8 Ge(HV) detectors, each with an exposure of 44 kg-days. We also assume perfect efficiency in the energy range 0.04 keV (taken from Table VIII of [204]) to 2 keV (taken to be consistent with the energy range suggested in the caption of Table V of [204]), perfect energy resolution, an ionization yield given by Lindhard theory (with parameters taken from [213]), and zero observed events. Using the maximum gap method (which coincides with using a Poisson likelihood in this case) we obtained a 90% CL limit very similar to the Ge(HV) limit shown

in Fig. 8 of [204]. SuperCDMS also plans to run a high-voltage silicon detector which is not included here because its projected sensitivity is inferior across most of the parameter space. Also note that if the energy ranges of the HV detectors could be extended to energies beyond 2 keV, these experiments could gain sensitivity to the exothermic models considered here.

4.3.9 LZ

The projected sensitivity for LZ is produced using the same energy resolution and efficiency function used in the LUX2016 analysis, and assuming a total exposure of 15.33 ton-years (i.e. a 5.6 ton fiducial volume with 1000 live-days) [198, 199]. We then apply the maximum gap method, under the assumption of zero observed events, with which we reproduce a sensitivity limit comparable to that shown in Fig.4 of [199].

4.3.10 DARWIN

The projected sensitivity limit for DARWIN is based on the design presented in [200], for a liquid xenon experiment with a 200 ton-year exposure. Following [200], we consider an energy range of 5 keV to 20.5 keV and a constant detection efficiency of 30%. We approximate the energy resolution as a Gaussian with $\sigma = E_{\rm R} \times 0.15$, which is roughly consistent with Fig. 1 of [200]. Assuming zero observed events, the bound is obtained using the maximum gap method. This procedure is found to produce a sensitivity limit in strong agreement with that shown in Fig. 7 of [200].

4.3.11 DarkSide-20k

The projected sensitivity for DarkSide-20k is produced assuming a flat nuclear recoil efficiency of 0.7 between energies 40 keV and 240 keV (and zero elsewhere), a 60 ton-year exposure (i.e. a 20 ton fiducial volume run for 3 years), and by applying the maximum gap method with zero observed events [201,202]. DarkSide-20k is not sensitive for the nuclear recoils imparted to argon nuclei by the particular candidates in our halo-independent analyses (we show $v_{\rm min} \leq 1000$ km/s), thus no DarkSide-20k bounds appear in the halo-independent plots.

4.3.12 PICO-250

The projected sensitivity for PICO-250 is produced assuming perfect detection efficiency for energies above 6 keV (see Sec. 4.3.6), a 250 kg fiducial volume, a 2 year runtime (or alternatively, a 500 kg fiducial volume run for one year), and by using Poisson statistics with zero observed events and zero expected background [170,203]. As in Sec. 4.3.6, we only consider scattering off fluorine.

4.4 Results

For the purpose of providing context, we begin by plotting in Fig. 4.1 a comparison of the 68% and 90% CDMS-II-Si regions with the current and projected 90% CL limits of other experiments, assuming the conventional elastic spin-independent contact interaction with isospin conserving couplings. Null results from LUX2013 and SuperCDMS have excluded this model at the 90% CL in both halo-dependent and halo-independent analyses (there

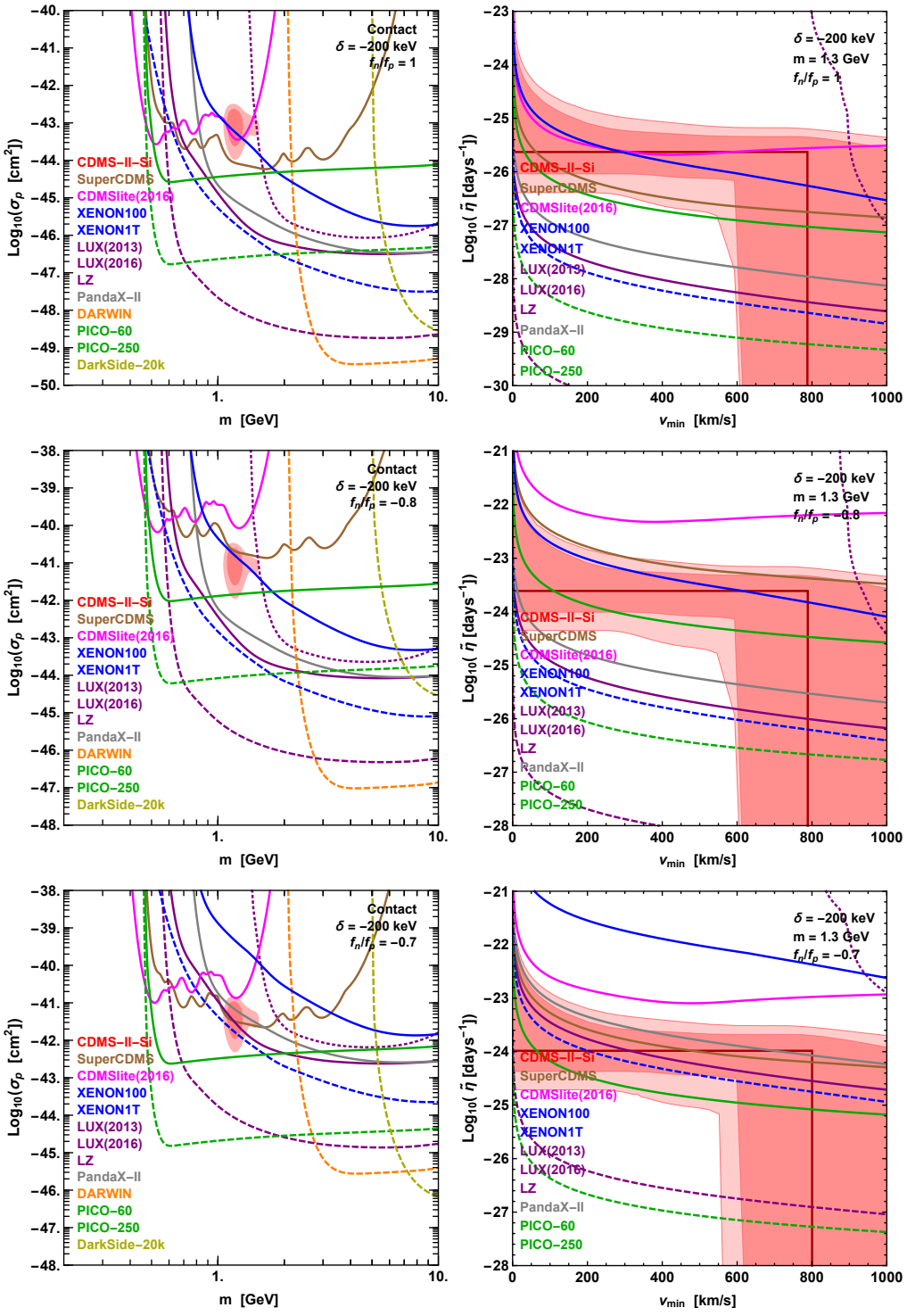

Figure 4.4: Same as Fig. 4.3, but for $\delta = -200$ keV and $m = 1.3$ GeV (halo-independent analyses only). The SuperCDMS Ge(HV) discovery limit is not shown as it cannot probe the WIMP candidates shown.

exist small discrepancies in the preferred CDMS-II-Si regions of [92] and those presented below, a mistake that arose because the factor of 2 in the definition of $L[\tilde{\eta}]$ was missing in [92]) [92, 177].

We present in Fig. 4.2 a halo-dependent (left) and halo-independent (right) analysis of an elastic spin-independent contact interaction with 'Xe-phobic' couplings (i.e. $f_n/f_p = -0.7$). In the halo-dependent analysis, the 90% CL CDMS-II-Si region is excluded by the 90% CL upper limits of LUX2016, PandaX-II, and PICO-60. This is consistent with the results of [195]. In the halo-independent analysis, the upper limit of PandaX-II does not entirely exclude the 68% CL CDMS-II-Si region, the LUX2016 limit only marginally excludes the 90% CL CDMS-II-Si region, and only the very recent PICO-60 90% CL bound definitively excludes 90% CL CDMS-II-Si region. This is shown for $m = 9$ GeV, but other choices of masses lead to similar results. In the halo-independent analysis, we also show the $v_{\rm min}$ value corresponding to the energy of the event with the largest observed energy, assuming $E_{\rm R} = E' = 12.3$ keV (shown with vertical dot dashed dark red line). Had our analysis of the CDMS-II-Si data assumed a perfect energy resolution, the location of the highest step of the best-fit $\tilde{\eta}$ would identically correspond to this value of $v_{\rm min}$; with finite energy resolution, the locations of the steps of the best-fit $\tilde{\eta}$ function occur at slightly larger values of $v_{\rm min}$. For highly exothermic models, it becomes important to verify that the dark matter speeds capable of producing such recoils are physical, i.e. they do not exceed the galactic escape velocity, which for the Standard Halo Model is $v_{\rm esc} \simeq 765$ km/s (in the lab frame).

In Figs. 4.3, 4.4 and 4.5 we plot halo-dependent (left) and halo-independent (right) analyses of exothermic spin-independent contact interactions with $\delta = -50$ keV, $\delta = -200$ keV,

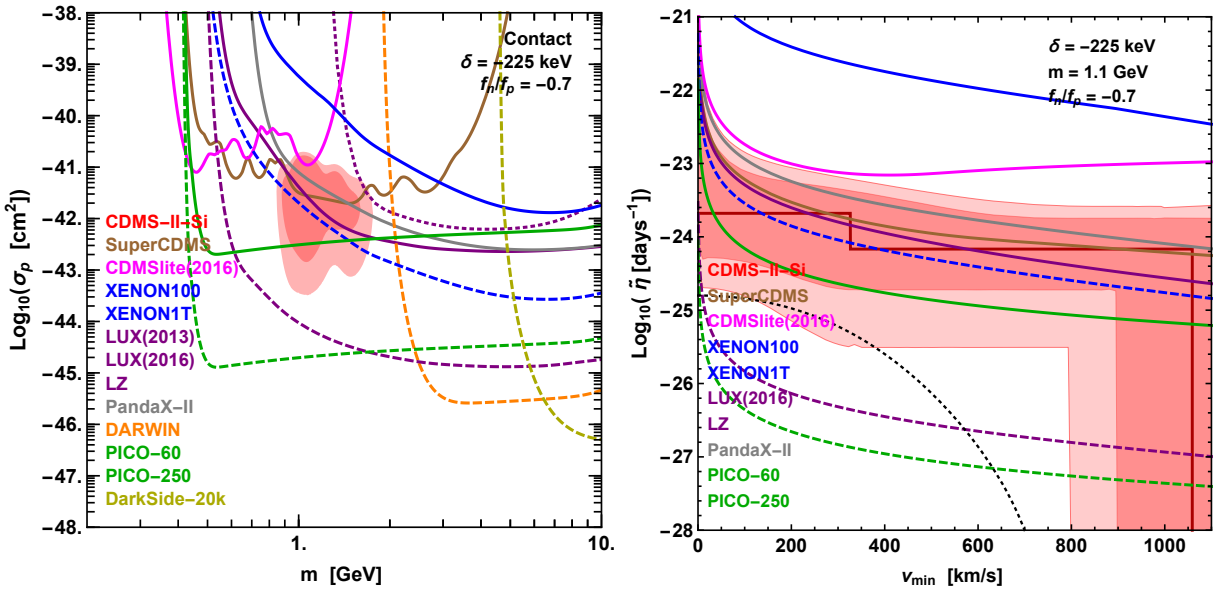

Figure 4.5: Same as Fig. 4.2 but for $\delta = -225$ keV. The halo-independent analysis is shown for $m = 1.1$ GeV. The dotted black line in the halo-independent analysis shows the SHM $\tilde{\eta}(v_{\rm min})$ function for $\sigma_p = 2 \times 10^{-43}{\rm cm}^2$, a value included in the 68% CL region in the halo-dependent analysis.

and $\delta = -225$ keV respectively. In Figs. 4.3 and 4.4 results are shown for isospin conserving (top), 'Ge-phobic' (middle), and 'Xe-phobic' (bottom) models. The halo-dependent analyses in Fig. 4.3 show that the present 90% CL limits reject the 68% and 90% CL CDMS-II-Si regions. The Fig. 4.3 halo-independent analyses, shown for $m = 3.5$ GeV, illustrate that the CDMS-II-Si 90% CL region for a 'Xe-phobic' interaction with $\delta = -50$ keV is only excluded by the recent PICO-60, and not by the PandaX-II or LUX limits. Note that the 2 keV upper cutoff imposed on the recoil energy in the SuperCDMS Ge(HV) data analysis implies that this experiment only tests very light exothermic candidates, and does not probe the CDMS-II-Si regions. Similarly, DARWIN's relatively large low energy threshold prevents this experiment from probing the WIMP candidate presented in the halo-independent analysis. This is a consequence of only showing WIMP speeds less than 1000 km/s.

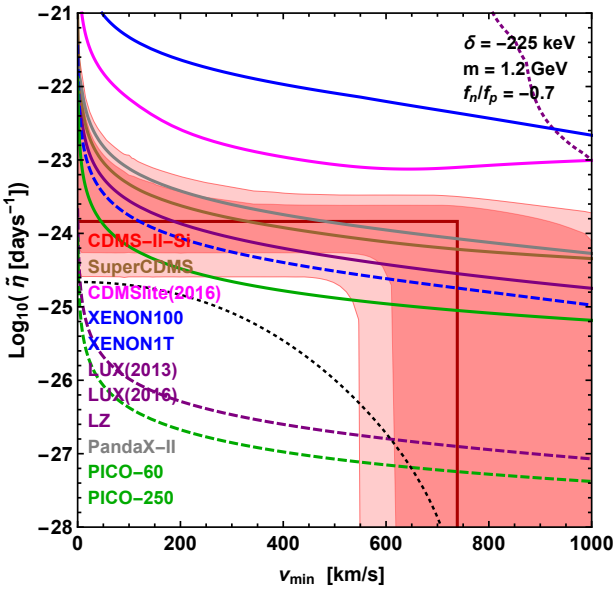

Figure 4.6: Same as right panel of Fig. 4.5 but for $m = 1.2$ GeV. The dotted black line in the halo-independent analysis shows the SHM $\tilde{\eta}(v_{\text{min}})$ function for $\sigma_p = 3 \times 10^{-43}\text{cm}^2$, a value included in the 90% CL region in the halo-dependent analysis.

The results shown in Fig. 4.4 are similar to those in Fig. 4.3, except that in the halo-independent analyses (shown for $m = 1.3$ GeV), the 90% CL CDMS-II-Si region for the 'Xe-phobic' interaction with $\delta = -200$ keV is no longer ruled out for a small set of halo functions which deviate considerably from the SHM. It would seem that increasingly exothermic scattering kinematics (i.e. more negative values of δ) may alleviate the tension between the dark matter interpretation of CDMS-II-Si and the null results of other experiments. This is not the case, however, as increasingly negative values of δ decrease the range of recoil energies that can be imparted by WIMPs (see Eq. (4.5)). This implies that highly exothermic candidates traveling at speeds less than the galactic escape velocity may not be able to account for all three events observed by CDMS-II-Si (as illustrated in Fig. 1 of [180]). While the largest step in the best-fit $\tilde{\eta}$ function in Fig. 4.4 does lie above what is conventionally taken to be the galactic escape velocity, ~ 765 km/s in the lab frame, the v_{min} value corresponding to the

12.3 keV event is clearly below this value (additionally, there are non-negligible astrophysical uncertainties in the value of the galactic escape velocity.) To further illustrate this point, we show in Fig. 4.5 an analysis of a 'Xe-phobic' dark matter candidate with $\delta = -225$ keV. It can be clearly seen in the halo-independent analysis (shown in the right panel for $m = 1.1$ GeV) that the third event of CDMS-II-Si can only be attributed to WIMPs traveling at speeds $v \simeq 1000$ km/s (in the lab frame), far above the galactic escape velocity. Notice that we have not included in our halo-independent analyses a term in the likelihood penalizing large unphysical halo speeds (as was done e.g. in [138]), which in this case would allow only two of the events observed by CDMS-II-Si to be attributed to dark matter. Also shown in Fig. 4.5 is the SHM $\tilde{\eta}$ function with a normalization set to $\sigma_p = 2 \times 10^{-43}\text{cm}^2$, a value which is allowed the 68% CL region in the halo-dependent analysis. The halo-independent analysis clearly rejects this function at the 90% CL, showing that, for this particular dark matter particle candidate, the SHM does not fit the CDMS-II-Si data well.

For strongly exothermic candidates, a small change in the particle mass leads to a considerable change in the range of recoil energies probed by acceptable values of v_{min}. In Fig. 4.6, we show the halo-independent analysis for the same interaction (i.e. spin-independent with $f_n/f_p = -0.7$ and $\delta = -225$ keV) and a WIMP mass $m = 1.2$ GeV instead of $m = 1.1$ GeV. This small change in the mass eliminates the problem of requiring unacceptably large WIMP speeds. However, in this case the new PICO-60 90% CL limit rejects the halo-independent CDMS-II-Si 90% CL region, which would otherwise be allowed by all other bounds. Again, the SHM $\tilde{\eta}$ function with values of σ_p allowed in the 90% CL region in the halo-dependent analysis, lies outside the halo-independent 90% CL confidence band. These examples clearly

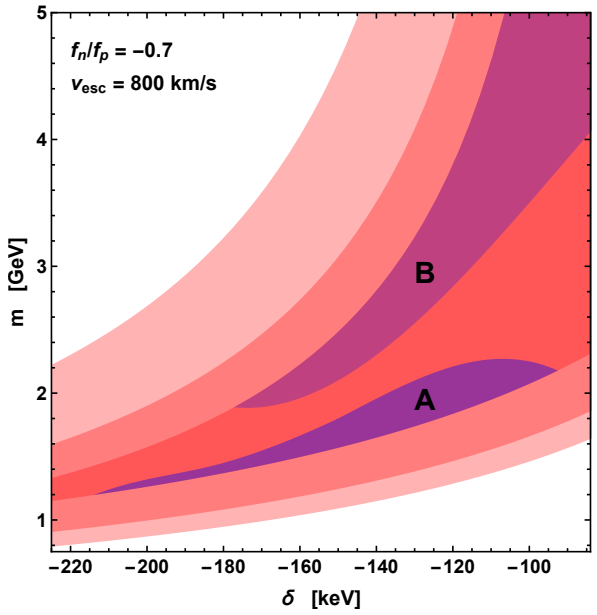

Figure 4.7: Values of m and δ in the 'Xe-phobic' model for which one (light pink), two (pink), and all three (redder pink) of the CDMS-II-Si events are below the galactic escape velocity. The two purple regions indicate the part of the redder pink region not excluded by current experiments. While still viable, the light purple, region 'B', region provides a worse fit to the CDMS-II-Si data than the darker purple region, region 'A' (see text for details).

illustrate the point that one cannot continue to lower delta below -200 keV with the hope of increasing the viability of a dark matter interpretation of the CDMS-II-Si events.

For completeness, we show in Fig. 4.7 the viable parameter space in the $\delta - m$ plane for 'Xe-phobic' models. The pink regions are where either one (light pink), two (pink), or all three (redder pink) events observed by CDMS can be induced by WIMPs traveling at speeds $v \leq 800$ km/s in the lab frame (a conservative choice for the galactic escape velocity [214]), namely where their recoils are kinematically allowed. The purple regions highlight the subset of the dark red region that cannot be ruled out by current direct detection experiments (i.e. the viable parameter space where all three observed events can be due to WIMPs bound to the galactic halo). While the light purple region (region 'B') is still viable, the minus log likelihood evaluated in the light purple region is significantly larger than that of

the dark purple region (region 'A'), indicating a worse fit to the data. This is because two of the observed events are relatively close in energy and thus, given that the halo function is monotonically decreasing, the data prefers models in which the $v_{\rm min}$ values associated with the two lowest observed recoils are lower than the $v_{\rm min}$ value of the highest energy event.

Fig. 4.4 and Fig. 4.5 show that no viable parameter space for 'Xe-phobic' interactions will remain if an experiment like LZ or PICO-250 does not find any dark matter signal (i.e. the purple regions, both 'A' and 'B', shown in Fig. 4.7 will be rejected). Notice that, even though the exposure of PICO-250 is much smaller than the exposure of LZ, PICO is highly sensitive to light exothermic WIMPs because fluorine is much lighter than xenon (in general exothermic scattering favors lighter target nuclei) and both PICO and LZ have comparable energy thresholds. In this regard, although argon is much lighter than xenon, the higher energy threshold of DarkSide-20k makes this experiment insensitive to light exothermic WIMPs.

4.5 Conclusions

We have presented here updated halo-dependent and halo-independent constraints on dark matter particle candidates that could explain the CDMS-II-Si data. We have studied candidates with isospin conserving and isospin-violating spin-independent interactions, with either elastic or exothermic scattering. We included constraints from PandaX-II, LUX (complete exposure), and PICO-60, as well as projected sensitivities for XENON1T, SuperCDMS SNOLAB Ge(HV), LZ, DARWIN, DarkSide-20k, and PICO-250.

The results presented show that both spin-independent isospin conserving and 'Ge-phobic' ($f_n/f_p = -0.8$) interpretations of CDMS-II-Si are excluded at the 90% CL. 'Xe-

phobic' ($f_n/f_p = -0.7$) interpretations, however, are still marginally viable after the recent PICO-60 result if the dark matter particle scatters exothermically with nuclei (with $\delta \lesssim -200$ keV), and can only be ruled out in the future by an experiment comparable to LZ or PICO-250. Although still marginally viable, the highly tuned nature of these models make a dark matter interpretation of the CDMS-II-Si very unlikely.

5 Assessing Compatibility of Direct Detection Data: Halo-Independent Global Likelihood Analyses

5.1 Introduction

Astrophysical and cosmological evidence indicate that roughly 85% of the matter in the Universe is in the form of dark matter (DM) most likely composed of yet unknown elementary particles. Arguably the most extensively studied DM particle candidate is a weakly interacting massive particle (WIMP), which offers both theoretical appeal and hope for near-future detection. Most of the matter in our own galaxy resides in a spheroidal dark halo that extends much beyond the visible disk. Direct DM detection experiments represent one of the primary WIMP search methods currently employed. These experiments attempt to measure the recoil energy of nuclei after they collide with DM particles bound to the galactic dark halo passing through Earth. The current status of DM direct detection experiments remain ambiguous, with three experiments observing a potential DM signal and all others reporting upper bounds, some of which appear to be in irreconcilable conflict with the putative detection claims for most particle candidates [143, 150–166].

Interpreting the results of DM direct detection experiments typically requires assumptions on the local DM density, the DM velocity distribution, the DM-nuclei interaction, and the scattering kinematics. The uncertainties associated with these inputs can significantly affect the expected recoil spectrum (both in shape and magnitude) for a particular experiment, as well as the observed compatibility between experimental data. Attempts have been made to remove the astrophysical uncertainty from direct DM detection calculations, and compare

data in a "halo-independent" manner, by translating measurements and bounds on the scattering rate into measurements and bounds on a function we will refer to as $\tilde{\eta}(v_{\rm min}, t)$ common to all experiments, which contains all of the information on the local DM density and velocity distribution (see e.g. [91, 93, 122, 126, 138, 149, 171–191]).

The function $\tilde{\eta}(v_{\rm min}, t)$ depends on the time t and a particular speed $v_{\rm min}$. The physical interpretation of $v_{\rm min}$ depends on the type of analysis being used. If the nuclear recoil $E_{\rm R}$ is considered an independent variable, then $v_{\rm min}$ is understood to be the minimum speed necessary for the incoming DM particle to impart a nuclear recoil $E_{\rm R}$ to the target nucleus (and thus it depends on the target nuclide T through its mass m_T, $v_{\rm min}^T = v_{\rm min}(E_{\rm R}, m_T)$). This has been the more common approach [126, 171, 173]. Alternatively, one can choose $v_{\rm min}$ as the independent variable, in which case $E_{\rm R}^T$ is understood to be the extremum recoil energy (maximum for elastic scattering, and either maximum or minimum for inelastic scattering) that can be imparted by an incoming WIMP traveling with speed $v = v_{\rm min}$ to a target nuclide T. Note that for elastic scattering off a single nuclide target the two approaches are just related by a simple change of variables. We will choose to treat $v_{\rm min}$ as an independent variable for the remainder of this paper, as this choice allows us to account for any isotopic target composition by summing terms dependent on $E_{\rm R}^T(v_{\rm min})$ over target nuclides T, for any fixed detected energy E'.

Early halo-independent analyses were limited in the way they handled putative signals. Only weighted averages on $v_{\rm min}$ intervals of the unmodulated component of $\tilde{\eta}(v_{\rm min}, t)$, $\tilde{\eta}^0(v_{\rm min})$, and of the amplitude of the annually modulated component, $\tilde{\eta}^1(v_{\rm min})$, (see Eq. (5.14) below) were plotted against upper bounds in the $v_{\rm min} - \tilde{\eta}$ plane (see e.g. [91, 93, 171, 173]).

This type of analysis leads to a poor understanding of the compatibility of various data sets.

Recently, attempts have been made to move beyond this limited approach of taking averages over $v_{\rm min}$ intervals by finding a best fit $\tilde{\eta}^0$ function and constructing confidence bands in the $v_{\rm min} - \tilde{\eta}$ plane [92,179], from unbinned data with an extended likelihood [194]. One can then compare upper bounds at a particular confidence level (CL) with a confidence band at a particular CL to assess if they are compatible (see [92] for a discussion). From now on, when an upper index 0 or 1 is not written, $\tilde{\eta}(v_{\rm min})$ is understood to be $\tilde{\eta}^0(v_{\rm min})$.

An alternative approach to analyzing the compatibility of data has been studied in [138] using the "parameter goodness-of-fit" test statistic [215,216] derived from a global likelihood (an alternative approach is taken in [184]). In [138], the compatibility of various experiments within a particular theoretical framework was determined by obtaining a p-value from Monte Carlo (MC) simulated data, generated under the assumption that the true halo function is the global best fit halo function. This approach has an advantage in that one can make quantitative statements about the compatibility between the observed data given a dark matter candidate model. However, this procedure assigns only a single number to the whole halo-independent parameter space, and we would like to have the ability to assess compatibility of the data with less restrictive assumptions on the underlying halo function.

In this paper we extend the approaches of [138] and [92] by using the global likelihood function to assess the compatibility of multiple data sets within a particular theoretical model across the halo-independent $v_{\rm min} - \tilde{\eta}$ parameter space. This is done with two distinct approaches. First, we extend the construction of the halo-independent pointwise confidence band presented in [92] to the case of a global likelihood function, consisting of one (or more)

extended likelihood functions and an arbitrary number of Gaussian or Poisson likelihoods. The resultant global confidence band can be compared directly with the confidence band constructed from the extended likelihood alone, to assess the joint compatibility of the data for any choice of DM-nuclei interaction and scattering kinematics. The drawback of this method is that it cannot quantitatively address the level of compatibility of the data sets. To address this concern we also propose an extension of the parameter goodness-of-fit test, which we will refer to as the "constrained parameter goodness-of-fit" test, that quantifies the compatibility of various data sets for a given DM particle candidate assuming the halo function $\tilde{\eta}(v_{\rm min})$ passes through a particular point $(v^*, \tilde{\eta}^*)$. By calculating the p-values for each $(v^*, \tilde{\eta}^*)$ throughout the $v_{\rm min} - \tilde{\eta}$ plane, one can construct plausibility regions, such that for any halo function not entirely contained within the plausibility region the data are incompatible at the chosen level, e.g. $p < 10\%$.

In Sec. 5.2 we review the procedure for constructing the best fit halo function $\tilde{\eta}_{BF}$ and confidence band from an extended likelihood. Readers familiar with [92] may wish to skip this section and go directly to Sec. 5.3, which discusses how the construction of the best fit halo function and confidence band is altered when dealing with a global likelihood function that is the product of one (or more) extended likelihoods and an arbitrary number of Poisson or Gaussian likelihoods. In Sec. 5.4, we use the methods discussed in Sec. 5.3 to construct the best fit halo and global pointwise confidence band, for the combined analysis of CDMS-II-Si and SuperCDMS data assuming elastic isospin-conserving [205, 206, 217] and exothermic isospin-violating spin-independent (SI) interactions [180, 183]. Sec. 5.5 introduces the "constrained parameter goodness-of-fit" test statistic and the construction of the plausi-

bility regions. This method is illustrated using CDMS-II-Si and SuperCDMS data, assuming elastic isospin-conserving spin-independent interactions. We conclude in Sec. 5.6.

5.2 Review of the Extended Maximum-Likelihood Halo-independent (EHI) Analysis Method

5.2.1 Generalized halo-independent analysis

The differential rate per unit of detector mass as a function of nuclear recoil energy $E_{\rm R}$ for dark matter particles of mass m scattering off a target nuclide T with mass m_T is given by

$$\frac{{\rm d}R_T}{{\rm d}E_{\rm R}} = \frac{\rho}{m}\frac{C_T}{m_T}\int_{v\geqslant v_{\rm min}(E_{\rm R})} {\rm d}^3\, v\, f(\boldsymbol{v},t)\, v\, \frac{{\rm d}\sigma_T}{{\rm d}E_{\rm R}}(E_{\rm R},\boldsymbol{v})\,, \tag{5.1}$$

where ρ is the local dark matter density, C_T is the mass fraction of the nuclide T in the detector, $f(\boldsymbol{v},t)$ is the dark matter velocity distribution in Earth's frame, and ${\rm d}\sigma_T/{\rm d}E_{\rm R}$ is the WIMP-nuclide differential cross section in the lab frame. When multiple target elements are present in the detector, the differential rate is

$$\frac{{\rm d}R}{{\rm d}E_{\rm R}} = \sum_T \frac{{\rm d}R_T}{{\rm d}E_{\rm R}}\,. \tag{5.2}$$

To allow for the possibility of inelastic DM-nuclei scattering, we consider a DM particle scattering to a new state of mass $m' = m + \delta$, where $|\delta| \ll m$, and $\delta > 0$ (< 0) describes endothermic (exothermic) scattering. In the limit $\mu_T|\delta|/m^2 \ll 1$, $v_{\rm min}(E_{\rm R})$ is given by

$$v_{\rm min}(E_{\rm R}) = \frac{1}{\sqrt{2m_T E_{\rm R}}}\left|\frac{m_T E_{\rm R}}{\mu_T} + \delta\right|\,, \tag{5.3}$$

where μ_T is the reduced mass of the WIMP-nucleus system. Notice Eq. (5.3) reduces to the typical equation for elastic scattering when $\delta = 0$. Eq. (5.3) can be used to obtain the range of possible recoil energies, $[E_{\rm R}^{T,-}(v), E_{\rm R}^{T,+}(v)]$, that can be imparted to a target nucleus by a DM particle traveling at speed v in Earth's frame, given by

$$E_{\rm R}^{T,\pm}(v) = \frac{\mu_T^2 v^2}{2m_T}\left(1 \pm \sqrt{1 - \frac{2\delta}{\mu_T v^2}}\right)^2 . \tag{5.4}$$

Eq. (5.4) shows that for endothermic scattering there exists a nontrivial kinematic endpoint, given by the DM speed $v_\delta^T = \sqrt{2\delta/\mu_T}$, below which incoming DM particles cannot induce nuclear recoils. When multiple targets are present in a detector, we use v_δ to denote the minimum of all v_δ^T. For exothermic and elastic scattering $v_\delta = 0$.

Experiments do not actually measure the recoil energy of a target nucleus, but rather a proxy for recoil energy (e.g. the number of photoelectrons detected in a photomultiplier tube) denoted E'. The differential rate as a function of the detected energy E' is given by

$$\frac{{\rm d}R}{{\rm d}E'} = \sum_T \int_0^\infty {\rm d}E_{\rm R}\, \epsilon(E_{\rm R}, E')\, G_T(E_{\rm R}, E')\, \frac{{\rm d}R_T}{{\rm d}E_{\rm R}}\,, \tag{5.5}$$

where the differential rate in Eq. (5.1) has been convolved with the efficiency function $\epsilon(E_{\rm R}, E')$ and the energy resolution function $G_T(E_{\rm R}, E')$, which together give the probability that a detected recoil energy E' resulted from a true recoil energy $E_{\rm R}$.

Upon changing the order of integration, one can express the differential rate in detected

energy as

$$\frac{\mathrm{d}R}{\mathrm{d}E'} = \frac{\sigma_{\mathrm{ref}}\rho}{m}\int_{v\geqslant v_\delta} \mathrm{d}^3 v\, \frac{f(\boldsymbol{v},t)}{v} \sum_T \frac{\mathrm{d}\mathcal{H}_T}{\mathrm{d}E'}(E',\boldsymbol{v})\,, \tag{5.6}$$

where $\mathrm{d}\mathcal{H}_T/\mathrm{d}E'$ is given by

$$\frac{\mathrm{d}\mathcal{H}_T}{\mathrm{d}E'}(E',\boldsymbol{v}) \equiv \begin{cases} \dfrac{C_T}{m_T}\displaystyle\int_{E_{\mathrm{R}}^{T,-}}^{E_{\mathrm{R}}^{T,+}} \mathrm{d}E_{\mathrm{R}}\epsilon(E_{\mathrm{R}},E')\,G_T(E_{\mathrm{R}},E')\,\frac{v^2}{\sigma_{\mathrm{ref}}}\,\frac{\mathrm{d}\sigma_T}{\mathrm{d}E_{\mathrm{R}}}(E_{\mathrm{R}},\boldsymbol{v}) & \text{if } v \geqslant v_\delta^T, \\ 0 & \text{if } v < v_\delta^T. \end{cases} \tag{5.7}$$

and we define

$$\frac{\mathrm{d}\mathcal{H}}{\mathrm{d}E'} \equiv \sum_T \frac{\mathrm{d}\mathcal{H}_T}{\mathrm{d}E'}\,. \tag{5.8}$$

Here, we only consider differential cross sections that depend on the speed of the WIMP $v = |\boldsymbol{v}|$. The cross section depends only on the speed v if the incoming WIMPs and the target nuclei are unpolarized and the detector response is isotropic, as is most common. In Eqs. 5.6 and 5.7, we have incorporated the parameter σ_{ref} which denotes the overall strength of the interaction. For example in the case of the SI interaction, with differential cross section given by D where A_T and Z_T are the atomic and charge numbers of nuclide T, f_n and f_p are the neutron and proton couplings, and $F_T(E_{\mathrm{R}})$ is the form factor normalized to $F_T(0) = 1$ (taken here to be Helm form factor), we will choose $\sigma_{\mathrm{ref}} = \sigma_p$, the WIMP-proton cross section.

A halo-independent analysis relies on the separation of the astrophysical parameters from the particle physics and detector-dependent quantities. Here we follow [93]. Let us define

$$\tilde{\eta}(v_{\mathrm{min}},t) \equiv \frac{\rho\sigma_{\mathrm{ref}}}{m}\int_{v_{\mathrm{min}}}^{\infty} \mathrm{d}v\,\frac{F(v,t)}{v}\,, \tag{5.9}$$

where $F(v,t) \equiv v^2 \int \mathrm{d}\Omega_v f(\boldsymbol{v},t)$. Differentiating both sides of Eq. (5.9) gives

$$\frac{\sigma_{\mathrm{ref}}\rho}{m}\frac{F(v,t)}{v} = -\frac{\partial\tilde{\eta}(v,t)}{\partial v}\,, \tag{5.10}$$

which upon insertion into Eq. (5.6) leads to

$$\frac{\mathrm{d}R}{\mathrm{d}E'} = -\int_{v_\delta}^{\infty}\mathrm{d}v\,\frac{\partial\tilde{\eta}(v,t)}{\partial v}\,\frac{\mathrm{d}\mathcal{H}}{\mathrm{d}E'}(E',v)\,. \tag{5.11}$$

Using the fact that $\tilde{\eta}(\infty,t) = 0$ and $\mathrm{d}\mathcal{H}/\mathrm{d}E'(E',v_\delta) = 0$, integration by parts of Eq. (5.11) results in the following expression for the differential rate

$$\frac{\mathrm{d}R}{\mathrm{d}E'} = \int_{v_\delta}^{\infty}\mathrm{d}v_{\mathrm{min}}\tilde{\eta}(v_{\mathrm{min}},t)\,\frac{\mathrm{d}\mathcal{R}}{\mathrm{d}E'}(E',v_{\mathrm{min}})\,, \tag{5.12}$$

where we have now defined the differential response function $\mathrm{d}\mathcal{R}/\mathrm{d}E'$ as

$$\frac{\mathrm{d}\mathcal{R}}{\mathrm{d}E'}(E',v_{\mathrm{min}}) \equiv \frac{\partial}{\partial v_{\mathrm{min}}}\left[\frac{\mathrm{d}\mathcal{H}}{\mathrm{d}E'}(E',v_{\mathrm{min}})\right]\,. \tag{5.13}$$

$\tilde{\eta}(v_{\mathrm{min}},t)$ is a function of time due to the annual rotation of the Earth around the Sun. If one now makes the approximation

$$\tilde{\eta}(v_{\mathrm{min}},t) \simeq \tilde{\eta}^0(v_{\mathrm{min}}) + \tilde{\eta}^1(v_{\mathrm{min}})\cos(2\pi(t-t_0)/\mathrm{year}) \tag{5.14}$$

and integrates the differential rate over the energy range of interest, the unmodulated com-

ponent R^0 and annual modulation amplitude R^1 of the rate are given by

$$R^{\alpha}_{[E'_1,E'_2]} \equiv \int_{v_\delta}^{\infty} \mathrm{d}v_{\min}\, \tilde{\eta}^{\alpha}(v_{\min}) \int_{E'_1}^{E'_2} \mathrm{d}E'\, \frac{\mathrm{d}\mathcal{R}}{\mathrm{d}E'} \tag{5.15}$$

$$= \int_{v_\delta}^{\infty} \mathrm{d}v_{\min}\, \tilde{\eta}^{\alpha}(v_{\min})\, \mathcal{R}_{[E'_1,E'_2]}(v_{\min})\,, \tag{5.16}$$

where $\alpha = 0$ or 1, and the energy-integrated response function $\mathcal{R}$ is given by

$$\mathcal{R}_{[E'_1,E'_2]}(v_{\min}) = \int_{E'_1}^{E'_2} \mathrm{d}E'\, \frac{\mathrm{d}\mathcal{R}}{\mathrm{d}E'}(E', v_{\min})\,. \tag{5.17}$$

In the event that $\mathcal{R}_{[E'_1,E'_2]}(v_{\min})$ is a well-localized function in $v_{\min}$, measurements on unmodulated and modulated rate can be used to infer the average values of $\tilde{\eta}^0$ and $\tilde{\eta}^1$ over a $v_{\min}$ interval. This is the case for DM-nuclei differential cross sections proportional to $1/v^2$ (e.g. the typical SI and SD contact interactions). Should the differential cross section not be of this form, one may need to regularize the energy-integrated response function as described in [93].

5.2.2 Extended maximum likelihood analysis

It was initially proven in [179], that if there is no uncertainty in the measurement of recoil energies in a single nuclide target, then the extended likelihood, given by

$$\mathcal{L}[\tilde{\eta}(v_{\min})] \equiv e^{-N_E[\tilde{\eta}]} \prod_{a=1}^{N_O} MT\, \frac{\mathrm{d}R_{\mathrm{tot}}}{\mathrm{d}E'}\bigg|_{E'=E'_a}\,, \tag{5.18}$$

is maximized by a non-increasing piecewise constant $\tilde{\eta}^0(v_{\min})$ function (which we call simply $\tilde{\eta}(v_{\min})$) with at most N_O (the number of observed events) steps. $N_E[\tilde{\eta}]$ in Eq. (5.18) is the total number of expected events, and E'_a is the observed energy of event a. This proof was generalized to the case of realistic energy resolution and arbitrary target composition in [92]. The generalized proof presented in [92] applies the Karush-Kuhn-Tucker (KKT) conditions, which are only valid for systems with an objective function of finite number of variables subject to a finite number of constraints, to the likelihood functional in Eq. (5.18) by discretizing the variable $v_{\min}$, applying the KKT conditions, and then taking the continuum limit.

Here, we will briefly review the conclusions presented in [92]. If one defines the quantity

$$L[\tilde{\eta}] = -2 \ln \mathcal{L}[\tilde{\eta}] \,, \tag{5.19}$$

then instead of maximizing the likelihood, one can equivalently minimize $L[\tilde{\eta}]$. The KKT conditions, applied to Eq. (5.19) and taken in the continuum limit, lead to the following:

$$\text{(I)} \quad q(v_{\min}) = \int_{v_\delta}^{v_{\min}} \mathrm{d}v \, \frac{\delta L}{\delta \tilde{\eta}(v)} \tag{5.20}$$

$$\text{(II)} \quad q(v_{\min}) \geq 0 \tag{5.21}$$

$$\text{(III)} \quad \forall \epsilon > 0, \quad \tilde{\eta}(v_{\min} + \epsilon) \leq \tilde{\eta}(v_{\min}) \tag{5.22}$$

$$\text{(IV)} \quad q(v_{\min}) \lim_{\epsilon \to +0} \frac{\tilde{\eta}(v_{\min} + \epsilon) - \tilde{\eta}(v_{\min})}{\epsilon} = 0 \,. \tag{5.23}$$

A direct consequence of Eq. (5.23) is that $\tilde{\eta}(v_{\min})$ is a piecewise constant function with the

locations of the steps given by the $v_{\rm min}$ values which satisfy $q(v_{\rm min}) = 0$. For this reason, we need to analyze the behavior of $q(v_{\rm min})$. Eq. (5.18) and (5.20) can be used to show that

$$q(v_{\rm min}) = 2\xi(v_{\rm min}) - 2\sum_{a=1}^{N_O} \frac{H_a(v_{\rm min})}{\gamma_a[\tilde{\eta}]}\,, \tag{5.24}$$

where we have defined the following quantities:

$$\xi(v_{\rm min}) \equiv MT \int_{E'_{\rm min}}^{E'_{\rm max}} {\rm d}E' \, \frac{{\rm d}\mathcal{H}}{{\rm d}E'}(E', v_{\rm min})\,, \tag{5.25}$$

$$H_a(v_{\rm min}) \equiv \frac{{\rm d}\mathcal{H}}{{\rm d}E'}(E', v_{\rm min})\bigg|_{E'=E'_a}\,, \tag{5.26}$$

and

$$\gamma_a[\tilde{\eta}] \equiv \frac{{\rm d}R_{\rm tot}}{{\rm d}E'}\bigg|_{E'=E'_a}\,. \tag{5.27}$$

For the extended likelihood function in Eq. (5.18), the behavior of the terms in Eq. (5.24) were studied in [92] to determine how many steps can appear in the best fit $\tilde{\eta}$ function. We briefly review their behavior here (see [92] for additional details).

Consider first the $v_{\rm min}$-dependence of ${\rm d}\mathcal{H}/{\rm d}E'$ (see Eq. (5.7)), which appears in both the integrand of $\xi(v_{\rm min})$ and in $H_a(v_{\rm min})$. If the differential cross section is proportional to v^{-2}, as is the case for the standard SI and SD contact interactions, the only velocity dependence of ${\rm d}\mathcal{H}/{\rm d}E'$ is in the integration range $[E_R^{T,+}(v_{\rm min}), E_R^{T,-}(v_{\rm min})]$. For these interactions, as $v_{\rm min}$ increases, the integration covers a larger portion of the parameter space where the integrand is non-zero. At large values of $v_{\rm min}$, the entire region where the integrand is non-zero is included in the integration and ${\rm d}\mathcal{H}/{\rm d}E'$ becomes constant. For a fixed value of E', one

would expect the integrand of $\mathrm{d}\mathcal{H}/\mathrm{d}E'$ to be a well-localized function of E_{R} (i.e. an observed recoil E' can only result from a narrow range of E_{R} values). For this reason, the terms $H_a(v_{\mathrm{min}})$ appear as step-like functions in v_{min}.

The term $\xi(v_{\mathrm{min}})$ contains an additional integration of $\mathrm{d}\mathcal{H}/\mathrm{d}E'$ over E'. The only dependence on E' appears in the factor $\epsilon(E', E_{\mathrm{R}})G_T(E', E_{\mathrm{R}})$, which describes the probability a detected recoil energy E' is the result of some true recoil energy E_{R}. For small values of v_{min}, only a narrow range of recoil energies are integrated over and thus ξ will be quite small (i.e. , for v_{min} values such that $E_{\mathrm{R}}^{T,+}(v_{\mathrm{min}})$ is below threshold). As v_{min} increases, the integration range widens and $\xi(v_{\mathrm{min}})$ steadily increases. Eventually, the entire region where the integrand is nonzero is included in the integration, and $\xi(v_{\mathrm{min}})$ becomes constant.

The only term dependent on the halo function is $\gamma_a[\tilde{\eta}]$, which only alters the relative contribution of each step-like function to $q(v_{\mathrm{min}})$. The function $\tilde{\eta}_{BF}(v_{\mathrm{min}})$ can only be discontinuous when $q(v_{\mathrm{min}}) = 0$, which is equivalent to saying the steps of $\tilde{\eta}_{BF}$ occur where the step-like functions $H_a(v_{\mathrm{min}})/\gamma_a[\tilde{\eta}]$ touch $\xi(v_{\mathrm{min}})$ from below. Since there is a single term of the form $H_a(v_{\mathrm{min}})/\gamma_a[\tilde{\eta}]$ for each observed event, the number of steps appearing in $\tilde{\eta}_{BF}$ must be less than or equal to the number of observed events, N_O.

5.2.3 Construction of the best fit halo function and confidence band from an extended likelihood

In this section we briefly review the construction of the best fit function $\tilde{\eta}_{BF}(v_{\mathrm{min}})$ and the confidence band for an extended likelihood [92]. Let us define the function $f_L^{N_O}$ of $2N_O$ variables,

$$f_L^{N_O}(\vec{v}, \vec{\tilde{\eta}}) \equiv L[\tilde{\eta}^{N_O}(v_{\mathrm{min}}; \vec{v}, \vec{\tilde{\eta}})]\,, \tag{5.28}$$

where $\vec{v} = (v_1, ..., v_{N_O})$ and $\vec{\tilde{\eta}} = (\tilde{\eta}_1, ..., \tilde{\eta}_{N_O})$, and the various v_a and $\tilde{\eta}_a$ specify the location and height of each step. Here, we have defined the piecewise constant function $\tilde{\eta}^{N_O}$ as

$$\tilde{\eta}^{N_O}(v_{\min}; \vec{v}, \vec{\tilde{\eta}}) \equiv \begin{cases} \tilde{\eta}_a & v_{a-1} < v_{\min} \leq v_a \,, \\ \\ 0 & v_{N_O} < v_{\min} \,. \end{cases}$$

Using the result of the previous section, minimizing the functional $L[\tilde{\eta}]$, and thus finding the best fit $\tilde{\eta}(v_{\min})$, is now reduced to minimizing $f_L^{N_O}$ subject to the constraints

$$v_1 > v_\delta \,, \tag{5.29}$$

$$v_b - v_a \geq 0 \;\text{ and }\; \tilde{\eta}_a - \tilde{\eta}_b \geq 0 \;\text{ for }\; a < b \,. \tag{5.30}$$

We can define the confidence band as the region filled by all possible $\tilde{\eta}$ functions satisifying

$$\Delta L[\tilde{\eta}] \equiv L[\tilde{\eta}] - L_{\min} \leq \Delta L^* \,, \tag{5.31}$$

where $L_{\min}$ is the minimum of $L[\tilde{\eta}]$, and ΔL^* corresponds to the desired confidence level. However, in practice, finding all $\tilde{\eta}$ functions satisfying Eq. (5.31) is not possible. Instead, let us consider the possible subset of $\tilde{\eta}$ functions which minimize $L[\tilde{\eta}]$ subject to the constraint

$$\tilde{\eta}(v^*) = \tilde{\eta}^* \,. \tag{5.32}$$

Now let us define $L^c_{\min}(v^*, \tilde{\eta}^*)$ to be the minimum of $L[\tilde{\eta}]$ subject to the constraint in

Eq. (5.32), and

$$\Delta L^c_{\rm min}(v^*, \tilde{\eta}^*) = L^c_{\rm min}(v^*, \tilde{\eta}^*) - L_{\rm min}\,. \tag{5.33}$$

If the point $(v^*, \tilde{\eta}^*)$ lies within the confidence band, then there should exist at least one $\tilde{\eta}$ function passing through this point which satisfies $\Delta L[\tilde{\eta}] \leq \Delta L^*$. Should this be the case, it follows that $\Delta L^c_{\rm min}(v^*, \tilde{\eta}^*) \leq \Delta L^*$. Alternatively, if $\Delta L^c_{\rm min}(v^*, \tilde{\eta}^*) \geq \Delta L^*$, one can state that there does not exist a single $\tilde{\eta}$ which satisfies $\Delta L[\tilde{\eta}] \leq \Delta L^*$. Thus the confidence band can be constructed by finding the values of $(v^*, \tilde{\eta}^*)$ which satisfy $\Delta L^c_{\rm min}(v^*, \tilde{\eta}^*) \leq \Delta L^*$. This condition defines a two-sided interval around $\tilde{\eta}_{\rm BF}$ for each $v_{\rm min}$ value (with $v_{\rm min} = v^*$), and the collection of those intervals forms a pointwise confidence band in $v_{\rm min}$–$\tilde{\eta}$ space, which we are simply calling the confidence band.

To understand the meaning of $\Delta L^c_{\rm min}$, let us first discretize the continuous variable $v_{\rm min}$ into a collection of K discrete values $\vec{v}_{\rm min} = (v^0_{\rm min}, ..., v^{K-1}_{\rm min})$. The likelihood functional in Eq. (5.19) then becomes a function of the $K-$dimensional vector $\vec{\tilde{\eta}} = (\tilde{\eta}_0, \tilde{\eta}_1, ..., \tilde{\eta}_{K-1})$ which defines the piecewise constant function $\tilde{\eta}(v_{\rm min}; \vec{\tilde{\eta}})$ given by

$$\tilde{\eta}(v_{\rm min}; \vec{\tilde{\eta}}) \equiv \tilde{\eta}_i \text{ if } v^i_{\rm min} \leq v_{\rm min} < v^{i+1}_{\rm min}\,. \tag{5.34}$$

With this discretization, the constraint on $(v^*, \tilde{\eta}^*)$ in Eq. (5.32) corresponds to $v^k_{\rm min} \leq v^* < v^{k+1}_{\rm min}$ and $\tilde{\eta}^* = \tilde{\eta}_k$ for some integer $0 \leq k \leq K-1$. $\Delta L^c_{\rm min}(v^*, \tilde{\eta}^*)$ is then replaced by the function $\Delta L^{k,c}_{\rm min}(\tilde{\eta}^*)$ with the index k corresponding to v^*, defined by

$$\Delta L^{k,c}_{\rm min}(\tilde{\eta}^*) = -2\ln\left[\frac{\mathcal{L}(\hat{\tilde{\eta}}_0, ..., \hat{\tilde{\eta}}_{k-1}, \tilde{\eta}_k = \tilde{\eta}^*, \hat{\tilde{\eta}}_{k+1}, ..., \hat{\tilde{\eta}}_{K-1})}{\mathcal{L}(\hat{\tilde{\eta}}_0, ..., \hat{\tilde{\eta}}_k, ..., \hat{\tilde{\eta}}_{K-1})}\right], \tag{5.35}$$

where $\hat{\tilde{\eta}}_i$ are the $\tilde{\eta}_i$ values which maximize the likelihood function $\mathcal{L}(\tilde{\eta}_0, ...\tilde{\eta}_{K-1}) \equiv \mathcal{L}[\tilde{\eta}(v_{\rm min}; \vec{\tilde{\eta}})]$ subject to the constraint $\tilde{\eta}_k = \tilde{\eta}^*$, and $\hat{\tilde{\eta}}_i$ maximize $\mathcal{L}$ without the constraint. $\Delta L^{k,c}_{\rm min}(\tilde{\eta}^*)$ now defines the $-2\ln$ of the profile likelihood ratio with one parameter ($\tilde{\eta}_k$), and thus by Wilks' theorem the distribution of $\Delta L^{k,c}_{\rm min}(\tilde{\eta}^*)$ approaches the chi-square distribution with one degree of freedom in the limit where the data sample is very large. If we now recover the continuum limit by taking $K \to \infty$, we see that $\Delta L^{k,c}_{\rm min}(\tilde{\eta}^*)$ approaches $\Delta L^{c}_{\rm min}(v^*, \tilde{\eta}^*)$. Thus the construction of the confidence band is equivalent to finding the collection of confidence intervals in $\tilde{\eta}^*$ for each v^* at a given CL for which $\Delta L^{c}_{\rm min} < \Delta L^*$. Assuming that $\Delta L^{c}_{\rm min}$ is chi-square distributed, the choices $\Delta L^* = 1.0$ and $\Delta L^* = 2.7$ correspond to the confidence intervals of $\tilde{\eta}$ at 68% and 90% CL, respectively, for each $v_{\rm min}$ value. In [92] it was shown that the constrained best fit halo function $\tilde{\eta}^c_{BF}$ defining $L^{c}_{\rm min}(v^*, \tilde{\eta}^*)$ is a piecewise constant function with at most $N_O + 1$ steps, with the additional step potentially appearing at $(v^*, \tilde{\eta}^*)$. An in-depth discussion of the interpretation of the confidence band constructed from the profile likelihood ratio is provided in [92].

5.3 Extension of EHI analysis to a global maximum likelihood

In this paper we extend the analysis presented in [92] to make statistically meaningful statements about the data of multiple experiments in a halo-independent manner. Specifically, we (*i*) extend the formalism of constructing a pointwise confidence band from a profile likelihood in halo-independent parameter space to a global likelihood function (this section), and (*ii*) propose a method for creating plausibility regions, constructed from a new family of test statistics which can assess the compatibility of multiple data sets under the assumption that

the halo function $\tilde{\eta}(v_{\rm min})$ passes through each $(v^*, \tilde{\eta}^*)$ point (see Sec. 5.5). To accomplish these tasks one must first understand how to find the best fit halo function and constrained best fit halo function from a global likelihood.

In this section we extend the procedure of [92] to the global likelihood function, defined by the product of some number $N_{\rm exp}$ of individual likelihood functions, $\alpha = 1, 2, ...N_{\rm exp}$,

$$\mathcal{L}_{\rm G} = \prod_{\alpha=1}^{N_{\rm exp}} \mathcal{L}_\alpha \,. \tag{5.36}$$

The procedure of [92] relies on the fact that an extended likelihood function is maximized by a non-increasing piecewise constant $\tilde{\eta}_{BF}(v_{\rm min})$ function with a finite number of points of discontinuity. As discussed below, the methods and reasoning of [92] extend to a global likelihood, if it includes at least one extended likelihood. Thus, the global likelihood function we will work with for the remainder of the paper is

$$\mathcal{L}_{\rm G} = \mathcal{L}_{\rm EHI} \prod_{\alpha=1}^{(N_{\rm exp}-1)} \mathcal{L}_\alpha \,, \tag{5.37}$$

where $\mathcal{L}_{\rm EHI}$ is an extended likelihood (EHI stands for "extended halo-independent" [92]) as in Eq. (5.18) and, for each α, $\mathcal{L}_\alpha$ represents Poisson likelihoods,

$$\mathcal{L}_\alpha[\tilde{\eta}] = \prod_{j=1}^{N_{\rm bin}^{(\alpha)}} \frac{(\nu_j^{(\alpha)}[\tilde{\eta}] + b_j^{(\alpha)})^{n_j^{(\alpha)}} e^{-(\nu_j^{(\alpha)}[\tilde{\eta}]+b_j^{(\alpha)})}}{n_j^{(\alpha)}!} \,, \tag{5.38}$$

or Gaussian likelihoods

$$\mathcal{L}_\alpha[\tilde{\eta}] = \prod_{j=1}^{N_{\rm bin}^{(\alpha)}} \frac{1}{\sigma_j^{(\alpha)}\sqrt{2\pi}} \exp\left[-\left(\frac{\nu_j^{(\alpha)}[\tilde{\eta}] + b_j^{(\alpha)} - n_j^{(\alpha)}}{\sqrt{2}\sigma_j^{(\alpha)}}\right)^2\right] . \tag{5.39}$$

Here $\nu_j^{(\alpha)}[\tilde{\eta}]$, $b_j^{(\alpha)}$, and $n_{\rm j}^{(\alpha)}$ are respectively the expected number of dark matter events, the expected number of background events, and the number of observed events in bin j of experiment α. $N_{\rm bin}^{(\alpha)}$ is the number of bins used in the Poisson or Gaussian likelihood of experiment α, and $\sigma_j^{(\alpha)}$ is the standard deviation associated with the measurement of $n_j^{(\alpha)}$ in an experiment α employing a Gaussian likelihood.

We now prove that global likelihoods of the form Eq. (5.37) are maximized by non-increasing piecewise constant $\tilde{\eta}$ functions with at most $\mathcal{N}$ steps,

$$\mathcal{N} \equiv N_{\rm EHI} + \sum_\alpha N_{\rm bin}^{(\alpha)} , \tag{5.40}$$

where $N_{\rm EHI} = N_O$ in Eq. (5.18), i.e. the number of observed events in the extended likelihood.

The KKT conditions in Eq. (5.20–5.23) apply equally to any likelihood function $\mathcal{L}$. The KKT condition in Eq. (5.23) implies that $\tilde{\eta}_{BF}$ is constant in an open interval where $q(v_{\rm min}) \neq 0$. Thus if the $q(v_{\rm min})$ function given by Eq. (5.20) has only a finite number of isolated zeros within a range, the best fit $\tilde{\eta}$ in this range should be a piecewise constant function with steps located at the zeros of $q(v_{\rm min})$. Therefore, the problem of determining the potential number of steps of $\tilde{\eta}_{BF}$ is equivalent to counting the maximum possible number of isolated zeros of the $q(v_{\rm min})$ function.

For the global likelihood in Eq. (5.37), $q(v_{\rm min})$ is given by

$$q(v_{\rm min}) = 2\xi^{\rm EHI}(v_{\rm min}) - 2\sum_{a=1}^{N_{\rm EHI}} \frac{H_a^{\rm EHI}(v_{\rm min})}{\gamma_a^{\rm EHI}[\tilde{\eta}]} + \sum_{\alpha=1} Q^{(\alpha)}[\tilde{\eta}; v_{\rm min}]\,, \tag{5.41}$$

where $Q^{(\alpha)}[\tilde{\eta}; v_{\rm min}]$ is defined by either

$$Q^{(\alpha)}[\tilde{\eta}, v_{\rm min}] \equiv \int_{v_\delta}^{v_{\rm min}} {\rm d}v\, \frac{\delta(-2\ln\mathcal{L}_\alpha)}{\delta\tilde{\eta}(v)} = 2\sum_{j=1}^{N_{\rm bin}^{(\alpha)}} \left[\frac{\nu_j^{(\alpha)}[\tilde{\eta}] + b_j^{(\alpha)} - n_j^{(\alpha)}}{\nu_j^{(\alpha)}[\tilde{\eta}] + b_j^{(\alpha)}}\right] \xi_j^{(\alpha)}(v_{\rm min}) \tag{5.42}$$

for Poisson likelihoods of the form in Eq. (5.38), and

$$Q^{(\alpha)}[\tilde{\eta}, v_{\rm min}] = 2\sum_{j=1}^{N_{\rm bin}^{(\alpha)}} \left[\frac{\nu_j^{(\alpha)}[\tilde{\eta}] + b_j^{(\alpha)} - n_j^{(\alpha)}}{\sigma_j^2}\right] \xi_j^{(\alpha)}(v_{\rm min})\,, \tag{5.43}$$

for Gaussian likelihoods in Eq. (5.39). Changing the function $\tilde{\eta}(v_{\rm min})$ only alters the sign and magnitude of the prefactor of $\xi_j^{(\alpha)}(v_{\rm min})$ in each term of $Q^{(\alpha)}[\tilde{\eta}, v_{\rm min}]$. The $v_{\rm min}$ dependence of $Q^{(\alpha)}[\tilde{\eta}, v_{\rm min}]$ exclusively appears in the functions $\xi_j^{(\alpha)}(v_{\rm min})$, which is defined as in Eq. (5.25), replacing the integration range $[E'_{\rm min}, E'_{\rm max}]$ with the energy range of the bin, and $\mathcal{H}$ by $\mathcal{H}^{(\alpha)}$. The function $\xi_j^{(\alpha)}(v_{\rm min})$ has the same generic behavior as $\xi(v_{\rm min})$ described at the end of Sec. 5.2.2.

In Appendix A.1 we prove that above a certain value of $v_{\rm min}$, given by the minimum $v_{\rm low}^{\mu}$ (see Appendix A.1.1 for definition), the zeros of $q(v_{\rm min})$ in Eq. (5.41) are isolated, and the maximum number of isolated zeros is given by Eq. (5.40). However, in practice the number of steps is smaller than $\mathcal{N}$ and can be determined by studying the functional form of the functions $\xi^{\rm EHI}(v_{\rm min})$, $H_a^{\rm EHI}(v_{\rm min})$, and $\xi_j^{(\alpha)}(v_{\rm min})$ (which are independent of $\tilde{\eta}$). In Appendix

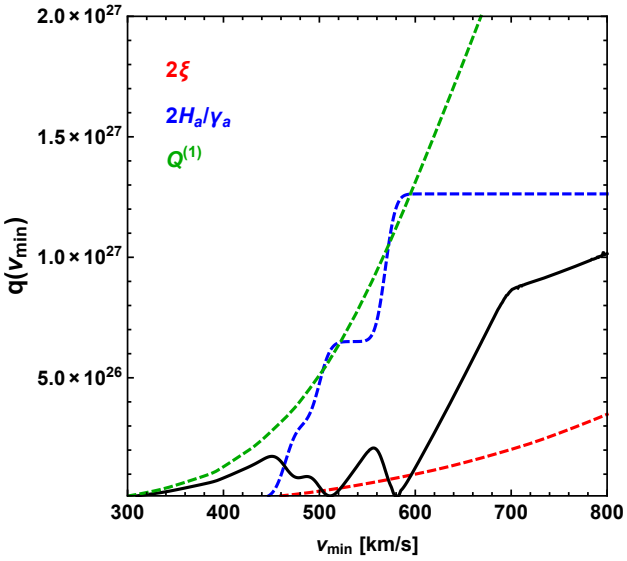

Figure 5.1: The function $q(v_{\rm min})$ (black), and absolute value of each of its three comprising terms in Eq. (5.41) (dashed lines) for the combined analysis of CDMS-II-Si and SuperCDMS, assuming a 9 GeV DM particle scattering elastically with a SI contact interaction and $f_n/f_p = 1$. The $v_{\rm min}$ values where $q(v_{\rm min}) = 0$ correspond to the locations of the steps in the global $\tilde{\eta}_{BF}$ halo function.

B we prove the uniqueness of the best fit halo function, $\tilde{\eta}_{BF}$.

An explicit example of the $q(v_{\rm min})$ function and its components is shown in Fig. 5.1 for the case of CDMS-II-Si combined with SuperCDMS data. For SuperCDMS we have taken a one-bin Poisson likelihood, summing over all detectors in Table 1 of [166], the contribution from which to $q(v_{\rm min})$ is shown in green. Also included in Fig. 5.1 are the contributions to $q(v_{\rm min})$ arising from $\xi^{\rm EHI}(v_{\rm min})$ (red) and the summation over the $H_a(v_{\rm min})/\gamma_a[\tilde{\eta}]$ (blue). Fig. 5.1 shows that $q(v_{\rm min})$ goes to 0 at $v_{\rm min} \simeq 510$ km/s and 580 km/s, denoting the locations of the steps of $\tilde{\eta}_{BF}$ (shown later in Fig. 5.2).

We would like to emphasize that all of the aforementioned arguments have relied on having a global likelihood that contains at least one extended likelihood. This likelihood has the essential feature of contributing an $\tilde{\eta}$-dependent term and an $\tilde{\eta}$-independent term to

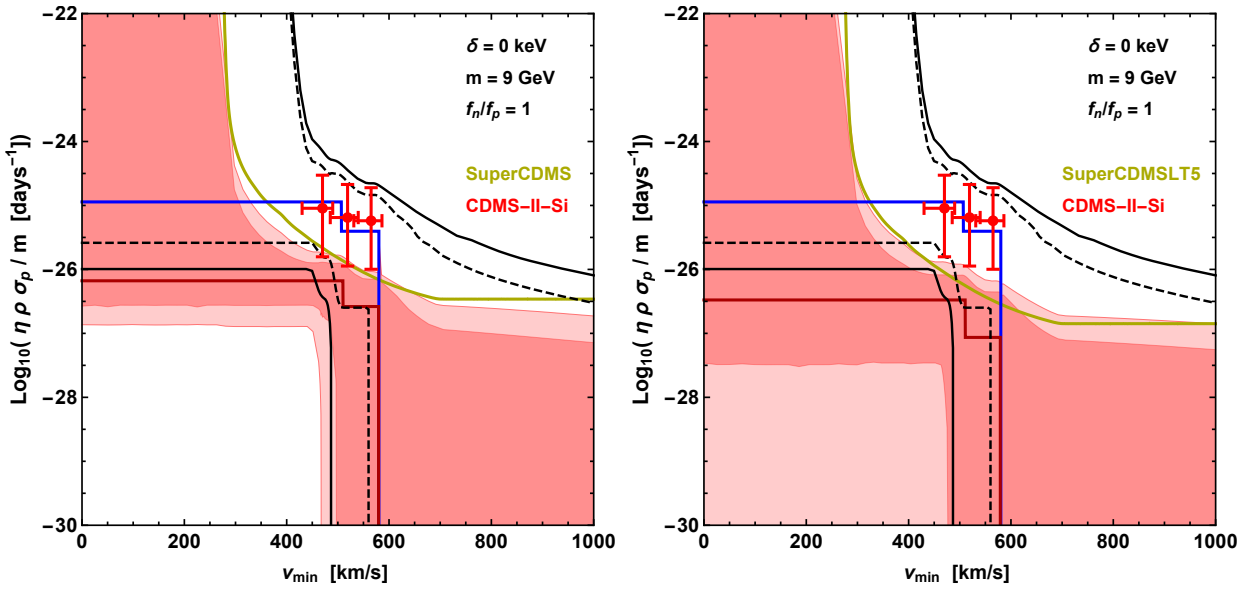

Figure 5.2: 68% (dark red region) and 90% (light red region) global confidence bands and $\tilde{\eta}_{\mathrm{BF}}$ (dark red) arising from the combined CDMS-II-Si and SuperCDMS (left) and SuperCDMSLT5 (right) halo-independent analysis. Results are compared with 90% CL bounds from SuperCDMS (dark yellow line), 68% (black dashed lines) and 90% (solid black lines) confidence bands and $\tilde{\eta}_{\mathrm{BF}}$ for CMDS-II-Si only analysis (blue line) [92]. The red crosses represent the 68% CL intervals of the averaged $\tilde{\eta}$ arising from binning the CDMS-II-Si events into 2 keVnr bins between 7 and 13 keV (see e.g. [175, 177, 182], in which we take the horizontal bars to be the v_{min} range where 90% of the area under $\mathcal{R}_{[E'_1,E'_2]}(v_{\mathrm{min}})$ is contained). The results shown assume a 9 GeV DM particle scattering elastically through a SI isospin-conserving contact interaction ($f_n/f_p = 1$).

$q(v_{\rm min})$, with different functional dependences on $v_{\rm min}$.

In order to construct the two sided confidence band, we compute at each value of $v_{\rm min} = v^*$ the two sided interval defined by

$$\Delta L^c_{\rm G,min} \equiv -2\ln\left[\frac{\hat{\mathcal{L}}_G(v^*,\tilde{\eta}^*)}{\hat{\mathcal{L}}_G}\right] \leq \Delta L^* \,, \tag{5.44}$$

where $\hat{\mathcal{L}}_G(v^*,\tilde{\eta}^*)$ is the maximum of the global likelihood subject to constraint Eq. (5.32), and $\hat{\mathcal{L}}_G$ is the maximum of the global likelihood. Using the same arguments of Sec. 5.2.3 and assuming that $\Delta L^c_{\rm G,min}$ is chi-square distributed, the distribution of $\Delta L^c_{\rm G,min}$ has one degree of freedom and $\Delta L^* = 1.0$ and $\Delta L^* = 2.7$ for the 68% and 90% CL intervals, respectively. In Sec. 4.2 of [92] it was shown that if $\mathcal{L}$ is maximized by an $\tilde{\eta}_{BF}$ function with a maximum of N steps, then $\mathcal{L}(v^*,\tilde{\eta}^*)$ (i.e. $\mathcal{L}$ subject to the constraint that $\tilde{\eta}(v_{\rm min})$ passes through the point $(v^*,\tilde{\eta}^*)$) is maximized by a halo function, which we call the constrained best fit $\tilde{\eta}^c_{BF}$, with a maximum of $(N+1)$ steps, one of which could occur at $v_{\rm min} = v^*$. This proof applies to $\mathcal{L}_G$ and $\mathcal{L}_G(v^*,\tilde{\eta}^*)$ as well.

5.4 Global Likelihood Analysis of CDMS-II-Si and SuperCDMS data

Here we apply the formalism described in Sec. 5.3 using the global likelihood function in Eq. (5.37) with an extended likelihood [194] for the three events observed by CDMS-II-Si [156], and a 1-bin Poisson likelihood for SuperCDMS [166]. To obtain background estimates for CDMS-II-Si, we take the normalized background distribution functions from [211] and rescale them such that 0.41, 0.13, and 0.08 events are expected from surface events,

neutrons, and ^{208}Pb respectively (see [156]). Since the resolution function for silicon in CDMS-II has not been measured, we take the energy resolution function for germanium from Eq.1 of [210].

In addition to implementing the full SuperCDMS data in Table 1 of [166] (11 events observed, 6.56 expected background events, 577 kg-days of exposure), we also use a subset of the SuperCDMS data which neglects the observed events (and the exposure) from tower 5 (4 events observed, 5.33 expected background events, 412 kg-days of exposure). The SuperCDMS collaboration acknowledges that tower 5 had a malfunctioning guard electrode which resulted in a poor understanding of the background in this tower. We will use the label "SuperCDMSLT5" for this analysis (where LT5 stands for "Less Tower 5").

The data analysis used throughout this paper is included in the CoddsDM software [218], an open-source Python program for the analysis of dark matter direct detection data.

In the left panel of Fig. 5.2 we show the 68% (dark red) and 90% (light red) CL confidence bands, calculated assuming $\Delta L^c_{\rm min}(v^*, \tilde{\eta}^*)$ is χ^2 distributed with one degree of freedom, for the combined analysis of CDMS-II-Si and SuperCDMS, assuming a 9 GeV DM particle scattering elastically off nuclei with a SI isospin-conserving contact interaction. Also shown in Fig. 5.2 is the global $\tilde{\eta}_{BF}$ function (dark red line), the $\tilde{\eta}_{BF}$ function for CDMS-II-Si data alone (blue line), the SuperCDMS 90% upper limit (dark yellow), and the upper and lower boundaries of the 68% (black dashed) and 90% (black solid) CL confidence bands obtained using CDMS-II-Si data alone (these coincide with those presented in Fig. 3 of [92]). Notice that the confidence bands are unbounded from above for $v_{\rm min} \lesssim 275$ km/s and $v_{\rm min} \lesssim 400$ km/s, for the global analyses and CDMS-II-Si analyses respectively (the lower boundaries of the confidence bands

are, however, well defined as $\tilde{\eta}(v_{\rm min})$ is a non-increasing function). This is because $q(v_{\rm min}) = 0$ in these intervals (i.e. the experiment/experiments are not sensitive to recoils imparted from DM traveling at these speeds), and thus the $\tilde{\eta}_{BF}$ is actually undetermined. Since the purpose of plotting these functions is to compare the compatibility of putative and null signals, we extend $\tilde{\eta}_{BF}$ in our plots to this region, in the most conservative way (i.e. constant). The red crosses in Fig. 5.2 represent the 68% CL intervals (vertical bars) of averaged $\tilde{\eta}$ over corresponding $v_{\rm min}$ intervals (indicated by horizontal bars) arising from binning the CDMS-II-Si events into 2 keVnr bins between 7 and 13 keV (see e.g. [175, 177, 182], except we take the horizontal bars to be defined by the $v_{\rm min}$ range where 90% of the area under $\mathcal{R}_{[E'_1,E'_2]}(v_{\rm min})$ is contained).

To determine the all upper bounds on $\tilde{\eta}^0$ arising throughout this paper from the Super-CDMS data, we follow the procedure first outlined in [171, 173]. Using the fact that $\tilde{\eta}^0(v_{\rm min})$ is a non-increasing function, this procedure argues the smallest possible function passing through a point $(v_0, \tilde{\eta}_0)$ is the downward step-function $\tilde{\eta}_0\Theta(v_0 - v_{\rm min})$. With this in mind, Eq. (5.15) can be rewritten such that an upper bound on the observed rate in the energy range $[E'_1, E'_2]$ can be translated into an upper bound $\tilde{\eta}^{\rm lim}(v_{\rm min})$ on $\tilde{\eta}^0$, using

$$\tilde{\eta}^{\rm lim}(v_0) = \frac{R^{\rm lim}_{[E'_1,E'_2]}}{\int_{v_\delta}^{v_0} {\rm d}v_{\rm min}\mathcal{R}_{[E'_1,E'_2]}(v_{\rm min})}\,. \tag{5.45}$$

This limit is conservative in that every $\tilde{\eta}^0$ function lying above the bound is excluded by the data, but not all $\tilde{\eta}^0$ functions lying below the bound are allowed by the data. The values of $R^{\rm lim}$ used in this paper are determined using the Feldman-Cousins approach [219]. Assuming

a Poisson distribution for both SuperCDMS ($n = 11$, $b = 6.56$) and SuperCDMSLT5 ($n = 4$, $b = 5.33$) and an energy range $[E'_1, E'_2]$ corresponding to the quoted experimental range (i.e. $E'_1 = 1.6$ keV and $E'_2 = 10.0$ keV), this leads to 90% CL upper limits on the number of DM events $\mu^{\rm lim}$ of 11.25 and 3.33 events respectively. The value of $R^{\rm lim}$ can then be obtained by dividing $\mu^{\rm lim}$ by the exposure of the relevant experiment.

The global $\tilde{\eta}_{BF}$ function is shifted to lower values of $\tilde{\eta}$ by over an order of magnitude relative to the $\tilde{\eta}_{BF}$ found using CDMS-II-Si data alone, and is outside the 68% and 90% CL confidence bands of CDMS-II-Si alone. Similarly, the $\tilde{\eta}_{BF}$ for CDMS-II-Si alone (in blue) is incompatible with the 68% and 90% Cl global confidence bands. Furthermore, in the range 360 km/s $\lesssim v_{\rm min} \lesssim$ 480 km/s the 68% CL global confidence band has no overlap with the 68% CL confidence band of CDMS-II-Si.

The right panel of Fig. 5.2 is the same as the left panel but using SuperCDMSLT5 instead of SuperCDMS. The global $\tilde{\eta}_{BF}$ function has shifted to slightly lower values of $\tilde{\eta}$ (relative to the SuperCDMS analysis), as have both confidence bands, but the general conclusions are the same – namely, there appears to be a strong level of incompatibility between the results arising from the global likelihood and those found using only CDMS-II-Si data. We also note that the increased conflict between CDMS-II-Si and SuperCDMSLT5 has resulted in the 90% CL confidence band extending down to $\tilde{\eta} \simeq 0$ (i.e. no DM) at low values of $v_{\rm min}$, as opposed to having a well defined non-zero lower boundary for the case of SuperCDMS.

We present one final illustration of this method in Fig. 5.3 for a 3.5 GeV DM particle with exothermic scattering ($\delta = -50$ keV) and a Ge-phobic SI interaction ($f_n/f_p = -0.8$) [180]. This example has been chosen to illustrate how the global $\tilde{\eta}_{BF}$ and confidence bands behave

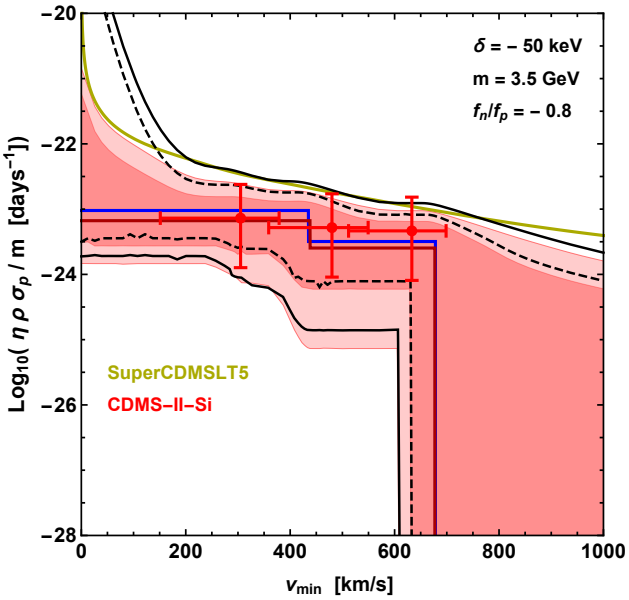

Figure 5.3: Same as the right panel of Fig. 5.2 but for a 3.5 GeV DM particle with exothermic scattering ($\delta = -50$ keV) and a Ge-phobic SI interaction ($f_n/f_p = -0.8$) [180]

in the case of non-conflicting data sets. As expected, the results from the global likelihood analysis of CDMS-II-Si and SuperCDMSLT5 are nearly identical to the results obtained from CDMS-II-Si alone, with the only significant change occurring at low values of v_{min}, where the upper bound of SuperCDMSLT5 is in conflict with the confidence bands of CDMS-II-Si alone.

5.5 Constrained Goodness-of-Fit Analysis

The global likelihood analysis presented in the previous section always produces a best fit halo function and confidence band, even when considering conflicting data sets. A particular goodness-of-fit test has been proposed in [215, 216] to assess the compatibility of different data sets in the framework of a given theoretical model. This so called "parameter goodness-of-fit" (PG) test was used in [138] to gauge the compatibility of CDMS-II-Si, SuperCDMS,

and LUX data, in a halo-independent way. It is defined as

$$q_{PG} \equiv -2 \left(\ln \hat{\mathcal{L}}_{\rm G} - \sum_{\alpha} \ln \hat{\mathcal{L}}_{\alpha} \right) , \tag{5.46}$$

where $\hat{\mathcal{L}}_{\rm G}$ is the maximum of the global likelihood and $\hat{\mathcal{L}}_{\alpha}$ is the maximum of the likelihood of experiment α. If the $\tilde{\eta}_{BF}$ of all individual experiments would coincide, then $q_{PG} = 0$. On the other hand a strong disagreement between the $\tilde{\eta}_{BF}$ of individual experiments would lead to a large value of q_{PG}. Thus q_{PG} quantifies the degree of compatibility of all data sets under the assumption of a particular DM particle model. To provide a quantitative statement about the compatibility, the p-value of the observed data was obtained from a MC simulation, assuming the global $\tilde{\eta}_{BF}$ is the true halo model [138]. This procedure assigns a single number, a single p-value, to the whole halo-independent parameter space, and we would like to identify regions of this space where $\tilde{\eta}(v_{\rm min})$ functions may lead to better or worse compatibility among data sets. With this purpose in mind, we define a family of test statistics similar to q_{PG}, one for each point in parameter space, using the profile likelihood, defined as the likelihood maximized subject to the constraint in Eq. (5.32), i.e. $\tilde{\eta}(v^*) = \tilde{\eta}^*$ (it is the continuum limit of the numerator inside the square bracket in Eq. (5.35)). We will then define a p-value for every point in the halo independent parameter space. We define the "constrained parameter goodness-of-fit" test statistic as

$$q^c_{PG}(v^*, \eta^*) \equiv -2 \left(\ln \hat{\mathcal{L}}^c_{\rm G}(v^*, \tilde{\eta}^*) - \sum_{\alpha} \ln \hat{\mathcal{L}}^c_{\alpha}(v^*, \tilde{\eta}^*) \right) , \tag{5.47}$$

where $\hat{\mathcal{L}}^c_G(v^*, \tilde{\eta}^*)$ is the global profile likelihood and $\hat{\mathcal{L}}^c_\alpha(v^*, \tilde{\eta}^*)$ is the profile likelihood of experiment α. q^c_{PG} tests the compatibility of the different data sets under the assumption that $\tilde{\eta}(v_{\min})$ passes through $(v^*, \tilde{\eta}^*)$. To infer the probability distribution for $q^c_{PG}(v^*, \tilde{\eta}^*)$ we use a Monte Carlo simulation, assuming the true halo model is given by the global best fit halo function that maximizes $\mathcal{L}_{\rm G}$ under the constraint $\tilde{\eta}(v^*) = \tilde{\eta}^*$. We call "constrained best fit halo function" $\tilde{\eta}^c_{BF}$ the function that maximizes a likelihood subjected to this constraint. There is a different $\tilde{\eta}^c_{BF}(v_{\min})$ function for each $(v^*, \tilde{\eta}^*)$ point (which certainly fulfills the condition $\tilde{\eta}^c_{BF}(v^*) = \tilde{\eta}^*$), one for the global likelihood and one for each single experiment extended likelihood. The p-value for a given $(v^*, \tilde{\eta}^*)$ is then obtained by comparing the observed value of q^c_{PG} to the distribution constructed from $\mathcal{O}(10^3)$ simulated data sets (for each choice of $(v^*, \tilde{\eta}^*)$).

We have only developed a method for maximizing the Poisson and Gaussian likelihoods subject to the constraint $\tilde{\eta}(v^*) = \tilde{\eta}^*$ for a single bin Poisson/Gaussian likelihood. In this case, the likelihood is maximized by an expected number of dark matter events $\hat{\nu}_1^{(\alpha)}$, where either $\hat{\nu}_1^{(\alpha)} = n_1^{(\alpha)} - b_1^{(\alpha)}$ if $n_1^{(\alpha)} \geq b_1^{(\alpha)}$, or $\hat{\nu}_1^{(\alpha)} = 0$ if $n_1^{(\alpha)} \leq b_1^{(\alpha)}$. In order to maximize the constrained likelihood, one needs to consider whether v^* lies above or below the experimental threshold. If v^* is below threshold, a halo function passing through $(v^*, \tilde{\eta}^*)$ produces a minimum number of 0 observed events (with $\tilde{\eta} = \tilde{\eta}^* \Theta(v^* - v_{\min})$), and a maximum number $\nu_{\max}$ of events given by the flat halo function $\tilde{\eta}(v_{\min}) = \tilde{\eta}^*$. If v^* is above threshold, a halo function passing through $(v^*, \tilde{\eta}^*)$ produces a minimum number $\nu_{\min}$ of observed events when $\tilde{\eta} = \tilde{\eta}^* \Theta(v^* - v_{\min})$, and there is no limit on the maximum number of observed events because $\tilde{\eta}$ can be unbounded from above for $v_{\min} < v^*$. If $\hat{\nu}_j^{(\alpha)}$ lies between the minimum and

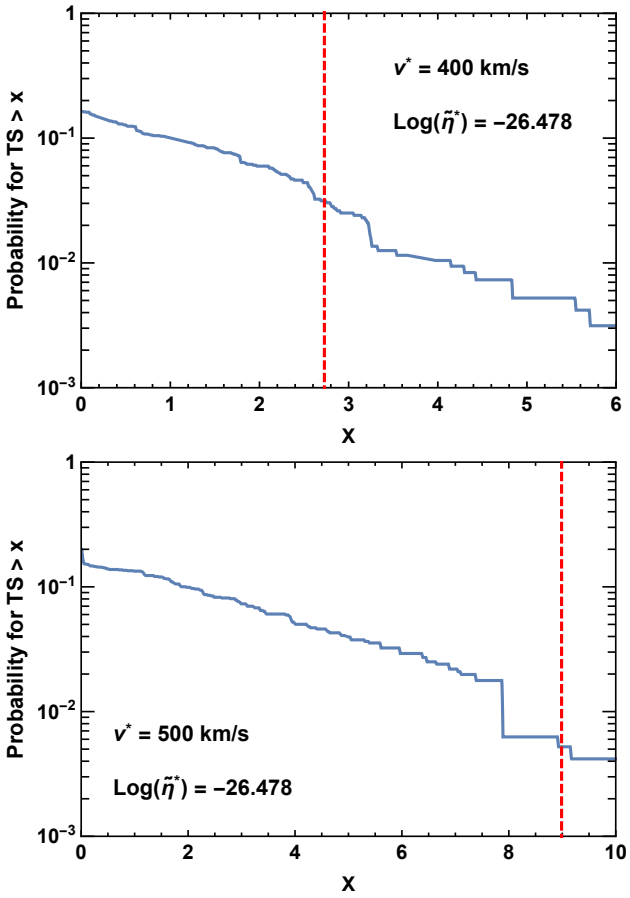

Figure 5.4: Monte Carlo generated distribution for q^c_{PG} for $v^* = 400$ km/s (left) and 500 km/s (right) and $\log(\tilde{\eta}^*) = -26.478$. Observed value of q^c_{PG} shown with red dashed line.

maximum number of predicted events for $\tilde{\eta}(v_{\rm min})$ passing through $(v^*, \tilde{\eta}^*)$ in each case, then the maximum of the constrained likelihood is the maximum of the likelihood. Otherwise, the maximum of the constrained likelihood is calculated using $\nu_{\rm max}$ or $\nu_{\rm min}$, depending on the respective case above.

The probability distributions of q^c_{PG} are shown in Fig. 5.4 for the combination of CDMS-II-Si and SuperCDMSLT5, for a SI contact interaction with $(m, \delta, f_n/f_p) = (9\ \text{GeV}, 0\,\text{keV}, 1)$, for $v^* = 400$ km/s (left) and 500 km/s (right) with $\tilde{\eta}^*$ chosen on the global $\tilde{\eta}_{BF}$ curve. The observed value of q^c_{PG} in Fig. 5.4 are indicated by the dashed red line. The p-values roughly correspond to 2.8% for $v^* = 400$ km/s, and 0.5% for $v^* = 500$ km/s. While the probability distributions shown in Fig. 5.4 do not appear to approach 1 in the limit $x \to 0$, there are in fact a large number of simulations which yield extremely small values of q^c_{PG} that are not depicted (the probabilities do in fact equal 1 at $x = 0$). This happens because the global best fit halo function predicts less than one observed event in CDMS-II-Si, which leads to many simulations in which 0 events are observed by CDMS-II-Si. In turn, this implies the global constrained best fit halo function and the constrained best fit halo function for CDMS-II-Si are the same, as they can only have a single step at the location of $(v^*, \tilde{\eta}^*)$. For SuperCDMSLT5, the expected background is larger than the number of observed events, and thus the profile likelihood of SuperCDMSLT5 is relatively insensitive to halo functions that predict small numbers of DM events. Consequently, it is not uncommon to find $\ln \hat{\mathcal{L}}^c_{\rm G}(v^*, \tilde{\eta}^*) \simeq \sum_\alpha \ln \hat{\mathcal{L}}^c_\alpha(v^*, \tilde{\eta}^*)$.

Fig. 5.4 already demonstrates a high level of incompatibility between the CDMS-II-Si and SuperCDMSLT5 data sets for the assumed WIMP candidate, because the global $\tilde{\eta}_{BF}(v_{\rm min})$

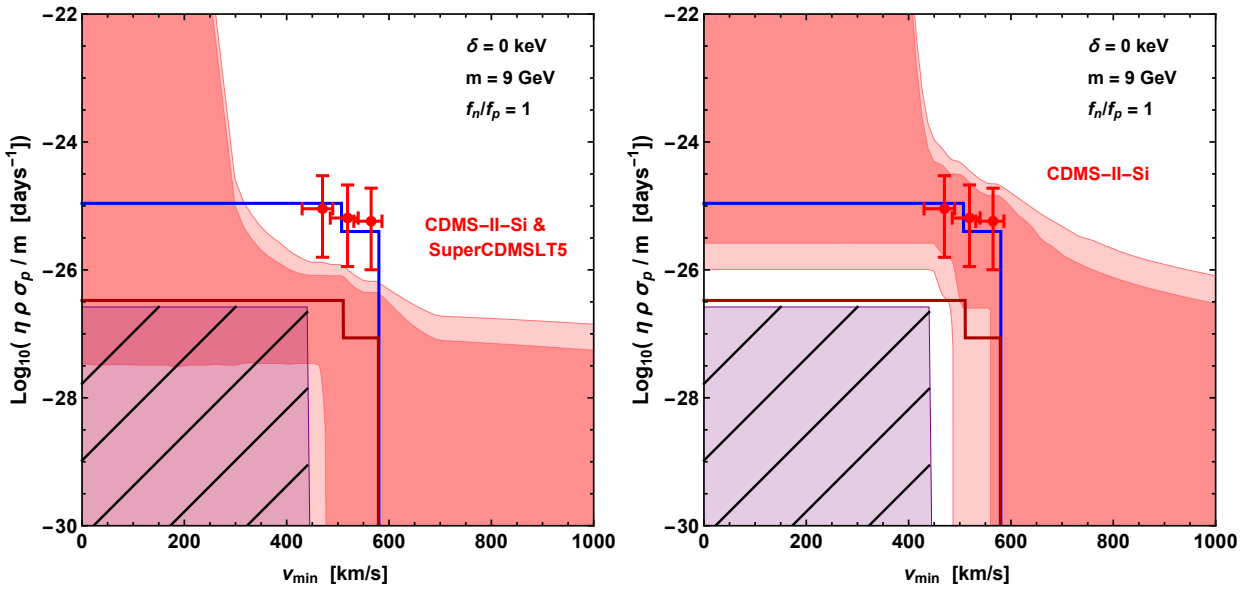

Figure 5.5: Plausibility region (light purple) generated from the constrained parameter goodness-of-fit test statistic for CDMS-II-Si and SuperCDMSLT5 (p-value larger than 10%), compared with the confidence bands (red shaded) generated for CDMS-II-Si data alone (left) [92] and the global confidence bands (red shaded) constructed in Sec. 5.4 (right). The plausibility regions are crossed over because halo functions entirely contained within these regions are not necessary allowed by our test, i.e. do not necessarily lead to a compatibility of the data sets at the level of p >10%. However, for any halo function not entirely contained within the plausibility region the data sets are incompatible at the chosen level (p <10%). Also shown are $\tilde{\eta}_{BF}$ for CDMS-II-Si alone (blue), the $\tilde{\eta}_{BF}$ resulting from the global likelihood analysis (dark red), and the v_{min}-averaged CDMS-II-Si data (crosses) as described in Sec. 5.4.

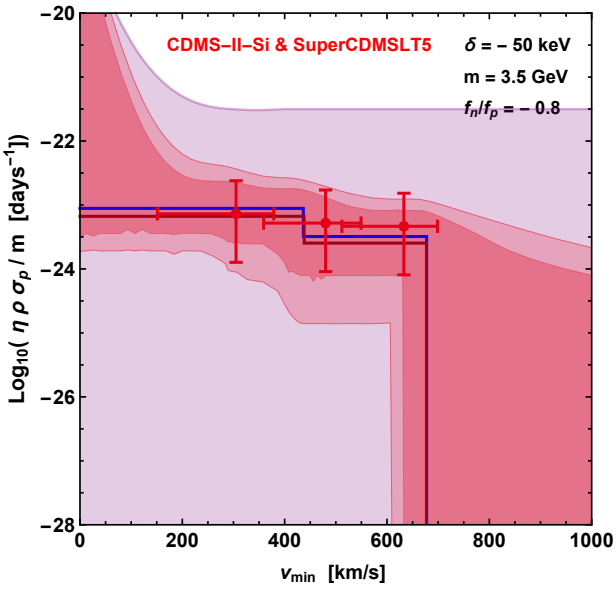

Figure 5.6: Same as the right panel of Fig. 5.5 but for a 3.5 GeV DM particle with exothermic scattering ($\delta = -50$ keV) and a Ge-phobic SI interaction ($f_n/f_p = -0.8$) [180] (as in Fig. 5.3). Halo functions $\tilde{\eta} v_{\mathrm{min}}$ entirely contained within the plausibility region (light purple) lead to a compatibility of the data sets at the chosen level (p >10%). For those not entirely contained within the plausibility region the data sets are incompatible at the chosen level (p <10%).

cannot produce a large p-value, say larger than 10%. We can construct intervals at each $v_{\mathrm{min}} = v^*$ in which the probability of obtaining a q^c_{PG} value larger than the one observed is $\geq 10\%$. By joining these intervals we build regions in $(v_{\mathrm{min}}, \tilde{\eta})$ which are referred to as "plausibility" regions.

Let us now clarify the meaning of the plausibility regions. A halo function $\tilde{\eta}(v_{\mathrm{min}})$ is a non-increasing continuous function which must be defined for any value of v_{min}. Consequently, any halo function not entirely contained within the plausibility region passes though points with $p < 10$ %, and thus for these functions the data sets are incompatible at the chosen level ($p < 10\%$). However, halo functions that are entirely contained within a plausibility region are not necessarily allowed by our test, i.e. do not necessarily lead to compatibility of all data at the chosen level. The issue is that the true halo model adopted at each point within

a plausibility region, namely the $\tilde{\eta}^c_{BF}$ of the profile global likelihood at each point, may also pass through points outside the plausibility region and be rejected by our test. If so, the p-value evaluation at the particular point in the plausibility region is inconsistent. This is the case for all points in the plausibility regions (light purple) shown in Fig. 5.5. The regions are crossed by thin black lines to indicate that halo functions entirely contained within them are not guaranteed to lead to compatibility of the data sets. However, if the true halo model adopted at all points within a plausibility region are entirely contained within it, the p-value calculation is reliable and halo functions entirely contained with this region are allowed by our test. This is the case of the plausibility region in Fig. 5.6 (shown in light purple).

The plausibility region for $p \geq 10\%$ arising from the constrained parameter goodness-of-fit test for the combination of CDMS-II-Si and SuperCDMSLT5 (light purple region) is compared in Fig. 5.5 to the confidence bands (red shaded regions) generated from the global likelihood described in Sec. 5.4 (right panel) and the confidence bands generated with CDMS-II-Si data alone (left panel). Also shown are the global best fit halo function $\tilde{\eta}_{BF}$ (dark red) and the best fit halo function for CDMS-II-Si alone (blue). The left panel of Fig. 5.5 shows that there does not exist a halo function in the CDMS-II-Si confidence bands that can describe the compatibility of the observed data sets. Not all halo functions contained within the 90% global confidence band in the right panel of Fig. 5.5 are excluded by the plausibility region, but the 68% region is entirely excluded, as is the global best fit halo function. As explained above the plausibility regions are crossed over because the functions entirely included within them are not allowed by our test (while those passing through points outside them are rejected). By contrast, we can see in Fig. 5.6 how the plausibility region

includes the entire global confidence bands (as well as the bands for CDMS-II-Si alone, which in this case are nearly identical, see Fig. 5.3) in the case of non-conflicting data sets. This is the example of a 3.5 GeV DM particle with exothermic scattering ($\delta = -50$ keV) and a Ge-phobic SI interaction ($f_n/f_p = -0.8$) [180]. The plausibility region provides in this case a further indication of compatibility of the CDMS-II-Si and SuperCDMSLT5 data sets for this particular DM particle model, besides the near complete overlap of the global and single experiment confidence bands.

A comment is in order regarding Fig. 5.6. While generating the probability distributions at large values of $\tilde{\eta}$ and $v_{\rm min}$ (above the 90% CL band), we found the predicted number of events in both experiments was too large for our computational methods to work. We resorted to using a nearest-neighbor extrapolation at fixed $v_{\rm min}$ to generate the probability distributions in this region. We found that in this region of the $v_{\rm min} - \tilde{\eta}$ plane, the probability distribution changes slowly with respect to the observed value of q^c_{PG}, and thus we believe we obtained a good estimate of the upper boundary of the plausibility region. This extrapolation was only used above the 90% CL confidence band boundary.

5.6 Summary

In this paper we have presented two distinct methods to assess the joint compatibility of data sets for a given DM particle model across halo-independent parameter space, using a global likelihood consisting of at least one extended likelihood and an arbitrary number of Gaussian or Poisson likelihoods. We have illustrated these methods by applying them to CDMS-II-Si and SuperCDMS data, assuming WIMP candidates with SI contact interactions.

The first method is a natural extension of the procedure presented in [92], in which a best fit halo function and pointwise confidence band are constructed from the profile likelihood ratio. Here we have proven that the best fit halo function $\tilde{\eta}_{BF}$ for the global likelihood we studied is a piecewise constant function with the number of steps at most equal to the number of unbinned data points plus the number of data bins in all the single likelihoods, and argued why in practice the number of steps is smaller than this maximum number (see Section 3 and Appendix A). A best fit piecewise constant halo function had already been found in the literature (see [138]) for a global likelihood of the type we use, but as a curiosity without any explanation (or proof of uniqueness). In addition to showing how to find the best fit halo function $\tilde{\eta}_{BF}$ and that this function is unique (see Appendix B), here we have shown for the first time how to construct two-sided confidence bands at any CL for the type of global likelihood we studied. As an illustration of the method we have found the best fit halo function and the 68% and 90% CL confidence bands assuming two different choices for the DM particle model parameters m, δ, and f_n/f_p. The choice of a 9 GeV DM particle scattering elastically ($\delta = 0$) with an isospin-conserving coupling ($f_n/f_p = 1$) leads to an apparent incompatibility between the observed CDMS-II-Si events and the SuperCDMS upper limit, in agreement with previous published results (see e.g. [92, 182]). This incompatibility can be assessed by comparing the overlap or lack thereof of the global confidence bands with those of CDMS-II-Si alone. As shown in Fig. 5.2, at the 68% CL, it is not possible to find a halo function passing through both confidence bands. The situation is very different for a 3.5 GeV DM particle with exothermic scattering ($\delta = -50$ keV) and a Ge-phobic SI interaction ($f_n/f_p = -0.8$) [180], for which the data sets are compatible. As shown in Fig. 5.3

the global and CDMS-II-Si alone confidence bands practically coincide.

The drawback of this method is that it cannot provide a quantitative measurement of the level of incompatibility of the various data sets that comprise the global likelihood. To address this concern, we have proposed in Section 5 a second method in which we construct a "plausibility region" arising from the global likelihood, using an extension of the parameter goodness-of-fit test [138, 215, 216], that we refer to as the "constrained parameter goodness-of-fit" test. By evaluating the ratio of the global profile likelihood and the product of the individual profile likelihoods (assuming $\tilde{\eta}(v^*) = \tilde{\eta}^*$), a plausibility region can be constructed by grouping together regions of parameter space for which, at each point $(v^*, \tilde{\eta}^*)$, our observed test statistic has a p-value e.g. $\geq 10\%$. This p-value was determined using a probability distribution constructed with Monte Carlo generated data assuming the true halo function is the constrained best fit $\tilde{\eta}^c_{BF}$ of the profile global likelihood, i.e. the halo function that maximizes the global likelihood subject to the constraint $\tilde{\eta}(v^*) = \tilde{\eta}^*$. For any halo function not entirely contained within this plausibility region the data are incompatible for the assumed DM particle model at the assumed level (e.g. $p < 10\%$). For halo functions entirely contained within the plausibility region the data sets are compatible at the chosen level only if the contained best fit at each point within the region are also entirely contained within the region. We have demonstrated this method for a 9 GeV DM particle scattering elastically with an isospin conserving coupling and for the aforementioned Ge-phobic particle candidate. The results are shown in Figs. 5.5 and 5.6 respectively. In the first case the confidence bands are largely outside the plausibility region, while in the second case the confidence bands are entirely included in the plausibility region and any halo function

entirely contained within the plausibility region lead to a compatibility of the data sets at the chosen level ($p > 10\%$).

Together these two methods provide complementary assessments of the compatibility of the data given a particular dark matter model, across the $v_{\rm min}-\tilde{\eta}$ halo-independent parameter space. We expect these tools to prove useful for future direct dark matter searches both to test compatibility of different data sets as to provide a guidance of which type of halo functions provide a better or worse compatibility of all the data.

6 Gamma Rays From Dark Matter Subhalos Revisited: Refining the Predictions and Constraints

6.1 Introduction

A wide range of experimental strategies are being pursued in an effort to observe dark matter's non-gravitational interactions and ultimately identify the particle nature of dark matter. This program includes but is not limited to experiments designed to detect the scattering of dark matter with nuclei, searches for the annihilation or decay products of dark matter, and efforts to produce and observe dark matter at accelerators. In all three of these areas, current experiments are probing important regions of parameter space and are sensitive to a wide range of well motivated dark matter candidates.

Particularly promising are searches for dark matter utilizing gamma-ray telescopes. Constraints from the Fermi Gamma-Ray Space Telescope's observations of dwarf spheroidal galaxies [220,221], the Galactic Center [222] and the extragalactic gamma-ray background [223, 224], are each currently sensitive to dark matter particles with masses in the range of ∼10-100 GeV and annihilation cross sections similar to that naively predicted from thermal relic abundance considerations, $\sigma v \simeq 2 \times 10^{-26}$ cm^3/s. Furthermore, the excess of GeV-scale gamma rays observed from the region surrounding the Galactic Center exhibits a spectrum and morphology that is consistent with the predictions of dark matter particles with a mass of $\sim 30 - 60$ GeV and an annihilation cross section of $\sigma v \sim 10^{-26}$ cm^3/s [225–234] (for discussions of other interpretations, see Refs. [235–244]).

Within the standard paradigm of cold and collisionless dark matter, structure forms

hierarchically, meaning that the smallest halos form first and gradually merge to form larger systems, including the halos that host galaxies and galaxy clusters [245]. As a consequence of this process, the dark matter halos that encompass galaxies are predicted to contain large numbers of smaller subhalos.

In the case of the Milky Way, the largest and most massive subhalos include the known dwarf galaxies, as well as the Large and Small Magellanic Clouds. This collection of very massive objects reflects only a small fraction of the subhalo population, however. A much larger number of subhalos that are too small to capture significant quantities of gas and form stars are also expected to be present, while remaining invisible to surveys at optical and other wavelengths. If dark matter particles annihilate with a cross section that is similar to that naively predicted for a thermal relic, nearby subhalos could be a promising target for gamma-ray telescopes [246–265].

The most recent catalog released by the Fermi Collaboration (the 3FGL) contains 992 gamma-ray sources that have not been associated with emission observed at other wavelengths [266], a small fraction of which could potentially be dark matter subhalos. Recent studies of the 3FGL identified a subset of 19 bright ($\Phi_\gamma > 7 \times 10^{-10}$ cm^{-2} s^{-1}, $E_\gamma > 1$ GeV) and high-latitude ($|b| > 20^\circ$) sources that show no evidence of variability and exhibit a spectral shape that is consistent with the predictions of annihilating dark matter [246, 247]. From the characteristics of these subhalo candidate sources, limits can be derived on the dark matter annihilation cross section. Such limits, however, can vary significantly depending on the assumptions that are made regarding the local abundance of dark matter subhalos and on the spatial distribution of dark matter within these systems. For example, the limits on

the dark matter's annihilation cross section placed in Ref. [246] and Ref. [248] differ by a factor of a few for most dark matter masses. Actually, there are a number of significant differences between the analyses of Ref. [246] and Ref. [248] which mitigate their apparent disagreement. Specifically, the mass range analyzed by Ref. [248] extends 2-3 orders of magnitude above what was used in Ref. [246], and the density profiles and halo-to-halo variations used in Ref. [246] predict significantly higher gamma-ray fluxes for the same mass subhalos. The various assumptions entering each of these analyses seem at face value to be quite reasonable. Consider, for example, the density profiles used to characterize the local subhalo population. The authors of Ref. [246] adopted density profiles that are described by an Einasto profile, tidally truncated to remove the outermost 99.5% of a given subhalo's mass, Ref. [248] chose instead to adopt a traditional NFW density profile, with concentrations chosen to match the parameters of a given subhalo identified within the Via Lactea II simulation. In reality, however, it is likely that the true population of nearby subhalos is not particularly well described by either of these simple halo profile parameterizations.

Ref. [265] has also recently performed a more comprehensive assessment of how various uncertainties associated with the subhalo distribution and parameterization may effect their observability with gamma-ray telescopes. In light of the large variability that is produced from seemingly reasonable assumptions, it has become clear that a focused and self-consistent analysis of the local subhalo population is necessary before reliable statements can be made regarding subhalo detectability.

In this paper, we revisit the characteristics of the local dark matter subhalo population, basing our analysis on the properties of the subhalos identified within the cosmological

simulations Via Lactea II and ELVIS. We find that the simulated subhalos in the local region of the Milky Way are generally well characterized by power-law density profiles with an exponential cutoff. Using this profile parameterization, and accounting for halo-to-halo variations as determined by the distribution of simulated subhalos, we estimate the number of subhalos that could be observed by the Fermi Large Area Telescope (Fermi-LAT) and use this information to place constraints on the dark matter's annihilation cross section. We also calculate the fraction of the observable subhalos that will be spatially extended at a level potentially discernible to experiments such as Fermi, providing us with a way of discriminating a dark matter subhalo population from a collection of point-like gamma-ray sources.

6.2 Subhalo Populations in Cosmological Simulations

Various groups have utilized Fermi's catalog of unassociated gamma-ray sources to derive limits on the dark matter annihilation cross section [246, 248, 249, 267]. The results of these studies, however, vary considerably depending on the assumed characteristics of the local subhalo population. Among the least understood characteristics, is the response of the subhalo density profile to extreme tidal forces.

There have been numerous attempts to study the intimate details of the subhalo radial density profile (e.g. see [264, 268–286] for an incomplete list). Specifically, these studies have largely focused on using either high-resolution simulations or semi-analytic tools to study the process by which tidal forces of the host halo disrupt the subhalo's density distribution. By analyzing the distribution of test particles within the tidally disrupted subhalos, various

groups (see e.g. [271, 272, 280]) have derived modified profiles, often taken to be extensions of the canonical NFW profile, that characterize the resolved subhalo profile as a function of e.g. mass, location, orbit, merger history, etc.

More recently, attempts have been made to simplify the characterization of these subhalos for the more practical purpose of implementing these modifications into calculations. For example, Ref. [286] attempted to characterize the subhalo population identified in the Via Lactea II and ELVIS simulations using an NFW profile, but with concentration parameters that were dependent on both the subhalo mass (or maximum circular velocity) and the location of the subhalo relative to the host center. This was done for the purpose of calculating boost factors.

Here in Sec. 6.2, we take a similar approach to [286], in that we adapt a more generalized parameterization of subhalos identified in the Via Lactea II and ELVIS simulations for the purpose of assessing the impact that tidal stripping has on the observability of subhalos. The primary difference between our approach to characterizing these subhalos and that of [286], is that we relax the assumption that tidally stripped halos are well-described by an NFW profile, and instead attempt to parametrize density distributions with a mass and location dependent profile. Thus, by deriving subhalo characteristics and distributions from a fixed set of simulations, we attempt here to provide a more self-consistent and reliable description of the observability of dark matter subhalos.

6.2.1 The Via Lactea II and ELVIS Simulations

In an effort to characterize the population of dark matter subhalos located within the local volume of the Milky Way, we utilize the publicly available data from the Via Lactea II (VL-II) [287] and ELVIS [288] cosmological simulations. The VL-II simulation contains over 1 billion particles, each with a mass of $4.1 \times 10^3 M_\odot$, and identifies approximately $20,000$ subhalos with a maximum circular velocity, $v_{c,\rm max}$, greater than 4 km/s. Since we are interested here in subhalos residing within Milky Way-like halos, we have chosen to restrict our attention to those subhalos that are located within 300 kiloparsecs (kpc) of the center of the host halo. Furthermore, in order to minimize the impact of thresholds and other ambiguities associated with subhalo identification and characterization, we limit our analysis to those subhalos that consist of 100 or more particles. These cuts reduce the number of VL-II subhalos used in our analysis to $5,268$.

The ELVIS suite consists of 48 simulated halos, each comprised of at least 53 million particles with masses of $1.9 \times 10^5 M_\odot$. Half of these simulations are of paired galaxies, intended to be representative of the Milky Way-Andromeda system in both mass and phase space. Three high-resolution simulations were performed on isolated halos (in addition to the aforementioned 48) with a particle mass of $2.35 \times 10^4 M_\odot$. In our analysis, we consider those subhalos that are comprised of at least 100 particles and with $v_{c,\rm max} > 8$ km/s in the paired and isolated simulations, and $v_{c,\rm max} > 4$ km/s in the high-resolution simulations. As with VL-II, we have restricted our attention to subhalos that are located within 300 kpc of the nearest host halo's center, leaving us with a total of $26,048$ subhalos from among the suite of ELVIS simulations.

For each subhalo found in either simulation catalogue, we extract $v_{c,\max}$, the radius at which maximum circular velocity occurs, $R_{v,\max}$, and the total gravitationally bound mass (each evaluated at $z = 0$). It is well known that the velocity profiles and concentrations of the subhalos extracted from dark matter simulations depend on the precise values of the adopted cosmological parameters. Ref. [289] derived a scaling relation for $R_{v,\max}$ (at fixed $v_{c,\max}$) on the cosmological parameters σ_8 and n_s, based on the results of various cold DM simulations. Specifically, they found the following:

$$R_{v,\max} \propto (\sigma_8 \, 5.5^{n_s})^{-1.5} \, . \tag{6.1}$$

Since the cosmological parameters adopted by VL-II and ELVIS are based on WMAP-3 ($\sigma_8 = 0.74$, $n_s = 0.951$) and WMAP-7 ($\sigma_8 = 0.80$, $n_s = 0.963$), respectively, we have rescaled both to the latest results from the Planck Collaboration ($\sigma_8 = 0.82$, $n_s = 0.967$) [32].

6.2.2 The Dark Matter Profiles of Simulated Subhalos

Here, we investigate the distribution of dark matter in subhalos identified within the VL-II and ELVIS simulations. Specifically, for each subhalo, we considered various parameterizations of the density profile and determined which can provide good agreement with the simulated values of $v_{c,\max}$, $R_{v,\max}$, and the total gravitationally bound mass.[11]

After determining that the subhalo profile parameterizations adopted in both Refs. [246, 249] and Ref. [248] provide poor fits to the subhalos located near the center of the host halo,

[11] Although we would ideally like to extract information for the $r < R_{v,\max}$ region of a given subhalo, statistical limitations make this impractical in most cases. We focus here on the values of the more reliably determined quantities, $v_{c,\max}$, $R_{v,\max}$, and $M_{\rm tot}$.

we further considered a doubly-generalized NFW profile of the following form:

$$\rho(r) = \frac{\rho_s}{\left(\frac{r}{r_s}\right)^{\gamma_1} \left(\frac{r}{r_s} + 1\right)^{\gamma_2}}, \tag{6.2}$$

where the case of a canonical NFW profile is recovered for $\gamma_1 = 1$ and $\gamma_2 = 2$. For those subhalos located in the outer regions of a host halo, we found that this parameterization could in most cases be tuned to match the characteristics found in the simulations. But for subhalos located within the innermost few tens of kiloparsecs of their host halo, we found that this class of profile shapes could generally *not* simultaneously accommodate both the mass contained within $R_{v,\rm max}$ (i.e. $M(< R_{v,\rm max})$) and the total mass, $M_{\rm tot}$, of the subhalo (for any profile with $\gamma_1 > 0$). We attribute the inability of the doubly-generalized NFW profile to describe these subhalos to the effects of tidal stripping, which are more pronounced in high density environments.

Next, inspired by Ref. [272] (see also Ref. [278]), we considered the following density profile for the local population of tidally truncated subhalos:

$$\rho(r) = \frac{\rho_0}{r^\gamma} \exp\left(-\frac{r}{R_b}\right). \tag{6.3}$$

For nearly all of the simulated subhalos considered in this analysis, we are able to identify choices of γ and R_b that can simultaneously accommodate the reported values of both $M(< R_{v,\rm max})$ and $M_{\rm tot}$.

Our goal in this work is to identify the properties and distributions of the local subhalo population. Unfortunately, there are simply not enough subhalos in the inner tens of kilo-

parsecs to meaningfully extract properties exclusively from this sample. We approached this problem by identifying trends in the behavior of γ and R_b as functions of the total subhalo mass and the distance to the center of the host halo. This was accomplished by dividing subhalos into four mass bins, and then dividing each mass bin into four bins that differentiate halos by their distance to the Galactic Center. Bin sizes were chosen in such a way that each bin contains an approximately equal number of subhalos. Scatter plots of these best-fit values are shown in Figs. 6.1 and 6.2.

As the result of tidal stripping, one can see in Fig. 6.2 that the average value of R_b decreases with proximity to the center of the host halo. This result is consistent, for example, with the recent findings of Ref. [286] (see also e.g. [271, 280]). Perhaps less anticipated is that the average inner slope, γ, is also found to be lower for those subhalos located near the Galactic Center.

To parameterize the distribution of the values of γ at Earth's location, we adopt a generalized normal distribution:

$$\frac{dP}{d\gamma} = \frac{1}{\sqrt{2\pi}} \frac{1}{\sigma - \kappa(\gamma - \langle\gamma\rangle)} \exp\left(- \frac{\ln^2(1 - \kappa(\gamma - \langle\gamma\rangle)/\sigma)}{2\kappa^2} \right), \tag{6.4}$$

where $\langle\gamma\rangle$ is the median value of γ, and σ and κ are parameters which jointly characterize the width and skew of the distribution [12]. Note that this distribution is defined on the domain $\gamma < \sigma/\kappa + \langle\gamma\rangle$. For each bin in subhalo mass and Galactic Center distance, we find the values of $\langle\gamma\rangle$, σ and κ which provide the best fit to the simulated dataset. Examples of the

[12] For clarification, the width and skew are *not* characterized by σ and κ, respectively, but rather are more complicated functions of both of these parameters.

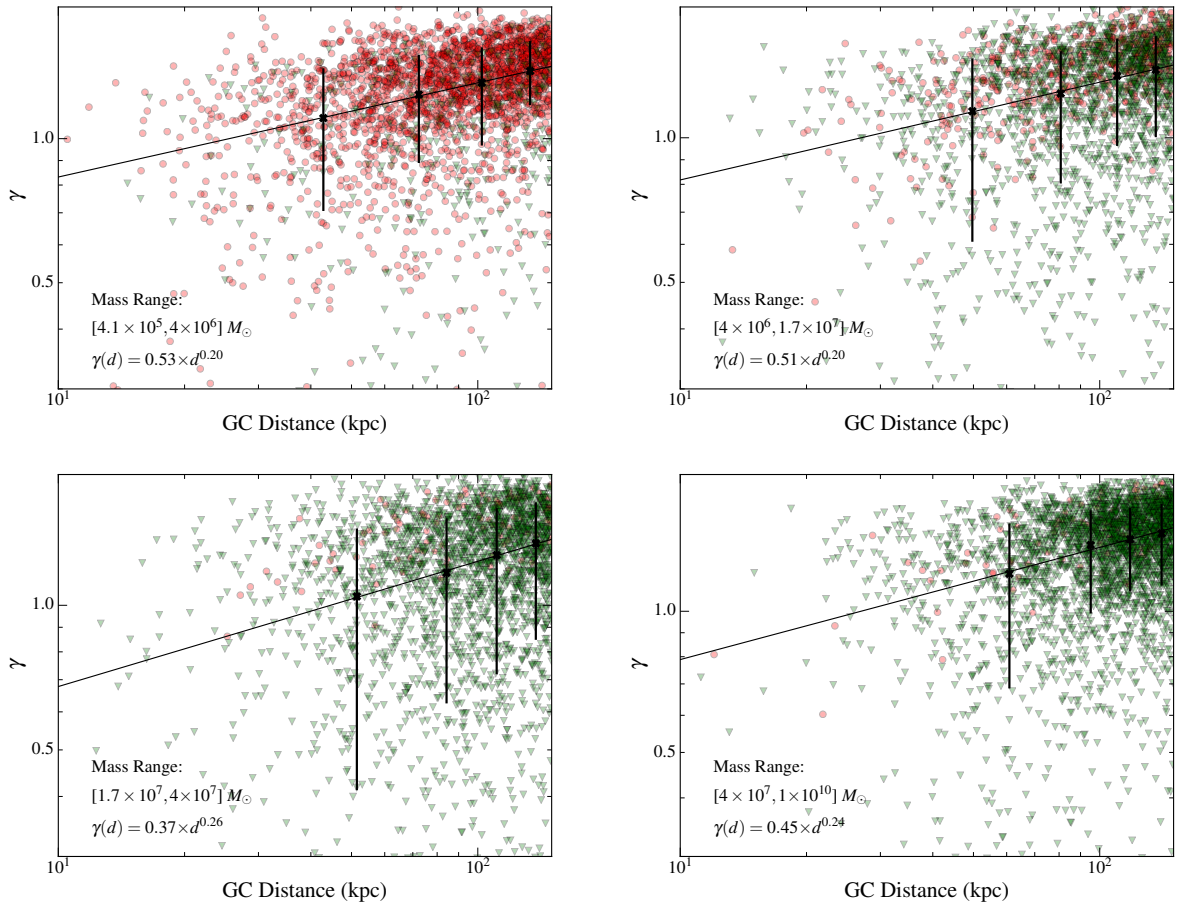

Figure 6.1: The best-fit values found for the inner slope, γ, for subhalos in the Via Lactea-II (red circles) and ELVIS simulations (green triangles), adopting a profile of the form $\rho(r) = \rho_0\, r^{-\gamma} \exp(-r/R_b)$. Results are presented as a function of the distance of the subhalo to the center of the host halo, with each frame corresponding to subhalos in a different mass range. The solid line denotes the power-law trend for the median value of this parameter (the equations for which are given in each panel, denoted $\gamma(d)$), while the error bars depict the range of values found among the central 68% of subhalos in each of four distance bins.

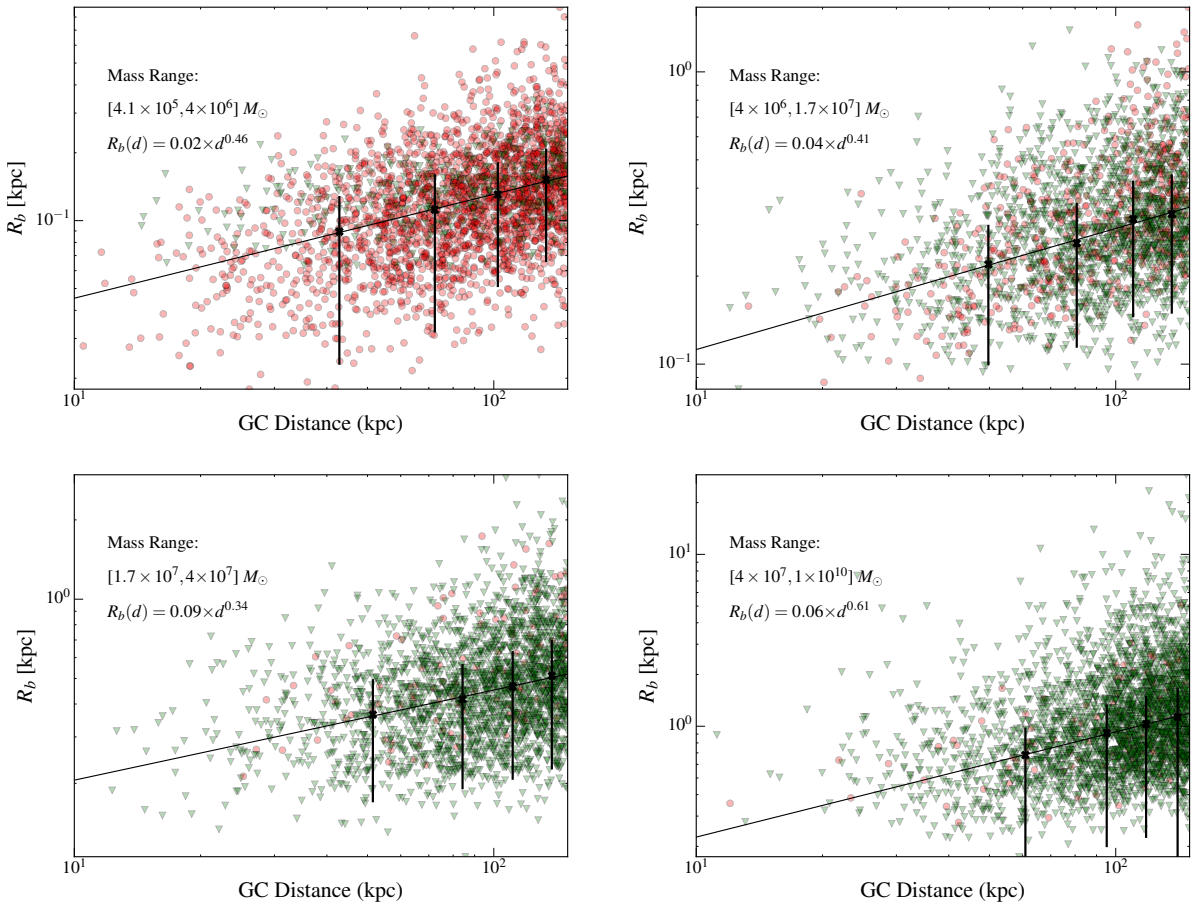

Figure 6.2: As in Fig. 6.1, but for the parameter R_b, where $\rho(r) = \rho_0\, r^{-\gamma} \exp(-r/R_b)$. As a result of tidal stripping, the average value of R_b decreases with proximity to the center of the host halo. In each bin, we display the median best fit value of R_b, i.e. $\langle R_b \rangle$, and 68% containment region for each bin (denoted with a black 'x' and vertical black lines respectively). The power law fit used to extrapolate the median R_b values is shown in each panel, and is denoted $R_b(d)$.

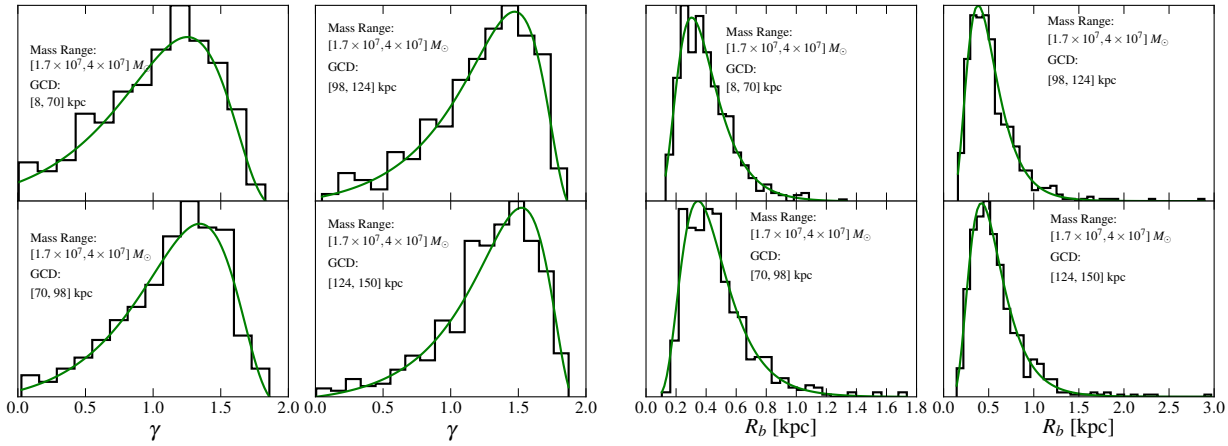

Figure 6.3: The distribution of the inner slope (left) and exponential scale radius (right) for subhalos in the ELVIS and Via Lactea II simulations, for subhalos with masses in the range of $(2-5)\times10^7 M_\odot$ and at various distances from the Galactic Center (GCD). The green line in each frame depicts the best-fit generalized normal (left) or lognormal (right) distribution.

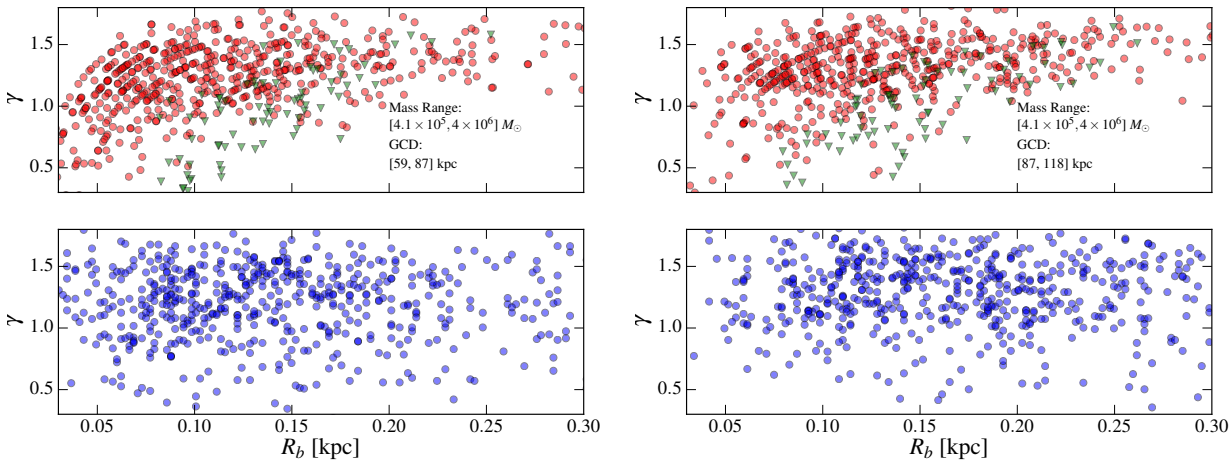

Figure 6.4: Comparison of best-fit parameters (top) γ and R_b to VL-II (red circles) and ELVIS subhalos (green triangles) and 'fake' subhalos (bottom, blue) derived using random draws from Eq. (6.5) and Eq. (6.4). Analysis is shown for subhalo masses between 4.1×10^5 and $4\times10^6 M_\odot$, and for GCD ranges $[59, 87]$ kpc (left) and $[87, 118]$ kpc (right).

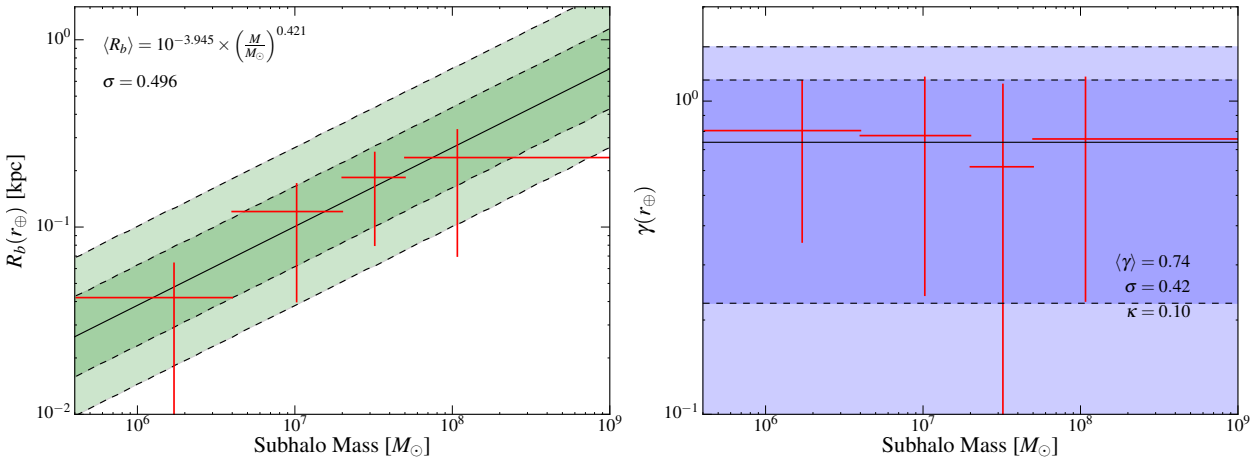

Figure 6.5: Left: The best-fit power law for the exponential scale parameter, R_b, as a function of subhalo mass, as determined from the ELVIS and Via Lactea II simulation data, for subhalos located 8.5 kpc from the Galactic Center. Right: The median inner slope, γ, as determined from the ELVIS and Via Lactea II simulation data, for subhalos located 8.5 kpc from the Galactic Center as a function of the subhalo mass. In each frame, the shaded regions depict the 68% and 95% containment contours.

fitted distributions are shown for in the left panel of Fig. 6.3 for subhalo masses in the range of $(2-5) \times 10^7 M_\odot$ and various ranges of distance to the Galactic Center. For a fixed mass range, we fit a power law to the median value of gamma as a function of Galactic Center distance (the resultant fit equations for $\langle\gamma\rangle$ are given in each panel of Fig. 6.1), as well as to the γ values demarcating the edges of the 68% containment region $\gamma_{68}^{+,-}$ — defined as the values of γ satisfying $\int_{\langle\gamma\rangle}^{\gamma_{68}^{+}} dP/d\gamma = 0.34$ and $\int_{\gamma_{68}^{-}}^{\langle\gamma\rangle} dP/d\gamma = 0.34$. The median *local* value of γ for a given range of subhalo masses is then determined using this power law fit. The equations defining the median power law fits for each mass range are provided in Fig. 6.1. For each mass bin, the values of σ and κ characterizing the distribution in γ are determined by requiring $\gamma_{68}^{+,-}$ equal the values determined by their respective power law extrapolations. Note that we take this approach, rather than attempting to extrapolate σ and κ directly, because there does not appear to be an obvious trend in either of these variables (this is

a consequence of the fact that these variables do not independently correspond to physical features of the distribution). This procedure results in local γ distributions for each of the 4 distinct mass intervals. The median local value of gamma for each mass range, as well as the extrapolated $\gamma_{68}^{+,-}$ values, are shown in the right panel of Fig. 6.5. Since this figure does not reveal any clear trend in the median value or in distribution of γ as a function of subhalo mass, we parameterize the local γ distribution as being independent of the subhalo mass, with values of $\langle\gamma\rangle$, σ, and κ set to be the median of the local fits shown in Fig. 6.5 (the parameters of which are provided in Fig. 6.5).

Similarly, to characterize the distribution of R_b we adopt a log-normal distribution:

$$\frac{dP}{dR_b} = \frac{1}{\sigma\sqrt{2\pi}}\frac{1}{R_b}\exp\left(-\frac{(\ln R_b - \ln\langle R_b\rangle)^2}{2\sigma^2}\right), \tag{6.5}$$

where $\langle R_b\rangle$ is the median value of R_b, and σ is the width of the distribution. Once again, we find the values of $\langle R_b\rangle$ and σ which provide the best fit to the simulated dataset in each bin in subhalo mass and Galactic Center distance. We find that the value of σ is not dependent on the subhalo mass or Galactic Center distance, and thus we average the preferred value across all bins. Examples of the fitted distributions are shown for in the right panel of Fig. 6.3 for subhalo masses in the range of $(2-5)\times 10^7 M_\odot$ and various ranges of distance to the Galactic Center. The local median value of R_b for each mass bin is determined using the power law fits to the median R_b value of each bin, shown in Fig. 6.2 (these equations are also provided in Fig. 6.2 for each mass interval). The local $\langle R_b\rangle$ fit and 68% containment regions for each subhalo mass bin are shown in the left panel of Fig. 6.5. We find that

the mass dependence of the exponential scale parameter is well described by a power-law, with $\langle R_b(M) \rangle \propto M^{0.421}$. We thus use this power law, along with the averaged σ value, to characterize the mass dependence of the local distribution of R_b (the final parameters characterizing this distribution are provided in left panel of Fig. 6.5). We have verified that our derived distributions in both R_b and γ are relatively insensitive to the choice of binning.

To address possible correlations between R_b and γ that are not captured by our one dimensional parameterizations, we compare in the $R_b - \gamma$ plane the VL-II and ELVIS best-fit parameters to the best-fit parameters that would be derived from randomly drawing values of R_b and γ from Eq. (6.5) and Eq. (6.4), assuming subhalo characteristics (mass and GC distance) are identical to those of the VL-II and ELVIS subhalos. The result of this test is shown in Fig. 6.4 for two different bins. The independent extrapolations appear to do a very reasonable job of capturing the subhalo properties. Fig. 6.4 does suggest, however, that our distributions may slightly over-estimate the number of small-γ large-R_b subhalos and the number of large-γ small-R_b subhalos. It is difficult to the assess the overall impact of this mis-modeling given that these overestimations lead to opposite effects. In Sec. 6.3.4 we will demonstrate the extent to which reducing halo-to-halo variations impacts the number of observable subhalos; from there, one many attempt to infer the effect that this mis-modeling may have on the derived limits.

If Fig. 6.6, we compare the median subhalo density profiles adopted in Ref. [246] (black), Ref. [248] (magenta), and as derived in this study (blue), for subhalos ranging in mass from $10^4 M_\odot$ to $10^7 M_\odot$. As the volume integral of the NFW profile adopted in Ref. [248] yields a subhalo mass that exceeds that reported by VL-II, we take the outer regions of the dark

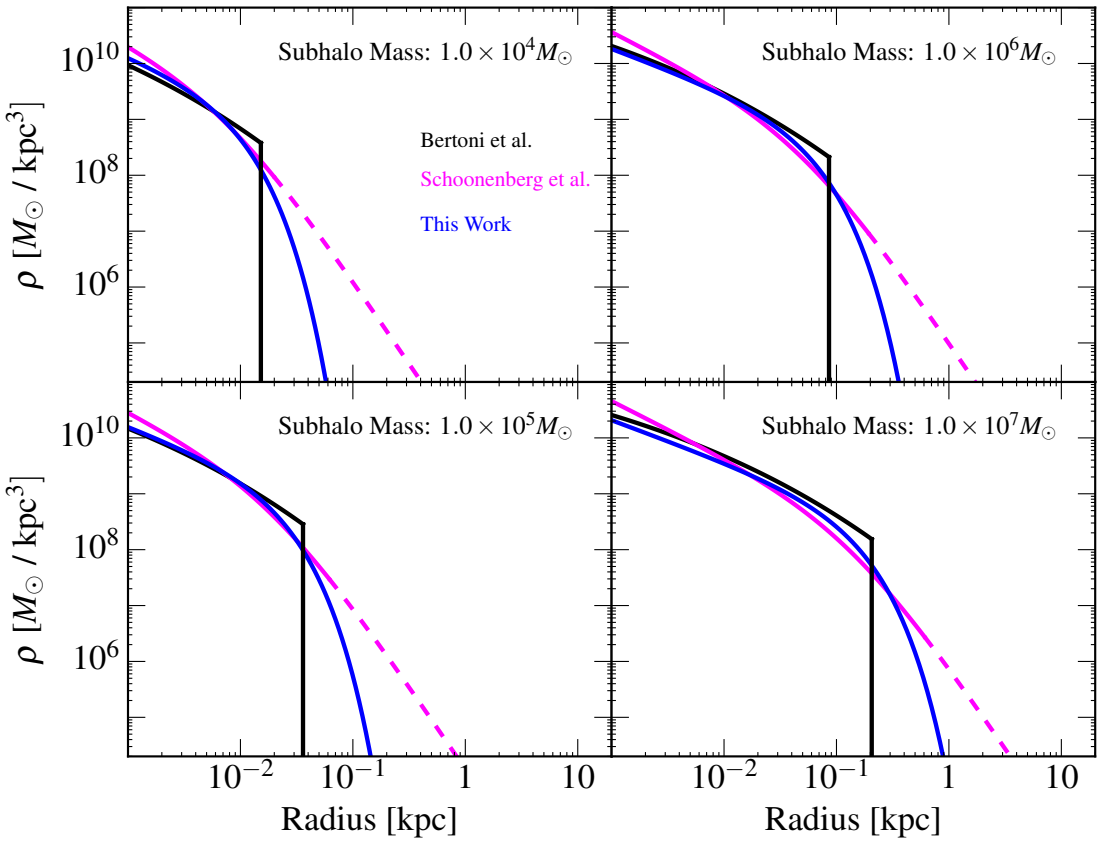

Figure 6.6: A comparison of the median density profiles adopted in Ref. [246] (black), Ref. [248] (magenta), and as derived in this study (blue) and for subhalos of four different masses.

matter distribution to be unspecified in this case. To convey this, we plot this profile as a solid line only within the radius that contains the mass reported by VL-II, and as a dashed line beyond this point.[13]

In order to predict the number of subhalos that could be observed by Fermi-LAT, one needs not only the shapes of the subhalo density profiles, but also the local number density

[13]We note that Ref. [248] does not explicitly state how they reconstruct density profiles at fixed subhalo mass from the extracted VL-II simulation results. The curves shown here are the result of a cubic spline interpolation function fit to $\ln R_{v,\rm max}(\ln M)$ and $\ln v_{c,\rm max}(\ln M)$ in the mass range where VL-II can resolve subhalos, and that we extrapolate to lower masses using a power law fit. The results obtained in this fashion appear to be quite similar to those presented in Ref. [248].

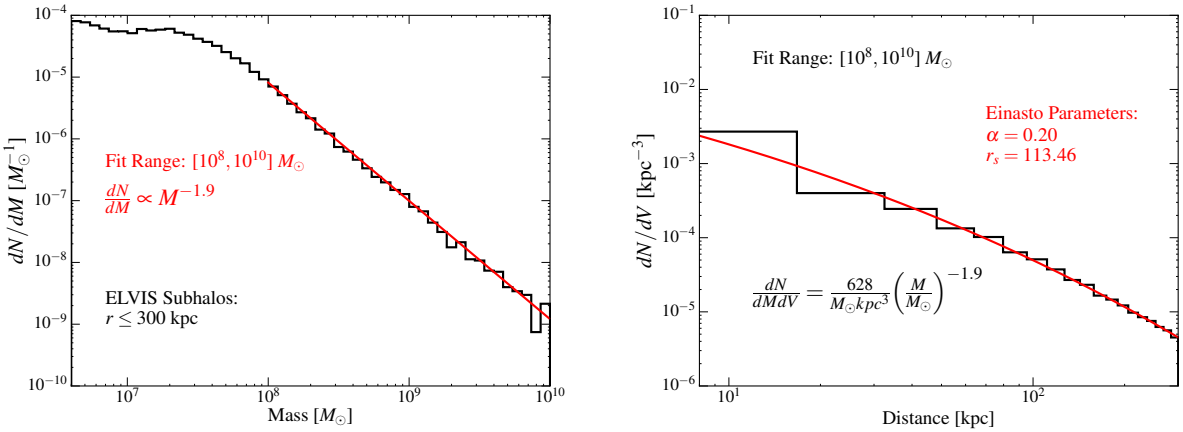

Figure 6.7: Left: The number of subhalos per unit mass within 300 kpc of the host halo's center as found in the ELVIS suite of simulations. The red line represents the best-fit power-law for subhalos with mass between 10^8 and $10^{10}\,M_\odot$. Right: The number of subhalos per unit volume in the ELVIS simulations for subhalos with masses between 10^8 and $10^{10} M_\odot$. The red line depicts the best-fit Einasto profile for this subhalo distribution. At a distance of 8.5 kpc from the center of the host halo, this corresponds to a local population described by $dN/dMdV = 628\,\mathrm{kpc}^{-3} M_\odot^{-1} \times (M/M_\odot)^{-1.9}$.

of subhalos of a given mass. In the left panel of Fig. 6.7, we plot the number of subhalos in the ELVIS simulation per unit subhalo mass as a function of subhalo mass. For masses above $10^8\,M_\odot$, we find that this distribution is well fit by $dN/dM \propto M^{-1.9}$, consistent with previous literature [287, 288, 290, 291]. Although the distribution appears to depart from this power-law at lower masses, we attribute this to the finite resolution of the ELVIS simulation.

In the right panel of Fig. 6.7, we plot the number density of subhalos as a function of the distance to the host center. Consistent with Refs. [290, 291], we find that this distribution is well-characterized by an Einasto profile. We use the fitted Einasto profile rather than the histogram itself to extract the local number density to avoid sensitivity to the choice of

binning. This allows us to derive the following distribution for the local subhalo population:

$$\frac{dN}{dMdV} = \frac{628}{M_{\odot}\,\mathrm{kpc}^3}\left(\frac{M}{M_{\odot}}\right)^{-1.9} . \tag{6.6}$$

In principle, a complete subhalo analysis would use the full radial dependence of the subhalo number density. However, we find that for the cross sections considered, effectively all observable subhalos reside very near to Earth where the subhalo number density is approximately constant. Note that had we considered more massive subhalos (e.g. dwarf galaxy sized objects), this would no longer have been the case and the radial dependence of the number density would be important. We thus approximate the number density as a location independent function using Eq. (6.6). We caution the reader that while this approximation is not thought to introduce significant error, it is possible that it results in a slight overestimation of the number of observable subhalos.

In the following section, we will use this subhalo distribution, along with the afore described distribution of subhalo density profiles, to calculate the gamma-ray luminosity function of local subhalos, and in turn the number of such subhalos that are predicted to be detectable to Fermi and other gamma-ray telescopes.

6.3 Detecting Dark Matter Subhalos With Gamma-Ray Telescopes

6.3.1 Gamma-Rays from Dark Matter Subhalos

A given subhalo will generate a gamma-ray flux that is given by:

$$\Phi_\gamma = \frac{\langle \sigma v \rangle N_\gamma}{8\pi m_\chi^2 D^2} \int \rho^2(r)\, dV, \tag{6.7}$$

where $\langle \sigma v \rangle$ is the dark matter's thermally averaged self-annihilation cross section, N_γ is the number of gamma rays produced per annihilation, m_χ is the dark matter mass, D is the distance to the center of the subhalo, and $\rho(r)$ is the density profile of the subhalo. For a given dark matter mass and annihilation channel, we calculate N_γ using Pythia 8 [292].

From the elements described in the previous section, we can calculate the number of subhalos that yield a gamma-ray flux above a given flux threshold, $\Phi_{\rm Thresh}$:

$$N_{\rm obs} = \Omega \int\int\int\int D^2 \frac{dN}{dM dV} \frac{dP}{d\gamma} \frac{dP}{dR_b} \Theta[\Phi_\gamma(M, D, R_b, \gamma) - \Phi_{\rm Thresh}]\, dM\, dD\, dR_b\, d\gamma, \tag{6.8}$$

where $dN/dMdV$ is the local subhalo number density per unit mass (Eq. 6.6) and $dP/d\gamma$ and dP/dR_b are the generalized normal and lognormal distributions for the parameters γ and R_b, respectively (Eqns. 6.4 and 6.5). The quantity Ω is the solid angle observed, which in the case of $|b| > 20^\circ$ corresponds to $4\pi(1 - \sin 20^\circ)$. We choose to limit the parameter γ to the range of 0 to 1.45, re-normalizing the distribution such that $\int_0^{1.45} (dP/d\gamma)\, d\gamma = 1$.

This is done for two reasons. First, subhalos with $\gamma < 0$ are unlikely to be physical, as there are no mechanisms at play in these dark matter only simulations which should cause the density profile to increase as a function of radius. Note that this truncation occurs only at the far tail of the distribution, resulting in a small effect. The far more important effect is truncating $\gamma > 1.45$. The density integral in Eq. (6.7) is divergent for $\gamma \geq 1.5$. This is not to say such halos cannot be physical, only that the density distribution must develop a core at some inner radii. In order to avoid having to specify the specific nature of such a core, we remove this part of the distribution. This truncation is conservative as subhalos with larger γ produce a noticeably larger flux, and are thus more observable. In order to compare our calculations to the list of subhalo candidates in the 3FGL gamma-ray source catalog as presented in Ref. [246], we adopt a value of $\Phi_{\rm Thresh} = 7 \times 10^{-10}$ cm^{-2} s^{-1} and consider only photons with energies above 1 GeV. We restrict our attention to subhalos with masses below $10^7\,M_\odot$ to avoid the inclusion of any dwarf galaxies and treat the minimum subhalo mass as a free parameter.

We note that because our analysis focuses on local subhalos and explicitly approximates the subhalo number density as independent of GC distance, $\log_{10}(N_{\rm obs}) \propto \frac{3}{2}\log_{10}(\langle\sigma v\rangle)$. This scaling relation differs from various published results, particularly for analyses that include dwarf-sized objects (see e.g. Fig. 5 of Ref. [248] and Fig. 9 of Ref. [293]). This is because dwarf-sized objects can be observed at much larger distances where the constant number density approximation may no longer be valid.

6.3.2 Placing Constraints on the Dark Matter Annihilation Cross Section

Analyses of the unidentified sources in Fermi's 3FGL catalogue have identified 19 bright ($\Phi_\gamma > 7 \times 10^{-10}$ cm^{-2} s^{-1}), high-latitude ($|b| > 20^\circ$) sources with no evidence of variability and which exhibit a spectral shape consistent with annihilating dark matter [246, 247].[14] In this subsection, we will use the observed number and characteristics of these subhalo candidates to place upper limits on the dark matter annihilation cross section.

Following the approach of Ref. [246], we calculate the χ^2 associated with the fit of a given dark matter model to the spectrum of each subhalo candidate, and define the weighted number of sources (WNS) to be twice the sum of the p-values associated with the fit, i.e.

$$\text{WNS} \equiv 2 \sum_{\text{i}} p_i = 2 \sum_{\text{i}} \int_{\chi^2_{\text{obs},i}}^{\infty} f_k(x)\, dx \tag{6.9}$$

(refer to the left panel of Fig. 10 in Ref. [246] for result). Here, p_i is the p-value associated with source i, $f_k(x)$ is the χ^2 distribution function for k degrees of freedom, and $\chi^2_{\text{obs},i}$ is the observed chi-square value of source i. We then apply Poisson statistics to the WNS to place a 95% upper limit on the annihilation cross section, for a given value of the dark matter mass and annihilation channel.

In Fig. 6.8, we plot the upper limit derived for dark matter annihilating to $b\bar{b}$ (purple). The upper (lower) boundary of this band represents the limit obtained assuming a minimum subhalo mass of $10^5\, M_\odot$ ($10^{-5} M_\odot$). We also show in this figure the limits that would have been obtained if no subhalo candidate sources had been detected (zero weighted sources).

[14] The 19 subhalo candidates are the same as those listed in Ref. [246], after removing the five sources that have more recently been associated with emission at other wavelengths [247].

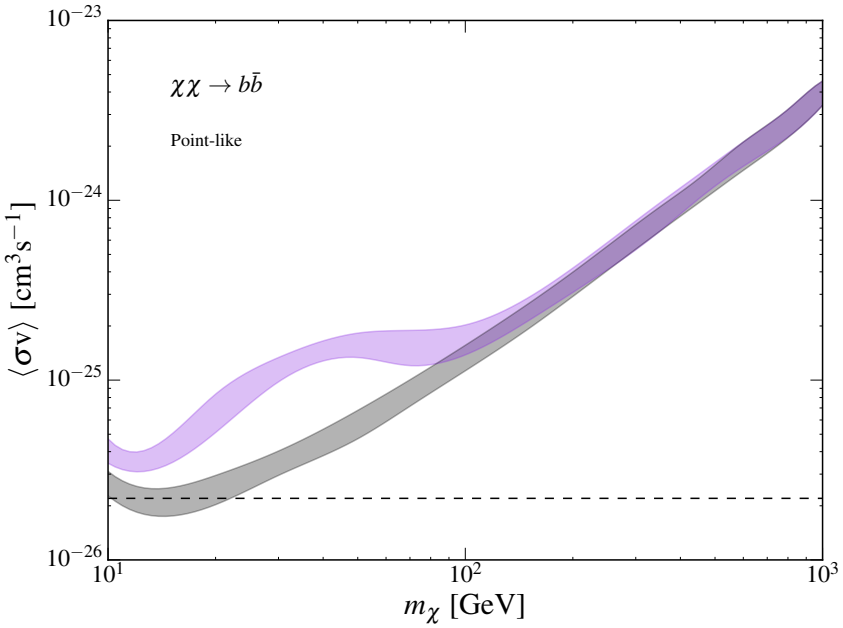

Figure 6.8: The 95% confidence level upper limit on the cross section for dark matter annihilation to $b\bar{b}$ as derived from the unassociated gamma-ray source population presented in Ref. [246] (purple). Also shown are the limits that would have been derived if no subhalo candidates been observed (grey).

As a benchmark, we plot as a dashed horizontal line the cross section associated with dark matter in the form of a simple thermal relic. In Fig. 6.9, we show the 95% upper limits for dark matter annihilating to various final states ($b\bar{b}$, $c\bar{c}$, $\tau^+\tau^-$, ZZ or W^+W^-), adopting a minimum mass of either $10^{-5} M_\odot$ (left) or $10^5 M_\odot$ (right).

In Fig. 6.10, we compare the limits on the annihilation cross section derived in this study to those previously obtained from Fermi's observations of dwarf galaxies (short-dashed blue) [220], the Galactic Center (long-dashed magneta) [222] and the isotropic gamma-ray background (dot-dashed green) [223]. Although the limits from subhalo searches are somewhat weaker than those derived from these other observational targets, they are reasonably competitive and highly complementary.

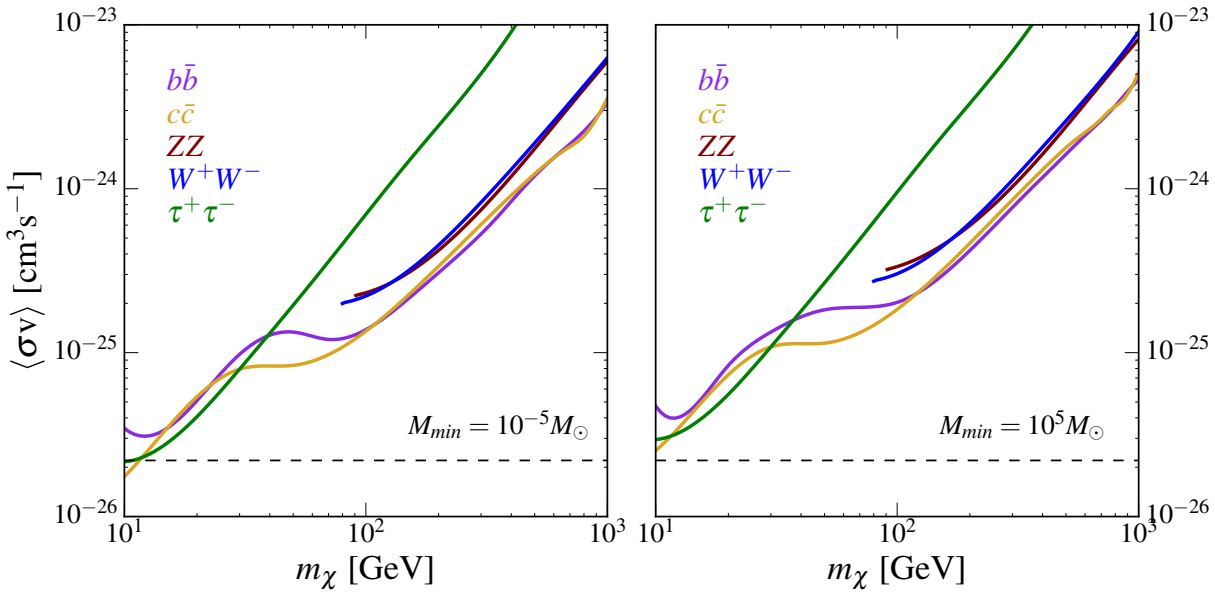

Figure 6.9: The 95% confidence level upper limit on the dark matter annihilation cross section for various annihilation channels, adopting a minimum subhalo mass of $10^{-5} M_\odot$ (left) or $10^5 M_\odot$ (right).

6.3.3 Prospects for Detecting Spatial Extension

Thus far our discussion has been restricted to the detection of dark matter subhalos as point-like gamma-ray sources. Of those subhalos detectable by Fermi, however, the most massive and nearby may be discernibly spatially extended, potentially enabling one to distinguish a dark matter subhalo from a pulsar, blazar, or other gamma-ray point source. The unambiguous observation of a spatially extended gamma-ray source with no corresponding emission at other wavelengths would constitute a smoking gun for annihilating dark matter [247].

To quantify the degree of spatial extension of the gamma-ray emission from a dark matter subhalo, we introduce the parameter, σ_{68}, defined as the angular radius which contains 68%

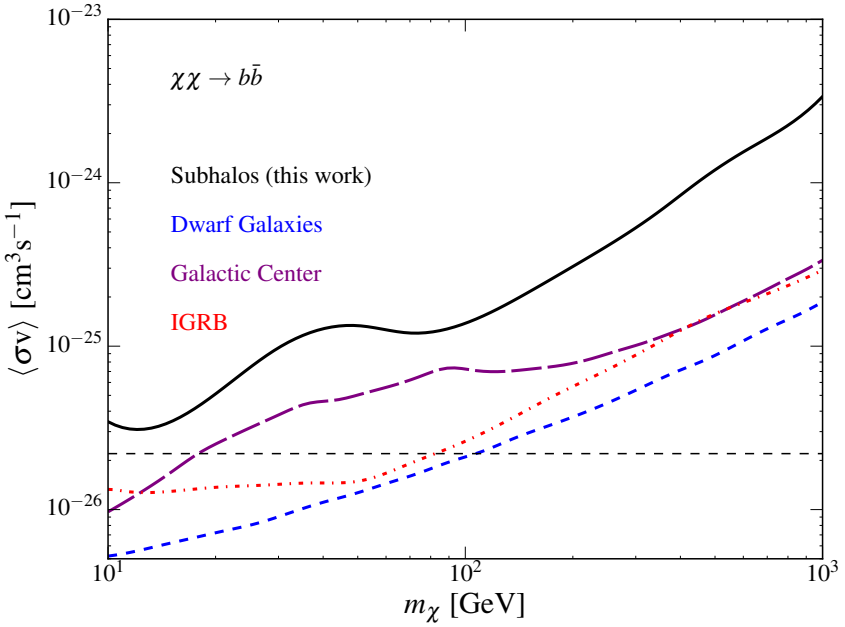

Figure 6.10: A comparison of the 95% confidence level upper limits on the dark matter annihilation cross section placed from gamma-ray searches for subhalos (solid black) and gamma-ray observations of dwarf galaxies (short-dashed blue) [220], the Galactic Center (long-dashed purple) [222] and the isotropic gamma-ray background (dot-dashed red) [223]. Here we have adopted a minimum subhalo mass of $10^{-5} M_\odot$ and consider the representative case of annihilations to $b\bar{b}$.

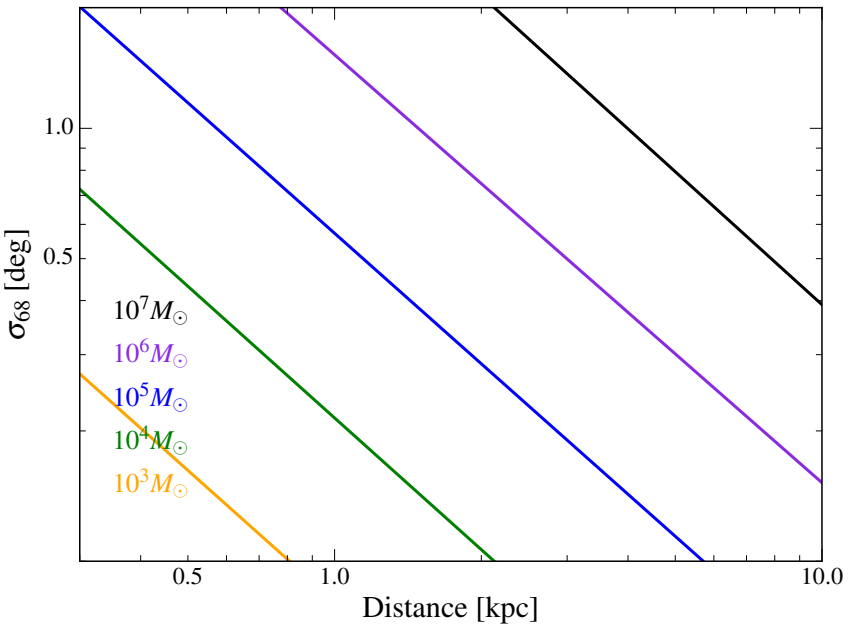

Figure 6.11: The 68% containment radius, σ_{68}, as a function of the distance to a given subhalo, for five values of the subhalo mass.

of the total photons from the source:

$$\frac{\int_0^{\sigma_{68}} \rho(r)^2 \, dl}{\int_0^{\theta_{\rm max}} \rho(r)^2 \, dl} = 0.68, \tag{6.10}$$

where the integrals are performed over the line-of-sight, and $\theta_{\rm max}$ is the angular radius encompassing the full extension of the subhalo. Given the point spread function of Fermi, a bright unassociated source can be potentially identified as spatially extended if $\sigma_{68} \gtrsim \mathcal{O}(0.1^\circ)$ [247]. In the case of bright point-like gamma-ray sources, Fermi can typically place upper limits on the degree of spatial extension at approximately the same level.

In Fig. 6.11 we plot σ_{68} as a function of the distance to a given subhalo, for five values of the subhalo mass and assuming a density profile as described by Eq. 6.3 (with R_b and γ set to their median values). This illustrates that in order for an observable subhalo to have

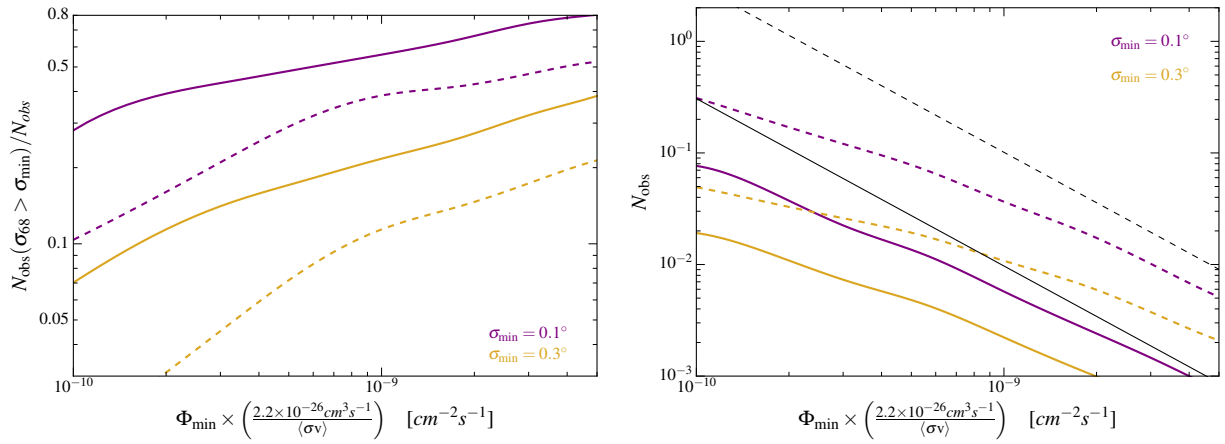

Figure 6.12: Left: The fraction of subhalos with spatial extension greater than 0.1° (purple) and 0.3° (yellow) as a function of minimum gamma-ray flux (above 1 GeV) and annihilation cross section. Results are shown for a dark matter particle with a mass of 100 GeV (solid) and 10 GeV (dashed), and for the case of annihilations to $b\bar{b}$. Right: Total number of observable subhalos as a function of minimum gamma-ray flux (above 1 GeV) and annihilation cross section, for $\sigma_{\rm min} = 0$ (i.e. point-like and extended, thin black), $\sigma_{\rm min} = 0.1°$ (purple), $\sigma_{\rm min} = 0.3$ (yellow). As in the left panel, results are shown for a dark matter particle with a mass of 100 GeV (solid) and 10 GeV (dashed), and for the case of annihilations to $b\bar{b}$.

potentially discernible extension ($\sigma_{68} \gtrsim 0.1°$), it must be very massive, very nearby, or both.

In the left panel of Fig. 6.12, we plot the fraction of subhalos for which $\sigma_{68} > 0.1°$ (purple) or $\sigma_{68} > 0.3°$ (yellow), as a function of the minimum gamma-ray flux and annihilation cross section. Results are shown for dark matter with a mass of 100 GeV (solid) or 10 GeV (dashed), and for the representative case of annihilations to $b\bar{b}$. The right panel of Fig. 6.12 shows the total number of observable subhalos for these same candidates and minimum σ_{68} values, and compares this result with the total number of predicted subhalos (shown in black). For dark matter particles in this mass range and with an annihilation cross section of $\langle\sigma v\rangle = 2.2 \times 10^{-26}$ cm^3/s, we predict that approximately 10-20% of subhalos with a gamma-ray flux above 10^{-9} cm^{-2} s^{-1} will be extended at a level of $\sigma_{68} > 0.3°$ and that 40-55% will be extended at $\sigma_{68} > 0.1°$. This can be directly compared to the degree of extension observed

among those subhalo candidate sources observed by Fermi.

A recent analysis of the 12 brightest ($\Phi_\gamma > 10^{-9} \mathrm{cm}^{-2} \mathrm{s}^{-1}$) dark matter subhalo candidates in the 3FGL catalog found that three of these sources prefer a spatially extended morphology at a level of $2\Delta \ln \mathcal{L} > 4$, corresponding to $\gtrsim 2\sigma$ significance [247]. These three sources (3FGL J2212.5+0703, 3FGL J1119.9-2204, and 3FGL J0318.1+0252) were found to be best-fit by extensions of $\sigma_{68} = 0.25^\circ$, 0.07° and 0.15°, respectively. The other nine sources in this sample showed little or no preference for spatial extension. Given the upper limits placed on the spatial extension of these twelve sources, eleven require $\sigma_{68} < 0.3^\circ$ while seven require $\sigma_{68} < 0.1^\circ$ (at the 95% confidence level). While this manuscript was being considered for publication, Ref. [294] identified an additional unassociated gamma-ray source with $\simeq 5\sigma$ preference for a spatial extension of $\sigma \simeq 0.1^\circ$. This is particularly interesting in light of the fact that the estimated background from overlapping point sources is $\mathcal{O}(2\%)$ per source. Assessing the consistency of subhalo interpretations of these sources will be of interest in the future as the uncertainties entering subhalo analyses are further reduced.

According to the analysis of Ref. [247], none of Fermi's subhalo candidates are compatible with extension greater than $\sigma_{68} > 0.31^\circ$. We can use this fact, in conjunction with the predicted distribution of subhalo extensions, to place an upper limit on the dark matter annihilation cross section. In Fig. 6.13, we plot the 95% upper limit derived from the non-observation of sources with spatial extension σ_{68} greater than 0.31° (green), for the case of annihilations to $b\bar{b}$ and a minimum subhalo mass of $10^5 M_\odot$. For comparison, we also show in this figure the limit derived from point-like sources (long dashed), assuming the same annihilation channel and minimum subhalo mass. The limit derived from the

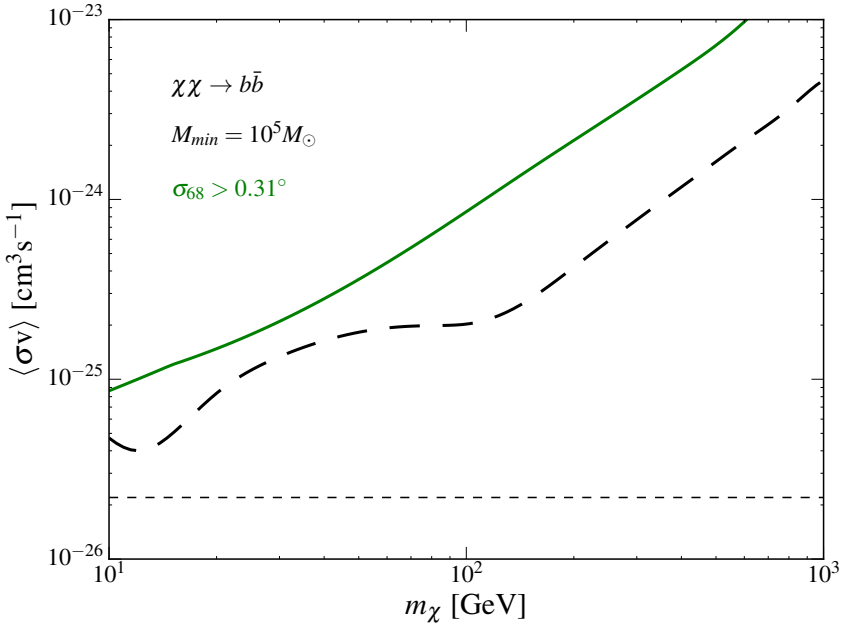

Figure 6.13: The 95% upper limit on the dark matter annihilation cross section for annihilation into $b\bar{b}$ derived from the non-observation of extended gamma ray sources with a flux above $10^{-9}\mathrm{cm}^{-2}\mathrm{s}^{-1}$ and a spatial extension σ_{68} greater than 0.31° (solid green). Shown for comparison are the limits derived from the total number of subhalo candidate sources as depicted in right panel of Fig. 6.9 (dashed black).

non-observation of spatially extended sources (with $\sigma_{68} > 0.31^{\circ}$) is somewhat weaker than that based on the total number of sources observed. That being said, as Fermi and other gamma-ray telescopes continue to accumulate catalogs of dark matter subhalo candidate sources, spatial extension will be essential for distinguishing any subhalo population from other gamma-ray source classes.

6.3.4 Uncertainties

Thus far in this study, we have not addressed the many uncertainties involved in our calculations. In this section, we will discuss the most important of these uncertainties and their likely impact on our results and conclusions.

We begin by considering the density profiles of the local subhalo population. With an ideal suite of numerical simulations, one could fully resolve the profiles of individual subhalos over a wide range of scales and masses. Current simulations, however, lack the resolution to probe the inner regions such subhalos, making it difficult to distinguish between different functional forms that might describe the distributions of dark matter in these systems. We also note that current simulations are not able to resolve any small-scale structure that may be present *within* a given subhalo, potentially inducing a boost factor to the annihilation rate in a given subhalo. Throughout this analysis, we have conservatively chosen to neglect any boost factors to the annihilation rate.

Arguably, the most significant assumption we have made in our analysis is that the distributions of the parameters γ and R_b which describe the local subhalo population can be safely extrapolated from the distributions describing the subhalos located throughout

the larger volume of the host halo. While the distributions of the simulated subhalos do appear to present a clear trend with respect to subhalo location with the host halo, there are simply not enough simulated subhalos in the inner tens of kiloparsecs to extract these parameters and distributions without relying on such an extrapolation. Despite the fact that it is difficult to meaningfully assess the uncertainty associated with our extrapolations of the distributions in γ and R_b, it is important to understand the impact of halo-to-halo variations on predictions for the observability of subhalos. To address this question, we plot in Fig. 6.14 the limits that would be derived should the value of σ characterizing of the distribution in γ (purple) and R_b (blue) be reduced by a factor of $\sqrt{2}$, assuming annihilations to $b\bar{b}$ and a minimum subhalo mass of $10^5 M_{\odot}$. We emphasize that there is no meaningful justification for the assumed values of σ shown in Fig. 6.14, but rather have included this figure to better understand how decreasing halo-to-halo variations can alter the derived limits. We believe that a proper understanding of these variations for the local population is instrumental for making concrete predictions of the observability of dark matter subhalos. Ideally, as the statistics associated with such simulations continue to improve, we hope to eventually be able to rely exclusively on simulated subhalos located in the inner regions of their host halo, eliminating the need for extrapolations in these distributions and leading to a more stable understanding of dark matter subhalos.

Similar to how current simulations tell us very little about the small scale structure of dark matter halos and subhalos, they are also not generally capable of revolving the lowest mass subhalos. Below roughly 10^6 to 10^8 $M_{\odot}$, we are forced to extrapolate the characteristics of the local subhalo population, both in terms of the number density and mass distribution

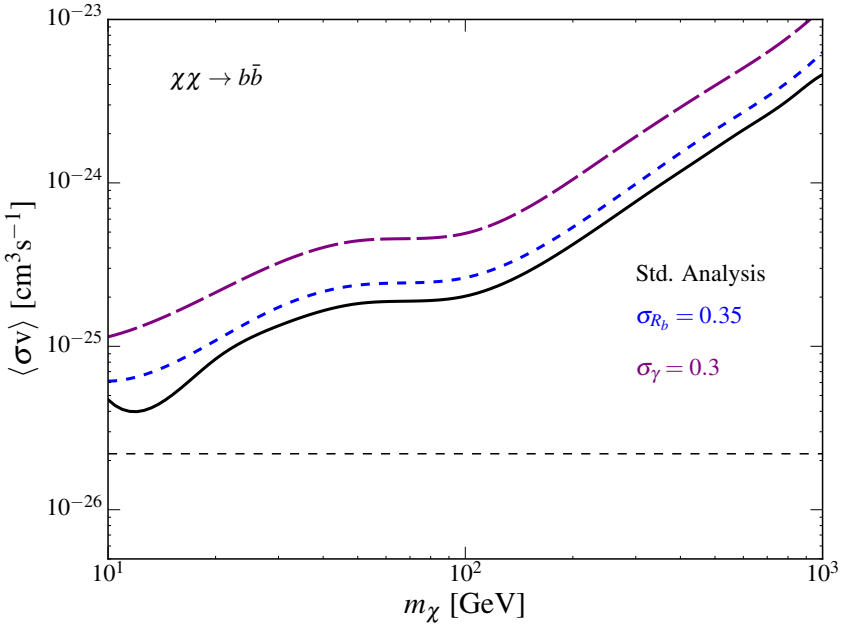

Figure 6.14: The 95% confidence level upper limit derived on the cross section for dark matter annihilating to $b\bar{b}$, varying independently the variance in R_b (short dashed, blue) and γ (long dashed, purple). Results are compared with the standard analysis (black). Calculations assume a minimum subhalo mass of $10^5 M_\odot$.

of such subhalos (see the left frame of Fig. 6.7), and in terms of the distributions of the halo parameters γ and R_b (see Fig. 6.5). Given that the subhalo distribution extends to masses as low as $\sim 10^{-8}$ to $10^{-3}\, M_\odot$ for typical WIMPs [282, 295–297], even modest departures from this extrapolation can have a non-negligible impact on the predicted number of observable subhalos. Some simulations actually suggest that the density profiles of the smallest scale subhalos may actually have much steeper inner slopes (with $\gamma \simeq 1.3 - 1.5$), potentially making our extrapolations slightly conservative [264, 282]. To assess the uncertainty associated with the distribution of subhalos, we plot in Fig. 6.15 the upper limit on the dark matter annihilation cross section when we change the power-law slope of the subhalo mass distribution over the range of -1.8 to -2.0 (in our earlier calculations, we adopted a value of -1.9;

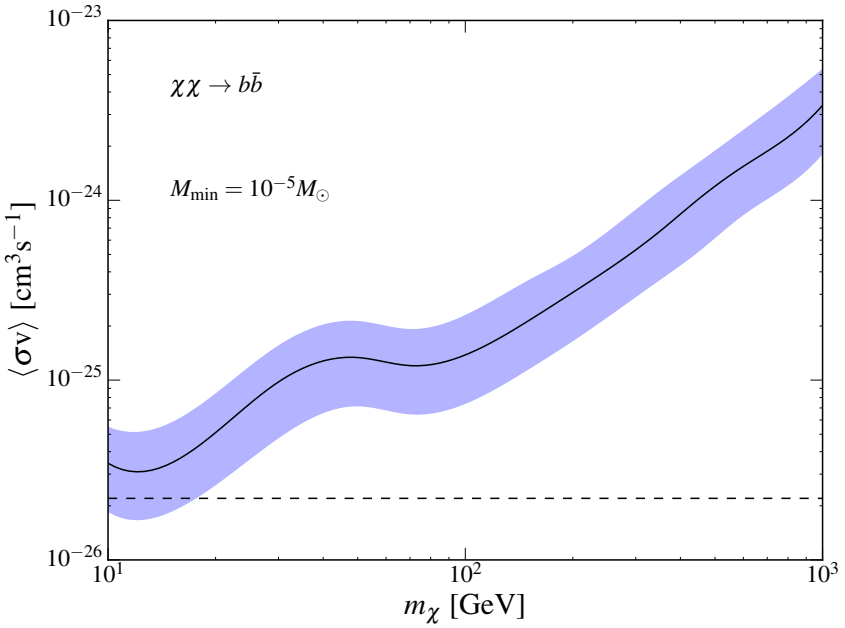

Figure 6.15: The 95% confidence level upper limit derived on the cross section for dark matter annihilating to $b\bar{b}$, varying the exponent of the subhalo mass distribution $dN/dMdV \propto M^\beta$ (see Eq. 6.6) between $\beta = -1.8$ (upper boundary) and $\beta = -2.0$ (lower boundary), and adopting a minimum subhalo mass of $10^{-5} M_\odot$. The solid black contour represents the limit for our default value of $\beta = -1.9$.

see Eq. 6.6) [287, 288, 298, 299]. Here, we have adopted a minimum subhalo mass of $10^{-5}\, M_\odot$ and again have considered the representative case of annihilations to $b\bar{b}$. This range of limits can vary by a factor of up to $\sim$2 (in either direction) from those presented in the left panel of Fig. 6.9.

Finally, we would like to emphasize that our results are based on the subhalo populations generated in dark matter-only simulations. As the physical effects of baryons in the Milky Way are not captured in such simulations, our results do not take into account the gravitational potential of our Galaxy's stars, gas and dust. In recent years, there has been considerable progress in understanding the impact of baryons on the evolution of dark matter structure in Milky Way-like systems. In particular, some groups have attempted to capture

the effect of the baryonic disk on the evolution of structure in the Milky Way without resorting to a full hydrodynamical treatment, but instead by artificially introducing a disk potential. Some of these simulations (utilizing either an artificial disk potential or a fully hydrodynamical approach) have shown that the presence of such a disk may non-negligibly reduce the local density of subhalos. For example, Refs. [299] and [300] each find that baryonic effects reduce the local number density of subhalos by a factor of approximately $\sim$2 (see also e.g. [291, 293, 301]). Depending on how these baryonic effects impact the shape of the surviving subhalo density profiles, they could have a wide range of possible impacts on the resulting cross section constraints. Until such hydrodyamical effects are able to be reliably implemented with higher resolution, it will be difficult to assess their impact on the observability of the nearby dark matter subhalo population.

While this manuscript was being prepared for journal publication, a study attempting to address the baryonic impact of subhalo detectability was released [293]. Ref. [293] found a minimal impact on subhalo detectability between hydrodynamical and dark matter only simulations. We do note, however, that the conclusions of [293] using the results of dark matter-only simulations differ slightly from the results shown here[15]. We attribute this difference primarily to the adopted subhalo parameterization.

Taking the impact of these various uncertainties together, we conclude that the predicted number of observable subhalos could quite plausibly vary from those values presented here by a factor of a few in either direction. Only with improvements in the resolution of numerical simulations (both dark matter-only and hydrodynamical simulations) will such predictions

[15]Ref. [293] bases their dark matter-only results on the $\sim$ 1200 subhalos identified in the AQ08 simulation [290], and adopts an analysis comparable to that of [248].

be able to be placed on firmer footing, allowing one to establish more robust limits on the dark matter annihilation cross section.

6.4 Summary and Conclusion

In this paper, we have revisited constraints on the dark matter annihilation cross section derived from searches for dark matter subhalo candidates among Fermi's list of unassociated gamma-ray sources. We have based our calculations on the properties of over $30,000$ subhalos identified within the Via Lactea-II and ELVIS simulations, which we used to constrain the density profiles and the mass distribution of the local subhalo population.

The density profiles of subhalos located within the innermost tens of kiloparsecs of a given host halo are significantly altered as a result of tidal stripping, and in most cases cannot be described by a traditional NFW profile. Instead, we find that these subhalos are well characterized by a power-law profile with an exponential cutoff. While the inner slope of these profiles is largely independent of the subhalo mass (consistently featuring a median value of $\langle\gamma\rangle \simeq 0.74$), the median cutoff radius is a function of mass. Using simulated subhalos from the ELVIS and Via Lactea-II simulations, we fit the distributions of these parameters as a function of the subhalo's mass and distance to the center of the host halo. From this information, we deduce the characteristics of the local subhalo population and calculate the dark matter annihilation rate within this collection of objects, determining the number of subhalos that will appear to Fermi as bright gamma-ray sources.

The limits on the dark matter annihilation cross section that have been derived in this study are somewhat weaker (by a factor of $\sim$2-3) than those presented previously by Bertoni,

Hooper and Linden [246], and somewhat stronger than those later presented by Schoonenberg *et al.* [248].

We have also calculated the fraction of gamma-ray bright subhalos that are predicted to have discernible spatial extension to a telescope such as Fermi. Such information provides an important test, enabling us to potentially distinguish a dark matter subhalo from a point-like astrophysical source, such as a radio-faint pulsar. We find that for typical WIMPs, roughly 10-50% of gamma-ray bright subhalos will be discernibly extended to Fermi, depending on the value of the dark matter's mass and annihilation cross section. This is particularly interesting in light of recent evidence for spatial extension among several of Fermi's subhalo candidates [247, 294]. The results presented here are compatible with the possibility that a significant fraction of these candidate sources could, in fact, be dark matter subhalos.

Although the limits on the dark matter annihilation cross section derived in this study are somewhat weaker than those based on observations of dwarf galaxies, the Galactic Center, and the isotropic gamma-ray background, these strategies are each subject to different uncertainties and limitations, and are thus highly complementary. Furthermore, the future prospects for dark matter subhalo searches using gamma-ray telescopes are particularly promising. In addition to further data that will be collected by Fermi, future space-based gamma-ray missions such as ComPair [302] and e-ASTROGAM [303] are anticipated to significantly improve upon the current point sensitivity at energies below $\sim$1 GeV, likely leading to the discovery of many new sources, and to the improved characterization of the sources already detected by Fermi.

7 Updated Collider and Direct Detection Constraints on Dark Matter Models for the Galactic Center Gamma-Ray Excess

7.1 The Galactic Center Excess

Over the past decade or so, a number of observations have been interpreted as possible signals of annihilating or decaying dark matter particles. Examples of such observations include the 511 keV emission from the Galactic Bulge [304], an excess of synchrotron emission known as the WMAP Haze [305, 306], an excess of high energy positrons in the cosmic ray spectrum [307, 308], a mono-energetic line of 130 GeV gamma rays from the Galactic Halo [309], and a 3.5 keV X-ray line from Perseus and other galaxy clusters [310,311]. Each of these anomalies, however, has either failed to be confirmed by subsequent measurements [312, 313], or has been shown to be quite plausibly explained by astrophysical phenomena [314–317].

In comparison to these other anomalous signals, the gamma-ray excess observed from the Galactic Center by the Fermi Gamma-Ray Space Telescope stands out. This signal has been studied in detail over the past seven years [225–227, 229–234, 318, 319] and has been shown with high statistical significance to exhibit a spectrum, morphology and overall intensity that is compatible with that predicted from annihilating dark matter particles in the form of a $\sim$30-70 GeV thermal relic distributed with a profile similar to that favored by numerical simulations. Although astrophysical interpretations of this signal have been proposed (consisting of either a large population of millisecond pulsars [235–241, 320], or a

series of recent leptonic cosmic-ray outbursts [242–244]), these explanations require either a significant degree of tuning in their parameters [243], or pulsar populations which are very different from those observed in the environments of globular clusters or in the field of the Milky Way [235, 240, 320]. In addition, some modest support for a dark matter interpretation of this signal has recently appeared in the form of excesses in the cosmic-ray antiproton spectrum [321–323], in the gamma-ray emission from the dwarf spheroidal galaxies Reticulum II and Tucana III [220, 324–327], and from the observation of spatially extended gamma-ray emission from two dark matter subhalo candidates [246, 247, 294, 328]. At this point in time, however, there is no clear resolution to the question of the origin of the Galactic Center excess.

Many groups have studied dark matter models that are capable of generating the observed features of the Galactic Center excess (for an incomplete list, see Refs. [329–347]). In this study, we follow an approach similar to that taken in Ref. [329], and consider an exhaustive list of simplified models that are capable of generating the observed gamma-ray excess while remaining consistent with all constraints from collider and direct detection experiments. Also following Ref. [329], we choose to not consider hidden sector models in this study, in which the dark matter annihilates to unstable particles which reside in the hidden sector, without sizable couplings to the Standard Model (SM) [339, 342, 343]. While such scenarios certainly remain viable, we consider them to be beyond the scope of this work.

The models found in Ref. [329] to be compatible with existing constraints from direct detection and collider experiments are listed in Table 7.1, and can be divided into three categories. First, there are models in which the dark matter annihilates into SM quarks

Dark Matter	***Mediator***	***Interactions***	**Direct Detection**
Dirac Fermion, χ	Spin-0	$\bar{\chi}\gamma^5\chi$, $\bar{f}f$	$\sigma_{\rm SI} \propto (q/2m_\chi)^2$
Majorana Fermion, χ	Spin-0	$\bar{\chi}\gamma^5\chi$, $\bar{f}f$	$\sigma_{\rm SI} \propto (q/2m_\chi)^2$
Dirac Fermion, χ	Spin-0	$\bar{\chi}\gamma^5\chi$, $\bar{f}\gamma^5 f$	$\sigma_{\rm SD} \propto (q^2/4m_n m_\chi)^2$
Majorana Fermion, χ	Spin-0	$\bar{\chi}\gamma^5\chi$, $\bar{f}\gamma^5 f$	$\sigma_{\rm SD} \propto (q^2/4m_n m_\chi)^2$
Complex Scalar, ϕ	Spin-0	$\phi^\dagger\phi$, $\bar{f}\gamma^5 f$	$\sigma_{\rm SD} \propto (q/2m_n)^2$
Real Scalar, ϕ	Spin-0	ϕ^2, $\bar{f}\gamma^5 f$	$\sigma_{\rm SD} \propto (q/2m_n)^2$
Complex Vector, X	Spin-0	$X^\dagger_\mu X^\mu$, $\bar{f}\gamma^5 f$	$\sigma_{\rm SD} \propto (q/2m_n)^2$
Real Vector, X	Spin-0	$X_\mu X^\mu$, $\bar{f}\gamma^5 f$	$\sigma_{\rm SD} \propto (q/2m_n)^2$
Dirac Fermion, χ	Spin-1	$\bar{\chi}\gamma^\mu\chi$, $\bar{b}\gamma_\mu b$	$\sigma_{\rm SI} \sim$ loop (vector)
Dirac Fermion, χ	Spin-1	$\bar{\chi}\gamma^\mu\chi$, $\bar{f}\gamma_\mu\gamma^5 f$	$\sigma_{\rm SD} \propto (q/2m_n)^2$ or $(q/2m_\chi)^2$
Dirac Fermion, χ	Spin-1	$\bar{\chi}\gamma^\mu\gamma^5\chi$, $\bar{f}\gamma_\mu\gamma^5 f$	$\sigma_{\rm SD} \sim 1$
Majorana Fermion, χ	Spin-1	$\bar{\chi}\gamma^\mu\gamma^5\chi$, $\bar{f}\gamma_\mu\gamma^5 f$	$\sigma_{\rm SD} \sim 1$
Dirac Fermion, χ	Spin-0 (t-ch.)	$\bar{\chi}(1\pm\gamma^5)b$	$\sigma_{\rm SI} \propto$ loop (vector)
Dirac Fermion, χ	Spin-1 (t-ch.)	$\bar{\chi}\gamma^\mu(1\pm\gamma^5)b$	$\sigma_{\rm SI} \propto$ loop (vector)
Complex Vector, X	Spin-1/2 (t-ch.)	$X^\dagger_\mu\gamma^\mu(1\pm\gamma^5)b$	$\sigma_{\rm SI} \propto$ loop (vector)
Real Vector, X	Spin-1/2 (t-ch.)	$X_\mu\gamma^\mu(1\pm\gamma^5)b$	$\sigma_{\rm SI} \propto$ loop (vector)

Table 1: A summary of the simplified models identified in Ref. [329] as being potentially capable of generating the observed characteristics of the Galactic Center gamma-ray excess without violating collider or direct detection constraints (as of June 2014). For each model, we list the nature of the dark matter candidate and the mediator, as well as the form of the mediator's interactions. In the final column, we list whether the leading elastic scattering cross section with nuclei is spin-independent (SI) or spin-dependent (SD) and whether it is suppressed by powers of momentum, q, or by loops.

through the s-channel exchange of a spin-zero mediator with pseudoscalar couplings. These models allow for an unsuppressed (s-wave) low-velocity annihilation cross section while generating a cross section for elastic scattering with nuclei that is suppressed by either two or four powers of momentum, thus evading direct detection constraints. In the second class of models, the dark matter annihilates through the s-channel exchange of a vector boson. In this case, it was found that direct detection constraints could be evaded if the mediator couples axially with quarks or couples only to the third generation. Lastly, there are models in which the dark matter annihilates to b-quarks through the t-channel exchange of a colored and electrically charged mediator.

In this paper, we revisit this collection of dark matter models, applying updated constraints from the Large Hadron Collider (LHC) and other collider experiments, in addition to recent constraints from the direct detection experiments LUX [168] and PandaX-II [169]. We find that many of the models previously considered within the context of the Galactic Center excess are now excluded by a combination of these constraints.

7.2 Constraints

In this section, we summarize the constraints that we apply in this study. In particular, we consider constraints from the LHC and other accelerators, as derived from searches for mono-X events with missing energy (where X denotes a jet, photon, or Z), di-jet resonances, di-lepton resonances, exotic Higgs decays, sbottom searches, and exotic upsilon decays [348–358]. We also summarize the current status of direct searches for dark matter, including the recent constraints presented by the LUX [168] and PandaX-II [169] Collaborations.

7.2.1 LHC

Searches at CMS and ATLAS provide some of the most stringent constraints on dark matter, as well as on the particles that mediate the interactions of dark matter. In this study, we consider the bounds from the LHC as applied to a wide range of simplified models, the most stringent of which arise from CMS searches for mono-jet+MET, di-jet resonances, di-lepton resonances, di-tau resonances, and sbottom searches. Although we also considered constraints from the ATLAS Collaboration, they were slightly less restrictive than those from CMS.

LHC limits are typically published in one of two ways: (1) assuming a particular model and choice of couplings, a limit is presented on the parameter space in the dark matter mass-mediator mass plane, or (2) a limit is presented on the product of the production cross section and the branching fraction for a particular process. In this study, we will present our results in terms of the mediator mass and the product of the dark matter-mediator and SM-mediator couplings. Thus applying limits from the LHC generally requires translating these bounds into the parameter space under consideration. To calculate the relevant production cross sections and branching ratios, models are built using FeynRules [359] and subsequently imported into MadGraph5_aMC@NLO [360, 361]. When necessary, we implement PYTHIA 8 [362] to hadronize the final state particles and DELPHES [363] to simulate the detector response. As appropriate, we apply the published cuts on MET, final state momentum, and final state rapidity in our calculations. Throughout this study, we calculate and present all LHC constraints at the 95% confidence level.

In scenarios with heavy mediators, it is not uncommon for the width of the mediator

to be unacceptably large (i.e. as large or larger than its mass). Such widths are clearly not physical and may indicate the presence of additional particles or interactions [364–368]. Imposing unitarity and gauge invariance often restricts the mass of such additional particles to be of the same order of magnitude as the other dark sector particles, making it difficult to define the properties of these new particles such that they are beyond the reach of the LHC. Although the construction of more complicated dark sectors is beyond the scope of the work, we emphasize that it is likely that constraints derived on such models would be more restrictive than those derived here. Throughout this study, in order to maintain the validity of the theory in this region of parameter space, we apply LHC constraints assuming $\Gamma/m = 0.1$ whenever the width of the mediator would otherwise exceed this value.

7.2.2 LEP-II

Constraints from LEP-II on Higgs bosons in the mass range between 10 GeV and 100 GeV are extremely constraining for a wide range of beyond the SM physics scenarios. In this study we consider such limits as derived from searches for a light Higgs decaying to $b\bar{b}$ [357]. Although powerful, these constraints are rather model dependent, and generally rely on the scalar mediator's coupling to the SM gauge bosons. LEP-II constraints are presented at the 95% confidence level throughout this work, and assume a coupling to the Z-boson identical to that of the SM Higgs.

7.2.3 BaBar

We also consider in this study constraints derived from BaBar on upsilon decays to light scalar or pseudoscalar particles, in particular focusing on channels where the mediator subsequently decays to hadrons, muons, taus or charm quarks [369–372]. We consider relativistic and QCD corrections for the decay of a vector meson as described in Ref. [358]. We note that the $\mu^+\mu^-$ channel provides the strongest constraints, but the precise values of the branching ratios of such light scalars are not well known (see e.g. Refs. [358, 373]). Here, we conservatively assume a 100% branching ratio to hadrons in the mass range of $1\,\text{GeV} \lesssim m_A \lesssim 2m_\tau$. This is conservative in the sense that introducing a small branching ratio to muons strengthens the resulting bound. For $2m_\tau \lesssim m_A < 9\,\text{GeV}$, we use the branching ratios as recently computed in Ref. [374] which incorporate QCD corrections. We find similar constraints as those previously obtained in the recent analysis of Refs. [358] and [373] for pseudoscalar and scalar mediators, respectively. All BaBar constraints are presented at the 90% confidence level in this study.

7.2.4 Direct Detection

The constraints utilized in this study on the dark matter's elastic scattering cross section with nuclei have been derived from the latest results of the LUX Collaboration [168], which are only slightly more stringent than those recently presented by the PANDA-X experiment [169].

For all tree-level cross sections, we use the expressions as presented in Appendices B and C of Ref. [329]. One-loop cross sections for the scalar mediated t-channel interaction and the s-channel vector mediated loop-suppressed interaction are provided in Refs. [334] and [375],

respectively. The remaining t-channel models, which are also loop suppressed, suffer from the problem that they are not generically gauge invariant. Consequently, scattering cross sections for these models are calculated by introducing a factor that suppresses the cross section by the same factor that would appear if the interaction were mediated by a massive photon, i.e. $(g^2 \log(m_b^2/m_{\rm med}^2)/(64\pi^2 m_{\rm med}^2))^2$.

For each model, we calculate the expected number of events in a xenon target following the procedure outlined in Ref. [376], adopting a standard Maxwellian velocity distribution ($v_0 = 220$ km/s, $v_{\rm esc} = 544$ km/s, $\bar{v}_{\rm Earth} = 245$ km/s), a local density of $0.3\,{\rm GeV/cm^3}$ and an exposure of 3.35×10^4 kg-day. Form factors and nuclear responses are calculated following the procedures outlined in Refs. [134, 377]. We take the efficiency for nuclear recoils as a function of energy from Fig. 2 of Ref. [168], and derive bounds at the 90% confidence level, assuming 4.2 expected background events and applying Poisson statistics.

7.3 Pseudoscalar Mediated Dark Matter

In this section, we will consider models in which the dark matter annihilates through the s-channel exchange of a spin-0 mediator, A. We begin by considering a fermionic dark matter candidate, χ, with interactions as described by the following Lagrangian:

$$\mathscr{L} \supset \left[a\bar{\chi}\lambda_{\chi p} i\gamma^5 \chi + \sum_f y_f \bar{f}(\lambda_{fs} + \lambda_{fp} i\gamma^5) f \right] A\,, \tag{7.1}$$

where $a = 1(1/2)$ for a Dirac (Majorana) dark matter candidate. Although we describe the interactions of the SM fermions in terms of their yukawas, $y_f \equiv \sqrt{2} m_f/v$, the quantities

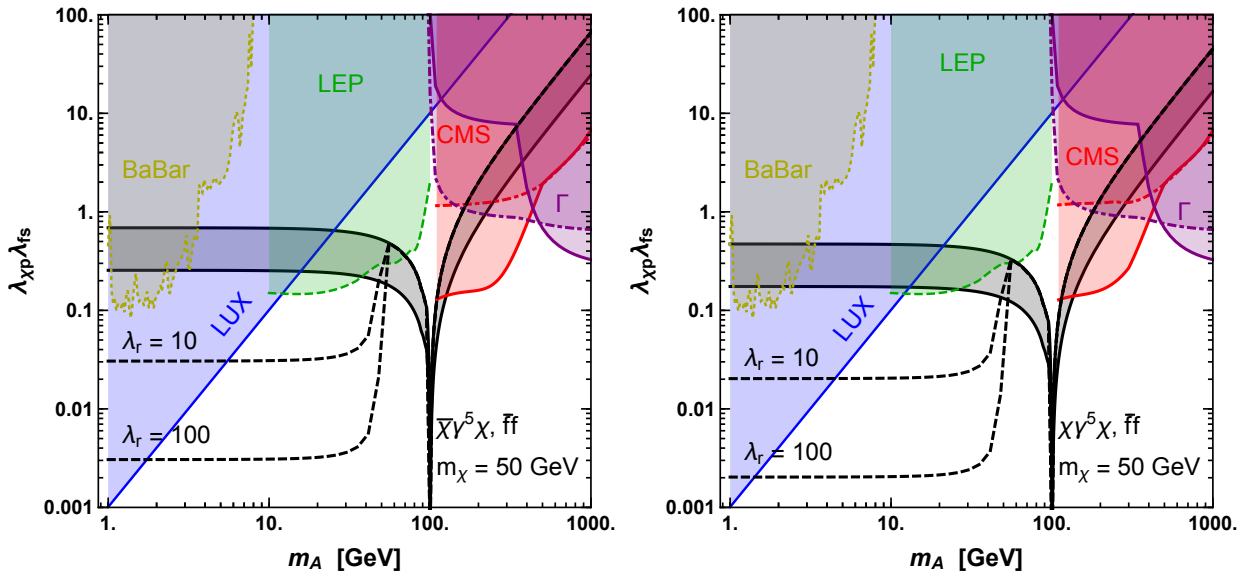

Figure 7.1: Constraints on a 50 GeV Dirac (left) and Majorana (right) dark matter candidate which annihilates through a spin-0 mediator with a pseudoscalar coupling to the dark matter and a (universal) scalar coupling to SM fermions. The black dashed (solid) lines include (neglect) annihilations to mediator pairs for several values of $\lambda_r \equiv \lambda_\chi/\lambda_b$. The upper boundary of the shaded black region is where the correct thermal relic abundance is obtained, whereas along the lower boundary the low-velocity annihilation cross section is at its minimum value required to potentially generate the observed gamma-ray excess. The constraints from CMS assume $\lambda_r = 1/3$ (solid) and $\lambda_r = 3$ (dash-dot), and are compared with the bounds enforcing $\Gamma_A/m_A = 0.1$ (purple) for the same coupling ratios. LEP and BaBar constraints are presented for $\lambda_r = 10$ and 1, respectively.

λ_{fs} and λ_{fp} allow for arbitrary values of each coupling. Here, v is the SM Higgs vacuum expectation value, i.e. $v \simeq 246$ GeV. Assuming that λ_{bs} or λ_{bp} is not much smaller than that of the other SM fermions, dark matter will annihilate largely to $b\bar{b}$ in this model. For this dominant annihilation channel, a dark matter mass of approximately 50 GeV is required to generate the observed spectral shape of the Galactic Center excess [227, 378], and we adopt this value throughout this section.

In the left (right) frame of Fig. 7.1, we plot the constraints on the parameter space of a simplified model with dark matter in the form of a Dirac (Majorana) fermion and a

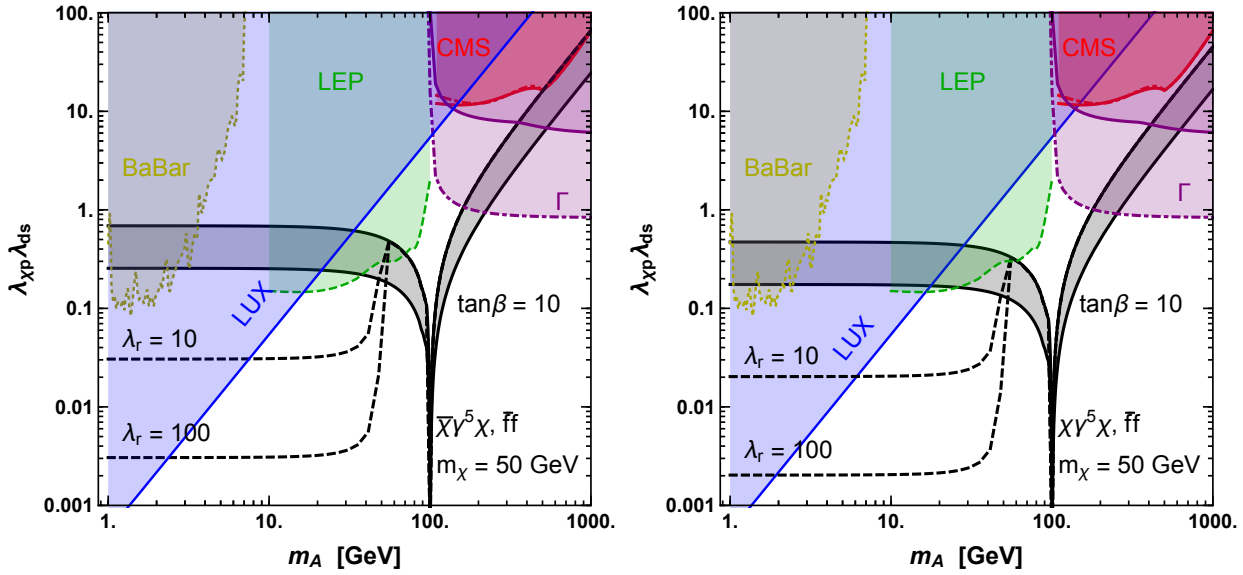

Figure 7.2: As in Fig. 7.1 but for $\tan\beta = 10$, where $\tan\beta$ is defined as the ratio of the mediator's couplings to down-type and up-type fermions.

mediator with a pseudoscalar coupling to the dark matter ($\bar{\chi}\gamma^5\chi$) and scalar couplings to SM fermions ($\bar{f}f$), assuming a common scalar coupling to all SM fermions (as motivated by minimal flavor violation), λ_{fs}[16]. In each frame, the upper boundary of the shaded black region represents the the value of the product of the couplings that is required to generate an acceptable thermal relic abundance, assuming standard cosmology. The lower boundary of this region corresponds to a more relaxed assumption, requiring only that the low-velocity annihilation cross section is large enough to potentially generate the observed gamma-ray excess, $\langle\sigma_{\chi\chi}v\rangle > 3\times10^{-27}$ cm^3/s (or twice this value in the case of a Dirac particle). If $m_A < m_\chi$, dark matter can annihilate directly to mediator pairs via t-channel χ exchange. In these figures, we plot as dashed black lines the parameter space which generates the observed thermal relic abundance for several values of $\lambda_r \equiv \lambda_\chi/\lambda_b$. One should keep in

[16]Note that the product of couplings in these models be quite large, occasionally appearing to violate perturbativity. This need not be the case, however, as we have not included the yukawa contribution to the SM coupling, which may significantly suppress this product.

mind that if the dark matter annihilates significantly to mediator pairs in the low-velocity limit, a higher value for the dark matter mass is generally required in order for the resulting gamma-ray spectrum to be consistent with the observed features of the Galactic Center excess [333, 342, 343]. We compare these curves to the constraints derived from LUX (blue), CMS/LHC (red), LEP (green), and BaBar (yellow).

In the case of CMS, the most stringent constraint in this class of models derives from searches for events with a single jet and missing transverse energy (MET). As the sensitivity of collider searches depends not only on the product of the couplings, but also on their ratio, we present constraints for multiple values of λ_r. In Fig. 7.1, the solid (dot-dashed) lines correspond to CMS constraints for $\lambda_r = 1/3$ (3), while LEP and BaBar constraints are derived assuming $\lambda_r = 10$ and $\lambda_r = 1$, respectively. The regions bounded by a purple solid (dot-dashed) line represent those in which the calculated width of the mediator exceeds one tenth of its mass, for $\lambda_r = 1/3$ (3). As described in Sec. 7.2.1, we set $\Gamma_A = 0.1\, m_A$ throughout this region of parameter space, and take this to be indicative of additional particles and/or interactions that are not described by our simplified model.

The constraints from LEP rely on an effective coupling of the SM Z to ZA, and are thus highly model dependent. While this constraint does apply, for example, to the case in which the couplings of the A to SM fermions are the result of mixing with the SM Higgs, there are many other scenarios in which a spin-0 mediator can couple to the SM fermions while having a suppressed coupling to the Z.

Several of the constraints shown in Fig. 7.1 depend on the ratios of the various couplings of the mediator. In particular, since the LHC constraints are dominated by diagrams in which

a scalar mediator is produced through a top quark loop, such constraints may be much weaker if the top quark coupling is suppressed. To illustrate this, we plot in Fig. 7.2 the derived constraints assuming $\tan\beta = 10$, where $\tan\beta$ is defined as the ratio of the mediator's couplings to down-type and up-type fermions, $\tan\beta \equiv \lambda_d/\lambda_u$. While bounds from LEP, LUX and BaBar are not significantly affected by the value of $\tan\beta$, mono-jet+MET bounds can be noticeably reduced, in particular in the case of $\lambda_r \ll 1$. Increasing $\tan\beta$ also reduces the width of the mediator for $m_A > 2m_t$, potentially opening up additional parameter space.

We repeat this exercise in Fig. 7.3 for the case of a mediator with pseudoscalar couplings to both the dark matter and to SM fermions. In this case, the dark matter's elastic scattering cross section with nuclei is both spin-dependent and heavily momentum suppressed ($\sigma_{SD} \propto q^4$), making direct detection experiments largely insensitive to these models. The bounds derived from colliders, however, are relatively insensitive to whether SM fermions couple via a scalar or pseudoscalar interaction. We emphasize that, as in the previous case, a large portion of parameter space remains viable for this model, especially should the top-mediator coupling be suppressed.

Next, we consider dark matter in the form of a scalar ϕ, with a Lagrangian given by:

$$\mathscr{L} \supset \left[a\mu_\phi |\phi|^2 + \sum_f y_f \bar{f} \lambda_{fp} i\gamma^5 f \right] A \,, \tag{7.2}$$

where $a = 1(1/2)$ for a complex (real) dark matter particle.

The phenomenology of this model is summarized in Fig. 7.4, for the cases of a complex (left frame) or real (right frame) scalar. LHC signatures for this model are rather different

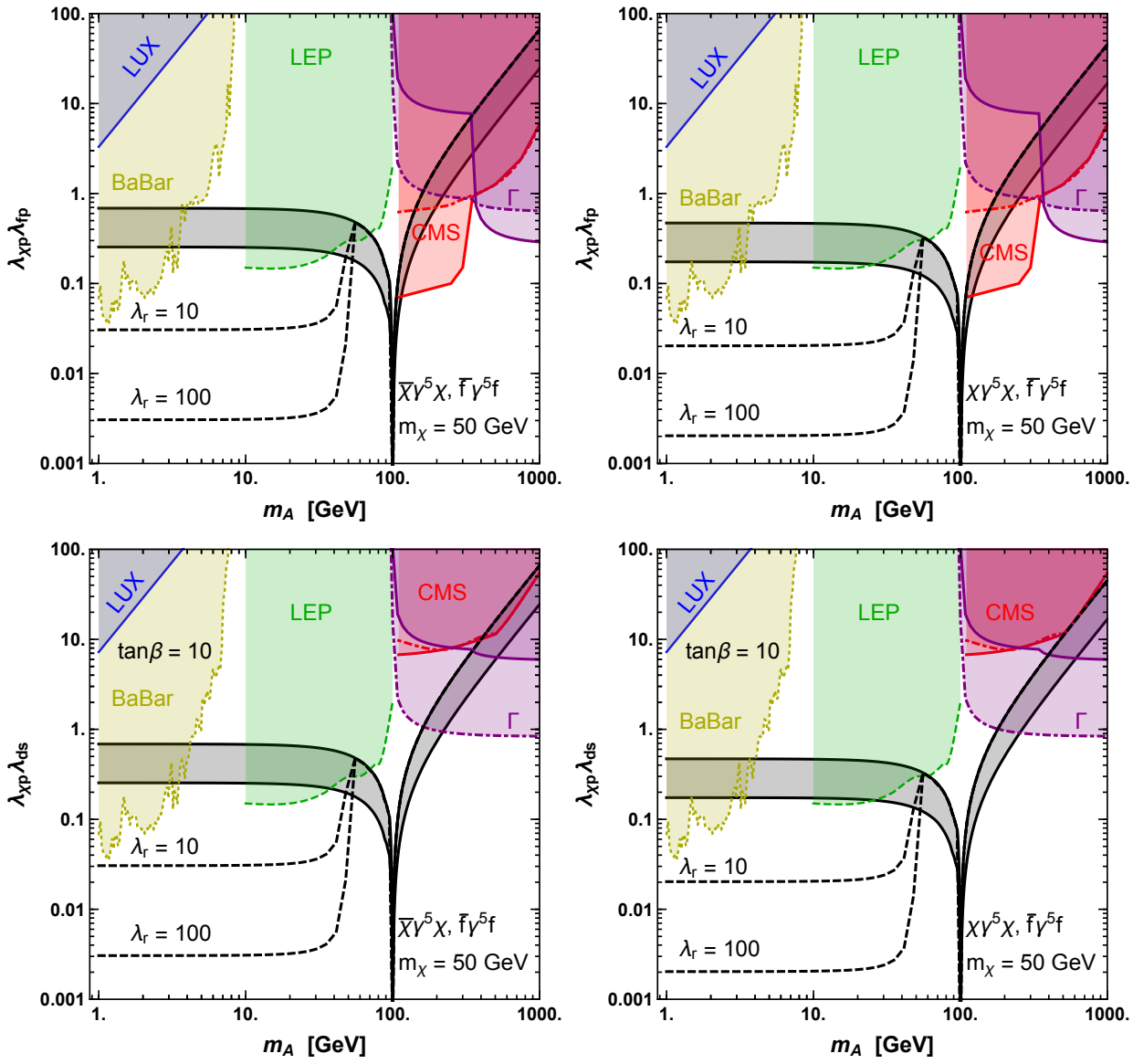

Figure 7.3: As in Fig. 7.1 but for a mediator with purely pseudoscalar couplings. The upper (lower) frames correspond to $\tan\beta = 1$ (10).

from in the case of fermionic dark matter as the decay of the spin-0 mediator to dark matter is heavily suppressed. Instead, the dominant constraint from the LHC results from searches for a Higgs-like particle decaying to $\tau^+\tau^-$. At very large mediators masses, however, ($m_A \gtrsim 600$ GeV), the branching ratio to $\tau^+\tau^-$ is reduced and di-jet resonances become slightly more constraining (this accounts for the dip-like feature appearing in the CMS bound). As in the previous scenarios, LEP bounds on scalar decays to $b\bar{b}$ are very constraining in the region $10\,\mathrm{GeV} < \mathrm{m_A} < 100$ GeV, but only apply in models in which the mediator couples either directly or indirectly to the Z.

In the lower frames of Fig. 7.4 , we show how these bounds change if the mediator does not couple to leptons and has an asymmetric coupling to up-like and down-like quarks with $\tan\beta = 2$. This choice can open a window of parameter space for $100\,\mathrm{GeV} \lesssim m_A \lesssim 2m_t$, depending on the precise values of $\tan\beta$ and λ_r.

Next, we consider the case of vector dark matter X^μ:

$$\mathscr{L} \supset \left[a\mu_X X^\mu X^\dagger_\mu + \sum_f y_f \bar{f}\lambda_{fp} i\gamma^5 f \right] A\,, \tag{7.3}$$

where $a = 1(1/2)$ for a complex (real) dark matter particle.

Constraints on this model are shown in Fig. 7.5. The dominant decay mode of the mediator in this model, and thus the most constraining LHC search, depends on the mass of the mediator. For $m_A \simeq 100$ GeV the dominant decay is to dark matter, and thus the most constraining search is that based on mono-jet+MET events. This picture is very different for larger mediator masses, however, for which constraints based on searches for Higgs bosons

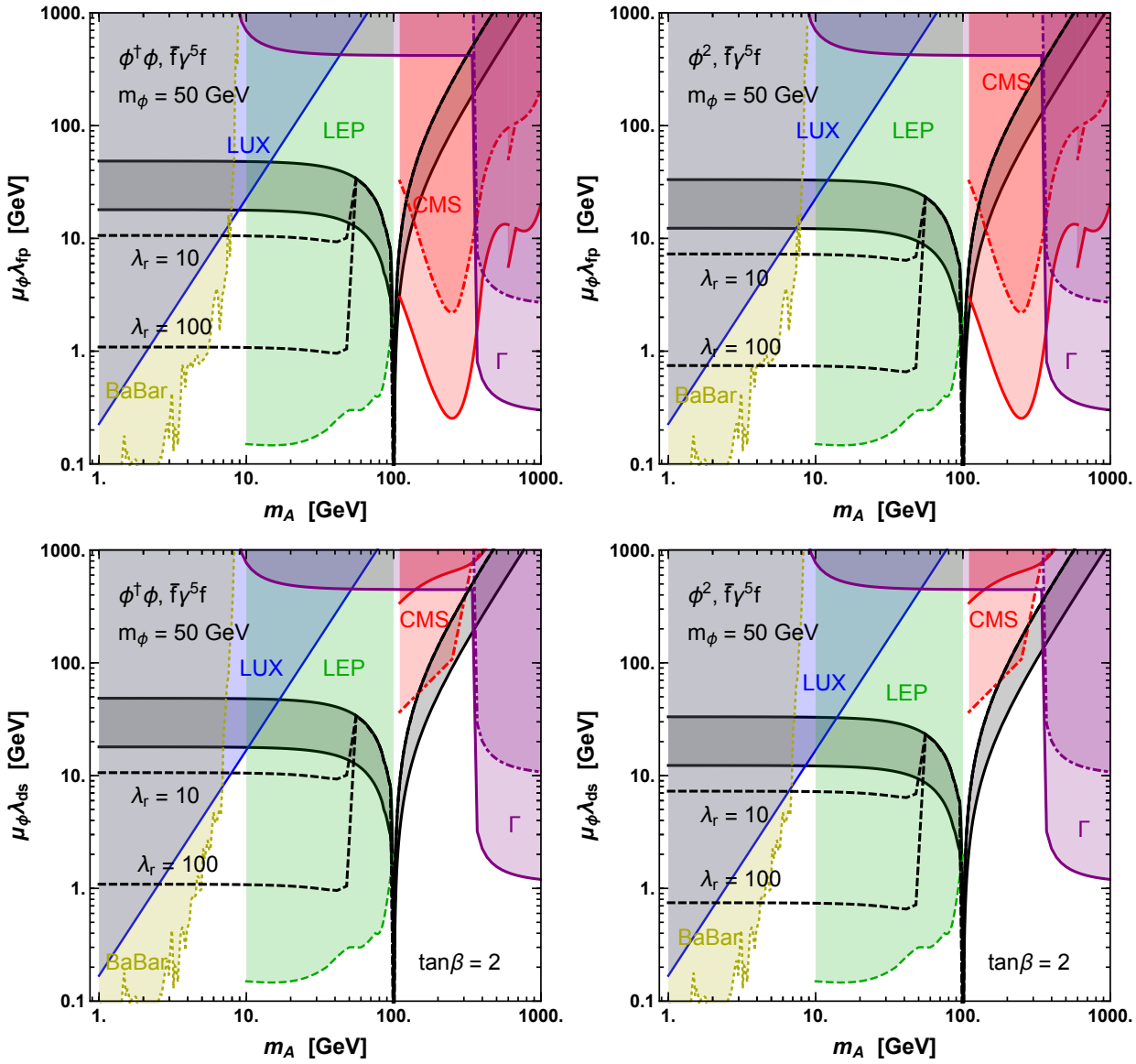

Figure 7.4: As in the previous figures, but for a 50 GeV complex (left) or real (right) scalar dark matter candidate, which annihilates through a spin-0 mediator with a pseudoscalar coupling to SM fermions. In the upper frames, we take the mediator's couplings to be equal for all SM fermions, whereas in the lower frames the mediator does not couple to leptons and $\tan\beta = 2$.

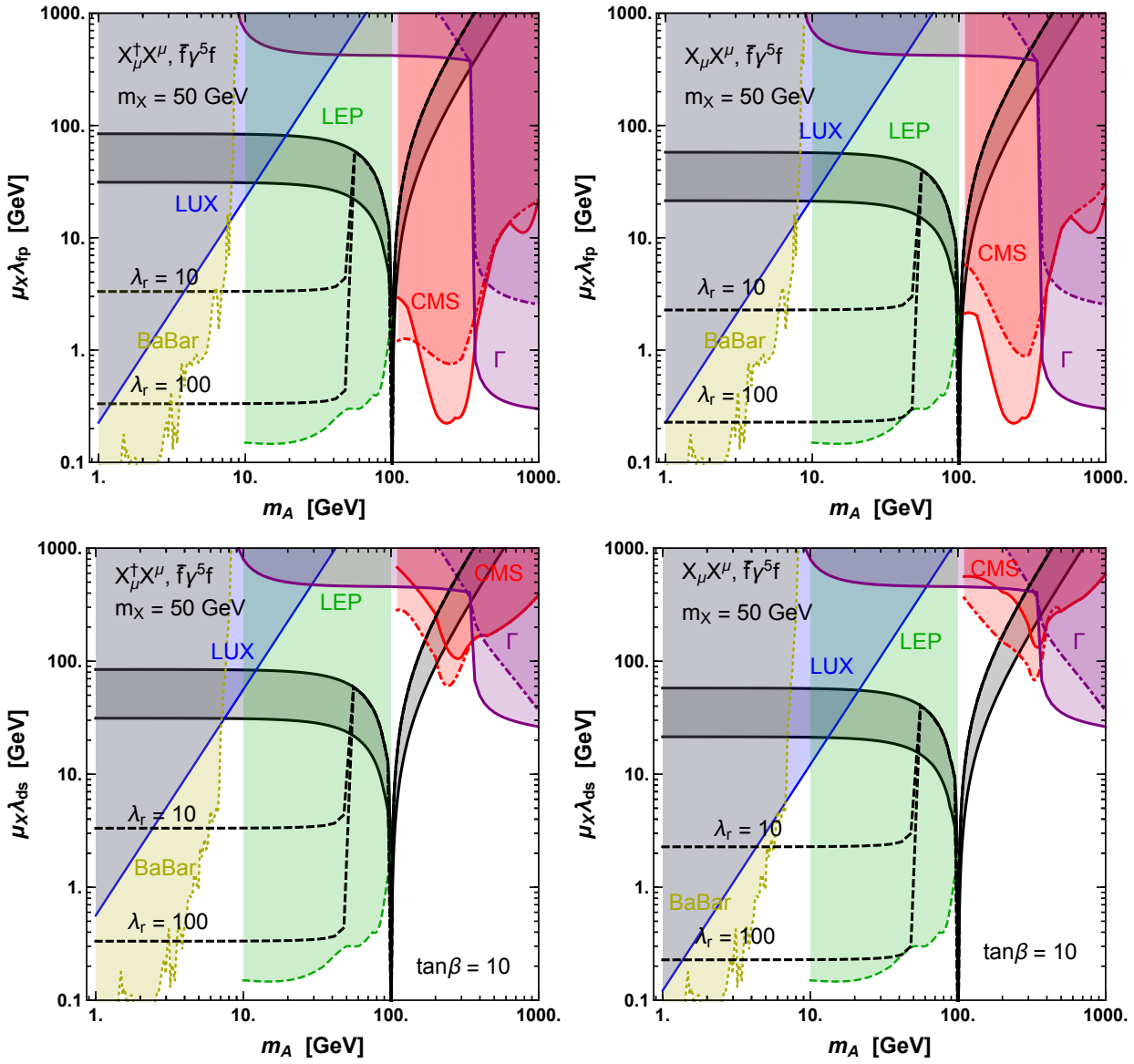

Figure 7.5: As in previous figures, but for a 50 GeV complex (left) and real (right) vector dark matter candidate which annihilates through a spin-0 mediator with a pseudoscalar coupling to SM fermions. In the upper frames, we take the mediator's couplings to be equal for all SM fermions, whereas in the lower frames the mediator does not couple to leptons and $\tan\beta = 10$.

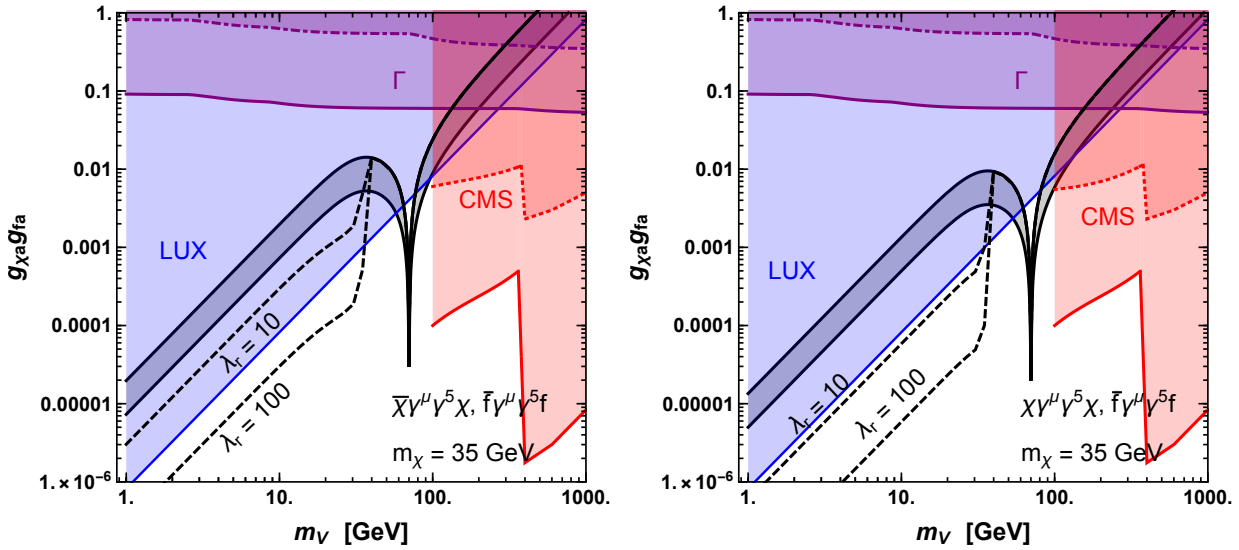

Figure 7.6: As in previous figures, but for a 35 GeV Dirac (left) and Majorana (right) dark matter candidate which annihilates through a spin-1 mediator with axial couplings to both dark matter and (universally) to SM fermions. In this figure, the dotted red (CMS) line corresponds to the case of $g_{\chi v} = 1$ (i.e. $\lambda_r >> 1$).

decaying to $\tau^+\tau^-$ become more stringent. Both of these search channels significantly exclude mediator masses above 100 GeV in this class of models, for both $\lambda_r = 3$ and $\lambda_r = 1/3$. Similar to in the scalar dark matter case, however, we can relax some of these constraints by suppressing the mediator's couplings to leptons and/or by increasing $\tan\beta$ (as shown in the lower frames of Fig. 7.5).

7.4 Vector Mediated Dark Matter

In this section we consider fermonic dark matter annihilating through the s-channel exchange of a spin-1 mediator, V_μ, with Lagrangians of the form [329, 332]:

$$\mathscr{L} \supset \left[a\bar{\chi}\gamma^\mu(g_{\chi v} + g_{\chi a}\gamma^5)\chi + \sum_f \bar{f}\gamma^\mu(g_{fv} + g_{fa}\gamma^5)f \right] V_\mu \,, \tag{7.4}$$

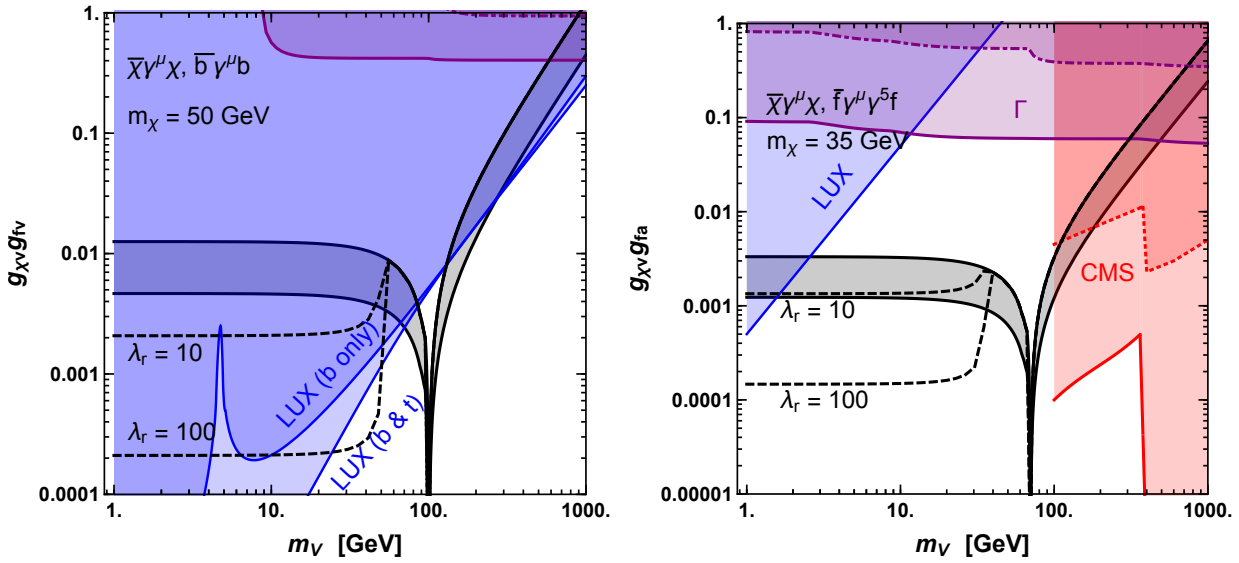

Figure 7.7: As in previous figures, but for a 50 GeV Dirac dark matter candidate with vector couplings to both dark matter and to b-quarks (left), and for a 35 GeV Dirac dark matter candidate with vector and axial couplings to dark matter and (universally) to SM fermions, respectively (right). LHC bounds are shown for $\lambda_r = 1/3$ (solid) and $g_{\chi v} = 1$ (i.e. $\lambda_r \gg 1$) (dotted).

where $a = 1(1/2)$ for a Dirac (Majorana) dark matter candidate. For the case of comparable couplings to various SM fermions this class of models require a $\simeq$ 35 GeV dark matter candidate to generate a signal consistent with the Galactic Center excess. Unless stated otherwise, we will adopt this value for the dark matter mass throughout this section.

We begin in Fig. 7.6 by considering the constraints on a Dirac (left) and Majorana (right) dark matter candidate that annihilates through a mediator with purely axial couplings. As spin-dependent elastic scattering with nuclei is unsuppressed in this class of models, current LUX constraints force such models to either live on resonance ($m_\chi \simeq m_V/2$), or have a mediator mass $m_V < m_\chi$ and with $\lambda_r \gg 1$. LHC constraints on this model from searches for di-lepton resonances ($m_V > 400$ GeV) and mono-jet+MET searches (100 GeV $< m_V <$ 400 GeV) limit mediator masses in this model to be below $\simeq$ 100 GeV. LHC bounds are shown

in this figure for $\lambda_r = 1/3$ (solid) and $g_{\chi v} = 1$ (i.e. $\lambda_r \gg 1$) (dotted). Collider constraints for this model are difficult to evade as they do not rely exclusively on couplings to leptons or to specific species of quarks. Such bounds could be evaded, however, if the mediator were to couple exclusively to third generation quarks. An example of such a model is shown in the left frame of Fig. 7.7, where we consider a 50 GeV Dirac dark matter candidate that annihilates through a spin-1 mediator with vector couplings to both dark matter and b-quarks (and possibly also t-quarks). While the leading order elastic scattering diagram arises at loop level in this case, the vector coupling leads to stringent constraints from direct detection experiments. The dominant constraints from the LHC on vector mediated models typically arise from searches for mono-jet+MET events and di-lepton resonances. Since the production of the vector mediator is in most cases dominated by valence quarks, however, the sensitivity of collider searches is heavily suppressed and thus do not probe significant parameter space in this model. We do not show any LHC constraints in this figure.

In the right panel of Fig. 7.7, we consider the phenomenology of models where the mediator couples to Dirac dark matter and fermions with a vector and an axial coupling, respectively. The elastic scattering cross section in this case is both spin-dependent and momentum suppressed, and thus such experiments have only recently begun probing this model. LHC constraints from di-lepton resonances ($m_V > 400$ GeV) and mono-jet+MET searches ($100\,\mathrm{GeV} < \mathrm{m_V} < 400$ GeV) are, as before, extremely constraining. That being said, di-lepton constraints can be easily avoided if the mediator couples only to quarks, and mono-jet constraints can be significantly relaxed if the mediator couples, for example, only to the third generation. LHC bounds are shown for $\lambda_r = 1/3$ (solid) and $g_{\chi v} = 1$ (i.e. $\lambda_r \gg 1$)

(dotted).

7.5 Dark Matter Annihilating Through t-Channel Mediators

Finally, we consider four scenarios in which the dark matter annihilates through the t-channel exchange of a colored and electrically charged mediator to $b\bar{b}$ [334, 379, 380]. These cases consist of a Dirac dark matter candidate, χ, and spin-0 mediator, A:

$$\mathscr{L} \supset \lambda_\chi \bar{\chi}(1+\gamma^5) f A + \lambda_\chi \bar{f}(1-\gamma^5)\chi A^\dagger \,, \tag{7.5}$$

a Dirac dark matter candidate, χ, and a spin-1 mediator, V_μ:

$$\mathscr{L} \supset g_\chi \bar{\chi}\gamma^\mu(1+\gamma^5) f V_\mu + g_\chi \bar{f}\gamma^\mu(1-\gamma^5)\chi V_\mu^\dagger \tag{7.6}$$

and a real or complex vector dark matter candidate, X_μ, with a fermionic mediator, ψ:

$$\mathscr{L} \supset g_X \bar{\psi}\gamma^\mu(1+\gamma^5) f X_\mu^\dagger + g_X \bar{f}\gamma^\mu(1-\gamma^5)\psi X_\mu \,. \tag{7.7}$$

Note that we consider these specific combinations of scalar and pseudoscalar or vector and axial couplings as they are the only examples for which the scalar contact interaction with nuclei is supressed. Instead, elastic scattering occurs in each of these models through a loop-suppressed vector coupling [329, 334, 381].

In Fig. 7.8, we summarize the phenomenology of this class of models. In the upper left frame we consider the case of a Dirac dark matter particle and spin-0 mediator. In the

remaining frames of this figure, we summarize the phenomenology of models with a Dirac dark matter candidate and a vector mediator (upper right), a complex vector dark matter candidate with a fermonic mediator (lower left), or a a real vector dark matter candidate with a fermonic mediator (lower right). In each case, we find that the combination of constraints from the CMS sbottom search and LUX exclude the entire parameter space of this class of models. We also note that the scenarios with a vector dark matter candidate are rather unphysical over much of the parameter space shown due to the very large width of the mediator.

7.6 Summary

In this section, we have revisited the range of dark matter scenarios that could potentially generate the observed characteristics of the Galactic Center gamma-ray excess, without conflicting with any constraints from colliders or direct detection experiments. We have taken a simplified models approach, considering the 16 scenarios that were previously found to be viable in Ref. [329] (and listed in Table 7.1). Each of these models features a low-velocity dark matter annihilation cross section that is unsuppressed (i.e. s-wave), and was found to be consistent with all constraints as of 2014. Note that we have not considered any hidden sector models (i.e. models in which the dark matter annihilates into unstable particles without sizable couplings to the Standard Model) which, although potentially viable [339, 342, 343], are beyond the scope of this work.

The main results of this study can be summarized as follows:

- Scalar, fermonic, or vector dark matter that annihilates through a mediator with pseu-

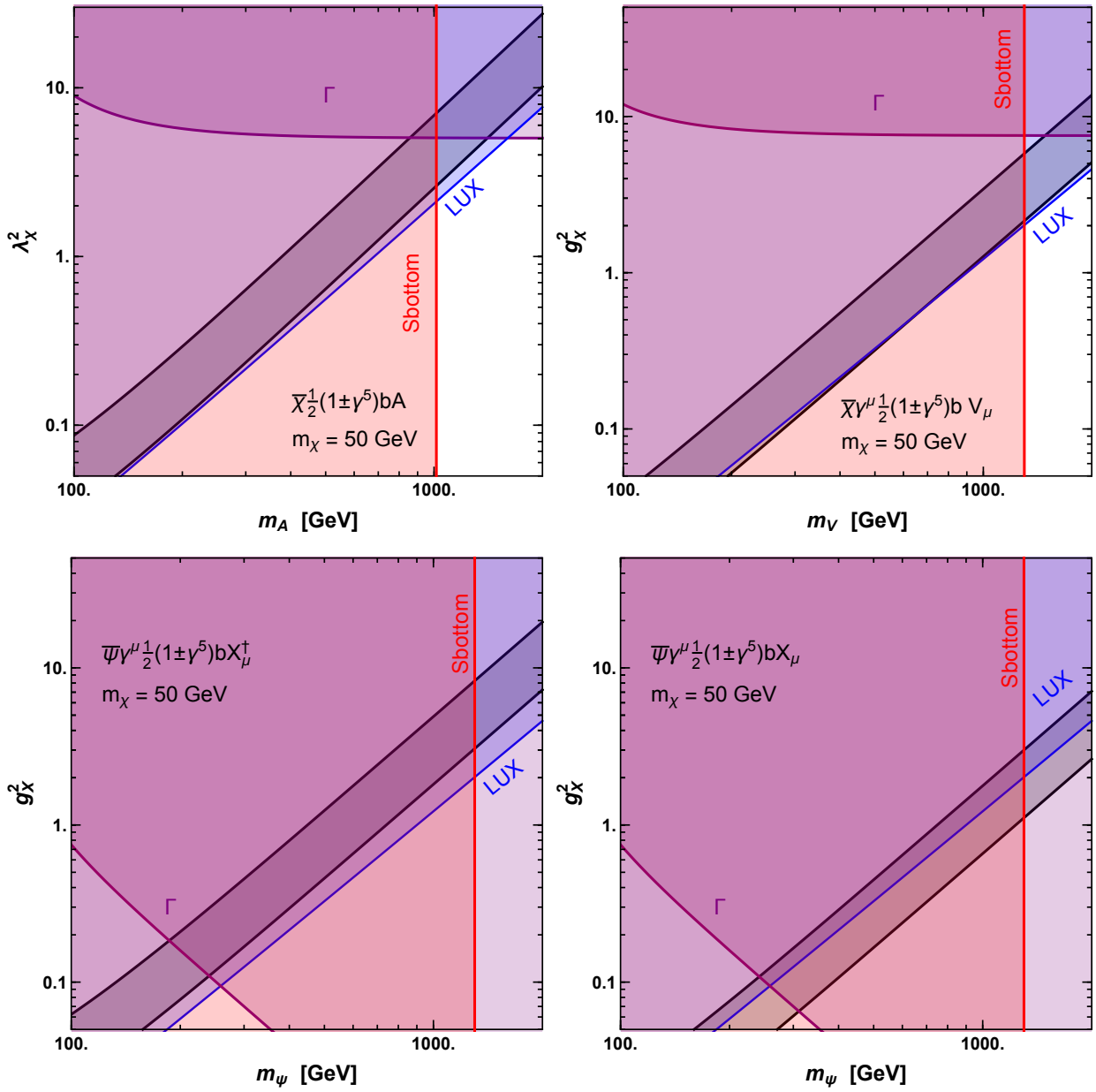

Figure 7.8: As in previous figures, but for a 50 GeV dark matter candidate which annihilates through a t-channel diagram to $b\bar{b}$. In the upper left (right) frame, we consider the case of a Dirac dark matter candidate with a scalar (vector) mediator. In the lower left (right) frame, the dark matter is a real (complex) vector, mediated by a Dirac fermion. The entire parameter space of these models is ruled out by the combined results of LUX and sbottom searches at the LHC.

doscalar couplings can in many cases evade all current constraints, for mediator masses between $\sim$10 GeV and several hundred GeV.

- Dark matter that annihilates through a spin-1 mediator is ruled out by the results of LUX/PandaX-II unless the mass of the mediator is approximately equal to twice the mass of the dark matter (near an annihilation resonance). An exception to this conclusion is found in the case of a mediator with a purely vector coupling to the dark matter and a purely axial coupling to Standard Model fermions, which is potentially viable for mediator masses between roughly $\sim$ 1 GeV and 200 GeV.

- All scenarios in which the dark matter annihilates through a t-channel process are now ruled out by a combination of constraints from LUX/PandaX-II and the LHC.

- Constraints from LEP-II and BaBar restrict many of the pseudoscalar mediated scenarios considered in this study. In particular, mediators with a mass in the $\sim$10-100 GeV range are often ruled out by LEP if they couple significantly to the Standard Model Z (such as in scenarios in which the mediator obtains its couplings to Standard Model fermions through mixing with the Higgs).

Dark matter scenarios that are capable of generating the Galactic Center excess are now significantly more constrained than they were even a few years ago. As the sensitivity of XENON1T, LZ and other direct detection experiments, as well as the LHC, continues to improve, either a discovery will be made, or the vast majority of the currently viable parameter space identified in this study will be excluded. If such searches do advance without the appearance of new signals, hidden sector scenarios will become increasingly attractive,

in particular within the context of the Galactic Center.

8 Prospects for Distinguishing Dark Matter Models Using Annual Modulation

8.1 Model Selection From Direct Detection Experiments

A vast array of independent astrophysical and cosmological observations testify to the existence of a non–baryonic form of matter that dominates gravitational potential wells and dictates the dynamics and structure in the Universe. However, the particles comprising this dark matter (DM) have so far evaded laboratory probes, despite a direct detection program that has now been mature for several decades. As the next–generation direct detection experiments that incorporate increasingly sensitive detection technologies come online, they will start to probe the final portions of DM parameter space before encountering the so–called 'irreducible neutrino background' [204, 382–390]. Generation 2 (G2) experiments that are currently, or will soon be, taking data (such as Xenon1T [383], SuperCDMS SNOLAB [204], and LZ [384]; see also [382] for a review) may well be on the cusp of important discoveries, as many interesting theories of DM predict scattering cross sections that live in these portions of parameters space. For example, heavy $SU(2)$–doublet and –triplet fermions, such as the Higgsinos and the wino of supersymmetry, are expected to have cross sections of order $\sigma_{\rm SI} \sim \mathcal{O}(\text{few} \times 10^{-48})\,\text{cm}^2$ [391–393] (about an order of magnitude below the current limits [168, 169]), fixed by their Standard Model gauge quantum numbers alone, while a heavy $SU(2)$–singlet fermion, like the bino, is around an order of magnitude lower depending on its coannihilation partner [394]. Models with kinematically suppressed tree–level scattering may also be embedded in more complete dark sectors that have loop–level cross sections in

this same range [330, 395–397].

Because so many theories can be accommodated in the parameter space that will be imminently probed by a variety of experiments, it is timely to plan for the science opportunities associated with the first detection of DM particles. Most notably, in case of a confirmed detection, understanding the dark sector dynamics at all energy scales will rely solely on examining low–energy recoils of detector elements and solving the "inverse problem" to identify the underlying description of DM–baryon interactions. At the same time, all the information about the dark sector interactions accessible to these measurements is contained within the coefficients of the effective field theory of dark matter direct detection (EFT) [134, 135, 398, 399]. The effective description captures the nontrivial nuclear physics induced by some of the best–motivated UV–complete theories of DM [123, 400, 401] through an exhaustible list of nuclear responses that these interactions trigger [134, 135, 398]. It thus provides a systematic framework for classifying and describing a wide variety of DM theories and corresponding phenomenologies observable with direct detection, and we will utilize it in this work.

On the other hand, due to Poisson noise in the number counts of recoil events per unit energy, and similarities in the shape of the nuclear–recoil–energy spectra amongst different interactions, correctly identifying the DM model will present a difficult task in practice, particularly for a single experiment. Recent studies have shown that discriminating between interactions in an agnostic analysis is possible only with strong signals with hundreds of observed recoil events, and only when measurements on targets with sufficiently diverse nuclear physics characteristics are jointly analyzed [400, 402] (or, potentially, by jointly analyzing di-

rect and indirect detection data [403]). Thus, using energy spectra to break degeneracies in the DM modeling space crucially relies on complementarity of available target materials [133, 388, 400, 402, 404–408], but this still does not guarantee successful model selection if a DM signal is confirmed [400, 402, 408].

Almost since the dawn of direct detection related DM studies, the motion of Earth relative to DM bound in the galactic halo has been predicted to provide a distinctive signature of DM through annual modulation of the nuclear recoil rate [81, 95, 409–412]. While the annual modulation signal is typically assumed to take an approximately experiment–independent form, recent work has pointed out that non–standard interaction cross sections could produce a modulation signal that is unique to each target element [94, 413]. More generally, a non–trivial velocity dependence in the cross section effectively changes the phase space integral that governs the total event rate of recoil events in a given experiment, producing a non–standard modulation signal. Thus, it may be expected that interactions differing solely by the DM velocity dependence of their corresponding cross sections may give rise to different phase and/or amplitude of the annual modulation signal.

Motivated by this argument, we propose here that an analysis of the time dependence of scattering events can help discriminate between interaction models whose recoil energy spectra are otherwise degenerate on a single target material. Using the method of [400], we create a suite of simulations under a variety of scattering theories, and apply a Bayesian model selection analysis on the simulated data to evaluate the chance for correctly identifying the underlying model. We statistically evaluate the enhancement in prospects for accurate model selection when the annual modulation signal is analyzed in combination with recoil–

energy measurements in the future–generation direct detection experiments.

The rest of the paper is organized as follows. In Sec. 8.2 we review the calculation of the direct detection scattering rate and discuss how direct detection observables (including the annual modulation) differ depending on the momentum and velocity dependence of the interaction. Sec. 8.3 summarizes the models and experiments considered in this work, and describes our simulations and analysis method. We present the results of this analysis in Sec. 8.5, and conclude in Sec. 8.6.

8.2 Scattering in Direct Detection Experiments

The key measurement of most direct detection experiments is the nuclear recoil energy spectrum — the number count of nuclear recoil events per recoil energy E_R, per unit time t, per unit target mass, which reads

$$\frac{dR}{dE_R dt}(E_R, t) = \frac{\rho_\chi}{m_T m_\chi} \int_{v_{\rm min}}^{v_{\rm esc,lab}} v f(\mathbf{v}, t) \frac{d\sigma_T}{dE_R}(E_R, v) d^3v \,. \tag{8.1}$$

Here, ρ_χ is the local DM density; m_χ is the DM particle mass; m_T is the mass of the target nucleus T; $\mathbf{v}$ is DM velocity vector of magnitude v (in the lab frame); $f(\mathbf{v}, t)$ is the observed DM velocity distribution; $d\sigma_T/dE_R = m_T \sigma_T / 2\mu_T^2 v^2$ is the differential cross section for DM scattering off a nucleus T; and $\mu_T \equiv \frac{m_T m_\chi}{m_T + m_\chi}$ is the reduced mass of the DM particle and the target nucleus. Integration limits are the minimum velocity a DM particle requires in order to produce a nuclear recoil of energy E_R, given by $v_{\rm min} = \sqrt{m_T E_R / 2\mu_T^2}$, and the Galactic escape velocity in the lab frame, $v_{\rm esc,lab}$. Here, we define the overall normalization of σ_T as

σ_p, and refer the interested reader to [400] for the interaction–dependent definitions (note that we also list these definitions in the final column of Table 2). We note that σ_p is one of the key free parameters of each scattering interaction.

The differential rate in Eq. (8.1) is determined by the experimental setup, the DM astrophysical and particle properties, the nuclear properties of the target material, and the DM–nucleus interaction. For the purposes of this study, we set the astrophysical parameters to the following values [96, 414]: $\rho_\chi = 0.3$ GeV/cm^3; $v_{\rm esc} = 533$ km/sec (in the Galactic frame), and assume that $f(\mathbf{v})$ is a Maxwellian distribution in the Galactic frame, with a rms speed of 155 km/sec and a mean speed equal to the Sun's rotational velocity around the Galactic center, $v_{\rm lag} = 220$ km/sec. The underlying particle physics interaction determines the calculation of the recoil rate through the differential scattering cross section $d\sigma_T/dE_R$ [123, 400]. Different interactions display different functional dependences on E_R and v, as discussed in detail in Refs. [123, 400] and summarized below in Sec. 8.2.1.

The total rate R of nuclear recoil events (per unit time and unit mass) is given by the integral of the differential rate within the nuclear–recoil energy window $\mathcal{E}$ of a given experiment, $R(t) = \int_{\mathcal{E}} \frac{dR}{dE_R dt} dE_R$. For simplicity, we assume unit efficiency of detection within the analysis window, and rescale individual experimental exposures to take this assumption into account when choosing experimental parameters to represent the capabilities of G2 experiments. In turn, the total expected number of events $\langle N \rangle$ for a fiducial target mass $\mathcal{M}_{\rm fid}$, in experiment that started observation at a time t_1 and ended at a time t_2, is given by

$$\langle N_{\rm tot} \rangle = \mathcal{M}_{\rm fid} \int_{t_1}^{t_2} \int_{\mathcal{E}} \frac{dR}{dE_R dt}(E_R, t)\, dE_R\, dt. \tag{8.2}$$

8.2.1 Momentum and Velocity Dependence

Traditional focus on the two standard scattering cases, spin–independent (SI) and spin–dependent (SD) scattering (the former involves coherent contributions from the entire nucleus, resulting in a cross section that scales quadratically with nucleon number, while the latter scales with the total nuclear spin), obscures the richness of phenomenologies which can arise when these two standard interactions are suppressed [123, 134]. Here we summarize the EFT that catalogues all possible energy and velocity dependencies of the cross section, and thus delineates the modeling space for interactions probed by these experiments, in most general terms. In the Sec. 8.3.1, we highlight several well–motivated examples of scattering models which we use in this work to examine the extent to which including time information can help identification of the underlying DM model.

The EFT of DM direct detection [134, 398] relies on an expansion in two small kinematic variables: $|\vec{q}|/m_n$ and $|\vec{v}_\perp|$; $\vec{q}$ is the change in momentum of the DM particle during the scattering, related to the recoil energy as $\vec{q}^2 = 2m_T E_R$, $|\vec{v}_\perp|$ is the component of the relative velocity of the initial–state particles that is orthogonal to the momentum transfer, and m_n is the mass of the nucleon. For an incoming (outgoing) DM three–momentum $\vec{p}$ ($\vec{p}'$), incoming (outgoing) nuclear three–momentum $\vec{k}$ ($\vec{k}'$), and a DM–nucleon reduced mass $\mu_{\chi n}$, these factors read $\vec{q} = \vec{p}' - \vec{p} = \vec{k} - \vec{k}'$, and $\vec{v}_\perp = \frac{\vec{p}}{m_\chi} - \frac{\vec{k}}{m_n} + \frac{\vec{q}}{2\mu_{\chi n}}$.

These expansion parameters are of the same order of magnitude, but it is important to note that they manifest differently in the observables of the scattering events (see e.g. [400] for a comprehensive discussion). In particular, terms that enter at higher order in $|\vec{q}|/m_n$ deliver a vanishing event rate at both small and large momentum transfer (or, equivalently, recoil

energy), with a maximum rate at some intermediate recoil energy, producing a "turnover" feature in the spectrum. Light mediator models can alternatively contain factors of $m_n/|\vec{q}|$, producing a steep enhancement of the recoil events at low values of $E_{\rm R}$. On the other hand, higher–order terms in $|\vec{v}_\perp|$ produce event rates that monotonically decrease with recoil energy, similar to the case of the standard SI and SD interactions (see Fig. 8.1 for illustration).

As was demonstrated by Ref. [400], interactions that feature different momentum dependence can be differentiated from each other using a single nuclear target, provided a sufficiently large number of events are observed; however, the latter class of models — those that differ only by the power of velocity dependence — are far more difficult to disentangle, leaving substantial degeneracy between well–motivated models. In the following, we develop an intuition for how this degeneracy might be overcome, using annual modulation and time dependence of the scattering rate.

8.2.2 Time Dependence

In Eq. (8.1), the differential rate of nuclear recoils is explicitly denoted as depending on time, which arises as a consequence of the Earth's harmonic motion around the Sun. This motion causes the total DM particle flux observable by direct detection experiments to modulate at the few percent level. The expected phase and amplitude of the modulation depend on the astrophysical and particle properties of DM (see e.g. [81, 87, 415]); they are additionally modified by the effect of gravitational focusing of DM by the Sun, which produces a characteristic energy dependence in the phase of the modulation [79, 81, 98, 416–418].

We illustrate differences in the recoil energy spectra and in the annual modulation sig-

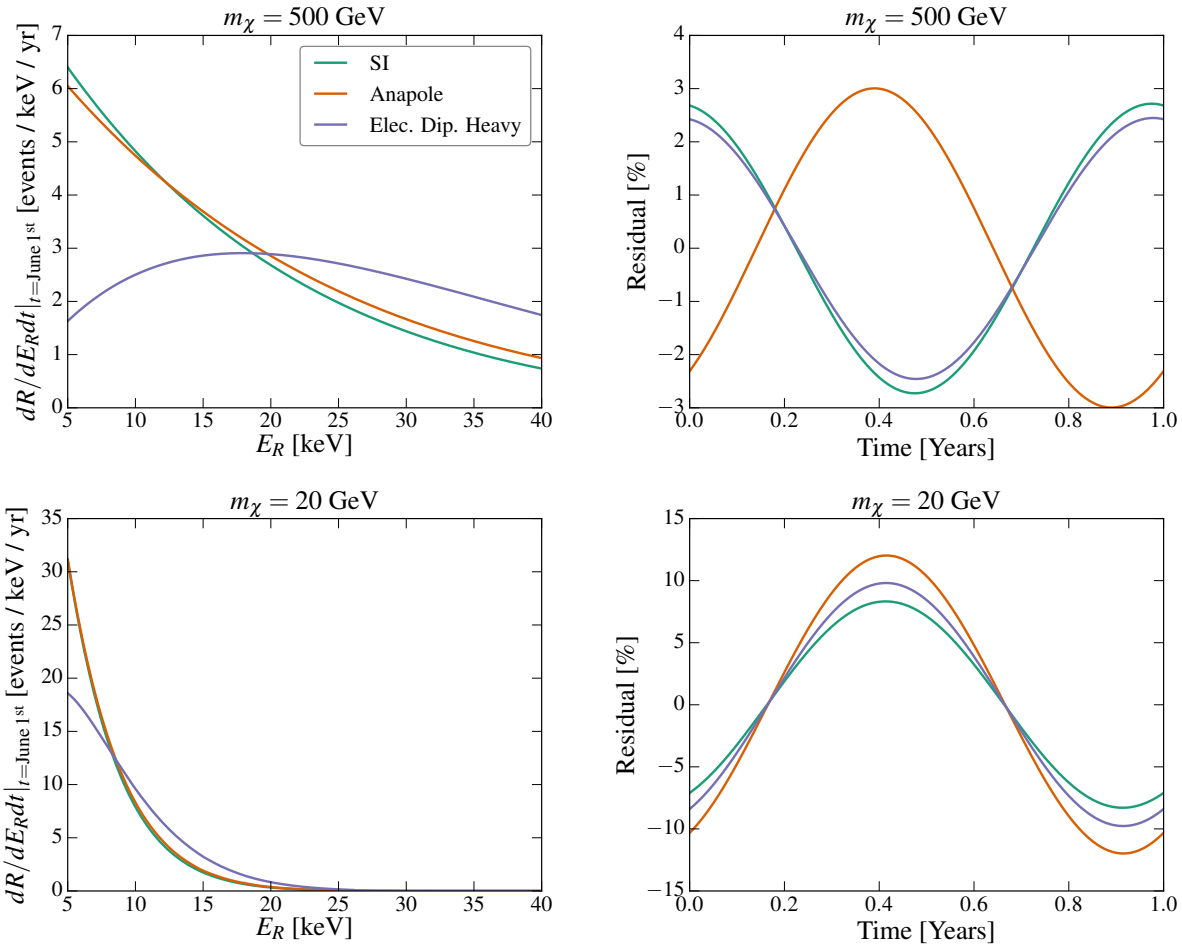

Figure 8.1: Comparison of the nuclear recoil energy spectra (left column) and annual modulation signals (right column) between the SI, anapole, and heavy–mediator electric dipole interaction models on a xenon target, where the cross sections have been normalized to the current LUX 90% confidence level exclusion limit [168]. Top row corresponds to a 500 GeV, and the bottom row to a 20 GeV DM particle. *Left:* Differential event rate (evaluated for June 1^{st}) as a function of the nuclear recoil energy. *Right:* Residual event rate (fractional deviation in the total event rate) as a function of time.

nal in the context of interactions with a differing functional dependence on the momentum transfer and DM velocity in Fig. 8.1, for several DM–nuclei interaction models. Specifically, we compare the standard SI, anapole, and heavy–mediator electric dipole (ED–heavy) interactions (see Sec. 8.3.1 for a more detailed definition of the models). The top row of panels corresponds to a 500 GeV, and the bottom row to a 20 GeV DM particle. Note that the energy spectra for the SI and ED–heavy interactions are distinct in a way that the SI and anapole interactions are not; thus, discerning the SI and anapole hypotheses using the energy spectrum alone is quite challenging, given even the most optimistic expectations for the Poisson noise [400].

However, the annual modulation of the standard SI and anapole interactions can be very different, owing to a non–trivial ($\sim |\vec{v}_\perp|^2$) velocity dependence of the anapole cross section. This non–trivial velocity dependence in turn alters the velocity integral in Eq. (8.1), and consequently leads to a different time dependence of the total event rate in the two interaction models (see also Figs. 1–3 of [413] for an overview of time–dependent behavior of various v–dependent cross sections). For large enough DM mass, this effect can produce a nearly *opposite modulation phase* between the standard SI scenario and the anapole case. Furthermore, differential cross sections which contain multiple non–negligible terms with different velocity dependences can produce annual modulation signals entirely unique to a given target element [94, 413]. The time variation of the rate, and thus the differences between the annual modulation produced by different interactions, is typically expected to be small — on the order of a few percent. Nonetheless, we will show in the following that this small difference can be used to supplement the information contained in the energy

spectrum and substantially aid the process of model selection using a single target element.

8.3 Distinguishing Scattering Models

Our approach, outlined below, follows that of Ref. [400]. To address our main question, we begin by selecting several well–motivated scattering models featuring a similar dependence on the momentum transfer, but a different dependence on the DM velocity (i.e. models with nearly degenerate recoil spectra but qualitatively different annual modulation); we summarize our choice of models in Sec. 8.3.1. Then, we simulate nuclear–recoil events under these models, for three different DM masses. For our simulations, described in detail in Sec. 8.4, we use cross sections that are at the current exclusion limit for a given interaction at hand. In order to capture in the impact of Poisson noise on future data analyses, we create a suite of simulations for each choice of model, mass, cross section, and target element. We then perform Bayesian model selection (described in detail in Sec. 8.4.1) between two competing models (hypotheses) — the one used to create the simulation ("true underlying model") and the competing model (i.e. a "wrong" model) that has a nearly degenerate recoil spectrum but different time dependence. We repeat this procedure on each simulation in a given suite, to evaluate chances that future data confidently selects the underlying model. Model selection is repeated two times for each simulation — once including and once neglecting the time dependence of the rate (i.e. the annual modulation) in the likelihood function. Comparison of the two corresponding results enables us to quantitatively assess the impact that the inclusion of time information may have on prospects for identifying the true model.

8.3.1 Summary of Models

Here, we illustrate a generic scenario which gives rise to the DM–nuclei interactions we consider in this paper. We emphasize that this scenario by no means represents and exhaustive list of possible, or even well–motivated, models, but is rather just an illustrative example for studying the operators we are interested in (for a more comprehensive discussion we refer the interested reader to [123, 400]).

We thus focus on a generic extension of the Standard Model, represented by a hidden $U(1)'$ that has several charged fermions ψ_i and a heavy gauge boson A'_μ with mass M that kinetically mixes with the Standard Model photon. At high energies, the Lagrangian contains

$$\mathcal{L} \supset -m_i\bar{\psi}_i\psi^i + i\bar{\psi}_i\not{D}_{ij}\psi^j - \frac{1}{2}M^2A'_\mu A'^\mu - \frac{1}{4}F'_{\mu\nu}F'^{\mu\nu} - \frac{\epsilon}{2}F'_{\mu\nu}F^{\mu\nu}\,, \tag{8.3}$$

where $F_{\mu\nu}$ and $F'_{\mu\nu}$ are the field strength tensor of the photon and the heavy gauge boson, respectively (i.e. $F_{\mu\nu} \equiv \partial_\mu A_\nu - \partial_\mu A_\nu$). At low energies, the A'_μ and most ψ particles are integrated out. We assume a mass hierarchy that results in an electrically neutral fermion χ as the lightest degree of freedom in the dark sector, thereby providing a DM candidate. Because of the kinetic mixing, the state χ couples to the Standard Model nucleon current [123],

$$\mathcal{J}_\mu = \partial^\alpha F_{\alpha\mu} = e\sum \bar{n}\left(Q_n\frac{K_\mu}{2m_n} - \tilde{\mu}_n\frac{i\sigma_{\mu\nu}q^\nu}{2m_n}\right)n, \tag{8.4}$$

where the sum runs over individual nucleons, $Q_n = 1(0)$ are proton (neutron) charges in units of the electron charge e, $K_\mu/2 = (k_\mu + k'_\mu)/2$ is the average nucleon momentum, and $\tilde{\mu}_n = \frac{\text{magnetic moment}}{\text{nuclear magneton}}$ is the dimensionless magnetic moment of the nucleon.

The details of the masses and charges of the dark fermions ψ_i that constitute or couple to the DM χ will determine interaction that is measured in an experiment. We will use $\mathcal{O}^\mu_\chi$ to denote the Lorentz–vector fermion bilinear that couples to the current in Eq. (8.4). Because we assume χ is electromagnetically neutral, the possible $\mathcal{O}^\mu_\chi$ are [123, 400]

$$\mathcal{O}^\mu_{\chi,\text{Anapole}} = g^{\text{Anapole}} \bar{\chi}\gamma^\mu\gamma_5\chi, \tag{8.5}$$

$$\mathcal{O}^\mu_{\chi,\text{MD}} = \frac{g^{\text{MD}}}{\Lambda}\bar{\chi}i\sigma^{\mu\nu}q_\nu\chi, \tag{8.6}$$

$$\mathcal{O}^\mu_{\chi,\text{ED}} = \frac{g^{\text{ED}}}{\Lambda}\bar{\chi}i\sigma^{\mu\nu}\gamma_5 q_\nu\chi. \tag{8.7}$$

If we had alternatively taken the mass of the new gauge boson to be small relative to the characteristic scale of momentum transfer, we would not be able to integrate out the mediator and a strict EFT power counting would not be appropriate [134]. However, the scattering in a direct detection experiment would differ only by inverse powers of momentum transfer. The operators that introduce dipole interactions through a light mediator couple directly to the photon field strength $F_{\mu\nu}$, and these are described by

$$\mathcal{O}^{\mu\nu}_{\chi,\text{MD}} = \frac{g^{\text{MD}}}{\Lambda}\bar{\chi}i\sigma^{\mu\nu}\chi, \tag{8.8}$$

$$\mathcal{O}^{\mu\nu}_{\chi,\text{ED}} = \frac{g^{\text{ED}}}{\Lambda}\bar{\chi}i\sigma^{\mu\nu}\gamma_5\chi. \tag{8.9}$$

As stated above, the interaction operator for χ is determined by the dynamics of the ψ fermion(s). The anapole current in Eq. (8.5) will arise if charged $\psi^\pm$ states condense to form a neutral Majorana state χ [419]. The dipole currents form if an electromagnetically neutral

ψ^0 couples to an electromagnetically charged pair of partner $\psi^\pm$ particles (of appropriate spin) [420]. The scale at which the charged ψ states are integrated out is Λ.

The model in Eq. (8.3) is quite simple, but the different dark matter interaction operators in Eqs. (8.5)–(8.9) lead to a rich assortment of momentum and velocity dependences in the nuclear scattering cross section, as described in detail in [123, 400]. The momentum and velocity dependence that appear in the differential cross section are characterized by one or more "responses" that contain information about the zero–momentum–transfer normalization, the overall momentum or velocity dependence, and a form factor that describes the shape of the spectrum at higher momentum transfer and relative velocity. We list these operators in Tab. 2, highlighting the overall momentum and velocity dependence that multiply the dominant response or responses (this is an abbreviated version of the more exhaustive table that appeared in [400], using results of [123, 400]). Terms in the third column of Tab. 2 that multiply different form factors are separated with a comma; more specifically, using the definition

$$\frac{d\sigma_T}{dE_{\rm R}}(E_{\rm R}, v) = \sum_{(n,n')} \sum_X f_X^T(E_{\rm R}, v) \mathcal{R}_X^{T,(n,n')}(y)\,, \tag{8.10}$$

where the two summations are over nucleon permutations $(n, n') \in [(p,p),(n,n),(p,n),(n,p)]$ and target-dependent nuclear response functions $X \in [M, \Sigma', \Sigma'', \Phi'', \Delta, M\Phi'', \Delta\Sigma']$ (as defined in [398]), the terms in the third column of Table 2 illustrated the EFT dependence of the various $f_X^T(E_{\rm R}, v)$. In the above definition of Eq. (8.10), the variable $y \equiv m_T E_{\rm R} b^2/2$, where $b \equiv \sqrt{41.467/(45A^{-1/3} - 25A^{-2/3})}$ fm is the harmonic oscillator parameter for an atom with atomic number A. In this work, we will focus on differentiating interactions that

Model name	Lagrangian	$\vec{q}$, v Dependence	σ_p
SI	$\frac{g}{M^2}\bar{\chi}\chi\bar{N}N$	1	$\frac{\mu_p^2}{\pi}\left(\frac{f_p}{M^2}\right)^2$
Anapole	$\frac{g}{M^2}\bar{\chi}\gamma^\mu\gamma_5\chi\,\mathcal{J}_\mu$	$v_\perp^2, \vec{q}^2/m_N^2$	$\frac{\mu_p^2}{\pi}\left(\frac{eg^{Anapole}}{M^2}\right)^2$
Magnetic Dipole (heavy)	$\frac{g}{M^2\Lambda}\bar{\chi}\sigma^{\mu\nu}\chi\,q_\nu\mathcal{J}_\mu$	$\frac{\vec{q}^4}{\Lambda^4}+\frac{\vec{q}^2v_\perp^2}{\Lambda^2}, \vec{q}^4/\Lambda^4$	$\frac{\mu_p^2}{\pi}\left(\frac{eg^{MD}}{M^2}\right)^2\frac{\vec{q}_{ref}^2}{\Lambda^2}$
Electric Dipole (heavy)	$\frac{g}{M^2\Lambda}\bar{\chi}\sigma^{\mu\nu}\gamma_5\chi\,q_\nu\mathcal{J}_\mu$	$\vec{q}^2/\Lambda^2$	$\frac{\mu_p^2}{\pi}\left(\frac{eg^{ED}}{M^2}\right)^2\frac{\vec{q}_{ref}^2}{\Lambda^2}$
Magnetic Dipole (light)	$\frac{g}{\Lambda}\bar{\chi}\sigma^{\mu\nu}\chi F_{\mu\nu}$	$1+\frac{v_\perp^2m_N^2}{\vec{q}^2}$, 1	$\frac{\mu_p^2}{\pi}\left(\frac{eg^{MD}}{\Lambda\lvert\vec{q}_{ref}\rvert}\right)^2$
Electric Dipole (light)	$\frac{g}{\Lambda}\bar{\chi}\sigma^{\mu\nu}\gamma_5\chi F_{\mu\nu}$	$m_N^2/\vec{q}^2$	$\frac{\mu_p^2}{\pi}\left(\frac{eg^{ED}}{\Lambda\lvert\vec{q}_{ref}\rvert}\right)^2$

Table 2: Test interaction models considered in this work, listed by name, Lagrangian, and definition of σ_p in the first, second, and third column respectively. In the third column we list their associated momentum and velocity dependences (adapted from [400]). The labels 'light' and 'heavy' in the dipole models denote the magnitude of the mediator mass relative to the characteristic momentum transfer. The nucleon electromagnetic current $\mathcal{J}_\mu$ is defined in Eq. (8.4); the transverse velocity $v_\perp$ and momentum transfer $\vec{q}$ are discussed in Sec. 8.2.1; f_p is the proton coupling (here we take $f_p = f_n$, where f_n is the neutron coupling); μ_p is the dark matter-proton reduced mass; $q_{\rm ref}$ is a reference momentum characterizing the 'turn-over' of the energy spectrum, taken here to be 100 MeV; and Λ is a heavy mass or compositeness scale appearing in the dipole models. Terms in the third column that induce different nuclear responses, and thus require different form factors, are separated by a comma (see e.g. [398] for more details).

have the same momentum scaling but different velocity dependence.

8.4 Simulations

For our simulations, we consider the interactions discussed in the previous Section (summarized in Table 2), for three benchmark DM particle masses: 20 GeV, 125 GeV, and 500. Furthermore, we optimistically set the cross sections to be the value maximally allowed by LUX [168] [17]. Our baseline analysis focuses on G2 experiments employing xenon, germa-

[17] We note that LUX currently produces the most constraining bound on the models and masses considered in this paper, although the constraint from PandaX–II is only marginally weaker [169].

Label	A (Z)	Energy window [keVnr]	Exposure [kg–yr]
Xe	131 (54)	5–40	2000
Ge	73 (32)	0.3–100	100
F	19 (9)	3–100	606
Xe(x3)	131 (54)	5–40	6000
Xe(x10)	131 (54)	5–40	20 000
XeG3	131 (54)	5–40	40 000

Table 3: Mock experiments considered in this work. The efficiency and the fiducialization of the target mass are included in the exposure. The first group of experiments is chosen such to be representative of the reach of G2 experiments for xenon, germanium, and fluorine targets. The exposure for xenon and germanium is chosen to agree with the projected exclusion curves for LZ and SuperCDMS presented in Ref. [386]. The second group of experiments is used to quantitatively assess the impact of including the timing information as a function of the exposure (i.e. the observed number of events).

nium, and fluorine targets. Since fluorine experiments measure only the energy–integrated rate, we assume that fluorine has no energy resolution. For the rest of the experiments, we assume a perfect energy resolution, which should be a good approximation for our purposes [400]. The exposure and energy window of our mock experiments are summarized in Table 3. Throughout the analysis, we assume unit detection efficiency and zero backgrounds. In addition to the aforementioned, we also consider the potential reach of a Generation 3 (G3) xenon experiment, as well as various xenon experiments with exposures lying somewhere between G2 and G3 (the properties of which are summarized in Table 3). We define G3 to be the experiments reaching the neutrino floor [387]. The predicted number of events for each interaction considered in these mock experiments are shown in Table 4.

Each simulated recoil data set is generated by randomly selecting from a Poisson distribution with a mean given by the predicted number of events; the predicted number of events

Interaction /target	Xe	Ge	F
SI	(106, 100, 99)	(10, 4, 4)	(5, 1, 2)
Anapole	(110, 99, 98)	(12, 5, 6)	(39, 3, 3)
Mag. dip. heavy	(111, 90, 89)	(4, 5, 5)	(5, 1, 1)
Mag. dip. light	(108, 103, 103)	(36, 15, 15)	(90, 16, 16)
Elec. dip. heavy	(108, 92, 89)	(4, 4, 4)	(1, 0, 0)
Elec. dip. light	(106, 103, 102)	(63, 15, 14)	(41, 12, 12)

Table 4: Predicted number of events in G2 experiments for various interactions with xenon, germanium, and fluorine targets assuming a DM mass of (20 GeV, 125 GeV, and 500 GeV), for a cross section set to the current upper limits. Labels 'light' and 'heavy' denote the relative relation between the mediator mass and the characteristic scale of momentum transfer.

is calculated using Eq. (8.2), using the astrophysical parameters listed in Sec. **??** and incorporating the effect of gravitational focusing by the Sun following the procedure of Ref. [79]. The recoil energy and time of each event is then obtained by applying a rejection sampling algorithm to the two–dimensional differential scattering rate. This procedure is repeated for $\mathcal{O}(50)$ simulations in order to assess the variability of results arising from Poisson noise.

8.4.1 Analysis method

We analyze each simulated data set using Bayesian inference framework. In this framework, the probability that the data $\vec{X}$ assigns to a given model $\mathcal{M}_j$ is given by

$$P(\mathcal{M}_j) = \frac{\mathcal{E}_j(\vec{X}|\mathcal{M}_j)}{\sum_i \mathcal{E}_i(\vec{X}|\mathcal{M}_i)}\,, \tag{8.11}$$

where the sum is performed over all competing hypotheses, and $\mathcal{E}(\vec{X}|\mathcal{M})$ is the evidence of model $\mathcal{M}$, defined as

$$\mathcal{E}(\vec{X}|\mathcal{M}) = \int d\Theta\, \mathcal{L}(\vec{X}|\Theta, \mathcal{M})\, p(\Theta, \mathcal{M})\,, \tag{8.12}$$

and is intuitively understood to be the factor required to normalize the posterior probability distribution $\mathcal{P}$,

$$\mathcal{P}(\Theta|\vec{X}, \mathcal{M}) = \frac{\mathcal{L}(\vec{X}|\Theta, \mathcal{M})\, p(\Theta, \mathcal{M})}{\mathcal{E}(\vec{X}|\mathcal{M})}\,. \tag{8.13}$$

Here, $\mathcal{L}(\vec{X}|\Theta, \mathcal{M})$ is the likelihood, i.e. the probability of obtaining the data, given a particular model $\mathcal{M}$ and parameters Θ (for the purpose of this analysis $\Theta = \{m_\chi, \sigma_p\}$), and $p(\Theta, \mathcal{M})$ is the prior. In order to remain as agnostic as possible, we take wide priors in both m_χ and σ_p[18]. We use an unbinned likelihood function of the form

$$\mathcal{L}(\vec{X}|\Theta, \mathcal{M}) = \frac{\langle N\rangle^N}{N!}\, e^{-\langle N\rangle} \prod_{x_i \in \vec{X}} \frac{1}{\langle N\rangle} \left.\frac{dR}{dE_{\rm R} dt}\right|_{E_{\rm R}, t = x_i}\,, \tag{8.14}$$

where $\langle N\rangle$ is the predicted number of events, N is the number of observed events, and the product runs over all observed events, with a recorded energy and time label $x_i \equiv \{E_{R,i}\,,\, t_i\}$. When time (or $E_{\rm R}$) information is neglected, the differential rate is taken to be averaged over that variable.

For each of our simulated recoil data sets, we use a nested sampling algorithm implemented in `MultiNest` software package [421–424] to reconstruct the posterior[19]. Once we

[18] Log priors are taken for both m_χ and σ_p, spanning $1 - -3000$ GeV in mass and 7 orders of magnitude in cross section.

[19] `MultiNest` runs are performed with 2000 live points, an evidence tolerance of 0.1, and a sampling efficiency of 0.3.

compute the evidence of all competing models, we estimate the probability of successfully identifying the true model using Eq. (8.11). This procedure is then repeated for $\mathcal{O}(50)$ simulations to assess the probability of successful model identification (the variability arises from Poisson fluctuations). A model is correctly identified if the probability determined using Eq. (8.11) is large. For the purpose of this paper, we define identify a "successful" model selection with an outcome: $P \geq 90\%$. The primary quantity of interest for future direct detection experiments is then the fraction of simulations which lead to a successful model identification, which we refer to as the "success rate" in the following Section.

To evaluate the success rate, we apply kernel density estimation (KDE) with a Gaussian kernel to an ensemble of posterior probabilities a simulated data set assigns to the true underlying model. In the following Section, we will show the KDE distribution for each experimental combination (derived from both with– and without–time analyses), and determine the success rate by integrating the distributions above the 90% threshold.

8.5 Results

We first examine the extent to which including time information in the analysis of G2 experiments can help break degeneracy between models with the same momentum dependence, using as a case study the SI and anapole interactions. For this purpose, we simulate future G2 data for the SI and anapole interactions, and fit each simulation with these two models. We then compare the Bayesian evidences for the two models to evaluate the probability of the true underlying model (used to create a given simulation ensemble), as defined in Eq. (8.11). We then derive the probability distribution function (PDF) of all possible

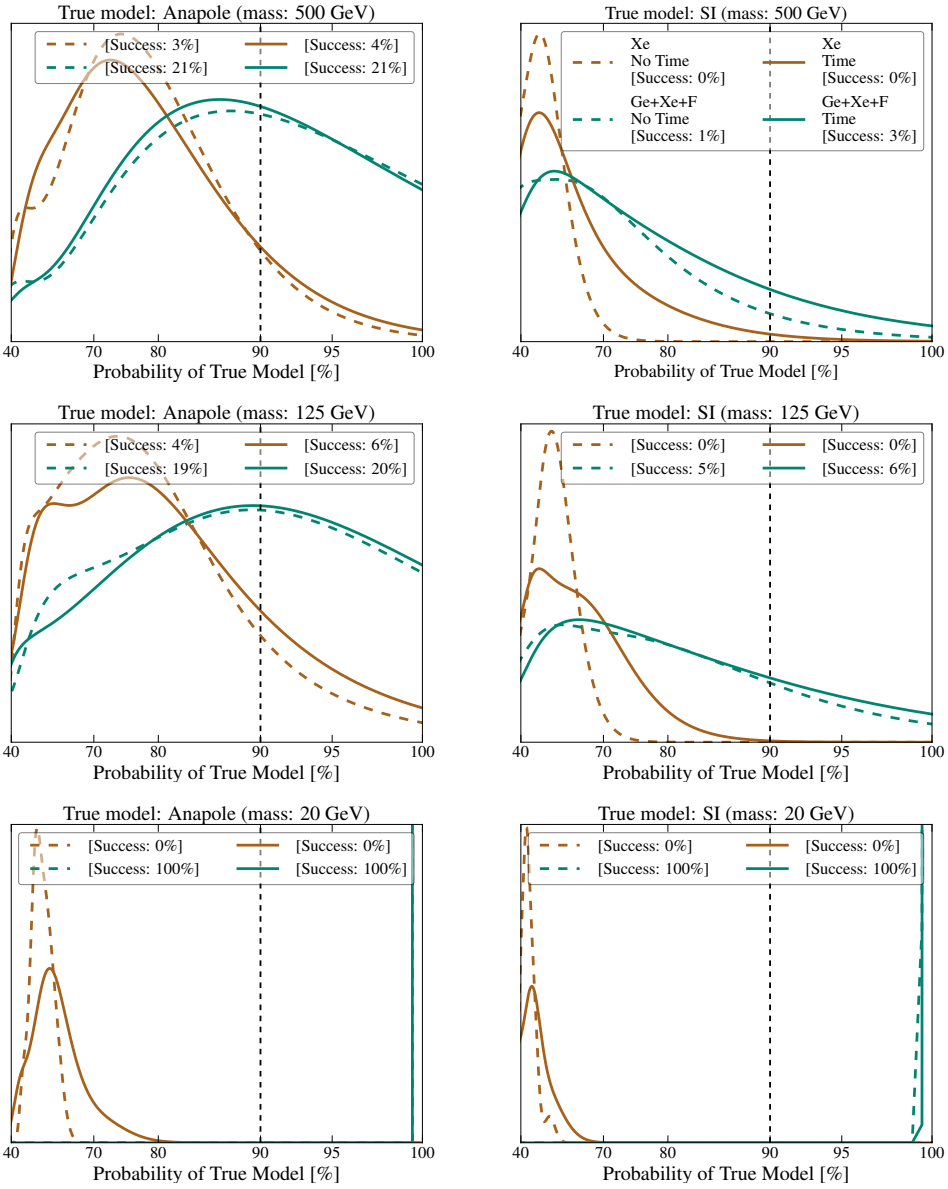

Figure 8.2: Model selection prospects with complementary G2 targets. The reconstructed PDFs for the posterior probability assigned to the true underlying interaction model are shown for the anapole (left column) and SI (right column) interactions, for a 500 GeV (top row), 125 GeV (middle row), and 20 GeV (bottom row) DM particle mass. Cross sections are set to current upper limits, and the PDFs are all normalized to unity between 0 and 100%. Results are shown for the analyses of simulated data from a xenon experiment alone, and for a combined likelihood analyses of xenon, germanium, and fluorine experiments. Solid lines are obtained from analyses that include time information of the recoil events, while dashed lines are from those that do not. Success rate displayed in the legend represents the fraction of simulations for which the correct model was assigned $\geq 90\%$ posterior probability (denoted by the vertical dashed line).

outcomes (i.e. a PDF of probabilities for identifying the true underlying model) from an ensemble of 50 simulations that had the same input model and parameters. Since we only consider two competing models, a PDF peaked around 50% means that the data is most likely to be agnostic between the two models, i.e. both models fit the data equally well[20]; this is the most pessimistic outcome possible. Conversely, a tail of the distribution at high probabilities, or a PDF shift in that direction, signifies improved model identification. Fig. 8.2 shows the results of this exercise for likelihood analysis only for xenon simulations, and for a joint likelihood analysis performed on a combination of data obtained on xenon, germanium, and fluorine experiments. DM particle masses used in the simulations are: 500 GeV, 125 GeV, and 20 GeV, with cross sections set to their respective current upper limits. We show the results obtained both without taking into account time dependence of the signals, and including the modulation analysis.

Consistent with the results of [400], we find that the two models can be confidently distinguished for a signal close to the current detection threshold, provided G2–level exposure on xenon and a detection with a fluorine experiment, but only if data from these experiments are jointly analyzed (xenon and germanium experiments are not complementary in the sense that a joint analysis does not significantly improve prospects for model selection, and thus we do not display results for this case). For a low–mass DM particle (20 GeV), the improvement upon combining these two types of experiments is drastic: the PDF of possible model–selection outcomes entirely shifts to a delta–function at 100% probability in favor of the correct model. For intermediate and high masses, the prospects are still visibly improved,

[20]For this reason we never plot the low probability region of the PDFs

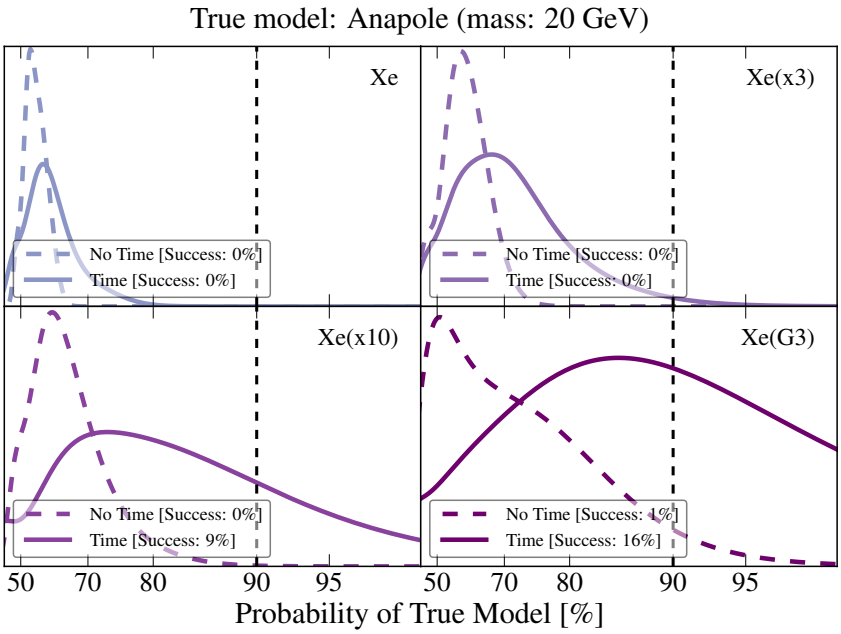

Figure 8.3: Model selection prospects for a single target (xenon), including (solid lines) and neglecting (dashed lines) time information in the likelihood analysis. The normalized PDFs are plotted for the probability of identifying the underlying model, here taken to be 20 GeV anapole DM, with a cross section that saturates the current upper limits. Panels from left to right, top to bottom, correspond to experimental exposures of 2, 6, 20, and 40 ton–years, respectively. Success rate displayed in the legend represents the fraction of simulations for which the correct model was assigned $\geq 90\%$ posterior probability (denoted by the vertical dashed line).

but not very optimistic (at best on the level of $\sim$20% success rate), mostly due to the reduced scattering rate on fluorine.

Comparison of no–time and with–time analyses (displayed in dashed and solid lines, respectively) demonstrates that inclusion of time information only negligibly changes model–selection prospects for G2 level of exposures. Given that G2 experiments will optimistically detect on the order of $\simeq$ 100 events, the statistical sample will be insufficient to clearly detect differences in the modulation signal that would otherwise aid differentiation between the two interactions.[21]

[21] See Sec. 4 of [81] for an estimation of the number of events needed for phase measurement.

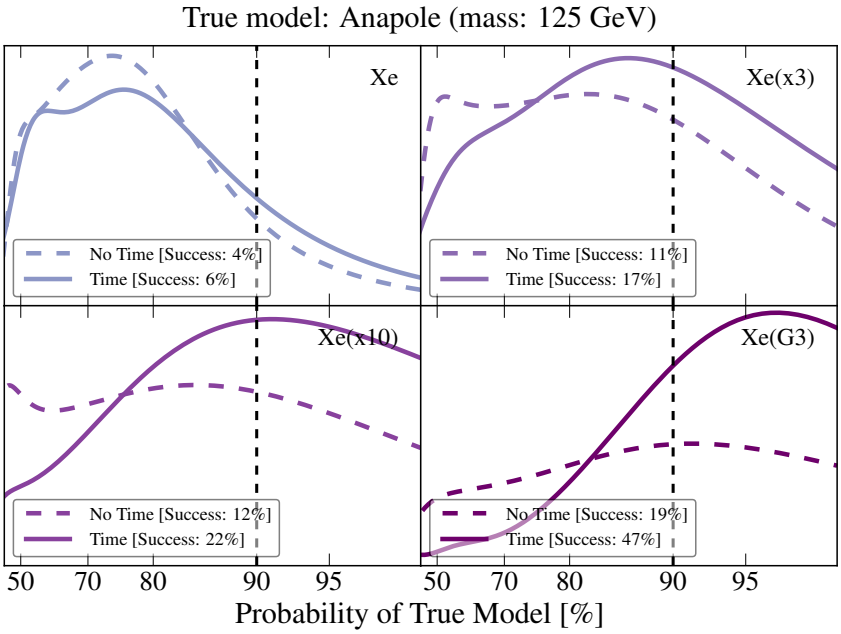

Figure 8.4: Same as Fig. 8.3 but for 125 GeV DM.

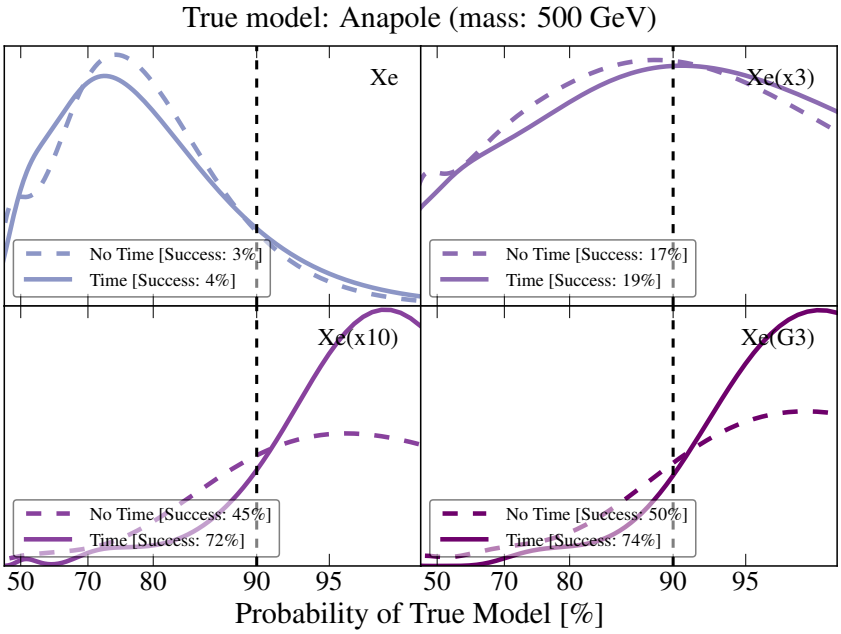

Figure 8.5: Same as Fig. 8.3 but for 500 GeV DM.

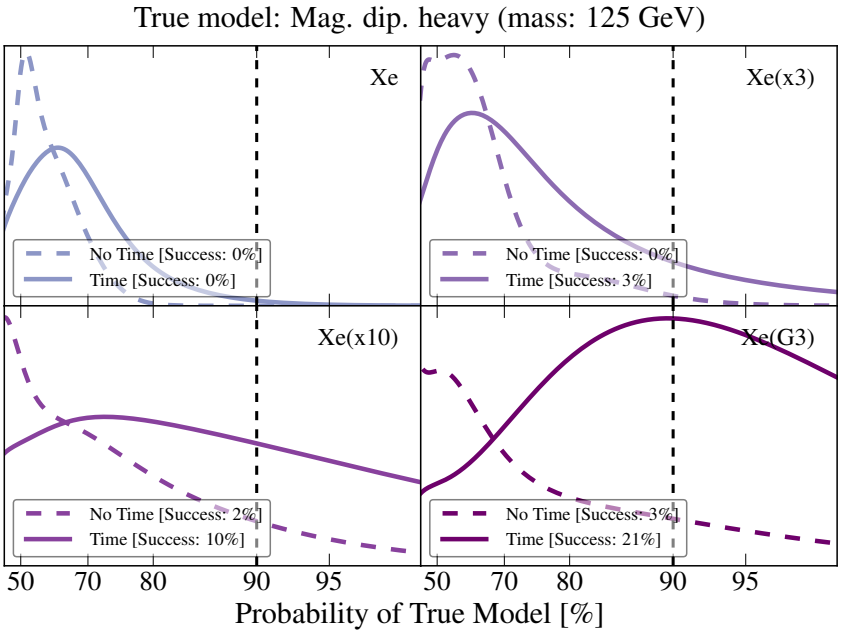

Figure 8.6: Same as Fig. 8.3, but now assessing the ability of xenon experiments to break the degeneracy of the magnetic dipole (heavy mediator) and electric dipole (heavy mediator) interactions, instead of SI and anapole interactions. Simulations assume a 125 GeV DM particle and a magnetic–dipole interaction.

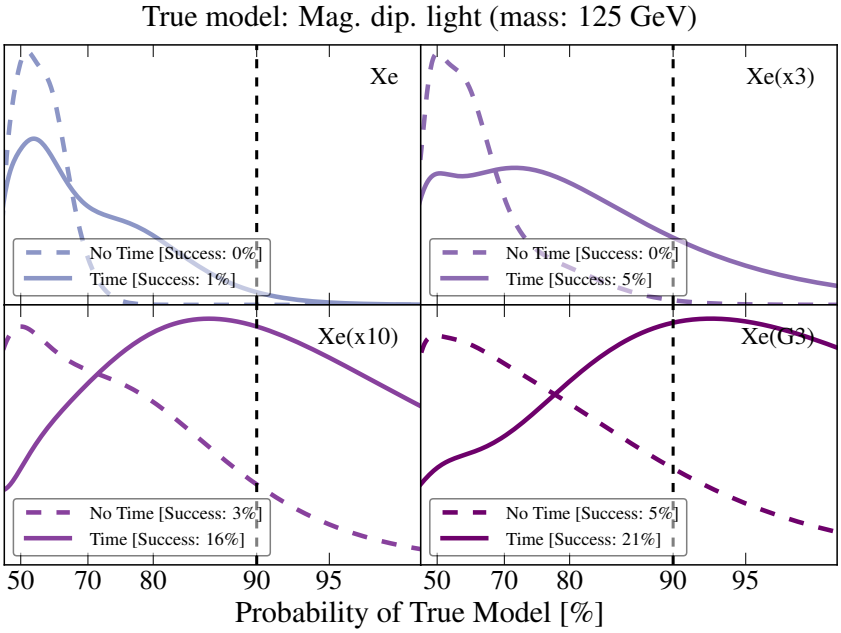

Figure 8.7: Same as Fig. 8.6 but for a light–mediator case.

The question then arises of how many events are needed before the inclusion of time information can significantly help model selection prospects. We address this question in Figs. 8.3–8.5 for a xenon experiment[22], showing the prospects (PDF of possible analysis outcomes) of successful model selection given a range of exposures: a 2, 6, 20, and 40 ton–year. Simulations used for these Figures all assume the anapole interaction and a DM mass of 20, 125, and 500 GeV, respectively. Results are shown for analyses that neglect (dashed) and include (solid) the time dependence of the rate. Simulations using the SI interaction are qualitatively similar and we defer these results to Appendix A.

From these Figures, we can infer that the addition of time information drastically improves prospects for successful model selection in the case of light DM particle (the solid–line PDFs are substantially shifted to the right in Fig. 8.3). In spite of this, even a G3 xenon experiment has only a $\simeq 16\%$ chance of disentangling these two interactions with high confidence. Fig. 8.1 gives an intuition for interpreting this outcome: both the recoil spectra and the phase of the modulation of the SI and anapole interactions (measured on a xenon experiment) are more degenerate for light than for heavy DM particles; thus, even when including time information in the analysis, a single–target experiment still must observe a large number of events in order to successfully distinguish between these models.

For larger DM masses, Figs. 8.4 and 8.5 show better model–discrimination prospects at a fixed exposure, particularly when time is included in the analysis. From these Figures, we see that including time in the analysis can improve model selection in G3 experiments by as much as $\simeq 30\%$ for heavy DM, where the phases of the modulation signal for these two interactions

[22]We choose to illustrate this point on a xenon target, as xenon experiments are projected to observe far more events than their germanium or fluorine counterparts.

may be misaligned by as much as $\simeq 5$ months (see again Fig. 8.1). Finally, it is important to keep in mind that all the results displayed here assume the most optimistic number of observed recoil events. Thus, despite the improvement in model selection obtained with the inclusion of time information, it is likely that model identification will still be challenging using a single target, even with G3 experiments; most likely, the experiments will need to exploit both target complementarity and the annual modulation in order to fully break the degeneracy between these types of models and ensure the highest chance of correctly identifying the interaction at hand.

The goal of this work was primarily a quantitative assessment of whether time information can be exploited in future direct detection analyses to break degeneracies in the recoil spectra of different interaction models — and SI and anapole interactions provided a particularly illuminating case study for this purpose. However, the main conclusions presented in this Section hold for other sets of interactions as well, and we now briefly illustrate this point. In Figs. 8.6 and 8.7 we consider a comparison of the magnetic dipole and electric dipole interactions for a 125 GeV DM particle, assuming a heavy and light mediator, respectively. As before, we consider putative detections in future xenon experiments with exposures varying from 2 to 40 ton–years. The results are rather similar to the SI and anapole comparison in that G3 experiments can expect a $\simeq 20\%$ improvement in model selection when time is included in the analysis, but again necessitate target complementarity to have a high chance of confidently differentiating these interactions.

8.6 Summary

We have considered here the potential impact of using time information in the likelihood analysis of data from future direct detection experiments in order to break degeneracies between the recoil energy spectra of different dark matter–baryon interactions. Specifically, we performed a statistical assessment of the prospects for successful Bayesian model selection between different interactions, using an ensemble of simulations that account for the impact of Poisson fluctuations. As a case study, we compared the standard spin–independent interaction and anapole dark matter, but also demonstrated that the main findings hold for other degenerate interaction models as well. We explored three different dark matter masses, and focused specifically on the most optimistic case where the cross sections for all interactions saturate the current upper limits.

We found that even under the most optimistic of circumstances, including time information in the analysis of Generation 2 direct detection experiments does not significantly improve prospects for distinguishing between models with degenerate recoil spectra. Rather, correct model identification in Generation 2 experiments will almost certainly require measurements and combined analyses on multiple target elements. We found that for the inclusion of time information to significantly increase chances for successful model selection (by $\mathcal{O}(10)\%$), for observations in an experiment employing a single target element, $\mathcal{O}(1000)$ and $\mathcal{O}(500)$ events must be observed for a 20 GeV and a 500 GeV DM particle respectively. These numbers are consistent with the 'back–of–the–envelope' calculations performed in [81]. Furthermore, even if time information is exploited in Generation 3 xenon experiments, target complementarity must also be exploited to unequivocally differentiate between interaction

models. We emphasize again that this finding holds even for the maximally optimistic scenario in which the interaction cross sections are as large as possible; it will be even more relevant for the case where the signals do not saturate current upper bounds.

In the event of a putative signal, direct detection experiments will be charged with the difficult task of illuminating the high energy behavior of dark matter solely from the observed low–energy recoils. This is a particularly daunting task in light of the fact that many feasible models produce nearly degenerate recoil spectra. Exploiting all of the information available, including the time dependence of nuclear recoil events explored in this work, will be necessary to make definitive statements regarding the true particle nature of dark matter.

9 Conclusion

Weakly interacting massive particles (WIMPs) have long been considered to be among the most promising dark matter candidates. Despite the comprehensive search strategy that has been implemented over the last 30 years to detect such particles, no definitive evidence has been found that suggests the existence of WIMPs.

This dissertation is comprised of a seven independent projects, the accumulation of eight published papers, that focus on identifying signals from, developing analysis techniques for, and deriving constraints on WIMP dark matter. The motivation for and conclusions of each project are briefly summarized below.

Chapter 2 attempts to address the extent to which the presence of dark matter sub-structure, such as a dark disk or a stream, may alter the expected scattering rate in direct detection experiments [81]. Here, it is shown that the total scattering rate, the amplitude of the modulation, and the phase of the modulation can be significantly altered, potentially producing distinctive signatures that may elucidate the presence of unconventional dark matter structure.

Chapter 3 is the combined result of Refs. [94, 413]. In contrast to popular sentiment, these works illustrate that observables associated with the annual modulation of the direct detection scattering rate (e.g. the time at which the scattering rate is maximum) are not necessarily common to all experiments. Rather, should the dark matter-nuclei differential cross section consistent of multiple non-negligible terms with a non-factorizable dependence on the dark matter velocity, the observables associated with the annual modulation of the

rate may actually be unique to each target element.

Chapter 4 assesses the extent to which a dark matter interpretation of the $\sim 3\sigma$ excess observed by CDMS-II-Si in 2013 can remain consistent with null search results of current and future direct detection experiments [425]. While LUX and PICO-60 exclude halo-dependent interpretations of this excess (assuming the Standard Halo Model), we identify a small highly-tuned region of parameter space using a halo-independent analysis for which an exothermic dark matter candidate interacting through a spin-independent interaction with 'Xe-phobic' couplings can remain viable. These models cannot be definitively excluded until an experiment like LZ or PICO-60.

In Chapter 5, we generalize an analysis tool that allows for direct detection experiments to be interpreted without any explicit assumptions on the astrophysical distribution of dark matter [192]. Specifically, we argue that for global likelihoods comprised of at least one extended likelihood (applied to unbinned data sets) and an arbitrary number of Poisson or Gaussian likelihoods, the best-fit halo function is piece-wise constant with only a small bounded number of steps, and this best-fit halo function is unique. Additionally, we the generalize the procedure for constructing halo-independent confidence bands from this joint likelihood. Lastly, we illustrate a method which tests the compatibility of the data sets that comprise the global likelihood.

Using the results of numerical N-body simulations, Chapter 6 assesses the prospects for observing gamma-rays that arise from the annihilation of dark matter in local low-mass subhalos [426]. Here, we attempt to extract distributions and parameterizations capable of characterizing local subhalos, which by virtue of their location have necessarily undergone

extensive tidal stripping. Using the derived distributions, we find that the Fermi Large Area Telescope may currently be probing thermal relics with a mass below $\sim$ 10 GeV (for particular annihilation channels and an unsuppressed annihilation cross section). However, the uncertainty in the derived parameterizations can significantly alter the predicted number of observable subhalos; thus making more definitive statements will necessitate larger, stable, higher-resolution simulations.

Chapter 7 updates constraints on an exhaustible list of simplified dark matter models that may be consistent with generating the observed Galactic Center gamma-ray excess [23] [427]. We show that spin-1 mediated models are nearly entirely ruled out by direct detection constraints, and models which annihilate through a t-channel exchange of a charged and colored mediator are entirely excluded by both direct detection and the LHC. Spin-0 mediator models, however, are still viable for mediator masses m_a between $\sim$ 10 GeV and $\sim$ 200 GeV.

In Chapter 8, we attempt to address the extent to which including time information in the analysis of future direct detection data may break the degeneracy that arises between dark matter models with a similar momentum dependence in the differential cross sections [428]. Using a Bayesian statistical analysis, we show that including time information in future generation experiments may increase model identification by as much as $\sim$ 40%, however this is not enough to fully break the degeneracy.

The experimental program developed to probe the WIMP parameter space has recently begun to substantially test the thermal dark matter paradigm, and will continue to do so

[23] Note that hidden sector models are not addressed in this work. Such models are notoriously difficult to exclude and certainly remain viable for wide ranges of parameter space.

for the next decade. The list of aforementioned manuscripts provide a broad insight into the current status and prospects for observing the non-gravitational interactions of WIMP dark matter candidates. Should nature be kind, experiments performed in the coming years may yield valuable insight into the mysterious substance known as dark matter.

A Dissertation Appendix

A.1 The zeros of the $q(v_{\min})$ function

[Pertains to Chapter 5]

We are first going to argue that the zeros of $q(v_{\min})$ are only isolated above a certain $v_{\min}$ range where all terms in the sum defining $q(v_{\min})$ are zero. We will then find the maximum possible number of isolated zeros, although the actual number of zeros can be much smaller than the maximum.

A.1.1 The zeros are isolated above a certain $v_{\min}$ value

The terms defining $q(v_{\min})$ in Eq. (5.41) are either positive semidefinite, e.g. $\xi^{\rm EHI}(v_{\min})$ and some of the terms proportional to $\xi_j^{(\alpha)}(v_{\min})$, or negative semidefinite, e.g. the terms proportional to $H_a^{\rm EHI}(v_{\min})$ and some of the terms proportional to $\xi_{j'}^{(\alpha')}(v_{\min})$. To facilitate a smooth discussion of the behavior of these functions, let us introduce the label μ, which will be used to denote either a quantity associated with the EHI experiment or an experiment-bin pair (α, j). This way, quantities like $\xi^{\mu}(v_{\min})$ can either represent $\xi^{\rm EHI}(v_{\min})$ or $\xi_j^{(\alpha)}(v_{\min})$.

Each term in the sum in Eq. (5.41) has a different $v_{\min}$-dependence. In particular the $\xi^{\mu}(v_{\min})$ functions (note the general behavior of $\xi_j^{(\alpha)}(v_{\min})$ is identical to that of $\xi(v_{\min})$ discussed in Sec. 5.2.2) are zero below certain values of $v_{\min}$, which we will refer to as $v_{\rm low}^{\mu}$, strictly increase with $v_{\min}$ (although the second derivative may exhibit sign changes), until at some value of $v_{\min}$, call it $v_{\rm high}^{\mu}$, they plateau and become constant. The $v_{\rm low}^{\mu}$ and $v_{\rm high}^{\mu}$ of each $\xi^{\mu}(v_{\min})$ function, as well as the height of the plateau, depend on theoretical framework and the specifics of the experiments (e.g. the scattering kinematics, the differential cross section,

the energy resolution functions, etc.). The $H_a^{\rm EHI}(v_{\rm min})$, also described in Sec. 5.2.2, are instead upward step-like functions, starting from zero at low $v_{\rm min}$, with the steps appearing roughly at the $v_{\rm min}$ values corresponding to the detected energy of the events observed in the EHI experiment.

In addition to having unique $v_{\rm min}$-dependencies, each of the terms in Eq. (5.41) has uniquely defined $\tilde{\eta}$-dependent coefficient. Thus the terms are all independent of each other and have very different functional forms.

For values of $v_{\rm min}$ below the minimum $v_{\rm low}^{\mu}$, i.e. where all the terms in Eq. (5.41) are zero, $q(v_{\rm min})$ is zero, which implies $\tilde{\eta}_{BF}(v_{\rm min})$ is undetermined. This is not detrimental to the arguments we have made as it reflects the fact that experiments under consideration do not probe the halo function at these values of $v_{\rm min}$. Notice that in order to have non-negative $q(v_{\rm min})$ values, the $v_{\rm low}$ of some of the positive terms must be smaller than the smallest $v_{\rm low}$ of all negative terms.

For values of $v_{\rm min}$ larger than the minimum $v_{\rm low}^{\mu}$, zeros of $q(v_{\rm min})$ can appear where the modulus of the sum of all negative terms in Eq. (5.41) touches from below the sum of all positive terms in Eq. (5.41) (recall that $q(v_{\rm min})$ is a non-negative function). The positive terms consist of different $\xi^{\mu}(v_{\rm min})$ (most of them multiplied by $\tilde{\eta}$-dependent coefficients). Thus, in general, the sum of all positive terms behaves as a monotonically increasing function starting from zero at the lowest $v_{\rm low}^{\mu}$ (lowest of all positive terms) and plateauing to a constant value at the largest $v_{\rm high}^{\mu}$ (again considering only positive terms). The negative terms in Eq. (5.41) include the step-like $H_a(v_{\rm min})$ (multiplied by $\tilde{\eta}$ dependent coefficients), which each add a "step-like" feature to the modulus of the sum of negative terms, and some of the

$\xi_j^{(\alpha)}(v_{\rm min})$ dependent terms (multiplied by $\tilde{\eta}$ dependent negative coefficients). Depending on the nature of these negative $\xi_j^{(\alpha)}(v_{\rm min})$ terms, they could add "shoulder-like" features, arising from changes in the sign of the second derivative, to the modulus of the sum of negative terms. The modulus of the sum of negative terms also plateaus above the largest $v^{\mu}_{\rm high}$ (largest of all negative terms). The plateau of the sum of positive terms and the plateau of the modulus of the sum of all negative terms are entirely independent of each other, and thus the possibility that the two plateaux would coincide to produce $q(v_{\rm min}) = 0$ is completely unrealistic since they both depend on entirely different experimental features. Furthermore, for most realistic cases, the maximum value of $v^{\mu}_{\rm high}$ is larger than the galactic escape velocity, and thus $\tilde{\eta}(v_{\rm min})$ should be zero in this region. Since these plateaus cannot feasibly coincide, $q(v_{\rm min})$ cannot equal 0 above the largest $v^{\mu}_{\rm high}$.

Typically isolated zeros of $q(v_{\rm min})$ would happen when some of the "step-like" or "shoulder-like" features of the modulus of the sum of negative terms in Eq. (5.41) touch from below the monotonically increasing sum of all positive terms in Eq. (5.41). Alternatively, if the sum of the positive terms has a region of negative curvature, it may be possible for that this sum could reach towards and touch the modulus of the sum of negative terms from above.

A practically impossible conspiracy between terms dependent on different experiments, energy intervals, and $\tilde{\eta}$ functions would be required for $q(v_{\rm min})$ to be zero in an extended $v_{\rm min}$ interval above the minimum $v^{\mu}_{\rm low}$, a conspiracy which would not survive infinitesimal changes in any of the elements defining each term in Eq. (5.41). We include in Appendix **??** a more mathematically rigorous proof illustrating why extended zeros of $q(v_{\rm min})$ cannot exist above the minimum $v^{\mu}_{\rm low}$. In the following we only consider the possibility that $q(v_{\rm min})$ has a finite

number of isolated zeros.

A.1.2 Maximum number of isolated zeros of the function $q(v_{\mathbf{min}})$ for a global likelihood

Before counting the number of isolated zeros of $q(v_{\min})$, let us introduce the notion of a "generic" solution. We say that a solution is generic if small changes in the quantities that define it do not affect the existence of the solution. In our context, the quantities defining the solutions are the input parameters and functions given to fully specify $\xi^{\rm EHI}$, $\xi_j^{(\alpha)}$, and $H_a^{\rm EHI}$, e.g. the efficiency function $\epsilon(E', E_R)$, the energy resolution function $G_T(E', E_{\rm R})$, the differential cross section $\mathrm{d}\sigma_T/\mathrm{d}E_{\rm R}$, and the exposure MT for each experiment and bin.

Let us briefly demonstrate the importance of the concept of generic solutions by considering the number of isolated zeros that can arise in the linear combination of two functions $f(x)$ and $g(x)$ which do not have the same functional form, since they are assumed to be derived from two independent experimental setups (i.e. changes in the experimental quantities of one experiment may affect e.g. $f(x)$, but do not affect $g(x)$ in the same manner). For an adjustable parameter λ, it is possible for $f(x)$ and $\lambda g(x)$ to have a generic point of osculation, i.e. a point where $f(x) = \lambda g(x)$ and $f'(x) = \lambda g'(x)$, at which the Wronskian $W[f, g]$ vanishes

$$W[f, g](x) \equiv f(x)g'(x) - f'(x)g(x) = 0\,. \tag{A.1}$$

In fact, $W[f, g]$ could vanish in more than one point, say $x_1, x_2, ...x_n$, or in various intervals. In this case the value of λ can be chosen so that $f(x_1) = \lambda g(x_1)$ at one of those discrete points, say x_1. This point of osculation defines an isolated zero of the function $[f(x) - \lambda g(x)]$,

with zero slope. Having two points of osculation, say x_1 and x_2, would require

$$\frac{f(x_1)}{g(x_1)} = \frac{f(x_2)}{g(x_2)}\,, \tag{A.2}$$

where $W[f,g](x_1) = W[f,g](x_2) = 0$, for points $x_1 \neq x_2$. Small changes in the defining experimental functions and parameters would certainly break the equality in Eq. (A.2) (or result in a non-vanishing Wronskian at those points), and thus solutions having more than one point of osculation are not generic. This same argument can be used to exclude the possibility of having a generic solution with both an isolated osculation point and an interval of osculation. Since we are interested in counting the maximum number of isolated points of osculation, we need not be concerned with the existence of intervals of osculation.

Let us denote with $X_m(v_{\rm min})$ either the functions $H_a^{\rm EHI}(v_{\rm min})$ or the functions $\xi_j^{(\alpha)}(v_{\rm min})$, so that Eq. (5.41) can be written in the form

$$\frac{1}{2}q(v_{\rm min}) = \xi^{\rm EHI}(v_{\rm min}) - \sum_m \lambda_m X_m(v_{\rm min})\,, \tag{A.3}$$

except here we will treat the λ_m as free parameters. The argument above ensures that there could be at most one generic point of osculation between $\xi^{\rm EHI}(v_{\rm min})$ and $\lambda_m X_m(v_{\rm min})$, or between $\lambda_m X_m(v_{\rm min})$ and $\lambda_k X_k(v_{\rm min})$ for $k \neq m$. Here, the coefficients λ_m are adjustable parameters, equivalent to a multidimensional generalization of the parameter λ in the above example. In the context of Eq. (5.41), one can identify the λ_m with the halo-dependent quantities, e.g. $1/\gamma[\tilde{\eta}]$ and the factors in the square bracket of Eq. (5.42) and Eq. (5.43).

For fixed $(n-1)$ coefficients, λ_1,...λ_{k-1}, λ_{k+1},...λ_n, we can consider two functions

$$f_k(v_{\min}) = \xi^{\rm EHI}(v_{\min}) - \lambda_1 X_1(v_{\min}) \cdots - \lambda_{k-1} X_{k-1}(v_{\min}) - \lambda_{k+1} X_{k+1}(v_{\min}) \cdots - \lambda_n X_n(v_{\min}) \tag{A.4}$$

and

$$\lambda_k g_k(v_{\min}) = \lambda_k X_k(v_{\min}). \tag{A.5}$$

Here we choose the parameter λ_k with $1 \leq k \leq n$ as the only adjustable parameter. Assume λ_k can be adjusted freely. Then by adjusting λ_k, we could find one point of osculation where $f_k(v_{\min}) = \lambda g_k(v_{\min})$, and we can treat such an adjusted value of λ_k as a function of the rest of the parameters, $\hat{\lambda}_k(\lambda_1, \ldots, \lambda_{k-1}, \lambda_{k+1}, \ldots, \lambda_n)$.

Now let us consider a n-dimensional manifold $\mathcal{M}_n$ of all the λ_k real parameters, i.e.

$$\mathcal{M}^{(n)} \equiv \{(\lambda_1, \ldots, \lambda_n) | \lambda_m \in \mathbb{R}, m = 1, \ldots, n\}. \tag{A.6}$$

Notice that here n is one less than the total number of terms defining $q(v_{\min})$ in Eq. (5.41) (because $\xi^{\rm EHI}(v_{\min})$ is treated separately), thus $n = \mathcal{N} = N^{\rm EHI} + \sum_\alpha N_{\rm bin}^{(\alpha)}$ (see Eq. (5.40)). The equation

$$\lambda_k = \hat{\lambda}_k(\lambda_1, \ldots, \lambda_{k-1}, \lambda_{k+1}, \ldots, \lambda_n) \tag{A.7}$$

defines a $(n-1)$-dimensional sub-manifold $M_{n-1}^{(k)}$ in the manifold $\mathcal{M}_n$, for each choice of k.

By construction, at every point in the sub-manifold $\mathcal{M}_{n-1}^{(k)}$, a point of osculation

$$v^{(k)}(\lambda_1, \ldots, \lambda_{k-1}, \lambda_{k+1}, \ldots, \lambda_n) \tag{A.8}$$

is assigned, so, assuming λ_k can be adjusted freely to be $\lambda_k = \hat{\lambda}_k$, the function

$$\begin{aligned} f_k(v_{\min}) - \lambda g_k(v_{\min}) &= \tfrac{1}{2} q^{(k)}(v_{\min}; \lambda_1, \ldots, \lambda_{k-1}, \lambda_{k+1}, \ldots, \lambda_n) \\ &= \xi^{\mathrm{EHI}}(v_{\min}) - \textstyle\sum_{m \neq k} \lambda_m X_m(v_{\min}) \\ &\quad - \hat{\lambda}_k(\lambda_1, \ldots, \lambda_{k-1}, \lambda_{k+1}, \ldots, \lambda_n) X_k(v_{\min}), \end{aligned} \tag{A.9}$$

has at least one isolated zero (with zero slope) at

$$v_{\min} = v^{(k)}(\lambda_1, \ldots, \lambda_{k-1}, \lambda_{k+1}, \ldots, \lambda_n), \tag{A.10}$$

for any given set of values $(\lambda_1, \ldots, \lambda_{k-1}, \lambda_{k+1}, \ldots, \lambda_n)$.

If we consider two such manifolds, $\mathcal{M}_{n-1}^{(k)}$ and $\mathcal{M}_{n-1}^{(k')}$, the intersection of them, $\mathcal{M}_{n-1}^{(k)} \cap \mathcal{M}_{n-1}^{(k')}$, is generically a $(n-2)$-dimensional sub-manifold. Assuming now that λ_k and $\lambda_{k'}$ $(k \neq k')$ can both be adjusted at will so that $\lambda_k = \hat{\lambda}_k$ and $\lambda_{k'} = \hat{\lambda}_{k'}$ at every point in this sub-manifold, we have two isolated zeros (with zero slope) given by the functions,

$$\begin{aligned} &v^{(k)}(\lambda_1, \ldots, \lambda_{k-1}, \lambda_{k+1}, \ldots, \lambda_{k'-1}, \lambda_{k'+1}, \ldots, \lambda_n) \\ &\quad \equiv v^{(k)}(\lambda_1, \ldots, \lambda_{k-1}, \lambda_{k+1}, \ldots, \lambda_n)|_{\lambda_{k'} = \hat{\lambda}_{k'}}, \end{aligned} \tag{A.11}$$

and

$$\begin{aligned} &v^{(k')}(\lambda_1, \ldots, \lambda_{k-1}, \lambda_{k+1}, \ldots, \lambda_{k'-1}, \lambda_{k'+1}, \ldots, \lambda_n) \\ &\quad \equiv v^{(k')}(\lambda_1, \ldots, \lambda_{k'-1}, \lambda_{k'+1}, \ldots, \lambda_n)|_{\lambda_k = \hat{\lambda}_k}, \end{aligned} \tag{A.12}$$

which are respectively induced from the functions defined on $\mathcal{M}_{n-1}^{(k)}$ and $\mathcal{M}_{n-1}^{(k')}$. The values of these two functions at the same point are in general different.

In a similar way, if all coefficients λ_k could be freely adjusted the intersection of all $(n-1)$-dimensional sub-manifolds,

$$\cap_{k=1}^{n} \mathcal{M}_{n-1}^{(k)} \,, \tag{A.13}$$

is generically a zero-dimensional sub-manifold of $\mathcal{M}_n$, i.e. a set of discrete points. For one of these points, which we call $(\hat{\lambda}_1, \ldots, \hat{\lambda}_n)$, we can define the function

$$\frac{1}{2} q(v_{\rm min}; \hat{\lambda}_1, \ldots, \hat{\lambda}_n) = \xi^{\rm EHI}(v_{\rm min}) - \sum_{m=1}^{n} \hat{\lambda}_m X_m(v_{\rm min}) \tag{A.14}$$

which has n isolated zeros, with zero slope. Here, $n = \mathcal{N} \equiv N_{\rm EHI} + \sum_\alpha N_{\rm bin}^{(\alpha)}$ (see Eq. (5.40)), i.e. the number of events observed by the EHI experiment plus the total number of bins employed by all Poisson and Gaussian experiments. This is what we wanted to prove. However we have so far assumed the coefficients λ_m could all be freely adjusted. This is not true, however, and the actual number of isolated zeros of $q(v_{\rm min})$ (with $q'(v_{\rm min}) = 0$) will be in most circumstances much smaller than the maximum $\mathcal{N}$.

In fact, the coefficients λ_m are quantities derived from a halo function $\tilde{\eta}$. All points in $\mathcal{M}_n$ that can be actually realized from halo functions $\tilde{\eta}$ form a continuous subset $\mathcal{S}$ of the manifold $\mathcal{M}_n$. The maximum number of the individual sub-manifolds $\mathcal{M}_{n-1}^{k}$ passing through a point in $\mathcal{S}$ gives the maximum number of actual possible steps in the best fit $\tilde{\eta}$ function. This number can be determined by carefully considering the functional form of $\xi^{\rm EHI}$, $\xi_j^{(\alpha)}$,

and $H_a^{\rm EHI}$, and is in general smaller than $\mathcal{N}$.

A.2 The uniqueness of the best-fit halo function

[Pertains to Chapter 5]

Here, we show that the halo function $\tilde{\eta}_{BF}(v_{\rm min})$ maximizing a global likelihood functional having at least one extended likelihood as a factor is unique in the $v_{\rm min}$ range wherein the experiments in consideration can probe the value of the halo function. The proof consists in showing that the second directional derivatives of the functional $L \equiv -2\ln\mathcal{L}$ with respect to variations of the $\tilde{\eta}$ function are all positive.

A.2.1 Statement of the proof

We start by stating two properties of the global likelihood (and the individual likelihoods) considered in this paper. First, the likelihood depends on the halo function only through physically observable quantities, which are either the scattering rate in a bin

$$R_j^{(\alpha)} \equiv MT \int_{v_\delta}^{\infty} {\rm d}v\ \mathcal{R}_{[E'_j,E'_{j+1}]}(v)\tilde{\eta}(v), \tag{A.15}$$

or the value of the differential rate at a given value of E',

$$\frac{{\rm d}R}{{\rm d}E'} \equiv MT \int_{v_\delta}^{\infty} {\rm d}v\ \frac{{\rm d}\mathcal{R}}{{\rm d}E'}(v)\tilde{\eta}(v)\,. \tag{A.16}$$

Secondly, if we treat these observable quantities (which we call "the rates" in the rest of this section) as independent parameters without restriction, the global likelihood $\mathcal{L}$ is a strictly

concave function of them, or, equivalently, the functional $L \equiv -2 \ln \mathcal{L}$ is a strictly convex function.

Since the rates depend linearly on the halo function, the functional L is a convex but not necessarily a strictly convex function of the halo function $\tilde{\eta}$. The strict convexity of the functional L as a function of the rates guarantees the uniqueness of the best fit rates (those which maximize the likelihood $\mathcal{L}$, and thus minimize the functional L), but not of the best fit halo function $\tilde{\eta}_{BF}(v_{\min})$, since, in general, the same values of the rates can be obtained from different halo functions.

While these two properties do not yet prove that the best fit halo function is unique, we know from the convexity of the functional L that if there are more than one best fit halo functions, the value of the likelihood is constant along the line of minima between any two best fit halo functions, and thus, along the direction of the line, the second (and also higher) order directional (functional) derivatives should vanish. Thus all the best fit halo functions are connected to each other by a continuous deformation and thus form a connected set.

Using this fact, the global uniqueness of the best fit halo function $\tilde{\eta}_{BF}(v_{\min})$ can be asserted by proving that the second order directional derivatives of L around a minimum are all larger than zero, i.e.

$$\int \mathrm{d}v \int \mathrm{d}w \; \Delta\tilde{\eta}(v)\Delta\tilde{\eta}(w) \; \frac{\delta^2}{\delta\tilde{\eta}(v)\delta\tilde{\eta}(w)} L[\tilde{\eta}]\bigg|_{\tilde{\eta}=\tilde{\eta}_{\mathrm{BF}}} > 0, \tag{A.17}$$

for all allowed $\Delta\tilde{\eta}$.

Up to this point, we have not used the fact that the halo function is a non-increasing

function, and that the KKT conditions should be satisfied by the best fit halo function. Since we have previously proven in Appendix A that the halo functions maximizing the global likelihood are piecewise constant with at most $\mathcal{N} = N_{\rm EHI} + \sum_\alpha N_{\rm bins}^{(\alpha)}$ points of discontinuity, we know that deformations of $\tilde{\eta}$ between two best fit halo functions must also respect this form. Thus, the positivity condition of the second order directional derivatives of L around a minimum, Eq. A.17, can be rewritten as

$$\begin{aligned} 0 < \quad & \sum_{a,b=1}^{\mathcal{N}} \Big[\Delta\tilde{\eta}_a \Delta\tilde{\eta}_b \tfrac{\delta^2}{\partial\tilde{\eta}_a \partial\tilde{\eta}_b} f_L(\{\vec{v},\vec{\tilde{\eta}}\}) \\ & + \Delta v_a \Delta v_b \tfrac{\delta^2}{\partial v_a \partial v_b} f_L(\{\vec{v},\vec{\tilde{\eta}}\}) \\ & + 2\Delta\tilde{\eta}_a \Delta v_b \tfrac{\delta^2}{\partial\tilde{\eta}_a \partial v_b} f_L(\{\vec{v},\vec{\tilde{\eta}}\}) \Big]_{\tilde{\eta}=\tilde{\eta}_{\rm BF}}, \end{aligned} \tag{A.18}$$

for all allowed infinitesimal variations $\Delta\tilde{\eta}_a$ and Δv_a, where $f_L(\{\vec{v},\vec{\tilde{\eta}}\}) \equiv L[\tilde{\eta}(v_{\rm min};\{\vec{v},\vec{\tilde{\eta}}\})]$.

When one finds the best fit halo function, the locations v_a and heights $\tilde{\eta}_a$ of the steps can be independently varied since the KKT conditions are automatically satisfied for the resultant best fit halo function. However, in Eq. A.18, if a variation of these parameters, $\Delta\tilde{\eta}_a$ and Δv_a, truly connects two best fit halo functions (and the ones between them, which are also best fit halo functions) by a continuous deformation, the KKT conditions should remain satisfied along the path of the deformation, and thus we only need to consider the variations respecting the KKT conditions. We will show now that these variations must all have $\Delta v_a = 0$, namely the positions of the steps in $v_{\rm min}$ cannot change.

A.2.2 Proof that the locations of the steps cannot change

Let us examine how the function $q(v)$ changes under an arbitrary deformation $\Delta\tilde{\eta}(v_{\rm min})$ of the halo function $\tilde{\eta}(v_{\rm min})$. Using the definition of the function $q(v)$ in Eq. 5.20, the induced variation $\Delta q(v)$ of the function $q(v)$, can be compactly written in terms of the second derivative of the functional L as

$$\begin{aligned}\Delta q(v) &\equiv \int_{v_\delta}^{\infty} {\rm d}w\ \Delta\tilde{\eta}(w)\frac{\delta q(v)}{\delta\tilde{\eta}(w)} \\ &= \int_{v_\delta}^{\infty} {\rm d}w\ \Delta\tilde{\eta}(w)\frac{\delta}{\delta\tilde{\eta}(w)}\left[\int_0^v {\rm d}u \frac{\delta L}{\delta\tilde{\eta}(u)}\right], \end{aligned} \tag{A.19}$$

or

$$\begin{aligned}\Delta q(v) &= \sum_{\alpha,j}\Delta R_j^{(\alpha)}\int_{v_\delta}^{v}{\rm d}u\frac{\delta}{\delta\tilde{\eta}(u)}\left(\frac{\partial L}{\partial R_j^{(\alpha)}}\right) \\ &\quad + \int {\rm d}E'\ \Delta\left(\frac{{\rm d}R}{{\rm d}E'}\right)\int_{v_\delta}^{v}{\rm d}u\frac{\delta}{\delta\tilde{\eta}(u)}\left(\frac{\partial L}{\partial({\rm d}R/{\rm d}E')}\right)\end{aligned} \tag{A.20}$$

where we have defined the changes $\Delta R_j^{(\alpha)}$ and $\Delta\left(\frac{{\rm d}R}{{\rm d}E'}\right)$ of the rate $R_j^{(\alpha)}$ and differential rate ${\rm d}R/{\rm d}E'$, respectively as

$$\Delta R_j^{(\alpha)} \equiv \int {\rm d}v\ \Delta\tilde{\eta}(v)\frac{\delta R_j^{(\alpha)}}{\delta\tilde{\eta}(v)} \tag{A.21}$$

and

$$\Delta\left(\frac{{\rm d}R}{{\rm d}E'}\right) \equiv \int {\rm d}v\ \Delta\tilde{\eta}(v)\frac{\delta}{\delta\tilde{\eta}(v)}\left(\frac{{\rm d}R}{{\rm d}E'}\right). \tag{A.22}$$

Eq. (A.20) shows that the function $q(v)$ is invariant under a variation $\Delta\tilde{\eta}$ of the best fit halo function that leaves the rates unchanged (all best fit halo functions should yield the same

unique best fit rates). This implies that all best fit halo functions must have their points of discontinuity (i.e. the locations of its steps) at the same $v_{\min}$ values. In other words, a variation having a non-zero Δv_a either breaks the KKT condition or changes the observable rates, and thus such a variation inevitably decreases the value of the likelihood functional.

A.2.3 Evaluation of the second directional derivatives of L

Since the positions of the steps cannot change, it is enough to evaluate the second derivative of the functional L with respect to an arbitrary variation of the heights of the steps $\Delta\tilde{\eta}_a$. Expanding the functional L around the best fit halo up to the second order we get

$$\begin{aligned}
\Delta L &= \frac{1}{2}\sum_{i,j=1}^{\mathcal{N}} \Delta\tilde{\eta}_i \Delta\tilde{\eta}_j \int_{v_{i-1}}^{v_i} \mathrm{d}v \int_{v_{j-1}}^{v_j} \mathrm{d}u \frac{\delta^2 L}{\delta\tilde{\eta}(v)\delta\tilde{\eta}(u)} && \text{(A.23)} \\
&= \frac{1}{2}\sum_{i,j=1}^{\mathcal{N}} \Delta\tilde{\eta}_i \Delta\tilde{\eta}_j \int_{v_{i-1}}^{v_i} \mathrm{d}v \frac{\delta}{\delta\tilde{\eta}(v)} \left(q(v_j) - q(v_{j-1})\right) && \text{(A.24)} \\
&= 2\sum_{A=1}^{\mathcal{N}} \left(\sum_{i=1}^{\mathcal{N}} \mathcal{K}_{Ai}\Delta\tilde{\eta}_i\right)^2 . && \text{(A.25)}
\end{aligned}$$

Here we defined the index A to run over all data points, namely all bins or single events of all experiments considered, so A runs from 1 to $\mathcal{N}$. Specifically, the summation over A runs over the observed events in the extended likelihoods and the bins j of all experiments α with Poisson and Gaussian likelihoods. The index i indicates instead each constant portion of the best fit halo function, between the steps at $v_{\min}$ values v_{i-1} and v_i. The maximum number of steps was found in Appendix A to be $\mathcal{N}$, so we can take take the number of steps to be equal to $\mathcal{N}$ and consider some of the step heights to be zero. In this way, i also runs from 1

to $\mathcal{N}$. The coefficients K_{Ai} are given by

$$\mathcal{K}_{Ai} \equiv \frac{H_A(v_i) - H_A(v_{i-1})}{\gamma_A[\tilde{\eta}]} \tag{A.26}$$

for extended likelihoods,

$$\mathcal{K}_{Ai} \equiv \sqrt{n_j^{(\alpha)}}\, \frac{\xi_j^{(\alpha)}(v_i) - \xi_j^{(\alpha)}(v_{i-1})}{\nu_j^{(\alpha)}[\tilde{\eta}] + b_j^{(\alpha)}} \tag{A.27}$$

for Poisson likelihoods, and

$$\mathcal{K}_{Ai} \equiv \frac{\xi_j^{(\alpha)}(v_i) - \xi_j^{(\alpha)}(v_{i-1})}{\sigma_j^{(\alpha)}}\,, \tag{A.28}$$

for Gaussian likelihoods. In the last two equations the index A accounts for the experiment-bin pairs indexes (α, j).

Notice that the quantities $\mathcal{K}_{Ai}$ can be interpreted as the components of $\mathcal{N}$ non-zero vectors $\vec{\mathcal{K}}_A$ in a vector space with dimension $\mathcal{N}$ with components denoted by i. We can also consider $\Delta\tilde{\eta}_i$ to be the components of a vector $\Delta\vec{\tilde{\eta}}$ with the same number of dimensions of the $\vec{\mathcal{K}}_A$ vectors. Each vector $\Delta\vec{\tilde{\eta}}$ is a possible infinitesimal variation of the heights of the steps $\tilde{\eta}_i$ around a best fit halo function. Eq. (A.23) is then a sum of the squares of the inner products of two vectors $\vec{\mathcal{K}}_A$ and $\Delta\vec{\tilde{\eta}}$.

Notice also that the vectors $\vec{\mathcal{K}}_A$ are generically linearly independent, because there is no reason that the experiment-specific quantities $\mathcal{K}_{Ai}$ should be dependent upon information contained in a different bin or experiment.

Since the vectors $\vec{\mathcal{K}}_A$ are generically linearly independent there is no non-zero vector $\Delta\vec{\tilde{\eta}}$

orthogonal to all of them. This implies that there is no infinitesimal variation of the heights of the steps $\tilde{\eta}_i$ around a best fit halo function for which the second order variation of L vanishes. This proves that the likelihood functional L is not invariant under any infinitesimal variation around the best fit halo function which would lead to another best fit halo function. Since all the second directional derivatives of L around a best fit halo function are positive the best fit halo function must be unique.

A.3 Model Selection Prospects in Xenon (SI Interaction)

[Pertains to Chapter 8]

We present in Figs. A.1–A.3 the model selection prospects for various exposures on a xenon experiment, including (solid lines) and neglecting (dashed lines) information on the modulation of the recoil rate, and assuming the SI interaction is the true model. Results are shown for 20 GeV (Fig. A.1), 125 GeV (Fig. A.2), and 500 GeV (Fig. A.3) DM particle. Results are similar to those presented in Sec. 8.5 for the case of the anapole interaction.

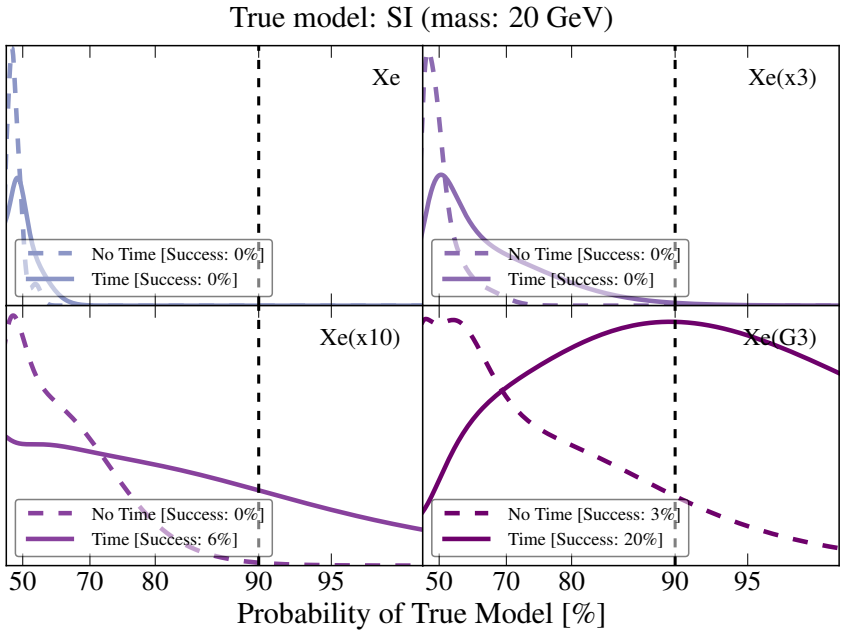

Figure A.1: Same as Fig. 8.3 but for the SI interaction as the true model.

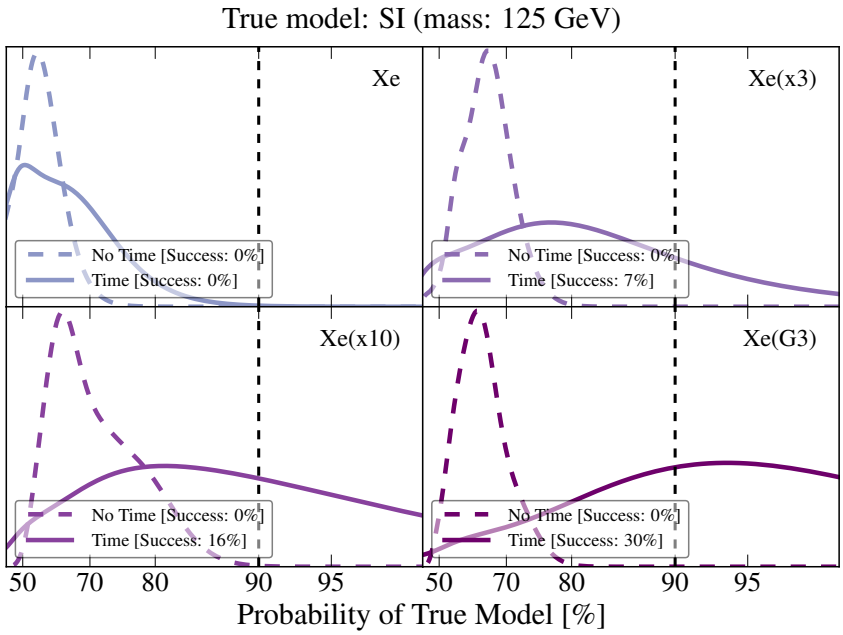

Figure A.2: Same as Fig. 8.3 but for a 125 GeV DM and the SI interaction as the true model.

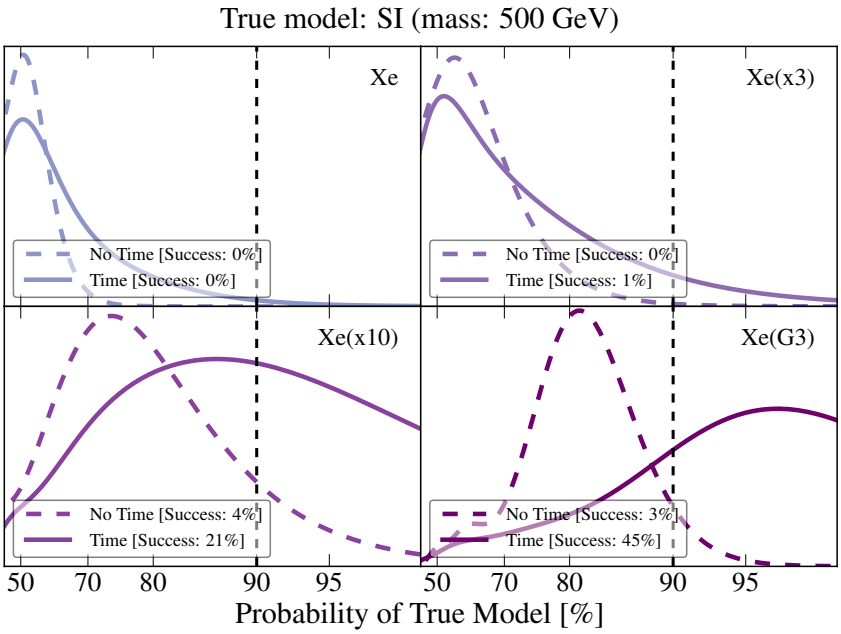

Figure A.3: Same as Fig. 8.3 but for a 500 GeV DM and the SI interaction as the true model.

References

[1] H. Poincaré*L'Astronomie* (1906) 158.

[2] W. T. B. Kelvin, *Baltimore lectures on molecular dynamics and the wave theory of light*. CJ Clay and Sons, 1904.

[3] E. Öpik*Bull. de la Soc. Astr. de Russie, 21* (1915) 150.

[4] J. Jeans, *The motions of stars in a kapteyn universe*, *Monthly Notices of the Royal Astronomical Society* **82** (1922) 122–132.

[5] J. H. Oort, *The force exerted by the stellar system in the direction perpendicular to the galactic plane and some related problems*, *Bulletin of the Astronomical Institutes of the Netherlands* **6** (1932) 249.

[6] E. Hubble and M. L. Humason, *The Velocity-Distance Relation among Extra-Galactic Nebulae*, *Astrophys. J.* **74** (1931) 43–80.

[7] F. Zwicky, *Die Rotverschiebung von extragalaktischen Nebeln*, *Helv. Phys. Acta* **6** (1933) 110–127.

[8] G. Bertone and D. Hooper, *A History of Dark Matter*, *Submitted to: Rev. Mod. Phys.* (2016) , [1605.04909].

[9] E. Holmberg, *On the clustering tendencies among the nebulae.*, *The Astrophysical Journal* **92** (1940) 200.

[10] M. Schwarzschild, *Mass distribution and mass-luminosity ratio in galaxies*, *The Astronomical Journal* **59** (1954) 273.

[11] A. Penzias, *Free hydrogen in the pegasus i cluster of galaxies.*, *The Astronomical Journal* **66** (1961) 293.

[12] H. J. Rood, *The dynamics of the coma cluster of galaxies.*, .

[13] V. C. Rubin and W. K. Ford, Jr., *Rotation of the Andromeda Nebula from a Spectroscopic Survey of Emission Regions*, *Astrophys. J.* **159** (1970) 379–403.

[14] K. C. Freeman, *On the disks of spiral and SO Galaxies*, *Astrophys. J.* **160** (1970) 811.

[15] D. Rogstad and G. Shostak, *Gross properties of five scd galaxies as determined from 21-centimeter observations*, *The Astrophysical Journal* **176** (1972) 315.

[16] M. Roberts and A. Rots, *Comparison of rotation curves of different galaxy types*, *Astronomy and Astrophysics* **26** (1973) 483–485.

[17] J. Einasto, A. Kaasik and E. Saar, *Dynamic evidence on massive coronas of galaxies*, *Nature* **250** (1974) 309–310.

[18] J. P. Ostriker, P. J. E. Peebles and A. Yahil, *The size and mass of galaxies, and the mass of the universe*, *Astrophys. J.* **193** (1974) L1–L4.

[19] M. S. Roberts and R. N. Whitehurst, *The rotation curve and geometry of m31 at large galactocentric distances.*, *The Astrophysical Journal* **201** (1975) 327–346.

[20] N. Krumm and E. Salpeter, *Rotation curves, mass distributions and total masses of some spiral galaxies.*, *Astronomy and Astrophysics* **56** (1977) 465–468.

[21] A. Bosma, *The distribution and kinematics of neutral hydrogen in spiral galaxies of various morphological types*, .

[22] V. C. Rubin, N. Thonnard and W. K. Ford, Jr., *Rotational properties of 21 SC galaxies with a large range of luminosities and radii, from NGC 4605 /R = 4kpc/ to UGC 2885 /R = 122 kpc/*, *Astrophys. J.* **238** (1980) 471.

[23] S. M. Faber and J. Gallagher, *Masses and mass-to-light ratios of galaxies*, *Annual review of astronomy and astrophysics* **17** (1979) 135–187.

[24] MACHO collaboration, C. Alcock et al., *The MACHO project: Microlensing results from 5.7 years of LMC observations*, *Astrophys. J.* **542** (2000) 281–307, [astro-ph/0001272].

[25] EROS collaboration, T. Lasserre, *Not enough stellar mass machos in the galactic halo*, *Astron. Astrophys.* **355** (2000) L39–L42, [astro-ph/0002253].

[26] EROS-2 collaboration, P. Tisserand et al., *Limits on the Macho Content of the Galactic Halo from the EROS-2 Survey of the Magellanic Clouds*, *Astron. Astrophys.* **469** (2007) 387–404, [astro-ph/0607207].

[27] S. Burles, K. M. Nollett and M. S. Turner, *Big bang nucleosynthesis predictions for precision cosmology*, *Astrophys. J.* **552** (2001) L1–L6, [astro-ph/0010171].

[28] S. Burles and D. Tytler, *The Deuterium abundance towards Q1937-1009*, *Astrophys. J.* **499** (1998) 699, [astro-ph/9712108].

[29] S. Burles and D. Tytler, *The Deuterium abundance toward QSO 1009+2956*, *Astrophys. J.* **507** (1998) 732–744, [astro-ph/9712109].

[30] J. M. O'Meara, D. Tytler, D. Kirkman, N. Suzuki, J. X. Prochaska, D. Lubin et al., *The Deuterium to hydrogen abundance ratio towards a fourth QSO: HS 0105 + 1619*, *Astrophys. J.* **552** (2001) 718–730, [astro-ph/0011179].

[31] WMAP collaboration, G. Hinshaw et al., *Nine-Year Wilkinson Microwave Anisotropy Probe (WMAP) Observations: Cosmological Parameter Results*, *Astrophys. J. Suppl.* **208** (2013) 19, [1212.5226].

[32] Planck collaboration, P. A. R. Ade et al., *Planck 2015 results. XIII. Cosmological parameters*, *Astron. Astrophys.* **594** (2016) A13, [1502.01589].

[33] P. J. E. Peebles, *Large scale background temperature and mass fluctuations due to scale invariant primeval perturbations*, *Astrophys. J.* **263** (1982) L1–L5.

[34] M. Milgrom, *A Modification of the Newtonian dynamics as a possible alternative to the hidden mass hypothesis*, *Astrophys. J.* **270** (1983) 365–370.

[35] M. Milgrom, *A Modification of the Newtonian dynamics: Implications for galaxies*, *Astrophys. J.* **270** (1983) 371–383.

[36] M. Milgrom, *A modification of the Newtonian dynamics: implications for galaxy systems*, *Astrophys. J.* **270** (1983) 384–389.

[37] J. Bekenstein and M. Milgrom, *Does the missing mass problem signal the breakdown of Newtonian gravity?*, *Astrophys. J.* **286** (1984) 7–14.

[38] J. D. Bekenstein, *Phase Coupling Gravitation: Symmetries and Gauge Fields*, *Phys. Lett.* **B202** (1988) 497–500.

[39] J. D. Bekenstein, *Relativistic gravitation theory for the MOND paradigm*, *Phys. Rev.* **D70** (2004) 083509, [astro-ph/0403694].

[40] D. Clowe, M. Bradac, A. H. Gonzalez, M. Markevitch, S. W. Randall, C. Jones et al., *A direct empirical proof of the existence of dark matter*, *Astrophys. J.* **648** (2006) L109–L113, [astro-ph/0608407].

[41] B. Famaey and S. McGaugh, *Modified Newtonian Dynamics (MOND): Observational Phenomenology and Relativistic Extensions*, *Living Rev. Rel.* **15** (2012) 10, [1112.3960].

[42] J. Fan, A. Katz, L. Randall and M. Reece, *Double-Disk Dark Matter*, *Phys. Dark Univ.* **2** (2013) 139–156, [1303.1521].

[43] Particle Data Group collaboration, C. Patrignani et al., *Review of Particle Physics*, *Chin. Phys.* **C40** (2016) 100001.

[44] M. Viel, G. D. Becker, J. S. Bolton and M. G. Haehnelt, *Warm dark matter as a solution to the small scale crisis: New constraints from high redshift lyman-α forest data*, *Physical Review D* **88** (2013) 043502.

[45] J. E. Gunn, B. W. Lee, I. Lerche, D. N. Schramm and G. Steigman, *Some Astrophysical Consequences of the Existence of a Heavy Stable Neutral Lepton*, *Astrophys. J.* **223** (1978) 1015–1031.

[46] F. W. Stecker, *Diffuse Fluxes of Cosmic High-Energy Neutrinos*, *Astrophys. J.* **228** (1979) 919–927.

[47] Fermi-LAT collaboration, M. Ackermann et al., *Searching for Dark Matter Annihilation from Milky Way Dwarf Spheroidal Galaxies with Six Years of Fermi-LAT Data*, 1503.02641.

[48] H. Liu, T. R. Slatyer and J. Zavala, *Contributions to cosmic reionization from dark matter annihilation and decay*, *Phys. Rev.* **D94** (2016) 063507, [1604.02457].

[49] M. W. Goodman and E. Witten, *Detectability of Certain Dark Matter Candidates*, *Phys. Rev.* **D31** (1985) 3059.

[50] G. B. Gelmini, *TASI 2014 Lectures: The Hunt for Dark Matter*, in *Theoretical Advanced Study Institute in Elementary Particle Physics: Journeys Through the Precision Frontier: Amplitudes for Colliders (TASI 2014) Boulder, Colorado, June 2-27, 2014*, 2015. 1502.01320.

[51] K. Freese, M. Lisanti and C. Savage, *Colloquium: Annual modulation of dark matter*, *Rev. Mod. Phys.* **85** (2013) 1561–1581, [1209.3339].

[52] M. Vogelsberger, A. Helmi, V. Springel, S. D. M. White, J. Wang, C. S. Frenk et al., *Phase-space structure in the local dark matter distribution and its signature in direct detection experiments*, *Mon. Not. Roy. Astron. Soc.* **395** (2009) 797–811, [0812.0362].

[53] A. M. Green, *Effect of realistic astrophysical inputs on the phase and shape of the WIMP annual modulation signal*, *Phys. Rev.* **D68** (2003) 023004, [astro-ph/0304446].

[54] G. Gelmini and P. Gondolo, *WIMP annual modulation with opposite phase in Late-Infall halo models*, *Phys. Rev.* **D64** (2001) 023504, [hep-ph/0012315].

[55] K. Freese, P. Gondolo, H. J. Newberg and M. Lewis, *The effects of the Sagittarius dwarf tidal stream on dark matter detectors*, *Phys. Rev. Lett.* **92** (2004) 111301, [astro-ph/0310334].

[56] K. Freese, P. Gondolo and H. J. Newberg, *Detectability of weakly interacting massive particles in the Sagittarius dwarf tidal stream*, *Phys. Rev.* **D71** (2005) 043516, [astro-ph/0309279].

[57] C. Savage, K. Freese and P. Gondolo, *Annual Modulation of Dark Matter in the Presence of Streams*, *Phys. Rev.* **D74** (2006) 043531, [astro-ph/0607121].

[58] N. Fornengo and S. Scopel, *Temporal distortion of annual modulation at low recoil energies*, *Phys. Lett.* **B576** (2003) 189–194, [hep-ph/0301132].

[59] P. Belli, R. Cerulli, N. Fornengo and S. Scopel, *Effect of the galactic halo modeling on the DAMA / NaI annual modulation result: an Extended analysis of the data for WIMPs with a purely spin independent coupling*, *Phys. Rev.* **D66** (2002) 043503, [hep-ph/0203242].

[60] M. Kuhlen, M. Lisanti and D. N. Spergel, *Direct Detection of Dark Matter Debris Flows*, *Phys. Rev.* **D86** (2012) 063505, [1202.0007].

[61] C. W. Purcell, J. S. Bullock and M. Kaplinghat, *The Dark Disk of the Milky Way*, *Astrophys. J.* **703** (2009) 2275–2284, [0906.5348].

[62] J. I. Read, G. Lake, O. Agertz and V. P. Debattista, *Thin, thick and dark discs in LCDM*, *Mon. Not. Roy. Astron. Soc.* **389** (2008) 1041–1057, [0803.2714].

[63] T. Bruch, J. Read, L. Baudis and G. Lake, *Detecting the Milky Way's Dark Disk*, *Astrophys. J.* **696** (2009) 920–923, [0804.2896].

[64] J. I. Read, L. Mayer, A. M. Brooks, F. Governato and G. Lake, *A dark matter disc in three cosmological simulations of Milky Way mass galaxies*, *Mon. Not. Roy. Astron. Soc.* **397** (2009) 44, [0902.0009].

[65] J. Fan, A. Katz, L. Randall and M. Reece, *Dark-Disk Universe*, *Phys. Rev. Lett.* **110** (2013) 211302, [1303.3271].

[66] C. W. Purcell, A. R. Zentner and M.-Y. Wang, *Dark Matter Direct Search Rates in Simulations of the Milky Way and Sagittarius Stream*, *JCAP* **1208** (2012) 027, [1203.6617].

[67] M. Lisanti and D. N. Spergel, *Dark Matter Debris Flows in the Milky Way*, *Phys. Dark Univ.* **1** (2012) 155–161, [1105.4166].

[68] D. Stiff, L. M. Widrow and J. Frieman, *Signatures of hierarchical clustering in dark matter detection experiments*, *Phys. Rev.* **D64** (2001) 083516, [astro-ph/0106048].

[69] J. I. Read, *The Local Dark Matter Density*, *J. Phys.* **G41** (2014) 063101, [1404.1938].

[70] G. R. Ruchti et al., *The Gaia-ESO Survey: a quiescent Milky Way with no significant dark/stellar accreted disc*, *Mon. Not. Roy. Astron. Soc.* **450** (2015) 2874–2887, [1504.02481].

[71] S. K. Lee, M. Lisanti and B. R. Safdi, *Dark-Matter Harmonics Beyond Annual Modulation*, *JCAP* **1311** (2013) 033, [1307.5323].

[72] M. S. Alenazi and P. Gondolo, *Phase-space distribution of unbound dark matter near the Sun*, *Phys. Rev.* **D74** (2006) 083518, [astro-ph/0608390].

[73] S. K. Lee, M. Lisanti, A. H. G. Peter and B. R. Safdi, *Effect of Gravitational Focusing on Annual Modulation in Dark-Matter Direct-Detection Experiments*, *Phys. Rev. Lett.* **112** (2014) 011301, [1308.1953].

[74] N. Bozorgnia and T. Schwetz, *Is the effect of the Sun's gravitational potential on dark matter particles observable?*, *JCAP* **1408** (2014) 013, [1405.2340].

[75] N. Bozorgnia, G. B. Gelmini and P. Gondolo, *Aberration features in directional dark matter detection*, *JCAP* **1208** (2012) 011, [1205.2333].

[76] F. J. Kerr and D. Lynden-Bell, *Review of galactic constants*, *Mon. Not. Roy. Astron. Soc.* **221** (1986) 1023.

[77] T. Piffl et al., *The RAVE survey: the Galactic escape speed and the mass of the Milky Way*, *Astron. Astrophys.* **562** (2014) A91, [1309.4293].

[78] A. K. Drukier, K. Freese and D. N. Spergel, *Detecting Cold Dark Matter Candidates*, *Phys. Rev.* **D33** (1986) 3495–3508.

[79] S. K. Lee, M. Lisanti, A. H. G. Peter and B. R. Safdi, *Effect of Gravitational Focusing on Annual Modulation in Dark-Matter Direct-Detection Experiments*, *Phys. Rev. Lett.* **112** (2014) 011301, [1308.1953].

[80] N. Bozorgnia and T. Schwetz, *Is the effect of the Sun's gravitational potential on dark matter particles observable?*, *JCAP* **1408** (2014) 013, [1405.2340].

[81] E. Del Nobile, G. B. Gelmini and S. J. Witte, *Gravitational Focusing and Substructure Effects on the Rate Modulation in Direct Dark Matter Searches*, *JCAP* **1508** (2015) 041, [1505.07538].

[82] N. Fornengo and S. Scopel, *Temporal distortion of annual modulation at low recoil energies*, *Phys. Lett.* **B576** (2003) 189–194, [hep-ph/0301132].

[83] A. M. Green, *Effect of realistic astrophysical inputs on the phase and shape of the WIMP annual modulation signal*, *Phys. Rev.* **D68** (2003) 023004, [astro-ph/0304446].

[84] A. M. Green, *The WIMP annual modulation signal and nonstandard halo models*, *Phys. Rev.* **D63** (2001) 043005, [astro-ph/0008318].

[85] C. Savage, K. Freese and P. Gondolo, *Annual Modulation of Dark Matter in the Presence of Streams*, *Phys. Rev.* **D74** (2006) 043531, [astro-ph/0607121].

[86] N. W. Evans, C. M. Carollo and P. T. de Zeeuw, *Triaxial haloes and particle dark matter detection*, *Mon. Not. Roy. Astron. Soc.* **318** (2000) 1131, [astro-ph/0008156].

[87] G. Gelmini and P. Gondolo, *WIMP annual modulation with opposite phase in Late-Infall halo models*, *Phys. Rev.* **D64** (2001) 023504, [hep-ph/0012315].

[88] K. Freese, P. Gondolo, H. J. Newberg and M. Lewis, *The effects of the Sagittarius dwarf tidal stream on dark matter detectors*, *Phys. Rev. Lett.* **92** (2004) 111301, [astro-ph/0310334].

[89] T. Bruch, J. Read, L. Baudis and G. Lake, *Detecting the Milky Way's Dark Disk*, *Astrophys. J.* **696** (2009) 920–923, [0804.2896].

[90] C. W. Purcell, A. R. Zentner and M.-Y. Wang, *Dark Matter Direct Search Rates in Simulations of the Milky Way and Sagittarius Stream*, *JCAP* **1208** (2012) 027, [1203.6617].

[91] P. Gondolo and G. B. Gelmini, *Halo independent comparison of direct dark matter detection data*, *JCAP* **1212** (2012) 015, [1202.6359].

[92] G. B. Gelmini, A. Georgescu, P. Gondolo and J.-H. Huh, *Extended Maximum Likelihood Halo-independent Analysis of Dark Matter Direct Detection Data*, *JCAP* **1511** (2015) 038, [1507.03902].

[93] E. Del Nobile, G. Gelmini, P. Gondolo and J.-H. Huh, *Generalized Halo Independent Comparison of Direct Dark Matter Detection Data*, *JCAP* **1310** (2013) 048, [1306.5273].

[94] E. Del Nobile, G. B. Gelmini and S. J. Witte, *Target dependence of the annual modulation in direct dark matter searches*, *Phys. Rev.* **D91** (2015) 121302, [1504.06772].

[95] S. K. Lee, M. Lisanti and B. R. Safdi, *Dark-Matter Harmonics Beyond Annual Modulation*, *JCAP* **1311** (2013) 033, [1307.5323].

[96] T. Piffl et al., *The RAVE survey: the Galactic escape speed and the mass of the Milky Way*, *Astron. Astrophys.* **562** (2014) A91, [1309.4293].

[97] F. J. Kerr and D. Lynden-Bell, *Review of galactic constants*, *Mon. Not. Roy. Astron. Soc.* **221** (1986) 1023.

[98] M. S. Alenazi and P. Gondolo, *Phase-space distribution of unbound dark matter near the Sun*, *Phys. Rev.* **D74** (2006) 083518, [astro-ph/0608390].

[99] M. Pospelov and T. ter Veldhuis, *Direct and indirect limits on the electromagnetic form-factors of WIMPs*, *Phys. Lett.* **B480** (2000) 181–186, [hep-ph/0003010].

[100] K. Sigurdson, M. Doran, A. Kurylov, R. R. Caldwell and M. Kamionkowski, *Dark-matter electric and magnetic dipole moments*, *Phys. Rev.* **D70** (2004) 083501, [astro-ph/0406355].

[101] V. Barger, W.-Y. Keung and D. Marfatia, *Electromagnetic properties of dark matter: Dipole moments and charge form factor*, *Phys. Lett.* **B696** (2011) 74–78, [1007.4345].

[102] S. Chang, N. Weiner and I. Yavin, *Magnetic Inelastic Dark Matter*, *Phys. Rev.* **D82** (2010) 125011, [1007.4200].

[103] W. S. Cho, J.-H. Huh, I.-W. Kim, J. E. Kim and B. Kyae, *Constraining WIMP magnetic moment from CDMS II experiment*, *Phys. Lett.* **B687** (2010) 6–10, [1001.0579].

[104] J. H. Heo, *Minimal Dirac Fermionic Dark Matter with Nonzero Magnetic Dipole Moment*, *Phys. Lett.* **B693** (2010) 255–258, [0901.3815].

[105] S. Gardner, *Shedding Light on Dark Matter: A Faraday Rotation Experiment to Limit a Dark Magnetic Moment*, *Phys. Rev.* **D79** (2009) 055007, [0811.0967].

[106] E. Masso, S. Mohanty and S. Rao, *Dipolar Dark Matter*, *Phys. Rev.* **D80** (2009) 036009, [0906.1979].

[107] T. Banks, J.-F. Fortin and S. Thomas, *Direct Detection of Dark Matter Electromagnetic Dipole Moments*, 1007.5515.

[108] J.-F. Fortin and T. M. P. Tait, *Collider Constraints on Dipole-Interacting Dark Matter*, *Phys. Rev.* **D85** (2012) 063506, [1103.3289].

[109] H. An, S.-L. Chen, R. N. Mohapatra, S. Nussinov and Y. Zhang, *Energy Dependence of Direct Detection Cross Section for Asymmetric Mirror Dark Matter*, *Phys. Rev.* **D82** (2010) 023533, [1004.3296].

[110] K. Kumar, A. Menon and T. M. P. Tait, *Magnetic Fluffy Dark Matter*, *JHEP* **02** (2012) 131, [1111.2336].

[111] V. Barger, W.-Y. Keung, D. Marfatia and P.-Y. Tseng, *Dipole Moment Dark Matter at the LHC*, *Phys. Lett.* **B717** (2012) 219–223, [1206.0640].

[112] E. Del Nobile, C. Kouvaris, P. Panci, F. Sannino and J. Virkajarvi, *Light Magnetic Dark Matter in Direct Detection Searches*, *JCAP* **1208** (2012) 010, [1203.6652].

[113] J. M. Cline, Z. Liu and W. Xue, *Millicharged Atomic Dark Matter*, *Phys. Rev.* **D85** (2012) 101302, [1201.4858].

[114] N. Weiner and I. Yavin, *How Dark Are Majorana WIMPs? Signals from MiDM and Rayleigh Dark Matter*, *Phys. Rev.* **D86** (2012) 075021, [1206.2910].

[115] S. Tulin, H.-B. Yu and K. M. Zurek, *Three Exceptions for Thermal Dark Matter with Enhanced Annihilation to $\gamma\gamma$*, *Phys. Rev.* **D87** (2013) 036011, [1208.0009].

[116] J. M. Cline, A. R. Frey and G. D. Moore, *Composite magnetic dark matter and the 130 GeV line*, *Phys. Rev.* **D86** (2012) 115013, [1208.2685].

[117] J. H. Heo and C. S. Kim, *Dipole-interacting Fermionic Dark Matter in positron, antiproton, and gamma-ray channels*, *Phys. Rev.* **D87** (2013) 013007, [1207.1341].

[118] G. Barello, S. Chang and C. A. Newby, *A Model Independent Approach to Inelastic Dark Matter Scattering*, *Phys. Rev.* **D90** (2014) 094027, [1409.0536].

[119] I. Lopes, K. Kadota and J. Silk, *Constraint on Light Dipole Dark Matter from Helioseismology*, *Astrophys. J. Lett.* **780** (2014) L15, [1310.0673].

[120] W.-Y. Keung, I. Low and G. Shaughnessy, *When CoGeNT met PAMELA*, *Phys. Rev.* **D82** (2010) 115019, [1010.1774].

[121] M. I. Gresham and K. M. Zurek, *Light Dark Matter Anomalies After LUX*, *Phys. Rev.* **D89** (2014) 016017, [1311.2082].

[122] E. Del Nobile, G. B. Gelmini, P. Gondolo and J.-H. Huh, *Direct detection of Light Anapole and Magnetic Dipole DM*, *JCAP* **1406** (2014) 002, [1401.4508].

[123] M. I. Gresham and K. M. Zurek, *Effect of nuclear response functions in dark matter direct detection*, *Phys. Rev.* **D89** (2014) 123521, [1401.3739].

[124] C. M. Ho and R. J. Scherrer, *Anapole Dark Matter*, *Phys. Lett.* **B722** (2013) 341–346, [1211.0503].

[125] A. L. Fitzpatrick and K. M. Zurek, *Dark Moments and the DAMA-CoGeNT Puzzle*, *Phys. Rev.* **D82** (2010) 075004, [1007.5325].

[126] M. T. Frandsen, F. Kahlhoefer, C. McCabe, S. Sarkar and K. Schmidt-Hoberg, *The unbearable lightness of being: CDMS versus XENON*, *JCAP* **1307** (2013) 023, [1304.6066].

[127] Y. Gao, C. M. Ho and R. J. Scherrer, *Anapole Dark Matter at the LHC*, *Phys. Rev.* **D89** (2014) 045006, [1311.5630].

[128] J. Goodman, M. Ibe, A. Rajaraman, W. Shepherd, T. M. P. Tait and H.-B. Yu, *Constraints on Dark Matter from Colliders*, *Phys. Rev.* **D82** (2010) 116010, [1008.1783].

[129] J. Goodman, M. Ibe, A. Rajaraman, W. Shepherd, T. M. P. Tait and H.-B. Yu, *Constraints on Light Majorana dark Matter from Colliders*, *Phys. Lett.* **B695** (2011) 185–188, [1005.1286].

[130] J.-M. Zheng, Z.-H. Yu, J.-W. Shao, X.-J. Bi, Z. Li and H.-H. Zhang, *Constraining the interaction strength between dark matter and visible matter: I. fermionic dark matter*, *Nucl. Phys.* **B854** (2012) 350–374, [1012.2022].

[131] Z.-L. Liang and Y.-L. Wu, *Direct detection and solar capture of spin-dependent dark matter*, *Phys. Rev.* **D89** (2014) 013010, [1308.5897].

[132] R. Catena and P. Gondolo, *Global fits of the dark matter-nucleon effective interactions*, *JCAP* **1409** (2014) 045, [1405.2637].

[133] R. Catena, *Prospects for direct detection of dark matter in an effective theory approach*, *JCAP* **1407** (2014) 055, [1406.0524].

[134] A. L. Fitzpatrick, W. Haxton, E. Katz, N. Lubbers and Y. Xu, *The Effective Field Theory of Dark Matter Direct Detection*, *JCAP* **1302** (2013) 004, [1203.3542].

[135] A. L. Fitzpatrick, W. Haxton, E. Katz, N. Lubbers and Y. Xu, *Model Independent Direct Detection Analyses*, 1211.2818.

[136] J. Kumar and D. Marfatia, *Matrix element analyses of dark matter scattering and annihilation*, *Phys. Rev.* **D88** (2013) 014035, [1305.1611].

[137] M. Cirelli, E. Del Nobile and P. Panci, *Tools for model-independent bounds in direct dark matter searches*, *JCAP* **1310** (2013) 019, [1307.5955].

[138] B. Feldstein and F. Kahlhoefer, *Quantifying (dis)agreement between direct detection experiments in a halo-independent way*, *JCAP* **1412** (2014) 052, [1409.5446].

[139] E. Del Nobile, M. Kaplinghat and H.-B. Yu, *Direct Detection Signatures of Self-Interacting Dark Matter with a Light Mediator*, *JCAP* **1510** (2015) 055, [1507.04007].

[140] LUX collaboration, D. S. Akerib et al., *First results from the LUX dark matter experiment at the Sanford Underground Research Facility*, *Phys. Rev. Lett.* **112** (2014) 091303, [1310.8214].

[141] R. Bernabei et al., *Final model independent result of DAMA/LIBRA-phase1*, *Eur. Phys. J.* **C73** (2013) 2648, [1308.5109].

[142] PICO collaboration, C. Amole et al., *Dark Matter Search Results from the PICO-2L C_3F_8 Bubble Chamber*, *Phys. Rev. Lett.* **114** (2015) 231302, [1503.00008].

[143] PICASSO collaboration, S. Archambault et al., *Constraints on Low-Mass WIMP Interactions on ^{19}F from PICASSO*, *Phys. Lett.* **B711** (2012) 153–161, [1202.1240].

[144] J. Cooley, *Overview of Non-Liquid Noble Direct Detection Dark Matter Experiments*, *Phys. Dark Univ.* **4** (2014) 92–97, [1410.4960].

[145] J. H. Davis, *The Past and Future of Light Dark Matter Direct Detection*, *Int. J. Mod. Phys.* **A30** (2015) 1530038, [1506.03924].

[146] DAMA collaboration, R. Bernabei et al., *The DAMA/LIBRA apparatus*, *Nucl. Instrum. Meth.* **A592** (2008) 297–315, [0804.2738].

[147] D. Tucker-Smith and N. Weiner, *Inelastic dark matter*, *Phys. Rev.* **D64** (2001) 043502, [hep-ph/0101138].

[148] P. W. Graham, R. Harnik, S. Rajendran and P. Saraswat, *Exothermic Dark Matter*, *Phys. Rev.* **D82** (2010) 063512, [1004.0937].

[149] E. Del Nobile, G. B. Gelmini, A. Georgescu and J.-H. Huh, *Reevaluation of spin-dependent WIMP-proton interactions as an explanation of the DAMA data*, *JCAP* **1508** (2015) 046, [1502.07682].

[150] DAMA, LIBRA collaboration, R. Bernabei et al., *New results from DAMA/LIBRA*, *Eur. Phys. J.* **C67** (2010) 39–49, [1002.1028].

[151] CoGeNT collaboration, C. E. Aalseth et al., *Results from a Search for Light-Mass Dark Matter with a P-type Point Contact Germanium Detector*, *Phys. Rev. Lett.* **106** (2011) 131301, [1002.4703].

[152] C. E. Aalseth et al., *Search for an Annual Modulation in a P-type Point Contact Germanium Dark Matter Detector*, *Phys. Rev. Lett.* **107** (2011) 141301, [1106.0650].

[153] CoGeNT collaboration, C. E. Aalseth et al., *CoGeNT: A Search for Low-Mass Dark Matter using p-type Point Contact Germanium Detectors*, *Phys. Rev.* **D88** (2013) 012002, [1208.5737].

[154] CoGeNT collaboration, C. E. Aalseth et al., *Search for An Annual Modulation in Three Years of CoGeNT Dark Matter Detector Data*, 1401.3295.

[155] C. E. Aalseth et al., *Maximum Likelihood Signal Extraction Method Applied to 3.4 years of CoGeNT Data*, 1401.6234.

[156] CDMS collaboration, R. Agnese et al., *Silicon Detector Dark Matter Results from the Final Exposure of CDMS II*, *Phys. Rev. Lett.* **111** (2013) 251301, [1304.4279].

[157] XENON10 collaboration, J. Angle et al., *A search for light dark matter in XENON10 data*, *Phys. Rev. Lett.* **107** (2011) 051301, [1104.3088].

[158] XENON100 collaboration, E. Aprile et al., *Dark Matter Results from 100 Live Days of XENON100 Data*, *Phys. Rev. Lett.* **107** (2011) 131302, [1104.2549].

[159] XENON100 collaboration, E. Aprile et al., *Dark Matter Results from 225 Live Days of XENON100 Data*, *Phys. Rev. Lett.* **109** (2012) 181301, [1207.5988].

[160] M. Felizardo et al., *Final Analysis and Results of the Phase II SIMPLE Dark Matter Search*, *Phys. Rev. Lett.* **108** (2012) 201302, [1106.3014].

[161] COUPP collaboration, E. Behnke et al., *First Dark Matter Search Results from a 4-kg CF_3I Bubble Chamber Operated in a Deep Underground Site*, *Phys. Rev.* **D86** (2012) 052001, [1204.3094].

[162] CDMS-II collaboration, Z. Ahmed et al., *Search for annual modulation in low-energy CDMS-II data*, 1203.1309.

[163] SuperCDMS collaboration, R. Agnese et al., *Improved WIMP-search reach of the CDMS II germanium data*, *Phys. Rev.* **D92** (2015) 072003, [1504.05871].

[164] LUX collaboration, D. S. Akerib et al., *Improved Limits on Scattering of Weakly Interacting Massive Particles from Reanalysis of 2013 LUX Data*, *Phys. Rev. Lett.* **116** (2016) 161301, [1512.03506].

[165] SuperCDMS collaboration, R. Agnese et al., *New Results from the Search for Low-Mass Weakly Interacting Massive Particles with the CDMS Low Ionization Threshold Experiment*, *Phys. Rev. Lett.* **116** (2016) 071301, [1509.02448].

[166] SuperCDMS collaboration, R. Agnese et al., *Search for Low-Mass Weakly Interacting Massive Particles with SuperCDMS*, *Phys. Rev. Lett.* **112** (2014) 241302, [1402.7137].

[167] XENON100 collaboration, E. Aprile et al., *XENON100 Dark Matter Results from a Combination of 477 Live Days*, *Phys. Rev.* **D94** (2016) 122001, [1609.06154].

[168] LUX collaboration, D. S. Akerib et al., *Results from a search for dark matter in the complete LUX exposure*, *Phys. Rev. Lett.* **118** (2017) 021303, [1608.07648].

[169] PandaX-II collaboration, A. Tan et al., *Dark Matter Results from First 98.7 Days of Data from the PandaX-II Experiment*, *Phys. Rev. Lett.* **117** (2016) 121303, [1607.07400].

[170] PICO collaboration, C. Amole et al., *Dark Matter Search Results from the PICO-60 C_3F_8 Bubble Chamber*, 1702.07666.

[171] P. J. Fox, J. Liu and N. Weiner, *Integrating Out Astrophysical Uncertainties*, *Phys. Rev.* **D83** (2011) 103514, [1011.1915].

[172] P. J. Fox, G. D. Kribs and T. M. P. Tait, *Interpreting Dark Matter Direct Detection Independently of the Local Velocity and Density Distribution*, *Phys. Rev.* **D83** (2011) 034007, [1011.1910].

[173] M. T. Frandsen, F. Kahlhoefer, C. McCabe, S. Sarkar and K. Schmidt-Hoberg, *Resolving astrophysical uncertainties in dark matter direct detection*, *JCAP* **1201** (2012) 024, [1111.0292].

[174] J. Herrero-Garcia, T. Schwetz and J. Zupan, *Astrophysics independent bounds on the annual modulation of dark matter signals*, *Phys. Rev. Lett.* **109** (2012) 141301, [1205.0134].

[175] E. Del Nobile, G. B. Gelmini, P. Gondolo and J.-H. Huh, *Halo-independent analysis of direct detection data for light WIMPs*, *JCAP* **1310** (2013) 026, [1304.6183].

[176] N. Bozorgnia, J. Herrero-Garcia, T. Schwetz and J. Zupan, *Halo-independent methods for inelastic dark matter scattering*, *JCAP* **1307** (2013) 049, [1305.3575].

[177] E. Del Nobile, G. B. Gelmini, P. Gondolo and J.-H. Huh, *Update on Light WIMP Limits: LUX, lite and Light*, *JCAP* **1403** (2014) 014, [1311.4247].

[178] B. Feldstein and F. Kahlhoefer, *A new halo-independent approach to dark matter direct detection analysis*, *JCAP* **1408** (2014) 065, [1403.4606].

[179] P. J. Fox, Y. Kahn and M. McCullough, *Taking Halo-Independent Dark Matter Methods Out of the Bin*, *JCAP* **1410** (2014) 076, [1403.6830].

[180] G. B. Gelmini, A. Georgescu and J.-H. Huh, *Direct detection of light Ge-phobic" exothermic dark matter*, *JCAP* **1407** (2014) 028, [1404.7484].

[181] J. F. Cherry, M. T. Frandsen and I. M. Shoemaker, *Halo Independent Direct Detection of Momentum-Dependent Dark Matter*, *JCAP* **1410** (2014) 022, [1405.1420].

[182] E. Del Nobile, G. B. Gelmini, P. Gondolo and J.-H. Huh, *Update on the Halo-Independent Comparison of Direct Dark Matter Detection Data*, *Phys. Procedia* **61** (2015) 45–54, [1405.5582].

[183] S. Scopel and K. Yoon, *A systematic halo-independent analysis of direct detection data within the framework of Inelastic Dark Matter*, *JCAP* **1408** (2014) 060, [1405.0364].

[184] N. Bozorgnia and T. Schwetz, *What is the probability that direct detection experiments have observed Dark Matter?*, *JCAP* **1412** (2014) 015, [1410.6160].

[185] M. Blennow, J. Herrero-Garcia and T. Schwetz, *A halo-independent lower bound on the dark matter capture rate in the Sun from a direct detection signal*, *JCAP* **1505** (2015) 036, [1502.03342].

[186] A. J. Anderson, P. J. Fox, Y. Kahn and M. McCullough, *Halo-Independent Direct Detection Analyses Without Mass Assumptions*, *JCAP* **1510** (2015) 012, [1504.03333].

[187] M. Blennow, J. Herrero-Garcia, T. Schwetz and S. Vogl, *Halo-independent tests of dark matter direct detection signals: local DM density, LHC, and thermal freeze-out*, *JCAP* **1508** (2015) 039, [1505.05710].

[188] S. Scopel, K.-H. Yoon and J.-H. Yoon, *Generalized spin-dependent WIMP-nucleus interactions and the DAMA modulation effect*, *JCAP* **1507** (2015) 041, [1505.01926].

[189] F. Ferrer, A. Ibarra and S. Wild, *A novel approach to derive halo-independent limits on dark matter properties*, *JCAP* **1509** (2015) 052, [1506.03386].

[190] S. Wild, F. Ferrer and A. Ibarra, *Halo-independent upper limits on the dark matter scattering cross section with nucleons*, *J. Phys. Conf. Ser.* **718** (2016) 042063.

[191] F. Kahlhoefer and S. Wild, *Studying generalised dark matter interactions with extended halo-independent methods*, *JCAP* **1610** (2016) 032, [1607.04418].

[192] G. B. Gelmini, J.-H. Huh and S. J. Witte, *Assessing Compatibility of Direct Detection Data: Halo-Independent Global Likelihood Analyses*, *JCAP* **1610** (2016) 029, [1607.02445].

[193] B. J. Kavanagh and C. A. O'Hare, *Reconstructing the three-dimensional local dark matter velocity distribution*, *Phys. Rev.* **D94** (2016) 123009, [1609.08630].

[194] R. J. Barlow, *Extended maximum likelihood*, *Nucl. Instrum. Meth.* **A297** (1990) 496–506.

[195] C.-Q. Geng, D. Huang, C.-H. Lee and Q. Wang, *Direct Detection of Exothermic Dark Matter with Light Mediator*, *JCAP* **1608** (2016) 009, [1605.05098].

[196] XENON collaboration, D. Coderre, *Status of the XENON1T Dark Matter Search*, in *Proceedings, 10th Patras Workshop on Axions, WIMPs and WISPs (AXION-WIMP 2014): Geneva, Switzerland, June 29-July 4, 2014*, pp. 7–10, 2014. DOI.

[197] XENON collaboration, S. Diglio, *XENON1T: the start of a new era in the search for Dark Matter*, *PoS* **DSU2015** (2016) 032.

[198] LZ collaboration, D. S. Akerib et al., *LUX-ZEPLIN (LZ) Conceptual Design Report*, 1509.02910.

[199] LUX, LZ collaboration, M. Szydagis, *The Present and Future of Searching for Dark Matter with LUX and LZ*, in *38th International Conference on High Energy Physics (ICHEP 2016) Chicago, IL, USA, August 03-10, 2016*, 2016. 1611.05525.

[200] M. Schumann, L. Baudis, L. Btikofer, A. Kish and M. Selvi, *Dark matter sensitivity of multi-ton liquid xenon detectors*, *JCAP* **1510** (2015) 016, [1506.08309].

[201] DarkSide collaboration, P. Agnes et al., *Results from the first use of low radioactivity argon in a dark matter search*, *Phys. Rev.* **D93** (2016) 081101, [1510.00702].

[202] DarkSide collaboration, S. Davini, *The DarkSide awakens*, *J. Phys. Conf. Ser.* **718** (2016) 042016.

[203] A. Pullia, *Searches for Dark Matter with Superheated Liquid Techniques*, *Adv. High Energy Phys.* **2014** (2014) 387493.

[204] SuperCDMS collaboration, R. Agnese et al., *Projected Sensitivity of the SuperCDMS SNOLAB experiment*, *Submitted to: Phys. Rev. D* (2016) , [1610.00006].

[205] A. Kurylov and M. Kamionkowski, *Generalized analysis of weakly interacting massive particle searches*, *Phys. Rev.* **D69** (2004) 063503, [hep-ph/0307185].

[206] J. L. Feng, J. Kumar, D. Marfatia and D. Sanford, *Isospin-Violating Dark Matter*, *Phys. Lett.* **B703** (2011) 124–127, [1102.4331].

[207] D. P. Finkbeiner and N. Weiner, *Exciting Dark Matter and the INTEGRAL/SPI 511 keV signal*, *Phys. Rev.* **D76** (2007) 083519, [astro-ph/0702587].

[208] B. Batell, M. Pospelov and A. Ritz, *Direct Detection of Multi-component Secluded WIMPs*, *Phys. Rev.* **D79** (2009) 115019, [0903.3396].

[209] G. B. Gelmini, *Halo-Independent analysis of direct dark matter detection data for any WIMP interaction*, in *Proceedings, 37th International Conference on High Energy Physics (ICHEP 2014): Valencia, Spain, July 2-9, 2014*, 2014. 1411.0787.

[210] CDMS collaboration, Z. Ahmed et al., *Analysis of the low-energy electron-recoil spectrum of the CDMS experiment*, *Phys. Rev.* **D81** (2010) 042002, [0907.1438].

[211] K. McCarthy, "Dark matter search results from the silicon detectors of the cryogenic dark matter search experiment." 2013.

[212] S. Yellin, *Finding an upper limit in the presence of unknown background*, *Phys. Rev.* **D66** (2002) 032005, [physics/0203002].

[213] B. J. Scholz, A. E. Chavarria, J. I. Collar, P. Privitera and A. E. Robinson, *Measurement of the low-energy quenching factor in germanium using an $^{88}Y/Be$ photoneutron source*, *Phys. Rev.* **D94** (2016) 122003, [1608.03588].

[214] A. M. Green, *Astrophysical uncertainties on the local dark matter distribution and direct detection experiments*, 1703.10102.

[215] M. Maltoni, T. Schwetz, M. A. Tortola and J. W. F. Valle, *Ruling out four neutrino oscillation interpretations of the LSND anomaly?*, *Nucl. Phys.* **B643** (2002) 321–338, [hep-ph/0207157].

[216] M. Maltoni and T. Schwetz, *Testing the statistical compatibility of independent data sets*, *Phys. Rev.* **D68** (2003) 033020, [hep-ph/0304176].

[217] S. Chang, J. Liu, A. Pierce, N. Weiner and I. Yavin, *CoGeNT Interpretations*, *JCAP* **1008** (2010) 018, [1004.0697].

[218] A. Georgescu and S. Witte, "CoddsDM: Comparing data from direct searches for dark matter." GitHub repository https://github.com/SamWitte/Codds_DarkMatter, 2015–2016.

[219] G. J. Feldman and R. D. Cousins, *A Unified approach to the classical statistical analysis of small signals*, *Phys. Rev.* **D57** (1998) 3873–3889, [physics/9711021].

[220] Fermi-LAT, DES collaboration, A. Drlica-Wagner et al., *Search for Gamma-Ray Emission from DES Dwarf Spheroidal Galaxy Candidates with Fermi-LAT Data*, 1503.02632.

[221] A. Geringer-Sameth, S. M. Koushiappas and M. G. Walker, *A Comprehensive Search for Dark Matter Annihilation in Dwarf Galaxies*, 1410.2242.

[222] D. Hooper, C. Kelso and F. S. Queiroz, *Stringent and Robust Constraints on the Dark Matter Annihilation Cross Section From the Region of the Galactic Center*, *Astropart.Phys.* **46** (2013) 55–70, [1209.3015].

[223] Fermi-LAT collaboration, M. Ackermann et al., *Limits on Dark Matter Annihilation Signals from the Fermi LAT 4-year Measurement of the Isotropic Gamma-Ray Background*, 1501.05464.

[224] M. Di Mauro and F. Donato, *The composition of the Fermi-LAT IGRB intensity: emission from extragalactic point sources and dark matter annihilations*, 1501.05316.

[225] Fermi-LAT collaboration, M. Ajello et al., *Fermi-LAT Observations of High-Energy Gamma-Ray Emission Toward the Galactic Center*, 1511.02938.

[226] T. Daylan, D. P. Finkbeiner, D. Hooper, T. Linden, S. K. N. Portillo et al., *The Characterization of the Gamma-Ray Signal from the Central Milky Way: A Compelling Case for Annihilating Dark Matter*, 1402.6703.

[227] F. Calore, I. Cholis and C. Weniger, *Background model systematics for the Fermi GeV excess*, 1409.0042.

[228] K. N. Abazajian, N. Canac, S. Horiuchi and M. Kaplinghat, *Astrophysical and Dark Matter Interpretations of Extended Gamma-Ray Emission from the Galactic Center*, *Phys.Rev.* **D90** (2014) 023526, [1402.4090].

[229] D. Hooper and T. R. Slatyer, *Two Emission Mechanisms in the Fermi Bubbles: A Possible Signal of Annihilating Dark Matter*, *Phys.Dark Univ.* **2** (2013) 118–138, [1302.6589].

[230] C. Gordon and O. Macias, *Dark Matter and Pulsar Model Constraints from Galactic Center Fermi-LAT Gamma Ray Observations*, *Phys.Rev.* **D88** (2013) 083521, [1306.5725].

[231] K. N. Abazajian and M. Kaplinghat, *Detection of a Gamma-Ray Source in the Galactic Center Consistent with Extended Emission from Dark Matter Annihilation and Concentrated Astrophysical Emission*, *Phys.Rev.* **D86** (2012) 083511, [1207.6047].

[232] D. Hooper and T. Linden, *On The Origin Of The Gamma Rays From The Galactic Center*, *Phys.Rev.* **D84** (2011) 123005, [1110.0006].

[233] D. Hooper and L. Goodenough, *Dark Matter Annihilation in The Galactic Center As Seen by the Fermi Gamma Ray Space Telescope*, *Phys.Lett.* **B697** (2011) 412–428, [1010.2752].

[234] L. Goodenough and D. Hooper, *Possible Evidence For Dark Matter Annihilation In The Inner Milky Way From The Fermi Gamma Ray Space Telescope*, 0910.2998.

[235] I. Cholis, D. Hooper and T. Linden, *Challenges in Explaining the Galactic Center Gamma-Ray Excess with Millisecond Pulsars*, 1407.5625.

[236] S. K. Lee, M. Lisanti, B. R. Safdi, T. R. Slatyer and W. Xue, *Evidence for Unresolved Gamma-Ray Point Sources in the Inner Galaxy*, 1506.05124.

[237] R. Bartels, S. Krishnamurthy and C. Weniger, *Strong support for the millisecond pulsar origin of the Galactic center GeV excess*, 1506.05104.

[238] J. Petrovic, P. D. Serpico and G. Zaharijas, *Millisecond pulsars and the Galactic Center gamma-ray excess: the importance of luminosity function and secondary emission*, *JCAP* **1502** (2015) 023, [1411.2980].

[239] D. Hooper, I. Cholis, T. Linden, J. Siegal-Gaskins and T. Slatyer, *Pulsars Cannot Account for the Inner Galaxy's GeV Excess*, *Phys.Rev.* **D88** (2013) 083009, [1305.0830].

[240] D. Hooper and T. Linden, *The Gamma-Ray Pulsar Population of Globular Clusters: Implications for the GeV Excess*, *JCAP* **1608** (2016) 018, [1606.09250].

[241] T. D. Brandt and B. Kocsis, *Disrupted Globular Clusters Can Explain the Galactic Center Gamma Ray Excess*, *Astrophys. J.* **812** (2015) 15, [1507.05616].

[242] J. Petrovic, P. D. Serpico and G. Zaharijas, *Galactic Center gamma-ray "excess" from an active past of the Galactic Centre?*, *JCAP* **1410** (2014) 052, [1405.7928].

[243] I. Cholis, C. Evoli, F. Calore, T. Linden, C. Weniger et al., *The Galactic Center GeV Excess from a Series of Leptonic Cosmic-Ray Outbursts*, 1506.05119.

[244] E. Carlson and S. Profumo, *Cosmic Ray Protons in the Inner Galaxy and the Galactic Center Gamma-Ray Excess*, *Phys.Rev.* **D90** (2014) 023015, [1405.7685].

[245] S. D. White and C. S. Frenk, *Galaxy formation through hierarchical clustering*, *Astrophys.J.* **379** (1991) 52–79.

[246] B. Bertoni, D. Hooper and T. Linden, *Examining The Fermi-LAT Third Source Catalog In Search Of Dark Matter Subhalos*, *JCAP* **1512** (2015) 035, [1504.02087].

[247] B. Bertoni, D. Hooper and T. Linden, *Is The Gamma-Ray Source 3FGL J2212.5+0703 A Dark Matter Subhalo?*, *JCAP* **1605** (2016) 049, [1602.07303].

[248] D. Schoonenberg, J. Gaskins, G. Bertone and J. Diemand, *Dark matter subhalos and unidentified sources in the Fermi 3FGL source catalog*, *JCAP* **1605** (2016) 028, [1601.06781].

[249] A. Berlin and D. Hooper, *Stringent Constraints on the Dark Matter Annihilation Cross Section From Subhalo Searches with the Fermi Gamma-Ray Space Telescope*, *Phys. Rev.* **D89** (2014) 016014, [1309.0525].

[250] A. V. Belikov, D. Hooper and M. R. Buckley, *Searching For Dark Matter Subhalos In the Fermi-LAT Second Source Catalog*, *Phys.Rev.* **D86** (2012) 043504, [1111.2613].

[251] M. R. Buckley and D. Hooper, *Dark Matter Subhalos In the Fermi First Source Catalog*, *Phys.Rev.* **D82** (2010) 063501, [1004.1644].

[252] Fermi LAT Collaboration collaboration, M. Ackermann et al., *Search for Dark Matter Satellites using the FERMI-LAT*, *Astrophys.J.* **747** (2012) 121, [1201.2691].

[253] H.-S. Zechlin, M. Fernandes, D. Elsaesser and D. Horns, *Dark matter subhalos as Fermi gamma-ray sources and first candidates in the 1FGL catalog*, 1110.6868.

[254] N. Mirabal, V. Frias-Martinez, T. Hassan and E. Frias-Martinez, *Fermi's Sibyl: Mining the gamma-ray sky for dark matter subhaloes*, *Mon.Not.Roy.Astron.Soc.* **424** (2012) L64, [1205.4825].

[255] N. Mirabal, D. Nieto and S. Pardo, *The exotic fraction among unassociated Fermi sources*, 1007.2644.

[256] H.-S. Zechlin and D. Horns, *Unidentified sources in the Fermi-LAT second source catalog: the case for DM subhalos*, *JCAP* **1211** (2012) 050, [1210.3852].

[257] M. Kuhlen, J. Diemand and P. Madau, *The Dark Matter Annihilation Signal from Galactic Substructure: Predictions for GLAST*, *Astrophys.J.* **686** (2008) 262, [0805.4416].

[258] L. Pieri, G. Bertone and E. Branchini, *Dark Matter Annihilation in Substructures Revised*, *Mon.Not.Roy.Astron.Soc.* **384** (2008) 1627, [0706.2101].

[259] E. Baltz, B. Berenji, G. Bertone, L. Bergstrom, E. Bloom et al., *Pre-launch estimates for GLAST sensitivity to Dark Matter annihilation signals*, *JCAP* **0807** (2008) 013, [0806.2911].

[260] V. Springel, S. D. White, C. S. Frenk, J. F. Navarro, A. Jenkins et al., *A blueprint for detecting supersymmetric dark matter in the Galactic halo*, 0809.0894.

[261] V. Springel, S. White, C. Frenk, J. Navarro, A. Jenkins et al., *Prospects for detecting supersymmetric dark matter in the Galactic halo*, *Nature* **456N7218** (2008) 73–80.

[262] S. M. Koushiappas, A. R. Zentner and T. P. Walker, *The observability of gamma-rays from neutralino annihilations in Milky Way substructure*, *Phys.Rev.* **D69** (2004) 043501, [astro-ph/0309464].

[263] A. Tasitsiomi and A. Olinto, *The Detectability of neutralino clumps via atmospheric Cherenkov telescopes*, *Phys.Rev.* **D66** (2002) 083006, [astro-ph/0206040].

[264] T. Ishiyama, J. Makino and T. Ebisuzaki, *Gamma-ray Signal from Earth-mass Dark Matter Microhalos*, *Astrophys. J.* **723** (2010) L195, [1006.3392].

[265] M. Hütten, C. Combet, G. Maier and D. Maurin, *Dark matter substructure modelling and sensitivity of the Cherenkov Telescope Array to Galactic dark halos*, *JCAP* **1609** (2016) 047, [1606.04898].

[266] Fermi-LAT Collaboration collaboration, F. Acero et al., *Fermi Large Area Telescope Third Source Catalog*, 1501.02003.

[267] N. Mirabal, E. Charles, E. C. Ferrara, P. L. Gonthier, A. K. Harding, M. A. Snchez-Conde et al., *3FGL Demographics Outside the Galactic Plane using Supervised Machine Learning: Pulsar and Dark Matter Subhalo Interpretations*, *Astrophys. J.* **825** (2016) 69, [1605.00711].

[268] B. Moore, F. Governato, T. R. Quinn, J. Stadel and G. Lake, *Resolving the structure of cold dark matter halos*, *Astrophys. J.* **499** (1998) L5, [astro-ph/9709051].

[269] S. Ghigna, B. Moore, F. Governato, G. Lake, T. R. Quinn and J. Stadel, *Density profiles and substructure of dark matter halos. Converging results at ultra-high numerical resolution*, *Astrophys. J.* **544** (2000) 616, [astro-ph/9910166].

[270] B. Moore, T. R. Quinn, F. Governato, J. Stadel and G. Lake, *Cold collapse and the core catastrophe*, *Mon. Not. Roy. Astron. Soc.* **310** (1999) 1147–1152, [astro-ph/9903164].

[271] E. Hayashi, J. F. Navarro, J. E. Taylor, J. Stadel and T. R. Quinn, *The Structural evolution of substructure*, *Astrophys. J.* **584** (2003) 541–558, [astro-ph/0203004].

[272] S. Kazantzidis, L. Mayer, C. Mastropietro, J. Diemand, J. Stadel and B. Moore, *Density profiles of cold dark matter substructure: Implications for the missing satellites problem*, *Astrophys. J.* **608** (2004) 663–3679, [astro-ph/0312194].

[273] G. Taffoni, L. Mayer, M. Colpi and F. Governato, *On the life and death of satellite haloes*, *Mon. Not. Roy. Astron. Soc.* **341** (2003) 434, [astro-ph/0301271].

[274] J. E. Taylor and A. Babul, *The Evolution of substructure in galaxy, group and cluster haloes. 1. Basic dynamics*, *Mon. Not. Roy. Astron. Soc.* **348** (2004) 811, [astro-ph/0301612].

[275] E. Romano-Diaz, Y. Hoffman, C. Heller, A. Faltenbacher, D. Jones and I. Shlosman, *Evolution of Characteristic Quantities for Dark Matter Halo Density Profiles*, *Astrophys. J.* **657** (2007) 56–70, [astro-ph/0610090].

[276] L. V. Sales, J. F. Navarro, M. G. Abadi and M. Steinmetz, *Satellites of Simulated Galaxies: survival, merging, and their relation to the dark and stellar halos*, *Mon. Not. Roy. Astron. Soc.* **379** (2007) 1464–1474, [0704.1770].

[277] J. Diemand, M. Kuhlen and P. Madau, *Formation and evolution of galaxy dark matter halos and their substructure*, *Astrophys. J.* **667** (2007) 859–877, [astro-ph/0703337].

[278] J. Penarrubia, J. F. Navarro and A. W. McConnachie, *The Tidal Evolution of Local Group Dwarf Spheroidals*, *Astrophys. J.* **673** (2008) 226, [0708.3087].

[279] J.-H. Choi, M. D. Weinberg and N. Katz, *The dynamics of satellite disruption in cold dark matter haloes*, *Mon. Not. Roy. Astron. Soc.* **400** (2009) 1247, [0812.0009].

[280] J. Penarrubia, A. J. Benson, M. G. Walker, G. Gilmore, A. McConnachie and L. Mayer, *The impact of dark matter cusps and cores on the satellite galaxy population around spiral galaxies*, *Mon. Not. Roy. Astron. Soc.* **406** (2010) 1290, [1002.3376].

[281] S.-H. Oh, C. Brook, F. Governato, E. Brinks, L. Mayer, W. J. G. de Blok et al., *The central slope of dark matter cores in dwarf galaxies: Simulations vs. THINGS*, *Astron. J.* **142** (2011) 24, [1011.2777].

[282] T. Ishiyama, *Hierarchical Formation of Dark Matter Halos and the Free Streaming Scale*, *Astrophys. J.* **788** (2014) 27, [1404.1650].

[283] F. Jiang and F. C. van den Bosch, *Statistics of dark matter substructure I. Model and universal fitting functions*, *Mon. Not. Roy. Astron. Soc.* **458** (2016) 2848–2869, [1403.6827].

[284] F. C. van den Bosch and F. Jiang, *Statistics of Dark Matter Substructure: II. Comparison of Model with Simulation Results*, 1403.6835.

[285] S.-H. Oh et al., *High-resolution mass models of dwarf galaxies from LITTLE THINGS*, *Astron. J.* **149** (2015) 180, [1502.01281].

[286] A. Moline, M. A. Sanchez-Conde, S. Palomares-Ruiz and F. Prada, *Characterization of subhalo structural properties and implications for dark matter annihilation signals*, 1603.04057.

[287] J. Diemand, M. Kuhlen, P. Madau, M. Zemp, B. Moore, D. Potter et al., *Clumps and streams in the local dark matter distribution*, *Nature* **454** (2008) 735–738, [0805.1244].

[288] S. Garrison-Kimmel, M. Boylan-Kolchin, J. Bullock and K. Lee, *ELVIS: Exploring the Local Volume in Simulations*, *Mon. Not. Roy. Astron. Soc.* **438** (2014) 2578–2596, [1310.6746].

[289] E. Polisensky and M. Ricotti, *Massive Milky Way Satellites in Cold and Warm Dark Matter: Dependence on Cosmology*, *Mon. Not. Roy. Astron. Soc.* **437** (2014) 2922–2931, [1310.0430].

[290] V. Springel, J. Wang, M. Vogelsberger, A. Ludlow, A. Jenkins, A. Helmi et al., *The Aquarius Project: the subhalos of galactic halos*, *Mon. Not. Roy. Astron. Soc.* **391** (2008) 1685–1711, [0809.0898].

[291] G. Despali and S. Vegetti, *The impact of baryonic physics on the subhalo mass function and implications for gravitational lensing*, 1608.06938.

[292] http://home.thep.lu.se/~torbjorn/Pythia.html.

[293] F. Calore, V. De Romeri, M. Di Mauro, F. Donato and F. Marinacci, *Realistic estimation for the detectability of dark matter sub-halos with Fermi-LAT*, 1611.03503.

[294] Z.-Q. Xia et al., *A Spatially-Extended Stable Unidentified GeV Source: 3FGL J1924.8-1034*, 1611.05565.

[295] S. Profumo, K. Sigurdson and M. Kamionkowski, *What mass are the smallest protohalos?*, *Phys. Rev. Lett.* **97** (2006) 031301, [astro-ph/0603373].

[296] T. Bringmann, *Particle Models and the Small-Scale Structure of Dark Matter*, *New J. Phys.* **11** (2009) 105027, [0903.0189].

[297] J. M. Cornell, S. Profumo and W. Shepherd, *Kinetic Decoupling and Small-Scale Structure in Effective Theories of Dark Matter*, *Phys. Rev.* **D88** (2013) 015027, [1305.4676].

[298] J. Diemand, M. Kuhlen and P. Madau, *Dark matter substructure and gamma-ray annihilation in the Milky Way halo*, *Astrophys.J.* **657** (2007) 262–270, [astro-ph/0611370].

[299] T. Sawala, P. Pihajoki, P. H. Johansson, C. S. Frenk, J. F. Navarro, K. A. Oman et al., *Shaken and Stirred: The Milky Way's Dark Substructures*, 1609.01718.

[300] R. Errani, J. Penarrubia, C. F. P. Laporte and F. A. Gomez, *The effect of a disc on the population of cuspy and cored dark matter substructures in milky way-like galaxies*, *ArXiv e-prints* (aug, 2016) , [1608.01849].

[301] Q. Zhu, F. Marinacci, M. Maji, Y. Li, V. Springel and L. Hernquist, *Baryonic impact on the dark matter distribution in Milky Way-sized galaxies and their satellites*, *Mon. Not. Roy. Astron. Soc.* **458** (2016) 1559–1580, [1506.05537].

[302] A. A. Moiseev et al., *Compton-Pair Production Space Telescope (ComPair) for MeV Gamma-ray Astronomy*, 1508.07349.

[303] V. Tatischeff et al., *The e-ASTROGAM gamma-ray space mission*, *Proc. SPIE Int. Soc. Opt. Eng.* **9905** (2016) 99052N, [1608.03739].

[304] C. Boehm, D. Hooper, J. Silk, M. Casse and J. Paul, *MeV dark matter: Has it been detected?*, *Phys. Rev. Lett.* **92** (2004) 101301, [astro-ph/0309686].

[305] D. P. Finkbeiner, *WMAP microwave emission interpreted as dark matter annihilation in the inner galaxy*, astro-ph/0409027.

[306] D. Hooper, D. P. Finkbeiner and G. Dobler, *Possible evidence for dark matter annihilations from the excess microwave emission around the center of the Galaxy seen by the Wilkinson Microwave Anisotropy Probe*, *Phys. Rev.* **D76** (2007) 083012, [0705.3655].

[307] PAMELA collaboration, O. Adriani et al., *An anomalous positron abundance in cosmic rays with energies 1.5-100 GeV*, *Nature* **458** (2009) 607–609, [0810.4995].

[308] AMS collaboration, M. Aguilar et al., *First Result from the Alpha Magnetic Spectrometer on the International Space Station: Precision Measurement of the Positron Fraction in Primary Cosmic Rays of 0.5350 GeV*, *Phys. Rev. Lett.* **110** (2013) 141102.

[309] C. Weniger, *A Tentative Gamma-Ray Line from Dark Matter Annihilation at the Fermi Large Area Telescope*, *JCAP* **1208** (2012) 007, [1204.2797].

[310] E. Bulbul, M. Markevitch, A. Foster, R. K. Smith, M. Loewenstein and S. W. Randall, *Detection of An Unidentified Emission Line in the Stacked X-ray spectrum of Galaxy Clusters*, *Astrophys. J.* **789** (2014) 13, [1402.2301].

[311] A. Boyarsky, O. Ruchayskiy, D. Iakubovskyi and J. Franse, *Unidentified Line in X-Ray Spectra of the Andromeda Galaxy and Perseus Galaxy Cluster*, *Phys. Rev. Lett.* **113** (2014) 251301, [1402.4119].

[312] Fermi-LAT collaboration, M. Ackermann et al., *Search for Gamma-ray Spectral Lines with the Fermi Large Area Telescope and Dark Matter Implications*, *Phys. Rev.* **D88** (2013) 082002, [1305.5597].

[313] Hitomi collaboration, F. A. Aharonian et al., *Hitomi constraints on the 3.5 keV line in the Perseus galaxy cluster*, 1607.07420.

[314] D. Hooper, P. Blasi and P. D. Serpico, *Pulsars as the Sources of High Energy Cosmic Ray Positrons*, *JCAP* **0901** (2009) 025, [0810.1527].

[315] I. Cholis and D. Hooper, *Dark Matter and Pulsar Origins of the Rising Cosmic Ray Positron Fraction in Light of New Data From AMS*, *Phys. Rev.* **D88** (2013) 023013, [1304.1840].

[316] R. M. Crocker et al., *Sub-luminous '1991bg-Like' Thermonuclear Supernovae Account for Most Diffuse Antimatter in the Milky Way*, 1607.03495.

[317] M. Su, T. R. Slatyer and D. P. Finkbeiner, *Giant Gamma-ray Bubbles from Fermi-LAT: AGN Activity or Bipolar Galactic Wind?*, *Astrophys. J.* **724** (2010) 1044–1082, [1005.5480].

[318] B. Zhou, Y.-F. Liang, X. Huang, X. Li, Y.-Z. Fan, L. Feng et al., *GeV excess in the Milky Way: The role of diffuse galactic gamma-ray emission templates*, *Phys. Rev.* **D91** (2015) 123010, [1406.6948].

[319] X. Huang, T. Enlin and M. Selig, *Galactic dark matter search via phenomenological astrophysics modeling*, *JCAP* **1604** (2016) 030, [1511.02621].

[320] D. Hooper and G. Mohlabeng, *The Gamma-Ray Luminosity Function of Millisecond Pulsars and Implications for the GeV Excess*, *JCAP* **1603** (2016) 049, [1512.04966].

[321] A. Cuoco, M. Krmer and M. Korsmeier, *Novel dark matter constraints from antiprotons in the light of AMS-02*, 1610.03071.

[322] M.-Y. Cui, Q. Yuan, Y.-L. S. Tsai and Y.-Z. Fan, *A possible dark matter annihilation signal in the AMS-02 antiproton data*, 1610.03840.

[323] D. Hooper, T. Linden and P. Mertsch, *What Does The PAMELA Antiproton Spectrum Tell Us About Dark Matter?*, *JCAP* **1503** (2015) 021, [1410.1527].

[324] A. Geringer-Sameth, M. G. Walker, S. M. Koushiappas, S. E. Koposov, V. Belokurov et al., *Evidence for Gamma-ray Emission from the Newly Discovered Dwarf Galaxy Reticulum 2*, 1503.02320.

[325] D. Hooper and T. Linden, *On The Gamma-Ray Emission From Reticulum II and Other Dwarf Galaxies*, 1503.06209.

[326] S. Li, Y.-F. Liang, K.-K. Duan, Z.-Q. Shen, X. Huang, X. Li et al., *Search for gamma-ray emission from eight dwarf spheroidal galaxy candidates discovered in Year Two of Dark Energy Survey with Fermi-LAT data*, *Phys. Rev.* **D93** (2016) 043518, [1511.09252].

[327] DES, Fermi-LAT collaboration, A. Albert et al., *Searching for Dark Matter Annihilation in Recently Discovered Milky Way Satellites with Fermi-LAT*, *Astrophys. J.* **834** (2017) 110, [1611.03184].

[328] Y.-P. Wang et al., *Testing the dark matter subhalo hypothesis of the gamma-ray source 3FGL J2212.5+0703*, *Phys. Rev.* **D94** (2016) 123002, [1611.05135].

[329] A. Berlin, D. Hooper and S. D. McDermott, *Simplified Dark Matter Models for the Galactic Center Gamma-Ray Excess*, *Phys. Rev.* **D89** (2014) 115022, [1404.0022].

[330] S. Ipek, D. McKeen and A. E. Nelson, *A Renormalizable Model for the Galactic Center Gamma Ray Excess from Dark Matter Annihilation*, *Phys. Rev.* **D90** (2014) 055021, [1404.3716].

[331] C. Boehm, M. J. Dolan, C. McCabe, M. Spannowsky and C. J. Wallace, *Extended gamma-ray emission from Coy Dark Matter*, *JCAP* **1405** (2014) 009, [1401.6458].

[332] D. Hooper, *Z' mediated dark matter models for the Galactic Center gamma-ray excess*, *Phys. Rev.* **D91** (2015) 035025, [1411.4079].

[333] A. Berlin, P. Gratia, D. Hooper and S. D. McDermott, *Hidden Sector Dark Matter Models for the Galactic Center Gamma-Ray Excess*, *Phys. Rev.* **D90** (2014) 015032, [1405.5204].

[334] P. Agrawal, B. Batell, D. Hooper and T. Lin, *Flavored Dark Matter and the Galactic Center Gamma-Ray Excess*, *Phys. Rev.* **D90** (2014) 063512, [1404.1373].

[335] E. Izaguirre, G. Krnjaic and B. Shuve, *The Galactic Center Excess from the Bottom Up*, *Phys. Rev.* **D90** (2014) 055002, [1404.2018].

[336] C. Cheung, M. Papucci, D. Sanford, N. R. Shah and K. M. Zurek, *NMSSM Interpretation of the Galactic Center Excess*, *Phys. Rev.* **D90** (2014) 075011, [1406.6372].

[337] D. G. Cerdeo, M. Peir and S. Robles, *Low-mass right-handed sneutrino dark matter: SuperCDMS and LUX constraints and the Galactic Centre gamma-ray excess*, *JCAP* **1408** (2014) 005, [1404.2572].

[338] A. Alves, S. Profumo, F. S. Queiroz and W. Shepherd, *Effective field theory approach to the Galactic Center gamma-ray excess*, *Phys. Rev.* **D90** (2014) 115003, [1403.5027].

[339] D. Hooper, N. Weiner and W. Xue, *Dark Forces and Light Dark Matter*, *Phys. Rev.* **D86** (2012) 056009, [1206.2929].

[340] P. Ko, W.-I. Park and Y. Tang, *Higgs portal vector dark matter for* GeV *scale γ-ray excess from galactic center*, *JCAP* **1409** (2014) 013, [1404.5257].

[341] C. Boehm, M. J. Dolan and C. McCabe, *A weighty interpretation of the Galactic Centre excess*, *Phys. Rev.* **D90** (2014) 023531, [1404.4977].

[342] M. Abdullah, A. DiFranzo, A. Rajaraman, T. M. P. Tait, P. Tanedo and A. M. Wijangco, *Hidden on-shell mediators for the Galactic Center γ-ray excess*, *Phys. Rev.* **D90** (2014) 035004, [1404.6528].

[343] A. Martin, J. Shelton and J. Unwin, *Fitting the Galactic Center Gamma-Ray Excess with Cascade Annihilations*, *Phys. Rev.* **D90** (2014) 103513, [1405.0272].

[344] J. M. Cline, G. Dupuis, Z. Liu and W. Xue, *The windows for kinetically mixed Z'-mediated dark matter and the galactic center gamma ray excess*, *JHEP* **08** (2014) 131, [1405.7691].

[345] Y. G. Kim, K. Y. Lee, C. B. Park and S. Shin, *Secluded singlet fermionic dark matter driven by the Fermi gamma-ray excess*, *Phys. Rev.* **D93** (2016) 075023, [1601.05089].

[346] C. Karwin, S. Murgia, T. M. P. Tait, T. A. Porter and P. Tanedo, *Dark Matter Interpretation of the Fermi-LAT Observation Toward the Galactic Center*, 1612.05687.

[347] K. Ghorbani, *Fermionic dark matter with pseudo-scalar Yukawa interaction*, *JCAP* **1501** (2015) 015, [1408.4929].

[348] CMS collaboration, V. Khachatryan et al., *Search for narrow resonances in dilepton mass spectra in proton-proton collisions at $\sqrt{s} = 13$ TeV and combination with 8 TeV data*, *Submitted to: Phys. Lett. B* (2016) , [1609.05391].

[349] CMS collaboration, V. Khachatryan et al., *Search for narrow resonances decaying to dijets in proton-proton collisions at $\sqrt(s) = 13$ TeV*, *Phys. Rev. Lett.* **116** (2016) 071801, [1512.01224].

[350] CMS collaboration, C. Collaboration, *Search for dark matter in final states with an energetic jet, or a hadronically decaying W or Z boson using* 12.9 fb^{-1} *of data at* $\sqrt{s} = 13$ TeV, .

[351] CMS Collaboration collaboration, *An inclusive search for new phenomena in final states with one or more jets and missing transverse momentum at 13 TeV with the AlphaT variable*, Tech. Rep. CMS-PAS-SUS-16-016, CERN, Geneva, 2016.

[352] ATLAS collaboration, T. A. collaboration, *Search for new high-mass resonances in the dilepton final state using proton-proton collisions at* $\sqrt{s}$ *= 13 TeV with the ATLAS detector*, .

[353] ATLAS collaboration, M. Aaboud et al., *Search for new phenomena in final states with an energetic jet and large missing transverse momentum in pp collisions at* $\sqrt{s} = 13 TeV$ *using the ATLAS detector*, *Phys. Rev.* **D94** (2016) 032005, [1604.07773].

[354] ATLAS collaboration, M. Aaboud et al., *Search for new phenomena in events with a photon and missing transverse momentum in pp collisions at* $\sqrt{s} = 13$ *TeV with the ATLAS detector*, *JHEP* **06** (2016) 059, [1604.01306].

[355] CMS collaboration, C. Collaboration, *Search for a neutral MSSM Higgs boson decaying into* $\tau\tau$ *at 13 TeV*, .

[356] CMS collaboration, C. Collaboration, *Search for a narrow heavy decaying to bottom quark pairs in the 13 TeV data sample*, .

[357] OPAL, DELPHI, LEP Working Group for Higgs boson searches, ALEPH, L3 collaboration, R. Barate et al., *Search for the standard model Higgs boson at LEP*, *Phys. Lett.* **B565** (2003) 61–75, [hep-ex/0306033].

[358] M. J. Dolan, F. Kahlhoefer, C. McCabe and K. Schmidt-Hoberg, *A taste of dark matter: Flavour constraints on pseudoscalar mediators*, *JHEP* **03** (2015) 171, [1412.5174].

[359] A. Alloul, N. D. Christensen, C. Degrande, C. Duhr and B. Fuks, *FeynRules 2.0 - A complete toolbox for tree-level phenomenology*, *Comput. Phys. Commun.* **185** (2014) 2250–2300, [1310.1921].

[360] J. Alwall, R. Frederix, S. Frixione, V. Hirschi, F. Maltoni, O. Mattelaer et al., *The automated computation of tree-level and next-to-leading order differential cross sections, and their matching to parton shower simulations*, *JHEP* **07** (2014) 079, [1405.0301].

[361] V. Hirschi and O. Mattelaer, *Automated event generation for loop-induced processes*, *JHEP* **10** (2015) 146, [1507.00020].

[362] T. Sjostrand, S. Mrenna and P. Z. Skands, *A Brief Introduction to PYTHIA 8.1*, *Comput.Phys.Commun.* **178** (2008) 852–867, [0710.3820].

[363] DELPHES 3 collaboration, J. de Favereau, C. Delaere, P. Demin, A. Giammanco, V. Lematre, A. Mertens et al., *DELPHES 3, A modular framework for fast simulation of a generic collider experiment*, *JHEP* **02** (2014) 057, [1307.6346].

[364] M. Duerr, F. Kahlhoefer, K. Schmidt-Hoberg, T. Schwetz and S. Vogl, *How to save the WIMP: global analysis of a dark matter model with two s-channel mediators*, *JHEP* **09** (2016) 042, [1606.07609].

[365] C. Englert, M. McCullough and M. Spannowsky, *S-Channel Dark Matter Simplified Models and Unitarity*, *Phys. Dark Univ.* **14** (2016) 48–56, [1604.07975].

[366] G. Busoni et al., *Recommendations on presenting LHC searches for missing transverse energy signals using simplified s-channel models of dark matter*, 1603.04156.

[367] F. Kahlhoefer, K. Schmidt-Hoberg, T. Schwetz and S. Vogl, *Implications of unitarity and gauge invariance for simplified dark matter models*, *JHEP* **02** (2016) 016, [1510.02110].

[368] J. Abdallah et al., *Simplified Models for Dark Matter Searches at the LHC*, *Phys. Dark Univ.* **9-10** (2015) 8–23, [1506.03116].

[369] BaBar collaboration, J. P. Lees et al., *Search for hadronic decays of a light Higgs boson in the radiative decay* $\Upsilon \to \gamma A^0$, *Phys. Rev. Lett.* **107** (2011) 221803, [1108.3549].

[370] BaBar collaboration, J. P. Lees et al., *Search for a low-mass scalar Higgs boson decaying to a tau pair in single-photon decays of* $\Upsilon(1S)$, *Phys. Rev.* **D88** (2013) 071102, [1210.5669].

[371] BaBar collaboration, J. P. Lees et al., *Search for di-muon decays of a low-mass Higgs boson in radiative decays of the (1S)*, *Phys. Rev.* **D87** (2013) 031102, [1210.0287].

[372] BaBar collaboration, J. P. Lees et al., *Search for a light Higgs resonance in radiative decays of the Y(1S) with a charm tag*, *Phys. Rev.* **D91** (2015) 071102, [1502.06019].

[373] J. D. Clarke, R. Foot and R. R. Volkas, *Phenomenology of a very light scalar (100 MeV ¡ m_h ¡ 10 GeV) mixing with the SM Higgs*, *JHEP* **02** (2014) 123, [1310.8042].

[374] U. Haisch and J. F. Kamenik, *Searching for new spin-0 resonances at LHCb*, *Phys. Rev.* **D93** (2016) 055047, [1601.05110].

[375] J. Kopp, V. Niro, T. Schwetz and J. Zupan, *DAMA/LIBRA and leptonically interacting Dark Matter*, *Phys. Rev.* **D80** (2009) 083502, [0907.3159].

[376] C. Savage, G. Gelmini, P. Gondolo and K. Freese, *Compatibility of DAMA/LIBRA dark matter detection with other searches*, *JCAP* **0904** (2009) 010, [0808.3607].

[377] H.-Y. Cheng and C.-W. Chiang, *Revisiting Scalar and Pseudoscalar Couplings with Nucleons*, *JHEP* **07** (2012) 009, [1202.1292].

[378] F. Calore, I. Cholis, C. McCabe and C. Weniger, *A Tale of Tails: Dark Matter Interpretations of the Fermi GeV Excess in Light of Background Model Systematics*, *Phys.Rev.* **D91** (2015) 063003, [1411.4647].

[379] B. Batell, T. Lin and L.-T. Wang, *Flavored Dark Matter and R-Parity Violation*, *JHEP* **01** (2014) 075, [1309.4462].

[380] P. Agrawal, S. Blanchet, Z. Chacko and C. Kilic, *Flavored Dark Matter, and Its Implications for Direct Detection and Colliders*, *Phys. Rev.* **D86** (2012) 055002, [1109.3516].

[381] P. Agrawal, Z. Chacko, C. Kilic and R. K. Mishra, *A Classification of Dark Matter Candidates with Primarily Spin-Dependent Interactions with Matter*, 1003.1912.

[382] Snowmass 2013 Cosmic Frontier Working Groups 14 collaboration, D. Bauer et al., *Dark Matter in the Coming Decade: Complementary Paths to Discovery and Beyond*, *Phys. Dark Univ.* **7-8** (2015) 16–23, [1305.1605].

[383] XENON collaboration, E. Aprile et al., *Physics reach of the XENON1T dark matter experiment*, *JCAP* **1604** (2016) 027, [1512.07501].

[384] D. C. Malling et al., *After LUX: The LZ Program*, 1110.0103.

[385] J. L. Newstead, T. D. Jacques, L. M. Krauss, J. B. Dent and F. Ferrer, *Scientific reach of multiton-scale dark matter direct detection experiments*, *Phys. Rev.* **D88** (2013) 076011, [1306.3244].

[386] P. Cushman et al., *Working Group Report: WIMP Dark Matter Direct Detection*, in *Proceedings, 2013 Community Summer Study on the Future of U.S. Particle Physics: Snowmass on the Mississippi (CSS2013): Minneapolis, MN, USA, July 29-August 6, 2013*, 2013. 1310.8327.

[387] J. Billard, L. Strigari and E. Figueroa-Feliciano, *Implication of neutrino backgrounds on the reach of next generation dark matter direct detection experiments*, *Phys. Rev.* **D89** (2014) 023524, [1307.5458].

[388] F. Ruppin, J. Billard, E. Figueroa-Feliciano and L. Strigari, *Complementarity of dark matter detectors in light of the neutrino background*, *Phys. Rev.* **D90** (2014) 083510, [1408.3581].

[389] J. H. Davis, *Dark Matter vs. Neutrinos: The effect of astrophysical uncertainties and timing information on the neutrino floor*, *JCAP* **1503** (2015) 012, [1412.1475].

[390] J. B. Dent, B. Dutta, J. L. Newstead and L. E. Strigari, *Effective field theory treatment of the neutrino background in direct dark matter detection experiments*, *Phys. Rev.* **D93** (2016) 075018, [1602.05300].

[391] R. J. Hill and M. P. Solon, *Universal behavior in the scattering of heavy, weakly interacting dark matter on nuclear targets*, *Phys. Lett.* **B707** (2012) 539–545, [1111.0016].

[392] R. J. Hill and M. P. Solon, *WIMP-nucleon scattering with heavy WIMP effective theory*, *Phys. Rev. Lett.* **112** (2014) 211602, [1309.4092].

[393] R. J. Hill and M. P. Solon, *Standard Model anatomy of WIMP dark matter direct detection II: QCD analysis and hadronic matrix elements*, *Phys. Rev.* **D91** (2015) 043505, [1409.8290].

[394] A. Berlin, D. S. Robertson, M. P. Solon and K. M. Zurek, *Bino variations: Effective field theory methods for dark matter direct detection*, *Phys. Rev.* **D93** (2016) 095008, [1511.05964].

[395] S. D. McDermott, *Lining up the Galactic Center Gamma-Ray Excess*, *Phys. Dark Univ.* **7-8** (2015) 12–15, [1406.6408].

[396] T. Appelquist et al., *Stealth Dark Matter: Dark scalar baryons through the Higgs portal*, *Phys. Rev.* **D92** (2015) 075030, [1503.04203].

[397] T. Appelquist et al., *Detecting Stealth Dark Matter Directly through Electromagnetic Polarizability*, *Phys. Rev. Lett.* **115** (2015) 171803, [1503.04205].

[398] N. Anand, A. L. Fitzpatrick and W. C. Haxton, *Weakly interacting massive particle-nucleus elastic scattering response*, *Phys. Rev.* **C89** (2014) 065501, [1308.6288].

[399] F. Bishara, J. Brod, B. Grinstein and J. Zupan, *Chiral Effective Theory of Dark Matter Direct Detection*, *JCAP* **02** (2017) 009, [1611.00368].

[400] V. Gluscevic, M. I. Gresham, S. D. McDermott, A. H. G. Peter and K. M. Zurek, *Identifying the Theory of Dark Matter with Direct Detection*, *JCAP* **1512** (2015) 057, [1506.04454].

[401] F. D'Eramo and M. Procura, *Connecting Dark Matter UV Complete Models to Direct Detection Rates via Effective Field Theory*, *JHEP* **04** (2015) 054, [1411.3342].

[402] V. Gluscevic and A. H. G. Peter, *Understanding WIMP-baryon interactions with direct detection: A Roadmap*, *JCAP* **1409** (2014) 040, [1406.7008].

[403] L. Roszkowski, E. M. Sessolo, S. Trojanowski and A. J. Williams, *Reconstructing WIMP properties through an interplay of signal measurements in direct detection, Fermi-LAT, and CTA searches for dark matter*, *JCAP* **1608** (2016) 033, [1603.06519].

[404] S. D. McDermott, H.-B. Yu and K. M. Zurek, *The Dark Matter Inverse Problem: Extracting Particle Physics from Scattering Events*, *Phys. Rev.* **D85** (2012) 123507, [1110.4281].

[405] A. H. G. Peter, V. Gluscevic, A. M. Green, B. J. Kavanagh and S. K. Lee, *WIMP physics with ensembles of direct-detection experiments*, *Phys. Dark Univ.* **5-6** (2014) 45–74, [1310.7039].

[406] R. Catena, *Analysis of the theoretical bias in dark matter direct detection*, *JCAP* **1409** (2014) 049, [1407.0127].

[407] J. B. Dent, L. M. Krauss, J. L. Newstead and S. Sabharwal, *General analysis of direct dark matter detection: From microphysics to observational signatures*, *Phys. Rev.* **D92** (2015) 063515, [1505.03117].

[408] F. S. Queiroz, W. Rodejohann and C. E. Yaguna, *Is the dark matter particle its own antiparticle?*, 1610.06581.

[409] K. Freese, J. A. Frieman and A. Gould, *Signal Modulation in Cold Dark Matter Detection*, *Phys. Rev.* **D37** (1988) 3388–3405.

[410] K. Freese, M. Lisanti and C. Savage, *Colloquium: Annual modulation of dark matter*, *Rev. Mod. Phys.* **85** (2013) 1561–1581, [1209.3339].

[411] V. Britto and J. Meyers, *Monthly Modulation in Dark Matter Direct-Detection Experiments*, *JCAP* **1511** (2015) 006, [1409.2858].

[412] C. Kouvaris and N. G. Nielsen, *Daily modulation and gravitational focusing in direct dark matter search experiments*, *Phys. Rev.* **D92** (2015) 075016, [1505.02615].

[413] E. Del Nobile, G. B. Gelmini and S. J. Witte, *Prospects for detection of target-dependent annual modulation in direct dark matter searches*, *JCAP* **1602** (2016) 009, [1512.03961].

[414] J. Bovy and H.-W. Rix, *A Direct Dynamical Measurement of the Milky Way's Disk Surface Density Profile, Disk Scale Length, and Dark Matter Profile at 4 kpc $\lesssim R \lesssim$ 9 kpc*, *Astrophys. J.* **779** (2013) 115, [1309.0809].

[415] A. M. Green, *A Potential WIMP signature for the caustic ring halo model*, *Phys. Rev.* **D63** (2001) 103003, [astro-ph/0012393].

[416] J. M. A. Danby and G. L. Camm, *Statistical dynamics and accretion*, *Monthly Notices of the Royal Astronomical Society* **117** (1957) 50–71, [http://mnras.oxfordjournals.org/content/117/1/50.full.pdf+html].

[417] K. Griest, *Effect of the Sun's Gravity on the Distribution and Detection of Dark Matter Near the Earth*, *Phys. Rev.* **D37** (1988) 2703.

[418] P. Sikivie and S. Wick, *Solar wakes of dark matter flows*, *Phys. Rev.* **D66** (2002) 023504, [astro-ph/0203448].

[419] J. Bagnasco, M. Dine and S. D. Thomas, *Detecting technibaryon dark matter*, *Phys. Lett.* **B320** (1994) 99–104, [hep-ph/9310290].

[420] N. Weiner and I. Yavin, *UV completions of magnetic inelastic and Rayleigh dark matter for the Fermi Line(s)*, *Phys. Rev.* **D87** (2013) 023523, [1209.1093].

[421] Buchner, J., Georgakakis, A., Nandra, K., Hsu, L., Rangel, C., Brightman, M. et al., *X-ray spectral modelling of the agn obscuring region in the cdfs: Bayesian model selection and catalogue*, *A&A* **564** (2014) A125.

[422] F. Feroz, M. P. Hobson and M. Bridges, *MultiNest: an efficient and robust Bayesian inference tool for cosmology and particle physics*, *Mon. Not. Roy. Astron. Soc.* **398** (2009) 1601–1614, [0809.3437].

[423] F. Feroz and M. P. Hobson, *Multimodal nested sampling: an efficient and robust alternative to MCMC methods for astronomical data analysis*, *Mon. Not. Roy. Astron. Soc.* **384** (2008) 449, [0704.3704].

[424] F. Feroz, M. P. Hobson, E. Cameron and A. N. Pettitt, *Importance Nested Sampling and the MultiNest Algorithm*, 1306.2144.

[425] S. J. Witte and G. B. Gelmini, *Updated Constraints on the Dark Matter Interpretation of CDMS-II-Si Data*, *JCAP* **1705** (2017) 026, [1703.06892].

[426] D. Hooper and S. J. Witte, *Gamma Rays From Dark Matter Subhalos Revisited: Refining the Predictions and Constraints*, *JCAP* **1704** (2017) 018, [1610.07587].

[427] M. Escudero, D. Hooper and S. J. Witte, *Updated Collider and Direct Detection Constraints on Dark Matter Models for the Galactic Center Gamma-Ray Excess*, *JCAP* **1702** (2017) 038, [1612.06462].

[428] S. J. Witte, V. Gluscevic and S. D. McDermott, *Prospects for Distinguishing Dark Matter Models Using Annual Modulation*, *JCAP* **1702** (2017) 044, [1612.07808].